

International Atomic Energy Agency

INDC(NDS)-247

Distr.: L

INDC

INTERNATIONAL NUCLEAR DATA COMMITTEE

**METHODS FOR THE CALCULATION OF NEUTRON NUCLEAR DATA
FOR STRUCTURAL MATERIALS OF FAST AND FUSION REACTORS**

Texts of Papers Presented at the
Final Meeting of a Co-ordinated Research Programme
organized by the
International Atomic Energy Agency
and held in
Vienna, Austria, 20-22 June 1990

Compiled by

D.W. Muir
IAEA Nuclear Data Section

July 1991

IAEA NUCLEAR DATA SECTION, WAGRAMERSTRASSE 5, A-1400 VIENNA

**METHODS FOR THE CALCULATION OF NEUTRON NUCLEAR DATA
FOR STRUCTURAL MATERIALS OF FAST AND FUSION REACTORS**

Texts of Papers Presented at the
Final Meeting of a Co-ordinated Research Programme
organized by the
International Atomic Energy Agency
and held in
Vienna, Austria, 20-22 June 1990

Compiled by

D.W. Muir
IAEA Nuclear Data Section

July 1991

Reproduced by the IAEA in Austria
August 1991

91-03102

Foreword

This report contains the texts of the invited presentations delivered at the third Research Co-ordination Meeting of the Co-ordinated Research Programme on Methods for the Calculation of Neutron Nuclear Data for Structural Materials of Fast and Fusion Reactors. The meeting was held at the IAEA Headquarters, Vienna, Austria, from 20 to 22 June 1990. Since the meeting there have been many requests to make the texts of the presentations available in printed form. The texts are reproduced here, directly from the Authors' manuscripts with little or no editing, in the order in which the presentations were made at the meeting.

CONTENTS

Report to the coordinated research programme on methods for the calculation of neutron nuclear data for structural materials of fast and fusion reactors	7
S. Chiba, P.T. Guenther, R.D. Lawson, and A.B. Smith	
Neutron emission cross sections on ^{93}Nb at 20 MeV incident energy	23
A. Marcinkowski and D. Kielan	
Calculation of cross sections of the (n,p) reaction on zirconium isotopes	31
A. Marcinkowski and D. Kielan	
Effect of different level density prescriptions on the calculated neutron nuclear reaction cross-sections	39
S.B. Garg	
Investigation of neutron induced reaction cross- sections of Ni-58 and Ni-60 with various nuclear model evaluation schemes	49
S.B. Garg	
The use of dispersion relations to construct unified nucleon optical potentials	69
P.E. Hodgson	
Global calculations of (n,p) and (n, α) cross- sections from 10 to 20 MeV	77
D. Wilmore and P.E. Hodgson	
Analyses of multistep reaction cross-sections with the Feshbach-Kerman-Koonin Theory	87
P.E. Hodgson	
Evaluation of activation cross sections of Ni- and Mo-isotopes	103
Yutaka Nakajima and Nobuhiro Yamamuro	
Consequences from testing measured and calculated 14.6 MeV neutron inelastic scattering cross sections by means of comparison with results of fast proton inelastic scattering using DWBA and GDH approaches	113
S. Ercakir and H. Jahn	
Recent developments in the theory of nuclear level densities	131
A.M. Anzaldo Meneses	

Models and theory for precompound angular distributions	145
M. Blann, B.A. Pohl, B.A. Remington, W. Scobel	
M. Trabandt, R.C. Byrd, C.C. Foster, R. Bonetti,	
C. Chiesa and S.M. Grimes	
A real part of neutron optical potentials constrained by RMFA calculations	155
S. Gmuca	
Calculation uncertainties on neutron reaction cross- sections, particle emission spectra and angular distributions	169
V.A. Konshin and O.V. Konshin	
Isotopic effects and reaction mechanisms induced by fast neutrons in the mass range $A \approx 50$	197
M. Avrigeanu and V. Avrigeanu	
Analysis of experimental data on neutron induced reactions and development of PCROSS code for the calculation of the differential preequilibrium spectra	213
R. Capote, E. Herrera, R. Lopez, V. Osorio and	
M. Piris	
Efforts in Bologna on quasiparticle level density systematics and on comparison and development of different approaches to preequilibrium reaction mechanism	223
M. Herman, G. Reffo, H.A. Weidenmüller, H. Lenske,	
H.H. Wolter, G. Giardina, A. Italiano and	
M. Rosetti	
Calculation of $(n, x\gamma)$ cross sections between threshold and 100 MeV for Fe and Pb isotopes: comparisons with experimental data	239
P.G. Young, R.C. Haight, R.O. Nelson, S.A. Wender,	
C.M. Laymon, G.L. Morgan, D.M. Drake, M. Drosg,	
H. Vonach, A. Pavlik, S. Tagesen, D.C. Larson	
and D.S. Dale	
The statistics of multi-step direct reactions	251
A.J. Koning and J.M. Akkermans	
Influence of collective excitations on preequilibrium and equilibrium processes	269
A.V. Ignatyuk, V.P. Lunev	

"Methods for the Calculation of Neutron Nuclear Data
for Structural Materials of Fast and Fusion Reactors"

S. Chiba*, P.T. Guenther, R.D. Lawson and A.B. Smith
Argonne National Laboratory
Argonne, Illinois, U.S.A.

A B S T R A C T

The calculation of neutron inelastic-scattering cross sections of vibrational nuclei is discussed, and it is shown that they are large for the yrast levels for $A \approx 110$. It is shown that, in addition to common size and isospin effects, shell and collective effects are requisite to explanations of neutron elastic-scattering ratios. Explicit optical potentials are presented for the interaction of neutrons with ^{58}Ni (spherical and vibrational models), and with zirconium (spherical). It is shown that these potentials provide excellent descriptions of the results of recent comprehensive experimental results.

I. PREFACE

This Project has generally addressed generic issues, frequently at higher energies well above those of primary applied interest. As the Project draws to a close, it is proper to give focus to specific concepts suitable for the explicit calculation of structural-material nuclear data for applied purposes. This contribution is directed toward that end. Section II of this report briefly addresses two issues that arose at the prior meeting. New measurements and their interpretations have substantively contributed to resolving these issues. Section III presents two potentials explicitly suitable for use in the structural-material regions. The first is for ^{58}Ni , and is formulated in the context of both the spherical optical model (SOM), and the coupled-channels model (CCM). The second potential is for elemental zirconium and its isotopes, formulated in the context of the SOM. These potentials are suitable for quantitative applied calculations and demonstrate certain physical properties generic to the respective mass regions. Some suggestions for future studies are given.

II. ISSUES FROM PRIOR MEETING

A. Inelastic Excitation of Vibrational Levels in the
 $A = 100-110$ Region

At the previous meeting it was suggested that the inelastic neutron scattering cross sections of the first few vibrational levels of even isotopes in this mass region might be large (e.g., ≈ 1.5 b) at relatively low incident-neutron energies (e.g., at ≈ 1 MeV). Of particular applied interest are the even isotopes of palladium and ruthenium. This issue was examined using high-resolution experimental measurements and complementary CCM

*Visiting scientist from Japan Atomic Energy Research Institute

interpretations. The results of the work are extensively described in the Laboratory report, ANL/NDM-112, and outlined in a journal paper (Ann. Nucl. Energy 16 637 (1989)). The abstract of the Laboratory report follows:

ABSTRACT: The cross sections for the elastic-scattering of 5.9, 7.1 and 8.0 MeV neutrons from elemental palladium were measured at forty scattering angles distributed between $\approx 15^\circ$ and 160° . The inelastic-scattering cross sections for the excitation of palladium levels at energies of 260 keV to 560 keV were measured with high resolution at the same energies, and at a scattering angle of 80° . The experimental results were combined with lower-energy values previously obtained by this group to provide a comprehensive database extending from near the inelastic-scattering threshold to 8 MeV. That database was interpreted in terms of a coupled-channels model, including the inelastic excitation of one- and two-phonon vibrational levels of the even isotopes of palladium. It was concluded that the palladium inelastic-scattering cross sections, at the low energies of interest in assessment of fast-fission-reactor performance, are large ($\approx 50\%$ greater than given in widely used evaluated fission-product data files). They primarily involve compound-nucleus processes, with only a small direct-reaction component attributable to the excitation of the one-phonon, 2^+ , vibrational levels of the even isotopes of palladium.

B. Ambiguities in Elastic-Scattering Ratios

At the past meeting it was shown that observed ratios of the differential elastic-scattering of 8 MeV neutrons from ^{59}Co and ^{58}Ni were not consistent with the predictions of either a "global" or "regional" SOM. This type of ratio ambiguity has been extensively investigated over the mass range $A \approx 51 \rightarrow 209$, and a number of possible physical contributions to the phenomena have been examined. This work is described in the Laboratory report, ANL/NDM-114, and a shorter version has been submitted to Nucl. Phys. The abstract of the Laboratory report is as follows:

ABSTRACT: Ratios of the cross sections for the elastic scattering of 8 MeV neutrons from adjacent nuclei are measured over the angular range $\approx 20^\circ$ – 160° for the target pairs $^{51}\text{V}/\text{Cr}$, $^{59}\text{Co}/^{58}\text{Ni}$, Cu/Zn , $^{89}\text{Y}/^{93}\text{Nb}$, $^{89}\text{Y}/\text{Zr}$, $^{93}\text{Nb}/\text{Zr}$, In/Cd and $^{209}\text{Bi}/\text{Pb}$. The observed ratios vary from unity by as much as a factor of ≈ 2 at some angles for the lighter target pairs. Approximately half the measured ratios (Cu/Zn , In/Cd and $^{209}\text{Bi}/\text{Pb}$) are reasonably explained by a simple spherical optical model, including size and isospin contributions. In all cases (with the possible exception of the ^{51}V – Cr pair), the geometry of the real optical-model potential is essentially the same for neighboring nuclei, and the real-potential strengths are consistent with the Lane Model. In contrast, it is found that the imaginary potential may be quite different for adjacent nuclei, and the nature of this difference is examined. It is shown that the spin-spin interaction has a negligible effect on the calculation of the elastic-scattering ratios, but that channel coupling, leading to a large reorientation of the target ground state, can be a consideration, particularly in the $^{59}\text{Co}/^{58}\text{Ni}$ case. In the $A \approx 50$ – 60 region the calculated ratios are sensitive to spin-orbit effects, but the exact nature of this interaction must await more definitive polarization measurements. The measured and calculated results suggest that the concept of a conventional "global", or even "regional", optical potential provides no more than a qualitative representation of the physical reality for a number of cases.

III. EXPLICIT POTENTIALS FOR STRUCTURAL MATERIALS

A. Potential for ^{58}Ni

A-1. Introductory Comments

Nickel is a prominent component of radiation-resistant ferrous alloys. Sixty-eight percent of the element consists of ^{58}Ni , and the remainder is largely the

similar isotope ^{60}Ni . ^{58}Ni is a relatively simple nucleus consisting of closed neutron and proton shells ($N = Z = 28$), plus two $1p_{3/2}$ neutrons.¹ The fast-neutron interaction with ^{58}Ni shows characteristics of a direct process, but the details are not clear as the nucleus is neither a simple vibrator or rotator. It has recently been shown that SOMs in the $A = 50-60$ region are very specific to the particular target.² "Global", or even "regional", models fail to describe the interaction with a particular nucleus in quantitative detail. A comprehensive study of the fast-neutron interaction with ^{58}Ni , including measurements and calculations, has been undertaken and is now nearing completion. The following remarks summarize the status of this work, particularly defining detailed SOM and CCM interpretations suitable for quantitative structural-material calculations.

A-2. The Database

A-2-a. Total Cross Sections

Broad-resolution neutron total cross sections were measured from 1 → 10 MeV, with attention to self-shielding effects. These results are consistent with

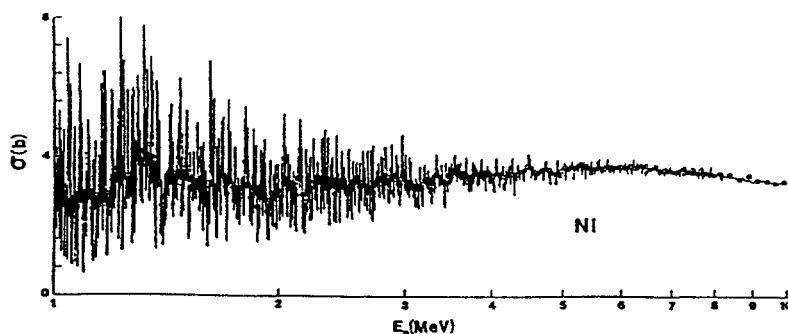


Fig. 1. Neutron total cross sections of ^{58}Ni . The present broad-resolution results are indicated by "O" symbols, and the high-resolution results of Ref. 3 by the curve.

energy averages of high-resolution measurements³, as illustrated in Fig. 1, and provide a database consistent with the concept of an energy-averaged model.

A-2-b. Elastic-Scattering Cross Sections

Differential elastic-scattering cross sections were measured from 1.5 → 10 MeV with sufficient energy-angle detail to define the energy-averaged behavior, with the results shown in Fig. 2. The results are in qualitative agreement with the few comparable distributions found in the literature.

A-2-c. Inelastic-Scattering Cross Sections

Cross sections for the inelastic excitation of the first 2^+ (1.454 MeV) level were measured concurrently with the above elastic scattering, with the results shown in Fig. 3. At lower energies the compound-nucleus process appears to dominate, while the direct reaction predominates at higher energies. High resolution measurements, illustrated in Fig. 4, gave additional information, particularly for the higher-lying levels.

A-2-d. Strength Functions

S- and p-wave strength functions were taken from the compilation of Ref. 4.

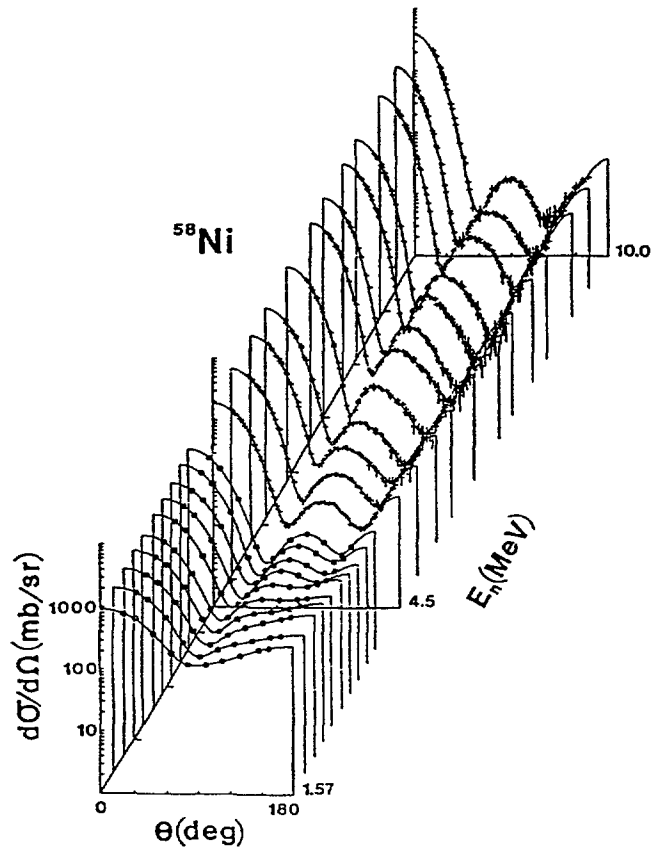


Fig. 2. Measured differential elastic-scattering cross sections. Symbols indicate the measured values, and the curves the results of Legendre-polynomial fits to the data. Data are in the laboratory coordinate system.

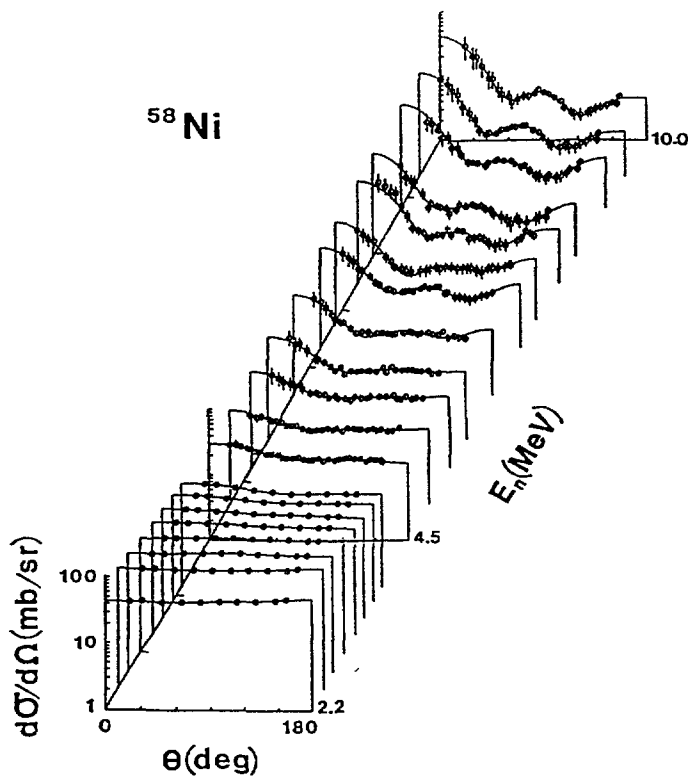


Fig. 3. Measured cross sections (symbols) for the excitation of the 1.454 MeV level of ^{58}Ni . Curves indicate the results of Legendre-polynomial fits. Data are given in the laboratory system.

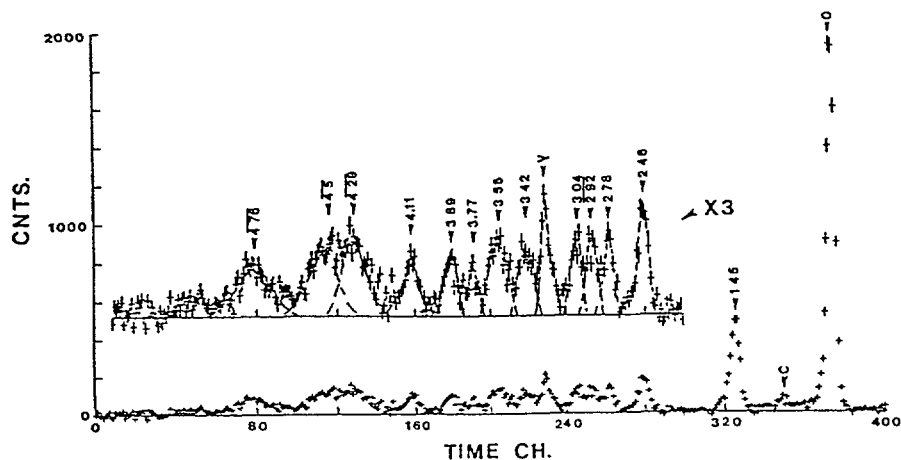


Fig. 4. Time-of-flight spectrum obtained by scattering 8 MeV neutrons from ^{58}Ni over a flight path of 14.65 m. Observed excitation energies are numerically given.

A-3. ^{58}Ni Model Derivation

A-3-a. Phenomenological Spherical Optical Model (SOM)

The objectives of the SOM interpretation were: (i) to provide a basis for the subsequent CCM interpretation, (ii) to gain some physical understanding of the interaction, and (iii) to obtain a simple SOM for applied use. The SOM interpretation was based upon explicit chi-square fitting of the elastic-scattering data, with supporting consideration of total cross sections and strength functions. The elastic-scattering database was taken from the present work to 10 MeV, with five additional distributions extending to 24 MeV taken from the literature.⁵⁻⁸

The interpretation assumed a Saxon-Woods real, a Saxon-Woods-derivative imaginary, and a real Thomas spin-orbit potential.⁹ Compound-nucleus processes were explicitly considered to 8 MeV using the Hauser-Feshbach formula¹⁰, as extended by Moldauer.¹¹ Discrete level excitations were considered to 3.5 MeV¹², and higher-lying levels were represented using the statistical formalism of Gilbert and Cameron.¹³ Above 8 MeV, it was assumed that the elastic scattering was entirely a "shape" process. The fitting is sensitive to the experimental error specification, and that is reasonably known only for the present measurements. For the higher-energy distributions, the uncertainties given in the literature were accepted, though they probably represent only statistical error.

The spin-orbit potential parameters were assumed to be

$$\begin{aligned} V_{\text{so}} &= 5.5 \text{ MeV} \\ r_{\text{so}} &= 1.0 \text{ fm} \\ a_{\text{so}} &= 0.65 \text{ fm.} \end{aligned} \quad (1)$$

These values are similar to those reported from polarization studies in this mass region.¹⁴

With the fixed spin-orbit potential, the elastic-scattering was fitted, starting with six parameters and working progressively to two parameters, constraining first the geometries of the real potential and then those of the imaginary potential. The resulting geometric parameters were

$$\begin{aligned}
r_V &= (1.305 - 0.0064 \cdot E) \text{ fm} \\
a_V &= 0.6461 \text{ fm} \\
r_W &= (1.16 + 0.0023 \cdot E) \text{ fm} \quad (E \geq 5 \text{ MeV}) \\
&= (1.50 - 0.066 \cdot E) \text{ fm} \quad (E \leq 5 \text{ MeV}) \\
a_W &= (0.26 + 0.0205 \cdot E) \text{ fm},
\end{aligned} \tag{2}$$

where E is neutron energy in MeV and the subscripts V and W refer to real and imaginary potentials, respectively. Using these geometries, two parameter fits gave the potential strengths, in volume integral per nucleon, shown in Fig. 5.

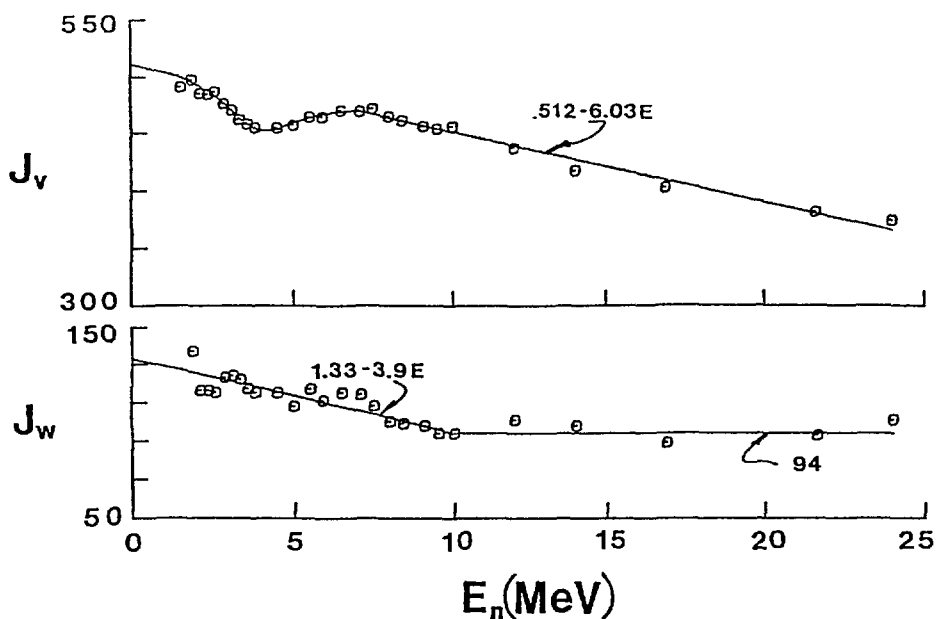


Fig. 5. Real (J_V) and imaginary (J_W) potential strengths for the SOM, as expressed in volume integrals per nucleon. The dimensionality is $\text{MeV}\text{-fm}^3$.

The above SOM provides a good description of the observed elastic scattering to more than 20 MeV, as illustrated in Fig. 6. Measured neutron total cross sections are also reasonably represented, as shown in Fig. 7. The calculated strength functions (in units of 10^{-4}) are $S_0 = 2.34$ and $S_1 = 0.79$, compared to the experimentally deduced values of (2.8 ± 0.6) and (0.5 ± 0.1), respectively.⁴ The SOM also qualitatively represents the compound-nucleus contribution to the inelastic scattering but, of course, cannot represent the direct-reaction contribution evident in Fig. 3. The real-potential geometry is common in this mass region, with the small energy dependence of r_V . J_V generally falls with energy in the familiar manner predicted by Hartree-Fock calculations, but the magnitude is large, and there is a pronounced "dip" in the few-MeV region. This dip is not associated with inappropriate treatment of compound-nucleus effects but, rather, may be a manifestation of collective structures. Above ≈ 6 MeV, the imaginary potential radius is significantly smaller than that of the real potential. This is characteristic of SOM interpretations of vibrational nuclei.¹⁵ Below ≈ 6 MeV, the imaginary potential radius sharply increases and the diffuseness decreases as $E \rightarrow 0$, and both become similar to values found for potentials largely based upon strength functions.¹⁶ The SOM does not contain a volume absorption term, as it could not be supported by the data.

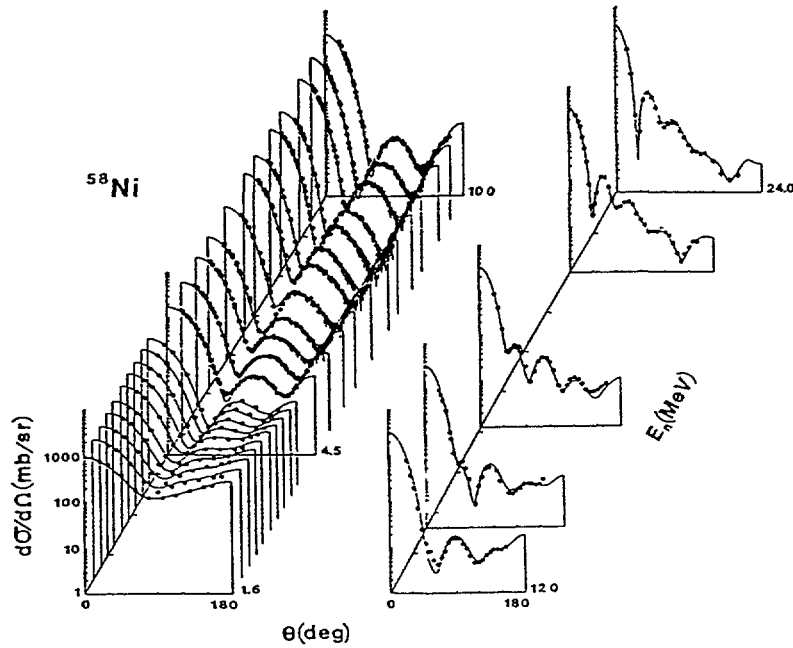


Fig. 6. Differential elastic-scattering cross sections of ^{58}Ni . Symbols indicate measured values and curves the results of SOM calculations. Data are in the laboratory system.

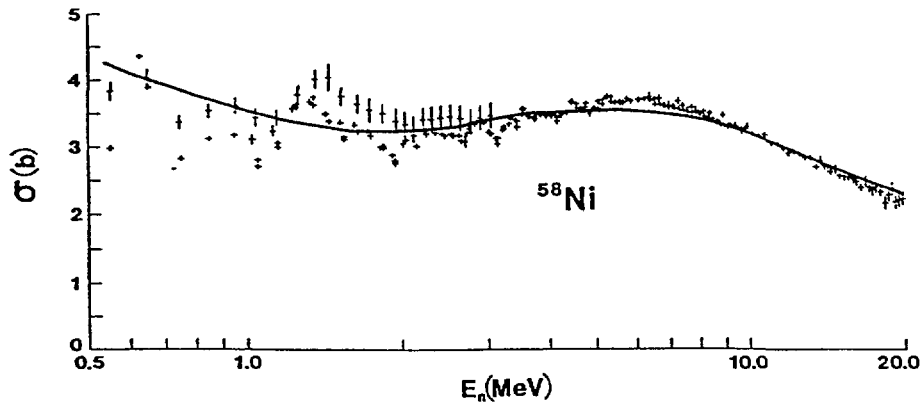


Fig. 7. Comparison of energy-averaged measured (symbols) and SOM (curve) total cross sections of ^{58}Ni .

A-3-b. Vibrational Coupled Channel Model (CCM)

It was assumed that ^{58}Ni is a simple vibrator, with one-phonon (2^+ , 1.454 MeV) and two-phonon (4^+ , 2.459 MeV, 2^+ , 2.776 MeV, and 0^+ , 2.942 MeV) excited states. β_2 was taken to be 0.25. With these assumptions, the fitting of the elastic-scattering data was repeated using the coupled-channels formalism, coupling the ground and four excited states. The spin-orbit potential was fixed to

$$\begin{aligned}
 V_{\text{SO}} &= (6.5 - 0.035 \cdot E) \text{ MeV} \\
 r_{\text{SO}} &= 1.017 \text{ fm} \\
 a_{\text{SO}} &= 0.60 \text{ fm.}
 \end{aligned}
 \tag{3}$$

This is the spin-orbit potential of Ref. 14 and similar to that given in Eq. 1. In addition, the real-potential radius was fixed to that of the SOM (see Eq. 2). With these constraints,

the fitting procedure was identical to that of the SOM derivation outlined above. The resulting potential geometries were

$$\begin{aligned}
 r_v &= (1.305 - 0.0064 \cdot E) \text{ fm} \\
 a_v &= 0.6531 \text{ fm} \\
 r_w &= (1.17 + 0.0033 \cdot E) \text{ fm} \quad (E > 5.6 \text{ MeV}) \\
 &= (1.50 - 0.055 \cdot E) \text{ fm} \quad (E < 5.6 \text{ MeV}) \\
 a_w &= (0.29 + 0.018 \cdot E) \text{ fm} \quad (E > 6 \text{ MeV}) \\
 &= (0.10 + 0.050 \cdot E) \text{ fm} \quad (E < 6 \text{ MeV}),
 \end{aligned} \tag{4}$$

with the volume integrals per nucleon given in Fig. 8.

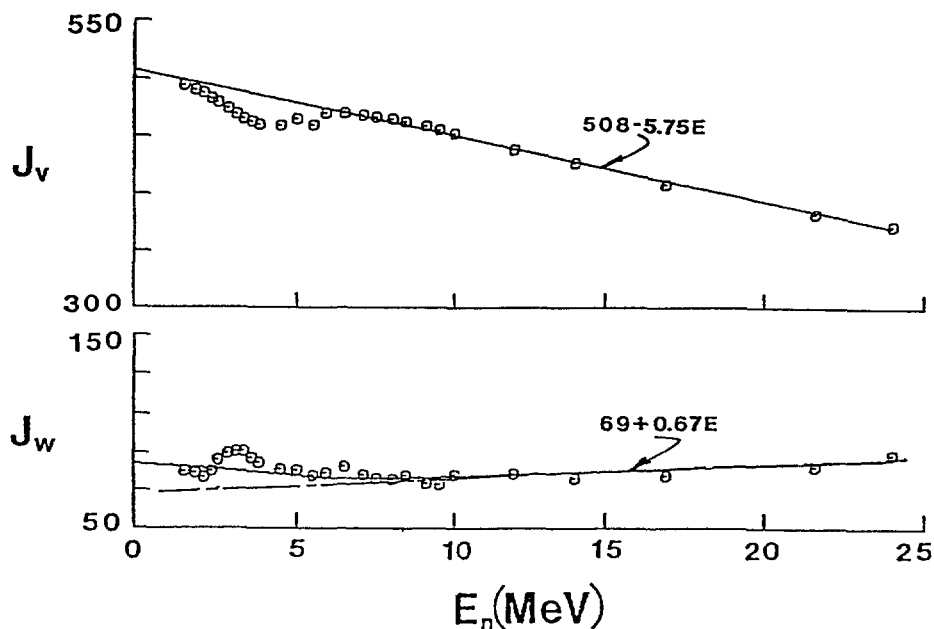


Fig. 8. Real (J_v) and imaginary (J_w) volume integrals per nucleon obtained using the CCM. The dimensionality is $\text{MeV}\cdot\text{fm}^3$.

The above CCM gave at least as good a description of the elastic-scattering as the above SOM representation, as illustrated in Fig. 9. The total cross section calculated with the CCM was essentially identical to the SOM result shown in Fig. 7, and the calculated s-wave strength function was 2.49×10^{-4} as compared to $(2.8 \pm 0.6) \times 10^{-4}$ deduced from resonance measurements.⁴ The calculated cross sections for the excitation of the 1.454 MeV (2^+) state are reasonably representative of the experimental results, as shown in Fig. 10. The prediction of the direct inelastic scattering from this level at higher energies is good, as shown in Fig. 11 where the angle-integrated cross section is significant to well above 20 MeV. The calculated angle-integrated cross sections in the ≈ 3.5 –5.5 MeV region are sensitive to the temperature used in the calculation of the compound-nucleus competition. In order to obtain the results shown in Figs. 10 and 11, the temperature had to be raised by ≈ 150 keV from the value given in Ref. 13. The cross sections calculated for the excitation of the higher-lying levels was reasonably consistent with the observed values, as discussed in Ref. 17.

The above SOM provides a simple calculational vehicle for many applications. Its inherent shortcoming is the lack of a direct reaction, and this is reflected in both unusual energy dependencies of some of the potential parameters and in the inability to describe inelastic processes of significant size. The CCM vibrational model alleviates some of these

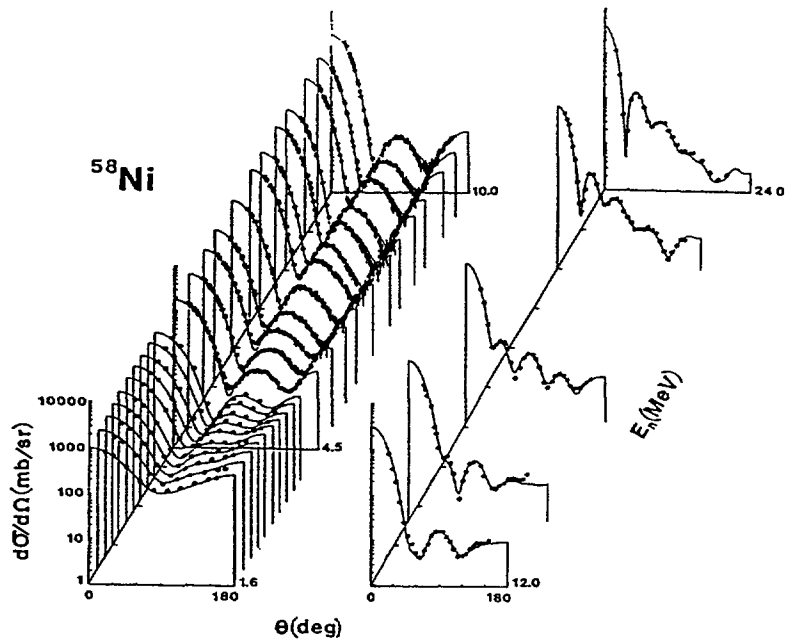


Fig. 9. Comparison of measured (symbols) and calculated (curves) CCM elastic-scattering cross sections. Data are in the laboratory system.

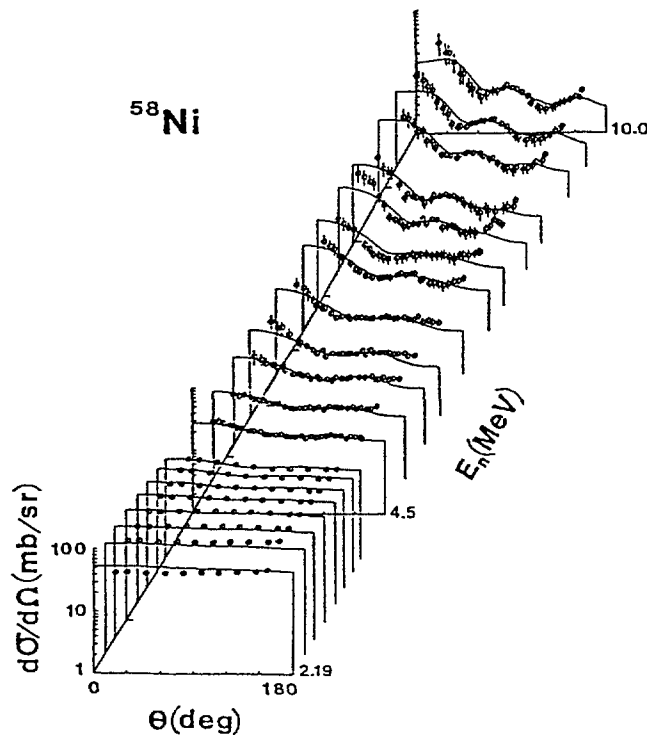


Fig. 10. Comparison of measured (symbols) and calculated (curves) CCM cross sections for the excitation of the 1.454 MeV level in ^{58}Ni . Data are in the laboratory system.

shortcomings, particularly those associated with the inelastic scattering. However, ^{58}Ni is neither a simple vibrator nor a rotator, and more complex coupling schemes than used above must be present. They are probably the source of the unusual parameter energy dependencies in the above vibrational model. They are most evident in the context of the imaginary potential, and will take a different character when a rotational-coupling scheme is assumed, as discussed in Ref. 15. If the fundamental character of the interaction could be reasonably represented using matrix elements derived, for example, from the shell model, it is hoped that a more general representation could be achieved, perhaps even on a regional or global basis. Such an effort is now being attempted.

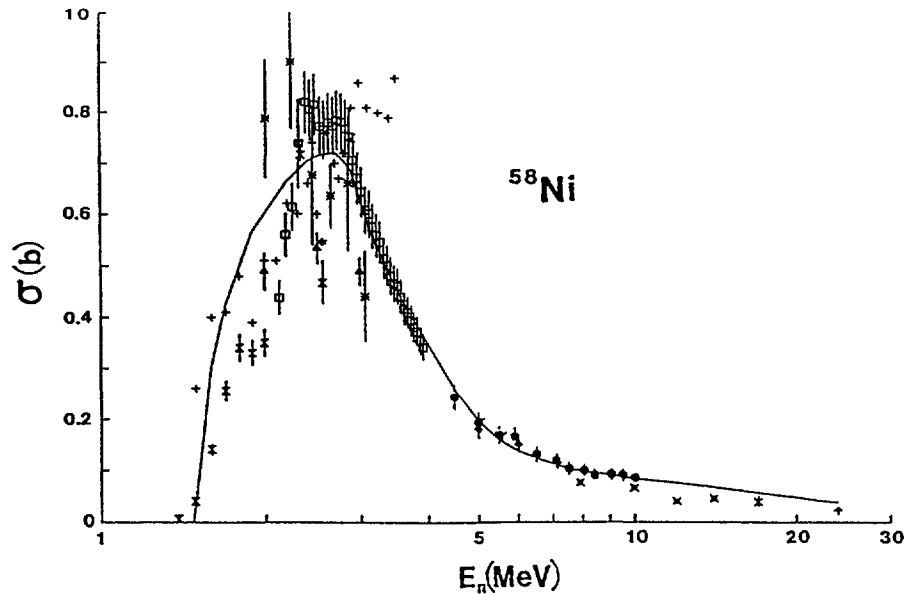


Fig. 11. Angle-integrated cross sections for the excitation of the 1.454 MeV level. Measured values are indicated by symbols and the results of CCM calculations (including compound-nucleus contributions) by the curve.

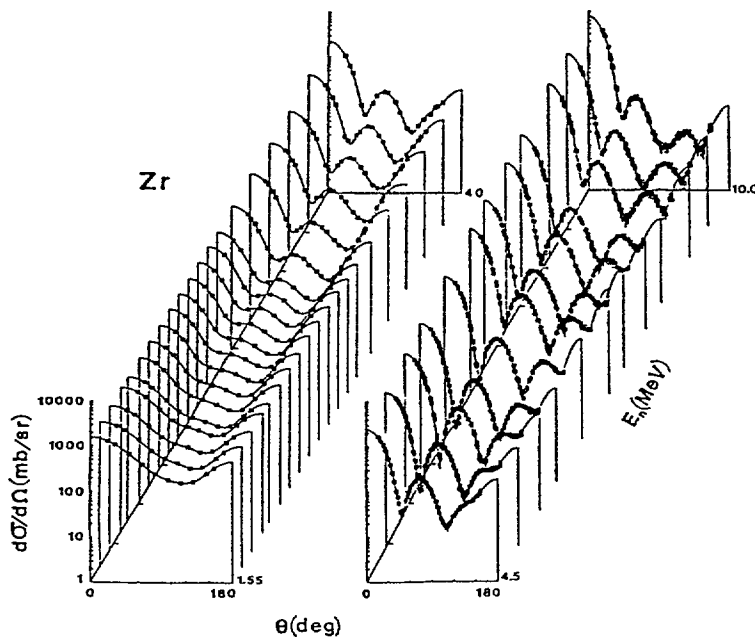


Fig. 12. Elastic scattering cross sections of zirconium. The measured values are indicated by symbols and the results of Legendre-polynomial fits to the data by curves. The data are in the laboratory system.

B. Potential for Elemental Zirconium

B-1. Introductory Comments

Zirconium has been a primary structural component of nuclear-energy systems for more than four decades. Elemental zirconium consists of five isotopes (^{90}Zr (51.45%), ^{91}Zr (11.27%), ^{92}Zr (17.17%), ^{94}Zr (17.33%), and ^{96}Zr (2.78%)). There is some information on the various isotopic reactions, but remarkably little directly relevant to the element that is used in the applications. The model development is complicated by the

multi-isotopic nature of the element and the variation of the potential parameters as the isotopes move away from the closed $N = 50$ neutron shell.¹⁸

B-2. The Database

B-2-a. Total Cross Sections

The experimental values were assembled from the literature, and combined with results obtained at this laboratory¹⁹, to provide a database extending to more than 20 MeV. This experimental database was evaluated using rigorous statistical methods.²⁰

B-2-b. Elastic-Scattering Cross Sections

The elemental elastic-scattering cross sections were measured from $\approx 1.5 \rightarrow 10$ MeV, with the results shown in Fig. 12. There is remarkably little zirconium elastic-scattering data in the literature. However, a 24 MeV distribution was available²¹ and was added to the present results to form the database for the interpretation.

B-2-c. Inelastic-Scattering Cross Sections

Due to the complex isotopic nature of the element, measurements of elemental inelastic-scattering cross sections do not provide unambiguous results. The literature does contain a few isotopic inelastic-scattering results that can be used to verify the calculational predictions.^{22,23} The primary obstacle to more definitive experimental definition is measurement-sample availability.

B-3. Zirconium Potential Derivation

The zirconium isotopes are near the closed neutron shell and, thus, the SOM should be appropriate. The major problem in the interpretation is the disparate structure of the five isotopes. The present model derivation was based upon the chi-square fitting of the elemental zirconium elastic-scattering data, concurrently explicitly treating the compound-nucleus processes in each isotope. J^π values for the discrete levels were taken from the Nuclear Data Sheets²⁴, and the Gilbert and Cameron statistical formalism was used to represent higher-energy excitations.¹³ The requisite calculational code was developed for this elemental fitting.

The interpretation was based upon the Saxon-Woods real, Saxon-Woods-derivative imaginary, and Thomas spin-orbit potentials.⁹ The fitting procedure was essentially the same as that outlined above for the ^{58}Ni SOM, progressively determining the real potential geometries, the imaginary potential geometries and then the potential strengths. The spin-orbit potential was fixed to

$$\begin{aligned} V_{so} &= 5.5 \text{ MeV} \\ r_{so} &= 1.0 \text{ fm} \\ a_{so} &= 0.65 \text{ fm,} \end{aligned} \tag{5}$$

which is similar to that of global models giving emphasis to polarization phenomena.¹⁴ The geometries resulting from the fitting were

$$\begin{aligned}
r_v &= (1.310 - 0.0064 \cdot E) \text{ fm} \\
a_v &= 0.667 \text{ fm} \\
r_w &= (1.390 - 0.0064 \cdot E) \text{ fm} \\
a_w &= (0.310 + 0.0182 \cdot E) \text{ fm},
\end{aligned}
\tag{6}$$

where the slight energy dependence of r_v was assumed to be suitable for r_w also. The potential strengths following from the fitting (in volume integral per nucleon) were

$$\begin{aligned}
J_v &= 474.64 - 5.3485 \cdot E \text{ MeV-fm} \\
J_w &= 62.493 + 0.4811 \cdot E \text{ MeV-fm}^3,
\end{aligned}
\tag{7}$$

where these numerical values are for ^{90}Zr . They will be slightly different for the other isotopes due to the simple $A^{1/3}$ size effect.

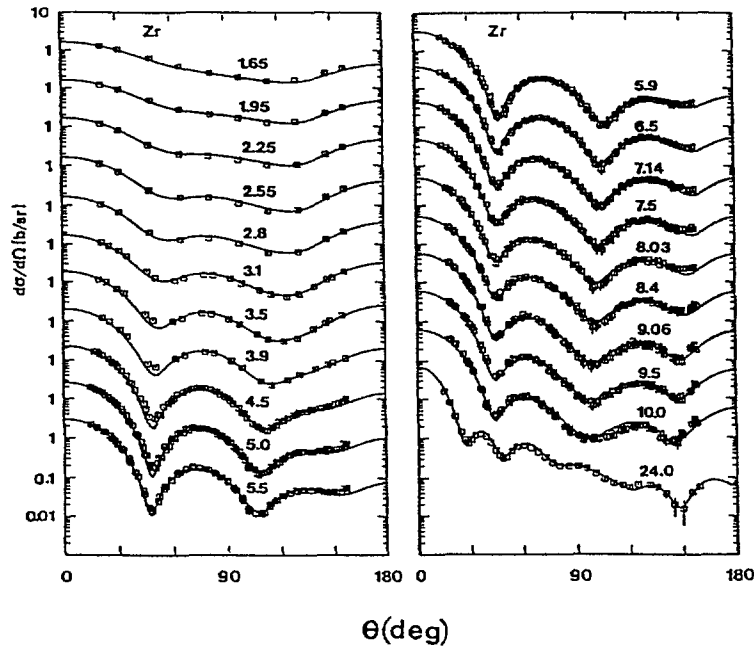


Fig. 13. Comparison of measured (symbols) and calculated (curves) elastic-scattering cross sections of elemental zirconium. The data are in the laboratory system.

The above potential provides a very good description of the elastic scattering, as illustrated in Fig. 13, and the total cross section, as shown in Fig. 14. The model reproduces the general trends of s- and p-wave strength functions²⁵, though it cannot reproduce the rather large fluctuations from isotope to isotope evident in the experimentally deduced values.⁴ Calculations give a reasonable description of the available inelastic-scattering data, but the latter are not particularly detailed and, thus, do not provide a stringent test of the model.

Some isotopic zirconium elastic-scattering data are available in the literature^{21,22,26,27}, particularly for ^{90}Zr and ^{92}Zr . The above model very nicely describes these isotopic elastic-scattering results, as illustrated in Fig. 15. The present model does not explicitly deal with symmetry effects (i.e., the effect of the isovector

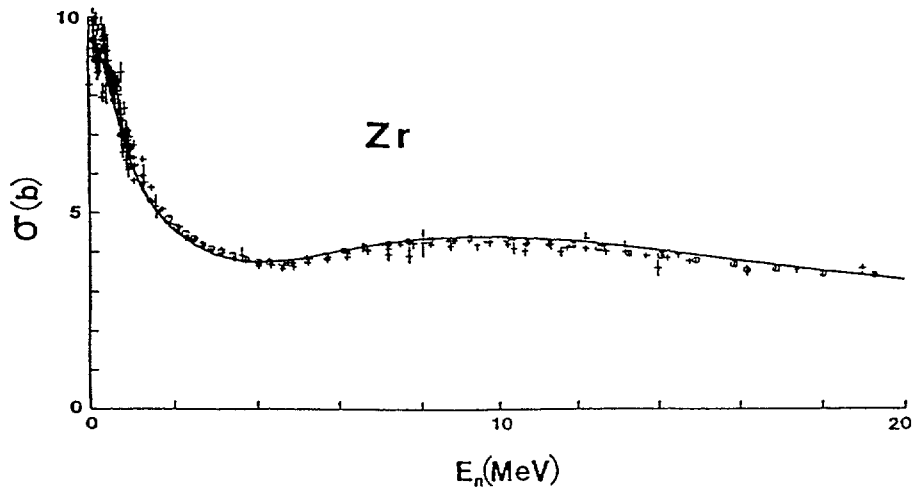


Fig. 14. Comparison of measured (symbols) and calculated (curve) total cross sections of zirconium.

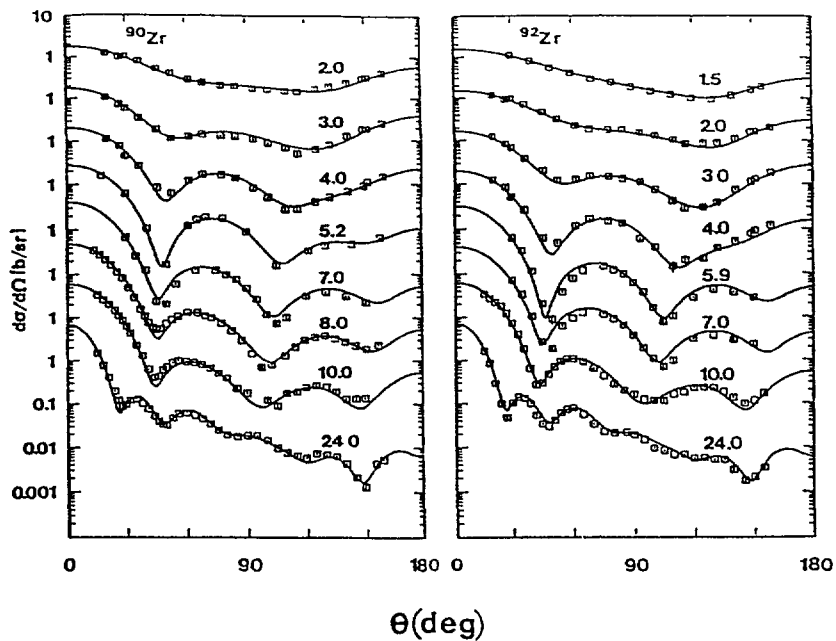


Fig. 15. Comparisons of measured (symbols) and calculated (curves) elastic-scattering cross sections of ^{90}Zr and ^{92}Zr . The data are in the laboratory system.

portion of the potential). The mass range of the zirconium isotopes of significant abundance is relatively small ($A = 90 \rightarrow 94$); therefore, there is not a strong isovector effect. This is illustrated in Fig. 16 where 10 MeV elastic scattering is calculated without (curves "A") and with (curves "B") the isovector potentials of Ref. 14. The curves are referenced to the mean elemental mass. The effect of the isovector potential is negligible except for the ^{94}Zr case, and even there the differences between curves A and B are less than the respective experimental uncertainties; furthermore, the isotope is only 17.33% abundant. The differences in the calculated results are most sensitive to the imaginary portion of the isovector strength.

The above potential is suitable for zirconium model calculations to well above 20 MeV. It is a relatively simple SOM formulation, strongly supported by experimental observation. The real potential geometry is conventional, with a reasonable energy dependence of J_v . The imaginary potential radius is somewhat larger than that of the real

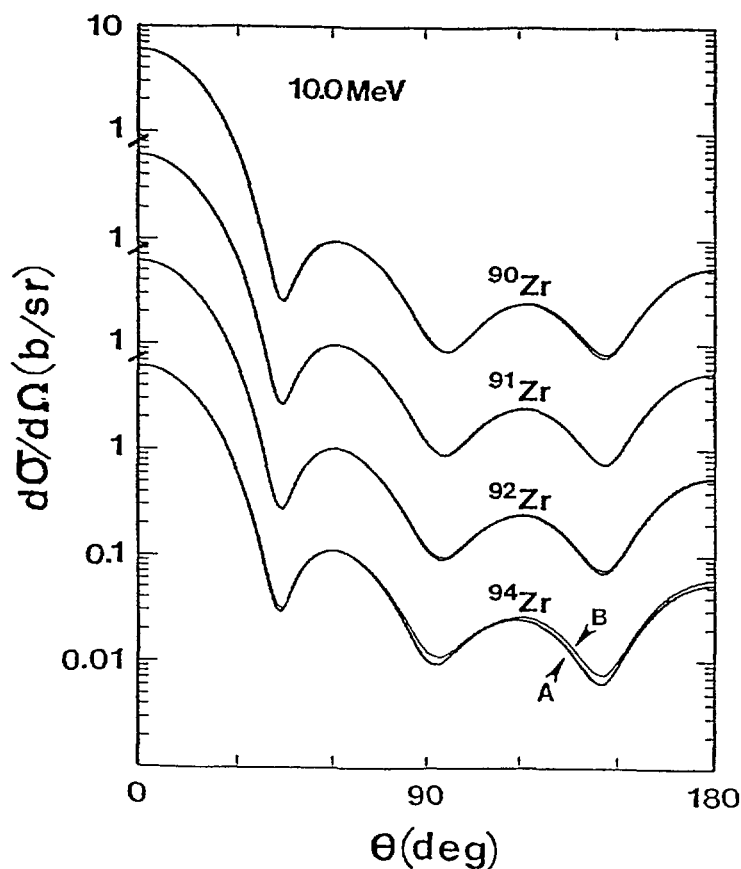


Fig. 16. Illustration of sensitivity to the isovector potential. Curves "A" were obtained with no isovector potential, and curves "B" with that of Ref. 14. Data are in the laboratory coordinate system.

potential, as is generally found for spherical nuclei at lower energies and as indicated by strength functions.¹⁶ The imaginary diffuseness increases quite sharply with energy, and there is a conventional increase of J_w . Clearly, the linear energy trends are approximations of a more complex behavior, applicable to the $\approx 0 \rightarrow 25$ MeV range, and they cannot extend well into the bound region or to very high energies. Below ≈ 25 MeV there is no experimental support for a volume absorption term.

IV. SUMMARY REMARK

This Report resolves some outstanding issues from the prior meeting. It also presents two explicit potentials that are very suitable for the calculation of quantitative nuclear data for ^{58}Ni and elemental zirconium, respectively. These potentials are the result of a comprehensive measurement and analysis program. The ^{58}Ni potential illustrates the difficulties in handling complex coupling schemes of collective vibrational and/or rotational nuclei. The conventional SOM is only an approximation in this case, and more complex physical concepts are probably required for detailed understanding. These are now being explored.¹⁵ In contrast, the elemental zirconium potential is illustrative of the success of the simple SOM in a region near shell closures. The potential presented is well-founded on experimental evidence and provides a basis for very quantitative calculations.

REFERENCES

1. R. D. Lawson The Theory of the Nuclear Shell Model, Clarendon Press, Oxford (1980).
2. A. B. Smith, P. T. Guenther and R. D. Lawson, Nucl. Phys. A483 50 (1988).
3. J. A. Harvey, private communication (1988).
4. S. Mughabghab, M. Divadeenam and N. Holden, Neutron Cross Sections, Academic Press, NY (1981).
5. P. Guss, R. Byrd, C. Floyd, C. Howell, K. Murphy, G. Tungate, R. Pedroni, R. Walter and J. Delaroche, Nucl. Phys. A438 187 (1985).
6. R. Pedroni, Bull. Am. Phys. Soc. 28 998 (1983).
7. N. Olsson, E. Ramstrom, B. Trostell and B. Holmqvist, NEA Report, NEANDC-222U, p-261 (1986).
8. Y. Yamanouti, J. Rapaport, S. Grimes, V. Kulkarni, R. Finlay, D. Bainum, P. Grabmayr and G. Randers-Pehrson, NBS Spec. Pub., NBS-594, p-146 (1980).
9. P. E. Hodgson, Nuclear Reactions and Nuclear Structure, Clarendon Press, Oxford (1971).
10. W. Hauser and H. Feshbach, Phys. Rev. 87 366 (1952).
11. P. A. Moldauer, Nucl. Phys. A344 185 (1980).
12. L. K. Peker, Nucl. Data Sheets 42 457 (1984).
13. A. Gilbert and A. Cameron, Can. J. Phys. 43 1446 (1965).
14. R. Walter and P. Guss, Proc. Conf. Nucl. Data for Basic and Applied Purposes, Vol.-2, p-1079, Gordon and Breach, NY (1986).
15. R. D. Lawson and A. B. Smith, unpublished memorandum (1990); also S. Chiba, P. Guenther, R. Lawson and A. Smith, to be published.
16. P. A. Moldauer, Nucl. Phys. 47 65 (1963).
17. S. Chiba, P. T. Guenther and A. B. Smith, to be published.
18. R. D. Lawson, P. T. Guenther and A. B. Smith, submitted to Nucl. Phys. (1990).
19. W. P. Poenitz and J. F. Whalen, Argonne National Laboratory Report, ANL-83-4 (1983).
20. W. P. Poenitz, Brookhaven National Laboratory Report, BNL-NCS-51363 (1981).
21. Y. Wang, private communication (1989).
22. J. Delaroche, Y. Wang and J. Rapaport, submitted to Phys. Rev.
23. P. Guenther, A. Smith and J. Whalen, Argonne National Laboratory Report, ANL/NDM-4 (1974).
24. D. Kocher, Nucl. Data Sheets 16 55 (1975); H. Muller, Nucl. Data Sheets 31 181 (1980); R. Luksch, Nucl. Data Sheets 30 573 (1980); H. Muller, Nucl. Data Sheets 44 277 (1985).
25. S. Chiba et al., to be published.
26. S. Tanaka, private communication, data at the National Nuclear Data Center, Brookhaven National Laboratory (1980).
27. R. W. Stooksberry, J. H. Anderson and M. Goldsmith, Phys. Rev. C13 1061 (1976).

Neutron Emission Cross Sections on ^{93}Nb
at 20 MeV Incident Energy

A. Marcinkowski and D. Kielan
Soltan Institute for Nuclear Studies
PL-00-681 Warsaw, Poland

A B S T R A C T

Over the last years fully quantum-mechanical theories of nuclear reactions have been developed that provide, at least in principle, parameter-free methods of calculating double-differential continuum cross sections. The DWBA-based theory of direct processes to the continuum was derived by Tamura et al. The statistical theory of Feshbach, Kerman and Koonin (FKK) introduced two reaction types in parallel as complementary mechanisms contributing to the preequilibrium decay. The multistep compound mechanism (MSC) results in symmetric angular distributions of the emitted particles, whereas the multistep direct mechanism (MSD) gives rise to the forward-peaked angular distributions. The theories of the MSC reactions differ in that the FKK theory incorporates the "never come back" hypothesis, which allowed the formulation of an applicable model that was successfully used in practical calculations. On the other hand the FKK theory of the MSD reactions differs conceptually from the theory of Tamura et al. and from the more general theory developed most recently by Nishioka et al. The latter theories were shown to be founded upon a postulated chaos located in the residual nucleus. In contrast, the theory of FKK assumes a chaotic interaction of the continuum particle to be emitted with the residual nucleus. The continuum or leading-particle statistics of the FKK theory results in the simple, convolution like, MSD cross section formula, which facilitates numerical calculations. Nevertheless two-step statistical DWBA calculations have been also performed. This paper extends the application of the FKK theory to the $^{93}\text{Nb}(n, xn)$ reaction at 20 MeV incident energy.

1. Introduction

Over the last years fully quantum-mechanical theories of nuclear reactions have been developed, that provide, at least in principle, parameter-free methods of calculating the required double-differential continuum cross sections. The DWBA based theory of direct processes into the continuum was derived by

Tamura et al.¹⁾ (TUL). The statistical theory of Feshbach, Kerman and Koonin²⁾ (FKK) introduced two reaction types in parallel as complementary mechanisms contributing to the pre-equilibrium decay. The one, referred to as the multistep compound mechanism (MSC) results in symmetric angular distributions of the emitted particles, whereas the multistep direct mechanism (MSD) gives rise to the forward-peaked angular distributions.

The theories of the MSC reactions differ in that the FKK theory incorporates the never come back hypothesis, which allowed to formulate an applicable model²⁾ successfully used in practical calculations^{3,4)}. On the other hand the FKK theory of the MSD reactions differs conceptually from the theory of Tamura et al.¹⁾ and from the more general theory developed most recently by Nishioka et al.⁵⁾. The latter theories were shown to be founded upon a postulated chaos located in the residual nucleus, in contrast the theory of FKK assumes a chaotic interaction of the continuum particle to be emitted with the residual nucleus⁶⁾. The continuum or leading particle statistics of the FKK theory results in the simple, convolution like, MSD cross section formula, which facilitates the numerical calculations^{7,8)}. Nevertheless the twostep statistical DWBA calculations have been also performed¹⁾. This paper extends the application of the FKK theory to the $^{93}\text{Nb}(n, xn)$ reaction at 20 MeV incident energy.

2.1 The multistep compound reactions

For the statistical multistep compound emission, due to the decay from a chain of quasi-bound states of the composite system this theory predicts a double-differential MSC cross section expressed via three multiplicative terms: the entrance channel strength function, the depletion term, describing that part of the absorbed projectile flux, which survived emission prior to reaching the N -th stage of the reaction and the probability of emission from the N -th stage states, which occurs only via the continuum states, accessible in the exit transitions $\nu=N\pm 1, N$. The latter two terms are expressed by the emission width, $\langle \Gamma_{NJ}^{1'S'\nu}(U)\rho_{\nu}^B(U, I') \rangle$, and the damping width, $\langle \Gamma_{NJ} \rangle$. The density of the bound-particle-hole states is ρ_{ν}^B . By assuming a δ -type residual interaction all the widths factorize,

$$\langle \Gamma_{NJ}^{1'S'\nu}(U)\rho_{\nu}^B(U, I') \rangle = 2\pi I_X^{\nu} Y_N^{\nu} \quad (1)$$

with I being the overlap integral of the radial wavefunctions for the two active bound-particles/holes and the two final particles/holes, X the angular momentum coupling function and Y the density of levels accessible in the transition. The MSC formulae describe the for neutron and proton channels only.

In the exciton representation $p+h=n=2N+1$, and the three possible exit transitions denote a particle-hole creation, annihilation and exciton scattering, respectively. The X- and Y-functions were calculated according to refs. ^{4, 9}) with corrections of ref. ¹⁰), e.g. for the exit transition annihilating a particle-hole pair, $\nu=n-2$, one obtains:

$$Y_n^{n-2} = \frac{\rho_{2,1}^B(E-U) \rho_{p-2,h-1}^B(U)}{\rho_{p,h}^B(E)}, \quad (2)$$

$$X_{nJ}^{n-2} = \frac{R_{n-3}(I')}{R_n(J)} \sum_{QJ_3} (2Q+1) F(Q) (2j_3+1) R_1(j_3) \left[\begin{matrix} J & J_3 & Q \\ \frac{1}{2} & -\frac{1}{2} & 0 \end{matrix} \right]^2, \quad (3)$$

where E and U are the excitation energies of the composite system and the residual nucleus, and j, j_1, j_2, j_3 and Q are the total angular momenta of: the ejectile, the exciton initiating the transition, the particle and the hole annihilated, and the total angular momentum of the pair of interacting particles (initiating particle and the particle of the annihilated pair), respectively. The spin distribution of the single particle states $g=A/13$ is $R_n(j)$. The r.h.s. of eq.(3) holds for $j-I' \leq J \leq j+I'$ and equals 0 otherwise.

2.2 The multistep direct reactions

In order to describe the forward peaked angular distributions observed in experiment it is assumed that the incident continuum particle loses stepwise its energy and direction in a sequence of collisions, each creating a new particle-hole pair. At each step emission may take place and the MSD cross section is considered as a sum of emissions in all the reaction stages N. By introducing the probability $W_{N,N-1}$ for transition from the (N-1)th to the Nth stage the multistep cross section becomes

$$\frac{d^2\sigma}{dUd\Omega}_{\text{multistep}} = \sum_N \sum_{\nu=N-1}^{N+1} \int \frac{d\bar{k}_1}{(2\pi)^3} \cdots \int \frac{d\bar{k}_N}{(2\pi)^3} W_{\nu,N} W_{N,N-1} \cdots W_{2,1} \frac{d^2\sigma}{dUd\Omega}_{\text{onestep}} \quad (4)$$

The integrations in eq. (8) are over all angles and momenta \bar{k}_N of the particle in the continuum, which makes the transition from stage N. The FKK theory provides the basis for expressing the transition probability

$$W_{N,N-1} = \frac{\pi \hbar^2 k_{N-1}^2}{m_{N-1}} \sum_l (2l+1) \rho_2(U_N, l) \left\langle \left[\frac{d\sigma(\Theta_{N,N-1})}{d\Omega_N} \right]_1^{DW} \right\rangle \quad (5)$$

and the one-step cross section,

$$\frac{d^2\sigma_{1,i}}{dU_1 d\Omega_{1\text{onestep}}} = \sum_l (2l+1) \rho_2(U_1, l) \left\langle \left[\frac{d\sigma(\Theta_{1,i})}{d\Omega_1} \right]_1^{DW} \right\rangle, \quad (6)$$

in terms of incoherent contributions of the DWBA angle-differential cross sections for spinless particles B_0 . The summation in formulae (9) and (10) is over the transferred orbital angular momenta l . m_{N-1} is the reduced mass of the continuum particle and $\Theta_{N,N-1}$ is the angle between $\bar{k}_{N,N-1}$ and \bar{k}_N . The angular brackets denote averaging of the elementary angular distributions, computed with microscopic two-particle form factor, over many final $1p1h$ configurations, e.g. of the shell model.

An adequate description of experimental neutron scattering data requires inclusion of the collective, low energy, surface vibrations of quadrupole and octupole multipolarity into consideration. This can be done by the method of Kalka et al.¹¹⁾, who have derived the cross sections for the one- and two-phonon transitions from Green's function and random matrix formalism. The one-phonon cross section is

$$\frac{d\sigma}{dU_{1\text{phon}}} = \left(\frac{mV}{2\pi\hbar^2} \right) \frac{4\pi}{(k_i R)^2} \delta_{i,1} \sum_{\lambda} \beta_{\lambda}^2 V_R^2 \delta(U - \omega_{\lambda}) \frac{k_1}{k_i} P_1(\epsilon_1) P_1(\epsilon_1), \quad (11)$$

where $V = \frac{4}{3}\pi R^3$, $R = r_0 A^{1/3}$, $\beta_{\lambda} = [4\pi(2\lambda+1)]^{1/2} = \beta_{\lambda}$; and λ , ω_{λ} and β_{λ} are the collective mode multipolarity, energy and deformation parameter, respectively. The penetrability factor $P_1(\epsilon_1)$ is equal unity for neutrons. The angular distributions of the collective, continuum cross sections have not been derived in ref.¹¹⁾, but they can be calculated with use of the collective form factors in the frame of the DWBA.

5. Calculations and comparison with experiment

In calculating of the particle-hole form factors, which enter the MSD cross sections we assumed spinless particles and a zero-spin target, so that the only contribution to the spins of the final states comes from the transferred orbital angular momentum l . For each value of l the final $1p1h$ configurations have been chosen according to the shell model of Seeger¹²⁾. For these configurations the angular distributions of emitted neutrons have been calculated microscopically by using the DWUCK-4 code. The Yukawa residual interaction of 1.0 fm range and with strength $V_0 = 25$ MeV, was acting on the bound state wavefunctions generated in a real Saxon-Woods potential. The distorted waves were calculated using the global optical model of Wilmore and Hodgson¹³⁾.

In order to obtain smooth neutron spectra the calculated cross sections were averaged over the final shell model particle-hole states contained in overlapping energy intervals of 5.0 MeV width and centered on the experimental energy bins. The densities of the final states, were evaluated with global parameter $a = A/8$ and the spin cut-off fixed at a value $\sigma = 2.6$ for ^{93}Nb . The calculated MSD cross sections are shown in fig. 1 as the dott-dashed (onestep) and two-dott-dashed (twostep) line. At the high energy end of the emission spectrum these MSD cross sections need to be completed by adding the contribution due to collective enhancement. The one-phonon quadrupole and octupole excitations contribute according to eq. (11), with following energies and deformation parameters of the low lying collective states: $\omega_2 = 0.93$ MeV, $\beta_2 = 0.13$, $\omega_3 = 2.30$ MeV, $\beta_3 = 0.18$ in ^{93}Nb . The delta function in (11) was replaced by a Lorentzian of a collective width 0.7 MeV¹¹⁾ broadened in accord with the experimental energy resolution. For the odd-mass nucleus the weak coupling model was adopted. The summed collective, one-phonon cross sections are shown by the dashed line labelled 1VIB.

The MSC calculations were split into the three steps and an r -th stage, i.e. the r -th stage emission contained all emissions from stages after the third, including the compound nucleus contribution. The entrance channel strength function was calculated from the optical model transmission coefficients reduced in order to account for the loss of the absorbed flux due to the MSD emission⁴⁾. The reduction was evaluated from

experimental angular distributions, by assuming that their forward peaked portions are due to MSD processes, or by calculating directly the MSD cross sections. Both ways provided consistent reduction factor $R=0.8$ for ^{93}Nb .

The harmonic-oscillator wavefunctions for the bound nucleons and the optical model scattering wavefunctions for the continuum particle were used for calculating the overlap integral I , which provides the absolute normalization in eq. (2). The particle-hole state densities, e.g. those entering eq. (4), were calculated with restriction to bound particle orbital only by the numerical cut-off technique developed by Bonetti et al.¹⁴⁾ with parameters like in the MSD calculations.

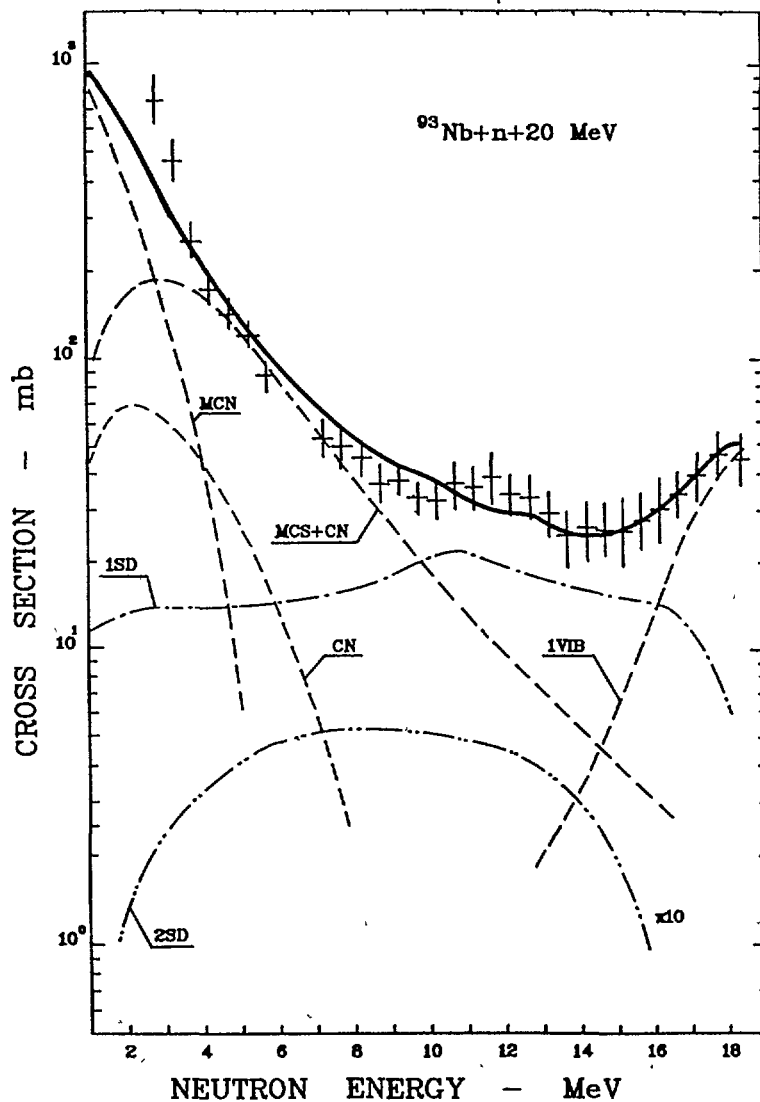


Fig. 1

The results of the MSC calculations are also shown in fig. 1 as the dashed line labelled CN, for all emissions after the third step (compound nucleus cross sections), and the dashed line labelled MSC+CN for all emissions (including the three MSC stages). One can see that the latter cross sections dominate the low energy part of the neutron emission spectra, up to about 9 MeV of the outgoing neutron energy. The multiparticle emission MCN contributes strongly into the lowest outgoing energy bins. In spite of it seems to be underestimated by the theory. The overall description of the recent Ohio experiment is good, this holds for the angular distributions as well.

References

- 1) T. Tamura, T. Udagawa and H. Lenske, Phys. Rev. C26 (1982) 379
- 2) H. Feshbach, A. Kerman and S. Koonin, Ann. Phys. (N.Y.) 125 (1980)
- 3) R. Bonetti, L. Colli-Milazzo and M. Melanotte, Phys. Rev. C25 (1982) 717
- 4) M. Herman, A. Marcinkowski and K. Stankiewicz, Nucl. Phys. A430 (1984) 69; A435 (1985) 859(E)
- 5) H. Nishioka, H. A. Weidenmuller and S. Yoshida, Ann Phys. (N.Y.) 183 (1988) 166
- 6) A. J. Koning and J. M. Akkermans, Stichting Energieonderzoek Centrum Nederland, Report ECN-89-155, September 1989
- 7) R. Bonetti, M. Camnasio, L. Colli-Milazzo and P. E. Hodgson, Phys. Rev. C24 (1981) 71
- 8) A. Marcinkowski, R. W. Finlay, J. Rapaport, P. E. Hodgson and M. B. Chadwick, Nucl. Phys. A501 (1989) 1
- 9) K. Stankiewicz, A. Marcinkowski and M. Herman, Nucl. Phys. A435 (1985) 67
- 10) P. Obložinský, Nucl. Phys. A453 (1986) 127
- 11) H. Kalka, M. Torjman and D. Seeliger, Report INDC(GDR)-054/LJ, June 1989, IAEA, NDS, Vienna
- 12) M. Hilman and J. R. Grover, Phys. Rev. 185 (1969) 1303
- 13) D. Wilmore and P. E. Hodgson, Nucl. Phys. 55 (1964) 673
- 14) R. Bonetti, L. Colli-Milazzo and M. Melanotte, Lett. Nuovo Cim. 31 (1981) 33

Calculation of Cross Sections of the (n,p) Reaction on
Zirconium Isotopes

A. Marcinkowski and D. Kielan
Soltan Institute for Nuclear Studies
PL-00-681 Warsaw, Poland

A B S T R A C T

In our earlier analyses of the (n,p) reaction cross sections on several isotopic chains in the medium-mass domain, we used the geometry-dependent hybrid model for calculating the preequilibrium emission cross sections. This model accounts for the enhanced emission from the nuclear surface by assuming that the reaction proceeds in spherical shell-shaped regions of a radius determined by the projectile impact parameter. These analyses indicate that good overall agreement between theory and experiment may be obtained at the expense of some parameter adjustment. In the present paper, a more rigorous treatment of preequilibrium emission, such as the statistical multistep compound and the multistep direct processes, in the framework of the theories developed by Feshbach et al. (FKK) and Tamura et al. (TUL), was applied in the calculations. The results of calculations are compared with the cross sections of the $^{90,91,92,94}\text{Zr}(n,p)$ reactions measured within a research programme coordinated by the International Atomic Energy Agency.

1. Introduction

In our earlier analyses of the (n,p) reaction cross sections, on several isotopic chains in the medium-mass domain ^{1,2)}, we used the geometry-dependent hybrid model ³⁾ for calculating the preequilibrium emission cross sections. This model accounts for the enhanced emission from the nuclear surface by assuming that the reaction proceeds in spherical shell-shaped regions of a radius determined by the projectile impact parameter. These analyses indicate that good overall agreement between theory and experiment may be obtained at the expense of some parameter adjustment. Here the more rigorous treatment of preequilibrium emission, such as the statistical multistep compound and the multistep direct processes, in the framework of the theories developed by Feshbach et al. ⁴⁾ (FKK) and Tamura et al. ⁵⁾ (TUL), was applied in the calculations. The results of calculations are

compared with the cross sections of the $^{90,91,92,94}\text{Zr}(n,p)$ reactions measured within the research project coordinated by the IAEA-NDS.

2. Theoretical formalism

The measured cross sections were analysed in terms of the decay of the compound nucleus preceded by the preequilibrium emission. For this purpose the extended version of the computer code EMPIRE ⁶⁾ was used. As described earlier the standard Hauser-Feshbach theory was applied for calculation of the evaporation spectra and the multistep compound theory of FKK was multistep direct emission, which is characterized by forward peaked angular distributions, can be calculated either by using the FKK, or the TUL theory. Both theories of the multistep direct reactions derive the one-step cross section in the same way. The calculational procedures are different however. In the FKK theory the microscopic DWBA cross sections are averaged over many final $1p1h$ states. On the other hand TUL average the microscopic form factors to get the macroscopic form factor, which subsequently was used in calculating the continuum cross sections. The latter approach reduces the number of the DWBA calculations to a few only, and is therefore more practical for comparison with the angle- and energy-integrated activation data. We used the TUL formalism in the present analysis.

2.1 Multistep compound emission

For the statistical multistep compound emission the FKK theory predicts the Hauser-Feshbach-like cross section consisting of three multiplicative terms: the entrance channel strength function, the factor describing the depletion of flux due to emission on preceding reaction stages and the emission probability. The entrance channel strength function has been related, for the purpose of the present calculation to the optical model absorption cross section via a reduction factor $R=0.86$, which accounts for the loss of flux due to multistep direct processes and which was evaluated from experimental angular distributions ⁶⁾. The depletion factor and the emission probability are expressed by the emission and the spreading widths, which for transition matrix elements of a δ -type factorize

$$\langle \Gamma_{NJ}^{jS\nu} \rho_{S\nu}^B(U) \rangle = 2\pi I^2 X_N^{\nu\nu} Y_N^{\nu} \quad (1)$$

Here j , S , and J are the spins of the ejectile, the residual nucleus and composite nucleus, respectively. The emission from stage N of the reaction, which involves states with $n=2N+1$ excitons, occurs via three exit modes $\nu=n-2, n$, corresponding to particle-hole creation, annihilation and exciton scattering, respectively. The radial overlap integral I is over the two initial interacting excitons and the two final ones. The functions Y are the densities of levels accessible in the transition and X are the angular momentum coupling functions. The particle-hole level density ρ^B involves only bound-particle orbitals (7,8).

From refs. (6,7) one finds, that e.g. for a transition creating a 1ph pair $\nu=n+2$;

$$Y_n^{n+2} = \frac{1}{2} g h (h+1) \frac{\rho_{p,h+1}^B(U)}{\rho_{p,h}^B(E)} \quad (2)$$

$$X_{nJ}^{n+2} = \frac{(2j+1)(2S+1)}{R_n(J)} \sum_{Qj_3j_4} (2Q+1) R_1(Q) (2j_3+1) F(j_3) R_{n-1}(j_4) \\ \times \left[\begin{matrix} j & Q & j_3 \\ \frac{1}{2} & -\frac{1}{2} & 0 \end{matrix} \right]^2 \left\{ \begin{matrix} j_3 & j & Q \\ J & j_4 & S \end{matrix} \right\}^2 \quad (3)$$

were j_1, j_2, j_3, j_4 and Q are the total angular momenta of the particle and the hole in the newly created pair, the total angular momentum of the pair, that of the noninteracting core and of the exciton initiating the transition, respectively. The single-particle state density is $g = A/13$ and its spin distribution is R_n . The function describing the angular momentum decomposition of the created pair is

$$F(j_3) = \sum_{j_1 j_2} (2j_1+1) R_1(j_1) (2j_2+1) R_1(j_2) \left[\begin{matrix} j_1 & j_2 & j_3 \\ \frac{1}{2} & -\frac{1}{2} & 0 \end{matrix} \right]^2 \quad (4)$$

The overlap integral I has been approximated by assuming, that the radial wavefunctions for the active excitons Q, j, j_1 and j_2 are constant inside the nucleus. These assumption results in an analytical formula for I (6).

In the present calculation three stages were found to contribute significantly. The Hauser-Feshbach theory was used to calculate the compound nucleus cross section due to the remaining stages.

2.2 One-step Direct emission

For the one-step direct transition with a zero spin transfer and for even targets TUL derived a cross section of the form,

$$\frac{d^2\sigma(E_b)}{dE_b d\Omega_b} = \sum_1 \rho_1(E_x) \frac{d\sigma_1(E_b, \theta_b)}{d\Omega_b}, \quad (5)$$

where the spectroscopic density takes the form,

$$\rho_1(E_b) = \beta_1^2 \sum_M C_M(E_x) (d_1^M)^2. \quad (6)$$

The function C_M is the probability per unit energy that there is a model state M at an excitation energy E_x . In practical calculations one takes, e.g. a lorentzian form

$$C_M(E_x) = (\Gamma/\pi) [(E_x - E_M)^2 + \Gamma^2]^{-1}, \quad (7)$$

with Γ being the spreading width of the model state. The model states were assumed to be the particle-hole states of the spherical shell model and the spectroscopic amplitude d_1^M , which is a purely geometric factor was assumed to be unity. The β_1 's are the transferred orbital angular momentum l -dependent parameters, which scale the average form factor.

3. Calculations and Comparison with Experiment

The cross sections, which are compared with experiment, are calculated as an incoherent sum of the contributions from the decay of the compound nucleus, from the multistep compound emission and of the one-step direct emission. The latter contributes, in the studied cases, at most 3% of the total proton emission yield

Global optical potentials were used in the calculations. For neutrons the potential of Moldauer⁹⁾ and of Bjorklund and

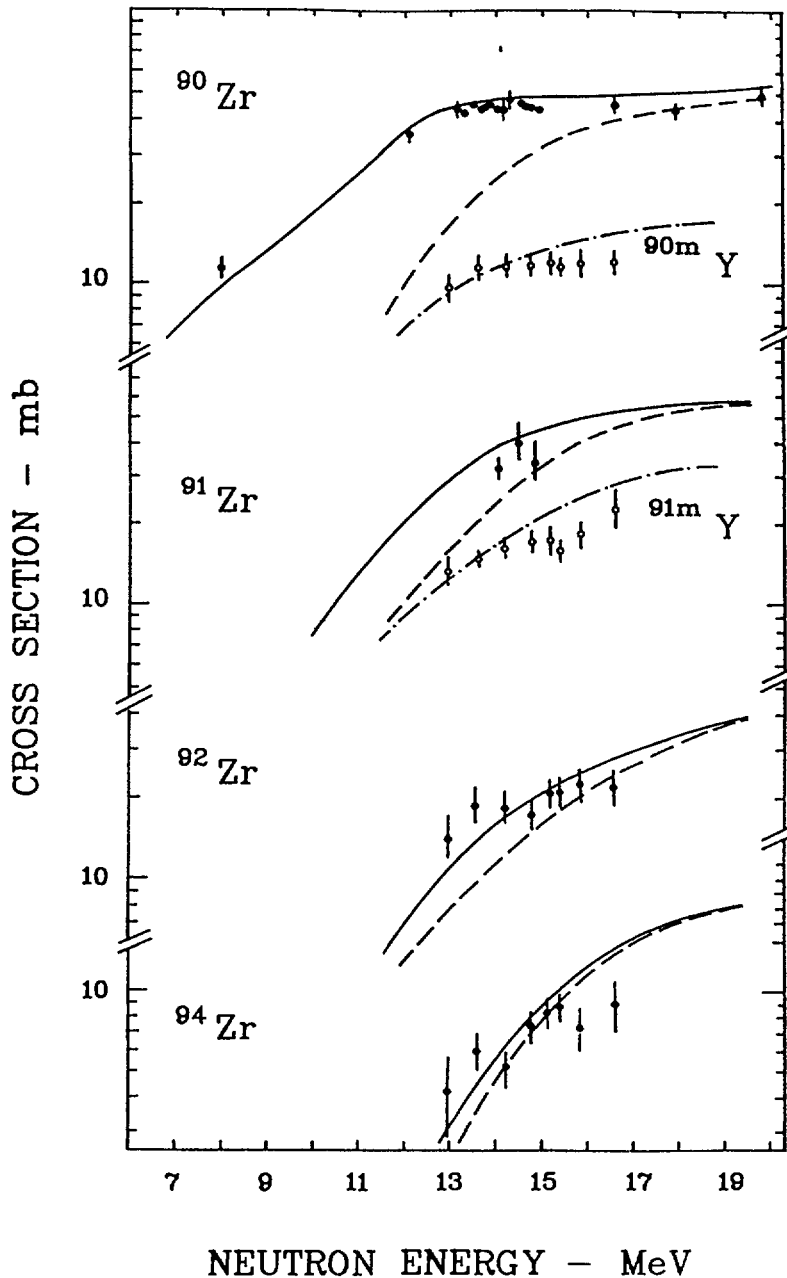


Fig. 1

Fernbach¹⁰⁾ were used. The potential of ref.¹⁰⁾ was also used for protons and the emission of alphas was described with use of the potential of McFadden and Satchler¹¹⁾.

The four parameter formulae, derived by Cameron and Gilbert¹²⁾, were used for calculating the compound nucleus level densities.

The one-step direct cross sections were calculated with the neutron-particle proton-hole states of the spherical Nilsson model and the spreading width $\Gamma = 4\text{MeV}$, was taken from Traxler et al.¹³⁾. The elementary DWBA angular distributions were calculated

with the code DWUCK-4, using a macroscopic form factor option with the deformation parameters $\beta_1 = 0.02$, for $l = 0-9$, adjusted to fit the measured angular distributions of protons ¹³). The comparison of the calculations with the measured excitation curves for the $^{90,91,92,94}\text{Zr}(n,p)$ reactions is shown in fig. 1. The compound nucleus dominates at low incident energies and for the lightest target. With increasing neutron number in the target the evaporation of protons decreases, falling below 10% of the total (n,p) reaction yield for ^{94}Zr . The multistep compound emission rises steeply with bombarding energy and dominates at about 18 MeV. The one-step direct cross section does not exceed 15% of the (n,p) reaction cross section. The applied formalism describes successfully also the proton emission spectrum measured at 14.8 MeV ¹⁴). For further details concerning both the calculations and the experimental data the reader is referred to ref. ¹⁵).

References

- 1) A. Marcinkowski, K. Stankiewicz, U. Garuska and M. Herman, Z. Phys. A323 (1986) 91
- 2) H.M. Hoang, U. Garuska, A. Marcinkowski and B. Zwiegliniski, Z. Phys. A334 (1989) 285
- 3) M. Blann, Nucl. Phys. A213 (1973) 570
- 4) H. Feshbach, A. Kerman and S. Koonin, Ann. Phys. 125 (1980) 429
- 5) T. Tamura, T. Udagawa and H. Lenske, Phys. Rev. C26 (1982) 379
- 6) M. Herman, A. Marcinkowski and K. Stankiewicz, Nucl Phys. A430 (1985) 69; A435 (1985) 859(E)
- 7) K. Stankiewicz, A. Marcinkowski and M. Herman, Nucl. Phys. A435 (1985) 67
- 8) P. Oblozinsky, Nucl. Phys. A453 (1986) 127
- 9) P. Moldauer, Nucl. Phys. 47 (1963) 65

- 10) F. Bjorklund and S. Fernbach, Proc. Intern. Conf. on nuclear optical model, Florida State University Studies No 32, Tallahassee, 1959
- 11) L. McFadden and G.R. Satchler, Nucl. Phys. 84 (1966) 177
- 12) A.G.W. Cameron and G. Gilbert, Can. J. Phys. 43 (1965) 1446
- 13) G. Traxler, A. Chalupka, R. Fischer, B. Strohmaier, M. Uhl and H. Vonach, Nucl. Sci. Eng. 90 (1985) 174
- 14) R.C. Haight, S.M. Grimes, R.G. Johnson and H.H. Barshall, Phys. Rev. C23 (1981) 700
- 15) A. Marcinkowski, U. Garuska, H.M. Hoang, D. Kielan and B. Zwiegliński, Nucl. Phys. A510 (1990) 93

Effect of Different Level Density Prescriptions on the
Calculated Neutron Nuclear Reaction Cross Sections

S.B. Garg
Neutron Physics Division
Bhabha Atomic Research Centre
Trombay, Bombay 400 085, India

A B S T R A C T

A detailed investigation is carried out to determine the effect of different level density prescriptions on the computed neutron nuclear data of Ni-58 in the energy range 5-25 MeV. Calculations are performed in the framework of the multistep Hauser-Feshbach statistical theory including the Kalbach exciton model and Brink-Axel giant dipole resonance model for radiative capture. Level density prescriptions considered in this investigation are based on the original Gilbert-Cameron, improved Gilbert-Cameron, backshifted Fermi-gas and the Ignatyuk, et al. approaches. The effect of these prescriptions is discussed, with special reference to (n,p), (n,2n), (n, alpha) and total particle-production cross sections.

1. INTRODUCTION

It is well known that level density parameter plays a pivotal role in the determination of various nuclear reaction cross-sections. In this paper a detailed investigation of the four different level density prescriptions has been carried out for Ni-58 with special reference to (n,p), (n, α), (n,2n) and total production cross-sections for neutron, proton, alpha-particle and gamma-rays in the neutron energy range 5-25 MeV. The study has been performed in the framework of the multistep Hauser-Feshbach statistical model scheme /1/ which includes Kalbach exciton model /2/ and the Brink-Axel giant dipole radiation model /3/. The following four level density recipes have been examined in this investigations :

- (i) Original Gilbert-Cameron Prescription /4/ (OGCP)
- (ii) Improved Gilbert-Cameron Prescription /5/ (IGCP)
- (iii) Back-Shifted Fermi-Gas Prescription /6/ (BSFGP) and
- (iv) Prescription to include the effect of shell closures developed by Ignatyuk et al /7/ called the Ignatyuk Prescription (IP) in this write up.

2. LEVEL DENSITY FORMULATIONS

(i) Original Gilbert-Cameron Prescription

It is a two energy region representation of level densities. In the higher excitation energy region a Fermi gas level density form of the following type is used :

$$\rho_2(E, J) = \sqrt{\pi} * \exp[2\sqrt{aU}] * P(J) / (12\sigma a^{1/4} U^{5/4} \sqrt{2\pi})$$

where

$$P(J) = (2J+1) * \exp[-(J+1/2)^2 / 2\sigma^2] / 2\sigma^2$$

This formula is valid for all energies greater than E_x defined by

$$U_x = 2.5 + 150/A$$

$$E_x = U_x + P(Z) + P(N)$$

Below this energy the following constant temperature formula is used :

$$\rho_1(E, J) = \exp[(E-E_0)/T] * P(J) / 2T$$

where

a = level density parameter

σ^2 = Spin cut-off factor

$$= 0.0888 * \sqrt{aU} * A^{2/3}$$

$$a/A = 0.00917 * [S(Z) + S(N)] + C$$

$C = 0.142$ for spherical nuclides

$= 0.120$ for deformed nuclides

$P(Z)$ and $P(N)$ are the pairing energy corrections for protons and neutrons respectively. $S(Z)$ and $S(N)$ are the corresponding shell energy corrections. These parameters are taken from Cook et al /8/.

The parameters T and E_0 are determined by fitting ρ_2 and ρ_1 and their derivatives at the matching energy E_x as given below :

$$\frac{1}{T} = \sqrt{a/U_x} - \frac{3}{2U_x}$$

$$E_0 = E_x - T \log [T \rho_2(U_x)]$$

(ii) Improved Gilbert-Cameron Prescription

This is essentially the same as given above except that the spin cut-off factor in this formulation is given by

$$\sigma^2 = 0.146 * \sqrt{aU} * A^{2/3}.$$

(iii) Back-Shifted Fermi-Gas Prescription

Here only a single form of the level density describes the entire excitation energy region. The formula used is

$$\rho(E, J) = \exp [2\sqrt{aU}] * P(J) / (12\sqrt{2} \sigma a^{1/4} (U+t)^{5/4})$$

where

$$P(J) = (2J+1) \exp [-J(J+1)/2\sigma^2] / 2\sigma^2$$

$$U = E - \Delta = a t^2 - t$$

$$\sigma^2 = 0.015 * t * A^{5/3}$$

Here t is the nuclear temperature and Δ is the energy shift. a 's and Δ 's are taken from Ivascu et al /9/ for this analysis.

(iv) Ignatyuk Prescription

The formulation accounts for the energy dependence of the 'a' parameter which is brought about by the effect of shell closures. In this prescription

$$a(U) = \tilde{a} [1 + f(U). W/U]$$

where \tilde{a} is the asymptotic value of the Fermi gas parameter occurring at high energies and is given by

$$\tilde{a}/A = 0.1375 - 8.36 * 10^{-5} * A$$

The shell effects are included in the term δW given by

$$W = M_{\text{exp}}(Z, A) - M_{\text{ld}}(Z, A, \alpha)$$

where

M_{exp} = experimental mass of the nuclide

M_{ld} = liquid drop model based mass of the nuclide with deformation

$f(U)$ gives the energy dependence expressed as

$$f(U) = 1 - \exp [- 0.05 U]$$

This model allows the shell effects to be included at low excitation energies while at higher energies such effects disappear.

The pairing energy corrections are again taken from Cook et al.

The level densities calculated with these four prescriptions are given in Fig.1. It may be noted that the level densities given by OGCP, IGP and IP are converging at about 5 MeV and then they start diverging with the increase in the excitation energy. Around 25 MeV IGCP and IP give level densities by factors of 2

and 6 respectively compared to that calculated with OGCP. BSFGP yields higher level density in the entire energy region by a factor of 10 compared to that given by OGCP.

3. CALCULATIONAL PROCEDURE AND DATA INPUT DETAILS

As already stated, the computations are carried out in the framework of the multistep Hauser-Feshbach data evaluation scheme. The reaction decay chain depicting the various participating nuclides considered in this investigation is shown in Fig. 2. Emissions of neutron, proton, alpha-particle and gamma-rays are included at every stage of the reaction in the equilibrium process while the emission of gamma-rays is excluded in the pre-equilibrium process.

Discrete energy levels, their spins, parities and gamma-ray branching ratios for all the nuclides depicted in Fig.2 are taken from the literature.

Transmission coefficients for neutron, proton and alpha-particles are calculated with good optical model potential parameters. For neutrons; optical model potential is that of Prince /10/, for protons; the potential is due to Mani /11/, and for alpha-particles; the potential is given by Strohmaier et al /12/. These potential parameters are listed below :

(i) Optical Model Potential Parameters For Neutrons

$$V \text{ (MeV)} = 49.33 - 0.48 E + 0.0024 E^2$$

$$W \text{ (MeV)} = 0.0$$

$$W_G \text{ (MeV)} = 12.0 + 3.358 E - 0.007 E^2 ; E < 25 \text{ MeV}$$

$$= 0.445 + 0.908 E - 0.011 E^2 ; 25 \leq E \leq 45 \text{ MeV}$$

$$U \text{ (MeV)} = 6.75$$

$$r_v \text{ (fm)} = 1.2583 + 0.00258 E ; E < 12 \text{ MeV}$$

$$r_w \text{ (fm)} = 1.4645 - 0.0146 E ; E < 12 \text{ MeV}$$

$$r_v = r_w = 1.3128 - 0.00196 E ; 12 \leq E \leq 100 \text{ MeV}$$

$$r_u = r_v, a_u = a_v = 0.7813 \text{ fm}$$

$$a_w = 0.63 \text{ fm.}$$

(ii) Optical Model Potential Parameters For Protons

$$V \text{ (MeV)} = 41.3 ; W \text{ (MeV)} = 0.9$$

$$W_D \text{ (MeV)} = 8.2 ; U \text{ (MeV)} = 7.5$$

$$r_v \text{ (fm)} = 1.2 ; r_w \text{ (fm)} = 1.25$$

$$r_u \text{ (fm)} = 1.16 ; r_c \text{ (fm)} = 1.25$$

$$a_v \text{ (fm)} = 0.64 ; a_w \text{ (fm)} = 0.56$$

(iii) Optical Model Potential Parameters For Alpha-Particles

$$V \text{ (MeV)} = 173.0 - 0.30 E$$

$$W \text{ (MeV)} = 20.5 + 0.1 E$$

$$r_V \text{ (fm)} = r_W \text{ (fm)} = 1.445$$

$$a_V \text{ (fm)} = a_W \text{ (fm)} = 0.51$$

$$r_C \text{ (fm)} = 1.3$$

The various symbols are defined below :

E = incident energy (MeV)

V = real well depth (Woods-Saxon)

W = imaginary well depth (Woods-Saxon)

W_G = imaginary well depth (Gaussian)

W_D = imaginary well depth (Derivative Woods-Saxon)

U = Spin-orbit well depth (Thomas)

r_V, r_W, r_U = radii for various potentials

r_C = radius for the Coulomb potential

a_V, a_W, a_U = diffuseness for various potentials.

(iv) Parameters for Gamma-Rays

The Brink-Axel model of giant dipole radiation has been employed to calculate the transmission coefficients for gamma-rays. For E1 radiation, the following resonance parameters due to Reffo /13/ have been used :

$$E1 = 16.0 \text{ MeV}; \quad \Gamma_1 = 3.70 \text{ MeV}$$

$$E2 = 18.6 \text{ MeV}; \quad \Gamma_2 = 5.10 \text{ MeV}$$

$$\langle \Gamma \rangle = 2200 \text{ meV}; \quad \langle D \rangle = 14 \text{ keV}$$

For M1 radiation default values of $E = 8 \text{ MeV}$ and $\Gamma = 5 \text{ MeV}$ are assumed.

In the pre-equilibrium description of the reaction, internal transition rates to the various exciton states are determined in terms of the average two body interaction matrix element as defined by Kalbach /14/. The exciton-state densities are calculated according to the Williams relation /15/. The K-parameter of the average reaction matrix element has been extracted as 135 MeV^3 in this analysis by matching the calculated and measured total neutron emission spectrum at 14.1 MeV as described in ref. /16/.

The computations have been performed with GNASH Code /17/.

4. CALCULATED CROSS-SECTIONS

The various computed cross-sections with the above described four level density recipes are intercompared in Figs. 3 to 8 with the OGCP case taken as the base case. A discussion of the suitability of data generated follows :

(i) (n,p) Cross-sections

The calculated (n,p) cross-sections are given in Fig.3 along with the measured data. It is noted that in the energy range extending upto 12 MeV the OGCP and IGCP yield similar results with deviations of 3% or less. The IP predictions are lower, variations being 15% or less. The data generated with BSFGP show variations ~20% or less when compared with the OGCP results.

In the energy range above 12 MeV all the four predictions fall within 15% of one-another or less. At several energy points close agreement is, however, noted between the different data sets.

The IGCP and OGCP predictions are close to the experimental values. However, in the energy range above 15 MeV all the four recipes reproduce the measured data reasonably well.

(ii) (n, α) Cross-sections

(n, α) cross-sections obtained with the four level density recipes are shown in Fig.4 together with the measured data. It is noted that in the energy range extending up to 12 MeV the data generated with BSFGP are quite low, by factors of 2 or more, when compared with the data obtained with the other three recipes which show close agreement at several energy points.

In the energy range above 12 MeV the various prescriptions yield similar cross-sections at several energy points although the maximum deviation is also seen around 30% among the different sets of data at some energy points.

The IGCP, OGCP and IP predictions are noted to be within the experimental error limits.

(iii)(n,2n) Cross-sections

The (n,2n) cross-sections are depicted in Fig.5 together with the measured data. It is noted that the IP predictions are higher throughout the entire energy range. The maximum deviation seen amongst the various sets of data is about 20% although close agreements are also noted at some energy points.

The more recent measured data of Hudson et al are represented well both in the IGCP and OGCP cases.

(iv) Total Neutron Production Cross-sections

Fig. 6 intercompares total neutron production cross-sections in the four cases. It is seen that the BSFGP case shows enhancement by 1-4% upto neutron energies of 15 MeV and above

this energy it shows depletions by about 5% compared to the OGCP case. The data is depleted by about 4% in the IGCP case whereas in the IP case it is enhanced by 1-10%.

(v) Total Hydrogen Production Cross-sections

The total hydrogen production cross-sections in the IGCP case are reduced over a wide energy range by 5-15% as shown in Fig.7. The IGCP and IP cases show marginal depletions amongst them but these two cases produce almost identical results above 12 MeV.

(vi) Total Helium Production Cross-sections

As shown in Fig.8 the total helium production cross-sections are most affected in the BSFGP case, the reduction being 40% or more. The IGCP case shows enhancement while the IP case is identical to the base OGCP case above 12 MeV.

(vii) Total Gamma-Ray Production Cross-sections

The gamma-ray production cross-section are somewhat enhanced in all cases as depicted in Fig.8 compared to the OGCP case. The IGCP and IP cases produce almost identical results.

5. CONCLUSIONS

The following conclusions are drawn from the analysis carried out in this paper :

- (i) Total neutron production cross-sections in all the four level density recipes are close to one another at several energy points although a maximum deviation of about 10% is noted at some of the energy points. The (n,2n) cross-sections also exhibit a similar variation.
- (ii) The (n,p) and total hydrogen production cross-sections show a maximum deviation of 20%.
- (iii) The (n, α) and total helium production cross-sections are adversely affected in the BSFGP case.
- (iv) The gamma-ray production cross-sections are enhanced in the BSFGP case by about 20% whereas they are comparable in other cases.
- (v) The IGCP and IP cases yield almost identical results for many of the reactions investigated in this study. Since the IP case accounts for the energy dependence of the 'a' parameter, it may be adopted in the binary, tertiary and total particle production cross-sections required in reactor technology.

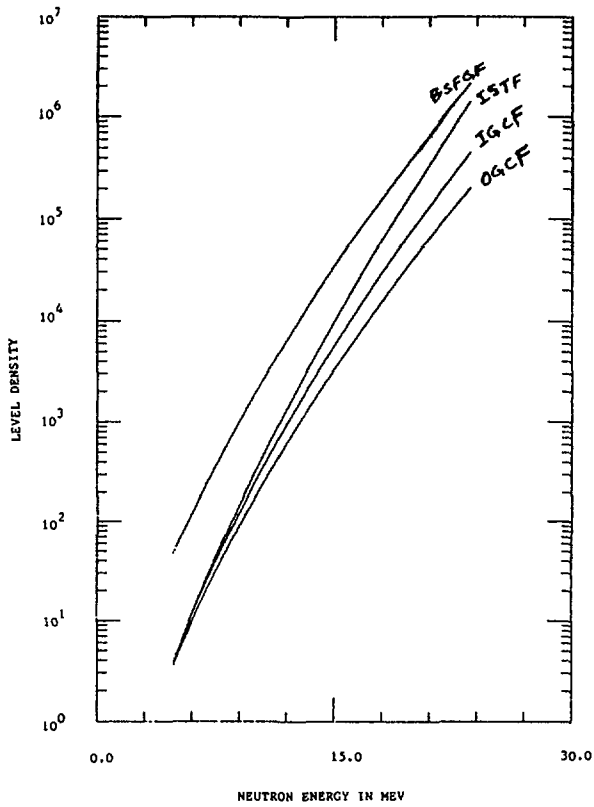


FIG. 1 LEVEL DENSITY VERSUS EXCITATION ENERGY FOR NI-58 WITH VARIOUS LEVEL DENSITY PRESCRIPTIONS

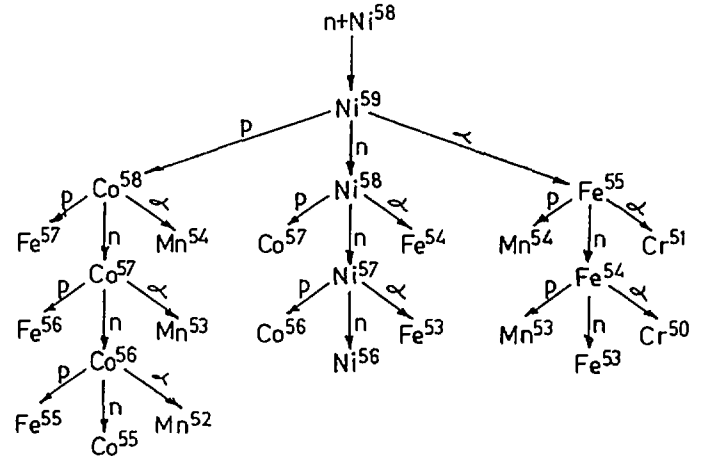


FIG.:2 NUCLIDES PARTICIPATING IN THE DECAY CHAIN OF $n+Ni^{58}$ REACTION

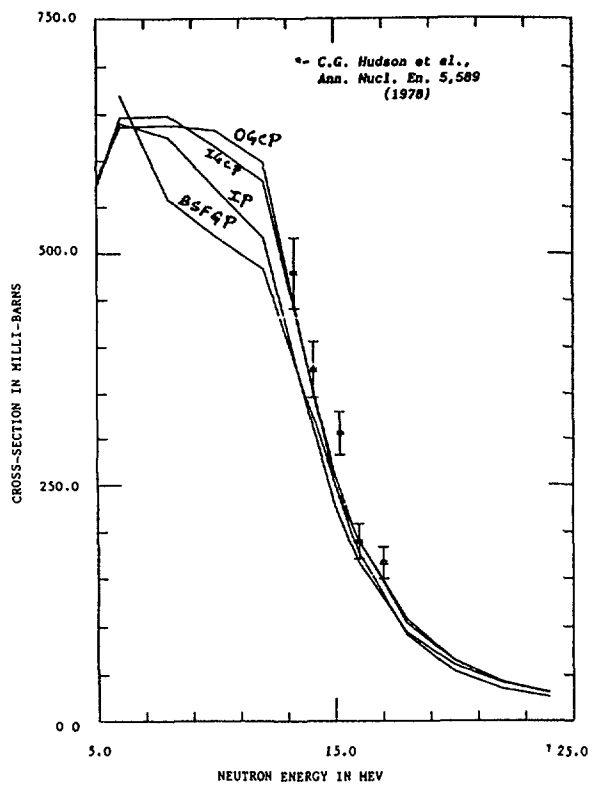


FIG. 3 INTER-COMPARISON OF (N,P) CROSS-SECTIONS OF NI-58 WITH DIFFERENT LEVEL DENSITY PRESCRIPTIONS

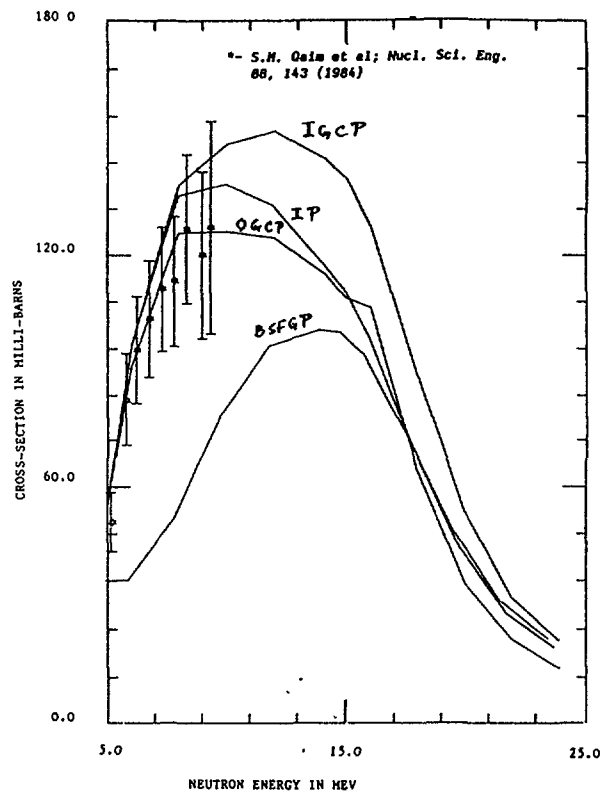


FIG 4 INTER-COMPARISON OF (N,α) CROSS-SECTIONS OF NI-58 WITH DIFFERENT LEVEL DENSITY PRESCRIPTIONS

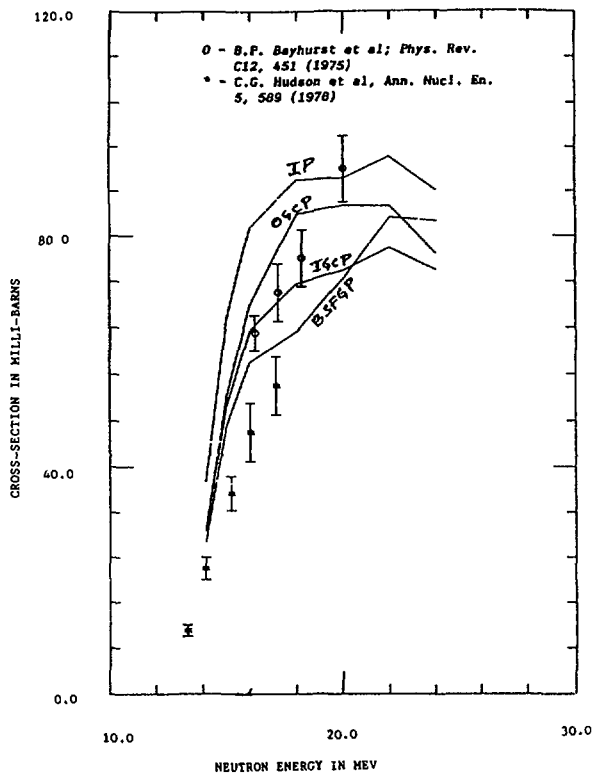


FIG. 5 INTER-COMPARISON OF (N,2N) CROSS-SECTIONS OF NI-58 WITH DIFFERENT LEVEL DENSITY PRESCRIPTIONS

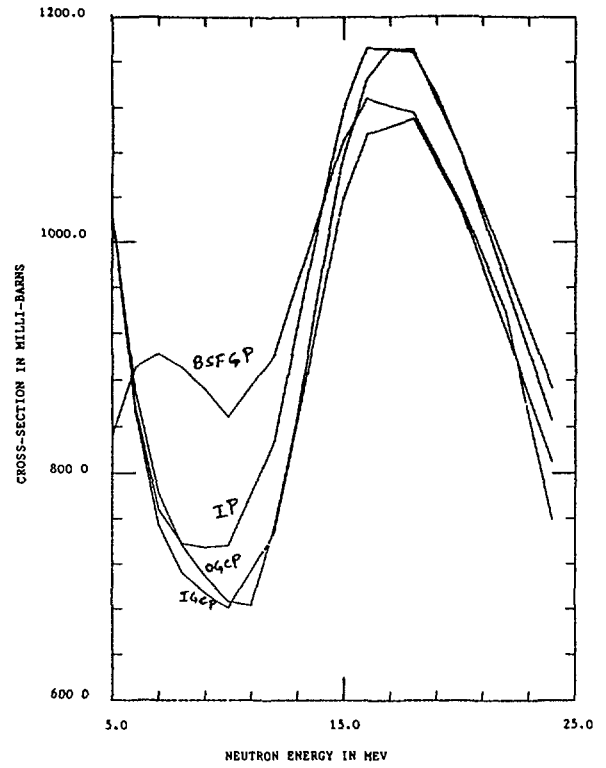


FIG. 6 INTER-COMPARISON OF TOTAL NEUTRON PRODUCTION CROSS-SECTIONS IN NI-58 WITH DIFFERENT LEVEL DENSITY PRESCRIPTIONS

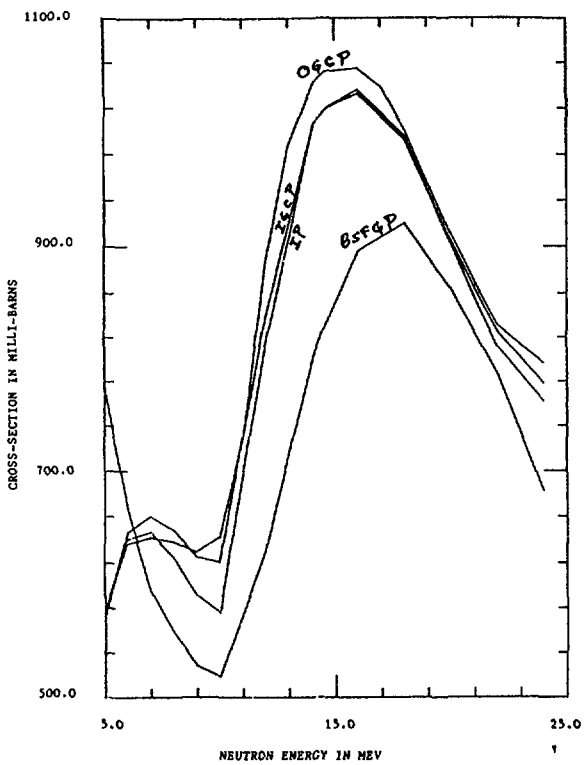


FIG. 7 INTER-COMPARISON OF TOTAL HYDROGEN PRODUCTION CROSS-SECTIONS IN NI-58 WITH DIFFERENT LEVEL DENSITY PRESCRIPTIONS

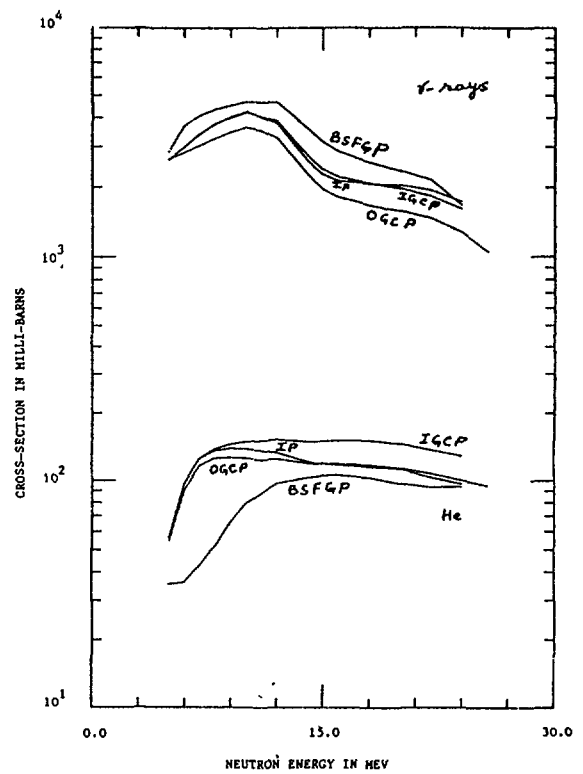


FIG. 8 TOTAL HELIUM AND GAMMA-RAY PRODUCTION CROSS-SECTIONS IN NI-58 WITH VARIOUS LEVEL DENSITY PRESCRIPTIONS

6. REFERENCES

1. W. Hauser and H. Feshbach; Phys. Rev. 87, 366 (1952)
2. C. Kalbach; Z. Phys. A283, 319 (1977)
3. D.M. Brink; Thesis, Oxford University (1955)
P. Axel; Phys. Rev. 126, 671 (1972)
4. A. Gilbert and A.G.W. Cameron; Can. J. Phys. 43, 1446 (1965)
5. U.E. Facchini and E. Saetta-Menichla; Energ. Nucl. 15, 54 (1968)
6. W. Dilg et al; Nucl. Phys. A 217, 269 (1973)
7. A.V. Ignatyuk et al; Sov. J. Nucl. Phys. 21, 255 (1975)
8. J.L. Cook et al; Aust. J. Phys. 20, 477, (1967)
9. M. Ivascu et al; Paper Presented at the IAEA Research Co-ordination Meeting, Bologna, Italy (1986)
10. A. Prince; Nucl. Data for Science and Technology, 574 (1983)
11. G.S. Mani; Nucl. Phys. A 165, 225 (1977)
12. B. Strohmaier et al; Paper Presented at the IAEA Advisory Group Meeting on Nuclear Data for Radiation Assessment and Related Safety Aspects, Vienna (1981)
13. G. Reffo; Paper Presented at the IAEA Advisory Group Meeting on Structural Materials, Vienna (1983)
14. C. Kalbach; Z. Phys. A 287, 319 (1978)
15. F.C. Williams; Nucl. Phys. A 116, 231 (1971)
16. S.B. Garg; Investigation of Neutron Induced Reaction Cross-sections of Ni-58 and Ni-60 with Various Nuclear Model Evaluation Schemes, Paper Presented at the IAEA Research Co-ordination Meeting, Vienna (1990)
17. P.G. Young and E.D. Arthur; LA - 6947 (1977); LA-UR-88-382 (1988)

Investigation of Neutron Induced Reaction Cross Sections
of Ni-58 and Ni-60 with Various Nuclear Model Evaluation Schemes

S.B. Garg
Neutron Physics Division
Bhabha Atomic Research Centre
Trombay, Bombay 400 085, India

A B S T R A C T

Three different nuclear data evaluation approaches, namely, the Multistep Hauser-Feshbach scheme (MSHF), the Geometry Dependent Hybrid Model (GDHM) and the Unified Exciton Model (UEM) are utilized to compute neutron nuclear cross-section data of Ni-58 and Ni-60 in the energy range 1-26 MeV. Multiparticle reaction cross sections, total particle and gamma-ray production cross sections, energy spectra of the emitted particles and gamma-rays and the angle-energy correlated double differential cross sections for the emitted neutrons are specially investigated. Appropriate optical model potential parameters are selected to include the competition of neutron, proton and alpha-particles in the reaction decay. The Brink-Axel approach is adopted to account for gamma-ray emission. Direct inelastic cross sections to the discrete states are determined using the DWBA technique. A detailed intercomparison of the above stated three evaluation schemes is presented.

1. INTRODUCTION

Various nuclear reaction model schemes are currently being applied in order to evaluate and generate neutron induced binary, tertiary and multiparticle reaction cross-sections for the structural and other reactor elements for applications in fission and fusion based nuclear technology. In this paper we have investigated the three data evaluation schemes, namely, multistep Hauser-Feshbach scheme (MSHF), geometry dependent hybrid model scheme (GMHM) and the unified exciton model scheme (UEM) with special reference to the neutron nuclear data of Ni-58 and Ni-60. In particular, we have evaluated the following types of neutron cross-section data in the energy range 1-26 MeV :

- i) (n,p) , (n,α) , (n,γ) , $(n,2n)$, (n,np) , (n,pn) , $(n,n\alpha)$, $(n,\alpha n)$ and $(n,2p)$ cross-sections.
- ii) Energy spectra of the emitted neutron, proton, alpha-particle and gamma-rays.
- iii) Discrete energy level excitation and total inelastic scattering cross-sections.

- iv) Angle-energy correlated double differential cross-sections for the secondary emitted neutrons.
- v) Total production cross-sections for neutron, hydrogen, helium and gamma-rays.

Measured cross-section data for several reactions listed above do not exist for Ni-58 and Ni-60 in the entire energy range considered in this paper and thus this study serves to extrapolate or generate such data for these reactions. In this regard, the above mentioned MSHF, GDHM and UEM schemes have been intercompared and appropriate conclusions are drawn.

2. OPTICAL MODEL POTENTIAL PARAMETERS

Appropriate optical model potential parameters are needed for neutron, proton and alpha-particles in-order to compute their transmission coefficients and inverse reaction cross-sections to account for their competition in the reaction decay mechanism. We have selected these parameters from the literature i.e. for neutrons ; potential used is that of Prince /1/, for protons ; potential is due to Mani /2/, and for alpha-particles ; potential selected is that of Strohmaier et al /3/. These parameters are listed below :

(i) Neutrons

(a) Ni-58

$$V \text{ (MeV)} = 49.33 - 0.48 E + 0.0024 E^2$$

$$W \text{ (MeV)} = 0.0$$

$$W_G \text{ (MeV)} = 12.0 + 0.358E - 0.007 E^2 ; E < 25 \text{ MeV}$$

$$= 0.445 + 0.908E - 0.011 E^2 ; 25 \leq E \leq 45 \text{ MeV}$$

$$U \text{ (MeV)} = 6.75$$

$$r_v \text{ (fm)} = 1.2583 + 0.00258 E ; E < 12 \text{ MeV}$$

$$r_w \text{ (fm)} = 1.4645 - 0.0146 E ; E < 12 \text{ MeV}$$

$$r_u = r_v = 1.3128 - 0.00196 E ; 12 \leq E \leq 100 \text{ MeV}$$

$$r_u = r_v ; a_u = a_v = 0.7813 \text{ fm}$$

$$a_w = 0.63 \text{ fm}$$

(b) Ni-60

$$V \text{ (MeV)} = 48.5514 - 0.474 E + 0.0022 E^2$$

$$W_G \text{ (MeV)} = 12.0 + 0.358 E - 0.007 E^2 ; E < 25 \text{ MeV}$$

$$= 0.2875 + 0.914 E - 0.0105 E^2 ; 25 \leq E \leq 45 \text{ MeV}$$

$$U \text{ (MeV)} = 6.55$$

$$r_v \text{ (fm)} = 1.2574 + 0.00255 E ; E < 12 \text{ MeV}$$

$$r_w \text{ (fm)} = 1.46 - 0.0146 E ; E < 12 \text{ MeV}$$

$$r_v = r_w = 1.3113 - 0.00194 E ; 12 \leq E \leq 100 \text{ MeV}$$

$$r_u = r_v ; a_v = a_u = 0.7851 \text{ fm}$$

$$a_w = 0.6331 \text{ fm}$$

where

E = incident energy (MeV)

V = real well depth (Woods-Saxon)

W = imaginary well depth (Woods-Saxon)

W_G = imaginary well depth (Gaussian)

U = spin-orbit potential depth (Thomas)

r_v, r_w, r_u = radii for various potentials

a_v, a_w, a_u = diffuseness for various potentials.

(ii) Protons

$$V \text{ (MeV)} = 41.3 ; W \text{ (MeV)} = 0.9$$

$$W_D \text{ (MeV)} = 8.2 ; U \text{ (MeV)} = 7.5$$

$$r_v \text{ (fm)} = 1.2 ; r_w \text{ (fm)} = 1.25$$

$$r_u \text{ (fm)} = 1.16 ; r_c \text{ (fm)} = 1.25$$

$$a_v \text{ (fm)} = 0.64 ; a_w \text{ (fm)} = 0.56$$

$$a_v = a_u$$

where

W_D = imaginary well-depth (Derivative Woods-Saxon)

r_c = coulomb radius

Optical model potential parameters due to Perey /4/ and Becchetti - Greenlees /5/ have also been applied in the analysis.

(iii) Alpha - Particles

$$V \text{ (MeV)} = 173.0 - 0.30 E$$

$$W \text{ (MeV)} = 20.5 + 0.1 E$$

$$r_v \text{ (fm)} = r_w \text{ (fm)} = 1.445$$

$$a_v \text{ (fm)} = a_w \text{ (fm)} = 0.51$$

$$r_c \text{ (fm)} = 1.3$$

(iv) Gamma-rays

Transmission coefficients for gamma-rays have been calculated according to the Brink-Axel giant dipole resonance model /6/. The following resonance parameters for E1 radiation due to Reffo /7/ have been used in the computations :

(a) Ni-58

$$\begin{aligned} E1 &= 16.0 \text{ MeV} ; & \Gamma_1 &= 3.70 \text{ MeV} \\ E2 &= 18.6 \text{ MeV} ; & \Gamma_2 &= 5.10 \text{ MeV} \\ \langle \Gamma \rangle &= 2200 \text{ meV} ; & \langle D \rangle &= 14 \text{ keV} \end{aligned}$$

(b) Ni-60

$$\begin{aligned} E1 &= 16.0 \text{ MeV} ; & \Gamma_1 &= 3.7 \text{ MeV} \\ E2 &= 18.4 \text{ MeV} ; & \Gamma_2 &= 5.1 \text{ MeV} \\ \langle \Gamma \rangle &= 1300 \text{ meV} ; & \langle D \rangle &= 14 \text{ keV} \end{aligned}$$

For M1 radiation default values of $E = 8 \text{ MeV}$ and $\Gamma = 5 \text{ MeV}$ are assumed.

3. DWBA PARAMETERS

Direct level excitation cross-sections for several discrete energy levels of Ni-58 and Ni-60 have been obtained using the distorted wave Born approximation (DWBA) /8/ of the direct reaction theory. The deformation parameters for the following energy levels are taken from Hetrick et al /9/ :

Ni-58			Ni-60		
E(MeV)	J π		E(MeV)	J π	
1.454	2+	0.1871	1.333	2+	0.2345
2.459	4+	0.0774	2.159	2+	0.0224
2.776	2+	0.0066	2.506	4+	0.0837
3.038	2+	0.0538	3.120	4+	0.0566
3.265	2+	0.0632	3.045	3-	0.1612
4.470	3-	0.140			

4. NUCLEAR REACTION MODELS AND CODES

As described earlier the following three data evaluation schemes are investigated in this analysis :

(i) Multistep Hauser-Feshbach scheme (MSHF) /10/ comprising optical model, Kalbach exciton model, Brink-Axel giant dipole

radiation model and the DWBA model. Computer codes SCAT2 /11/, DWUCK4 /12/ and GNASH /13/ are used.

(ii) Geometry dependent hybrid model scheme (GDHM) /14/ which includes optical model and Weisskopf-Ewing evaporation model. ALICE-87 code /15/ which accounts for the equilibrium and pre-equilibrium emission of gamma-rays in an approximate manner is employed in the computations.

(iii) Unified exciton model scheme (UEM) /16/ involving the Brink-Axel model and optical model. Calculations are carried out with GRAPE code package /17/.

All these schemes give consistent descriptions of all the energetically allowed reactions. Emission of neutrons, protons, alpha-particles and gamma-rays are included at each stage of the reaction. In the MSHF scheme gamma-decay competition is not included in the pre-equilibrium stage. The reaction decay chains selected in the MSHF scheme for Ni-58 and Ni-60 are shown in Figs.1 and 2 respectively. Discrete energy levels, their spins, parities and gamma-ray branching ratios for all the nuclides included in these figures are taken from the literature. In the GDHM and UEM schemes discrete level data are not used. This may affect the threshold reactions in these two schemes.

5. LEVEL DENSITY INFORMATION

The continuum energy region in the MSHF scheme is represented by the level density formulae of Gilbert and Cameron /18/ with the pairing energy corrections of Cook et al /19/. In the UEM scheme back-shifted Fermi-gas model is used with the parameters of Dilg et al /20/. In the GDHM scheme the level density parameter 'a' is taken as $A/9$, A being the mass no. of the composite nucleus and the pairing energy corrections are taken as zero for even-even nuclides, $-\delta$ for odd-even and -2δ for odd-odd nuclides, δ being equal to $11/\sqrt{A}$. Thus, the three evaluation schemes make use of different level density formulations.

In the pre-equilibrium decay considerations the exciton-state densities are calculated according to the Williams formula /21/. In the UEM scheme it is renormalized to coincide with the back-shifted Fermi gas formula.

6. INTERNAL TRANSITION RATES

The GDHM and UEM schemes make use of the nucleon-nucleon interaction cross-sections to calculate the internal transition rates. In the MSHF scheme these are defined in terms of the average matrix element for two body interaction which is parameterized by Kalbach /21/ as a function of energy involving a constant parameter K . K is determined by matching the calculated and measured particle emission cross-sections and their energy spectra.

7. CALCULATED CROSS-SECTIONS

The cross-sections calculated with the MSHF scheme are compared in the following with the available measured data. An intercomparison of the MSHF, GDHM and UEM schemes is also brought out in a separate section.

(i) Neutron Emission Energy Spectrum

Total neutron emission energy spectrum for Ni-58 at neutron incident energy of 14.1 MeV is shown in Fig.3 with the K-parameter of the average reaction matrix constant taken as 135 MeV³. The maximum deviation between the calculated and measured spectra in the applicability range of the model is about 25%, although there is a close agreement at several emission energies.

(ii) (n, α) Cross-sections

(n, α) reaction in structural materials is of importance since it leads to the production of helium gas which is considered to be responsible for swelling in these materials. (n, α) cross-sections for Ni-58 are shown in Fig.4 visa-vis the measured data. It is noted that the calculated cross-sections are within the experimental errors.

(iii) Inelastic-Scattering Cross-sections

Direct inelastic scattering cross-sections to the various levels of Ni-58 and Ni-60 computed with the DWBA technique are depicted in Figs. 5 and 6 respectively. Utilizing these direct contributions, total inelastic cross-section is estimated as a function of neutron incident energy. Figs. 7 and 8 represent this cross-section for Ni-58 and Ni-60 with the direct component included (curve 1) and without the direct component i.e. only compound statistical (curve 2). It is noted that curve 1 with the direct component included describes the measured data rather well.

It is also noted that the direct inelastic component becomes almost constant in the energy range 10 to 20 MeV. In the case of Ni-58 it is 85 mb and in Ni-60 it is about 130 mb.

(iv) (n,p) Cross-sections

The calculated and measured (n,p) cross-sections for Ni-58 and Ni-60 are shown in Figs. 9 and 10 respectively. In the case of Ni-58, it has been seen that the measured data given by the different authors are discrepant amongst themselves by a factor of 2 or more. The calculated solid curve in Fig.9, however, shows good agreement with the more recent data of Hudson et al. In the case of Ni-60, the calculated cross-sections (Fig.10) are within the experimental errors over a wide range of energy. However, above 16 MeV the measured data are higher by about 50%.

In order to investigate the effect of proton optical model potentials on (n,p) cross-section data, we have carried out a comparative study using three sets of potentials given by Mani, Perey and Becchetti-Greenlees for Ni-58. Fig.11 represents the

results. It is noted that the calculated cross-section data with these potentials are almost similar in the energy range above 14 MeV. Below this energy, deviations $\sim 10\%$ are, however, seen among the various predictions. In short, it may be stated that the different sets of potentials do not produce any significant change in (n,p) cross-section data.

(v) (n,2n) Cross-sections

(n,2n) cross-sections for Ni-58 are given in Fig.12. Measured cross-section data for this reaction are rather sparse for Ni-60 and therefore are not shown separately. It is seen from the figure that there is a close agreement between calculated and measured data.

(vi) Tertiary Reactions

(n,pn), (n,np), (n,n α), (n, α n) and (n,2p) reaction cross-sections for Ni-58 and Ni-60 are shown in Figs. 13 and 14 respectively along with (n,p), (n, α) and (n,2n) cross-sections for the sake of comparison. The measured tertiary cross-section data, being rare, are not shown. All the cross-sections depicted in these figures are consistently evaluated in the MSHF scheme.

(vii) Total Production Cross-sections

Total production cross-sections for neutron, hydrogen, helium and gamma-rays are given in Figs. 15 and 16 for Ni-58 and Ni-60 respectively. No comparison with the measured data is brought out for lack of such data. It is noted that helium production cross-section is the lowest ~ 100 mb and gamma-ray production cross-section is the highest ~ 1000 mb or more.

Proton production cross-sections calculated with the Mani, Perey and Becchetti-Greenlees potentials are shown in Fig.17. It is noted that the cross-sections are within 7% of one-another and show similar energy dependence.

(viii) Angle-Energy Correlated Double Differential Cross-Sections

Angle-energy correlated double differential cross-sections calculated in the framework of the GDHM scheme are depicted in Figs. 18 to 23 for Ni-58 at neutron incident energies of 14.1 MeV and 18 MeV and at emission angles of 45° , 60° and 120° . It is noted from these figures that the calculated data are within the experimental errors over the neutron emission energy range of 2 to 10 MeV. Above this energy, large deviations are, however, noted in some cases. This aspect may not be of much consequence in fusion or fission applications since the absolute magnitudes involved are insignificantly small.

The corresponding calculated double differential cross-sections for Ni-60 are given in Figs. 24 and 25. In this case no comparison is made with the measurements because of lack of data.

(ix) Gamma-Emission Energy Spectrum

The calculated gamma-emission energy spectra for Ni-58 and Ni-60 at 14.1 MeV are shown in Figs. 26 and 27 respectively. A resonant behaviour is noted in the emission energy region extending upto 5 MeV due to the presence of discrete energy levels.

8. INTER-COMPARISON OF MSHF, GDHM AND UEM SCHEMES

$(n,2n)$, (n,p) , (n,α) , n_{em} , p_{em} and α_{em} cross-sections calculated with the MSHF, GDHM and UEM schemes are intercompared in Figs. 28 to 35. The GDHM scheme predicts the highest $(n,2n)$ cross-sections for Ni-58 as noted from Fig.28. It is followed by the UEM scheme, the difference between them being about 25%. The MSHF scheme represents well the measured $(n,2n)$ cross-section data but there exist factors of 3 or more between the MSHF and GDHM predictions. The $(n,2n)$ cross-sections for Ni-60 shown in Fig. 29 do not show as violent a variation. In this case GDHM and UEM schemes yield comparable results while the MSHF predictions are low by about 20%.

The (n,p) cross-sections for Ni-58 given in Fig.30 are within 20% of one-another in the three schemes while those for Ni-60 depicted in Fig.31 show a variation of 30% or less.

The GDHM results for (n,α) cross-sections for Ni-58 and Ni-60 shown in Figs. 32 and 33 are lower than those for the MSHF scheme, the deviation being 20% to 70%. The UEM results for this reaction are the highest and differ from others by several factors. It has been already brought out in the text that the MSHF results closely reproduce the measured data. This analysis indicates that the mechanism of α -emission in the UEM scheme needs re-examination and improvements.

Total neutron emission cross-sections for Ni-58 represented in Fig.34 reveal that the UEM results are higher than the MSHF predictions by 1.5% to 15%. They are lower than the GDHM results by 5% to 15%. Similar trends are noted for Ni-60 in Fig.35, the UEM data being higher than the MSHF data by 10% or less and lower than the GDHM data by 6% or less.

Total proton emission cross-sections for Ni-58 in the MSHF scheme are higher than those in the UEM scheme by about 30% while these are higher by 5% to 20% compared to those in the GDHM scheme. In the case of Ni-60 also similar trends are seen with deviations being somewhat higher.

Total alpha-emission cross-sections for Ni-58 show agreement within 5% over most of the energy range in the MSHF and GDHM schemes. The UEM scheme gives higher results by 25% to 50%. In the case of Ni-60 variations ranging upto 70% are noted among the various schemes.

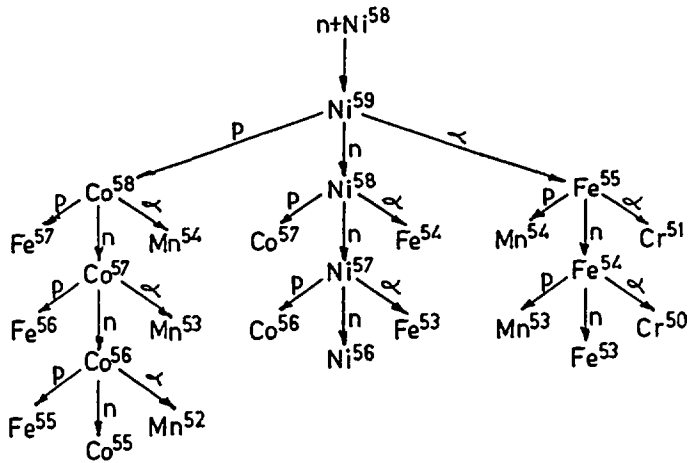


FIG.:1 NUCLIDES PARTICIPATING IN THE DECAY CHAIN OF $n+Ni^{58}$ REACTION

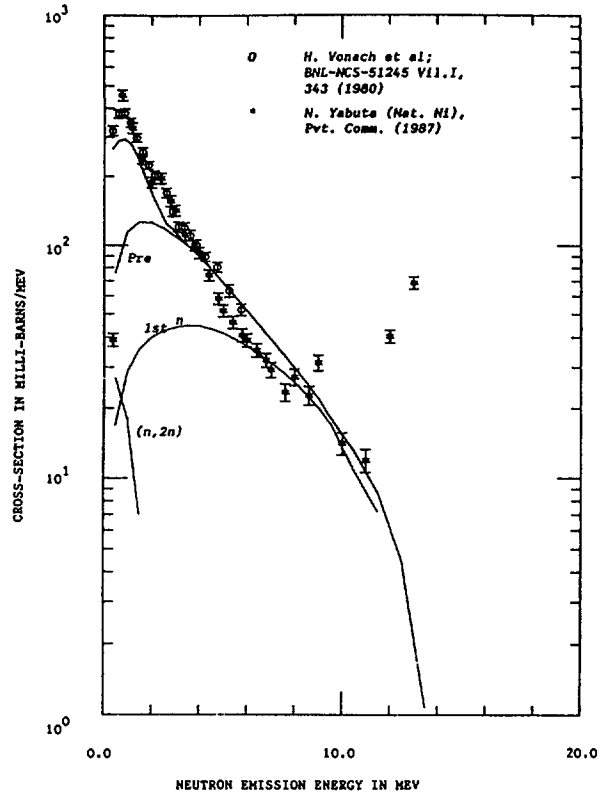


FIG. 3 NEUTRON EMISSION SPECTRUM IN NI-58 AT 14.1 MEV

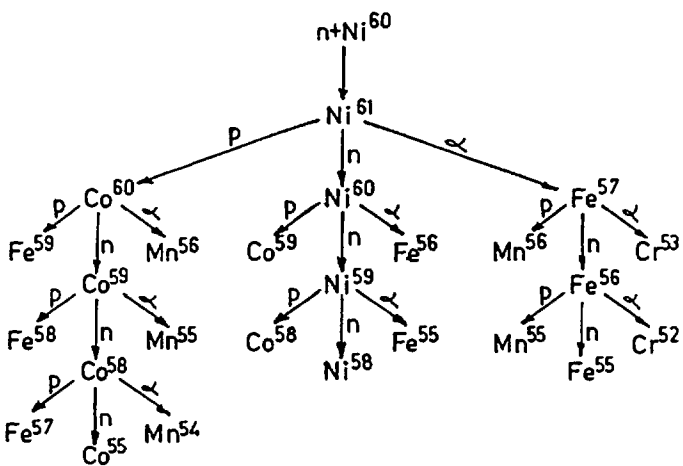
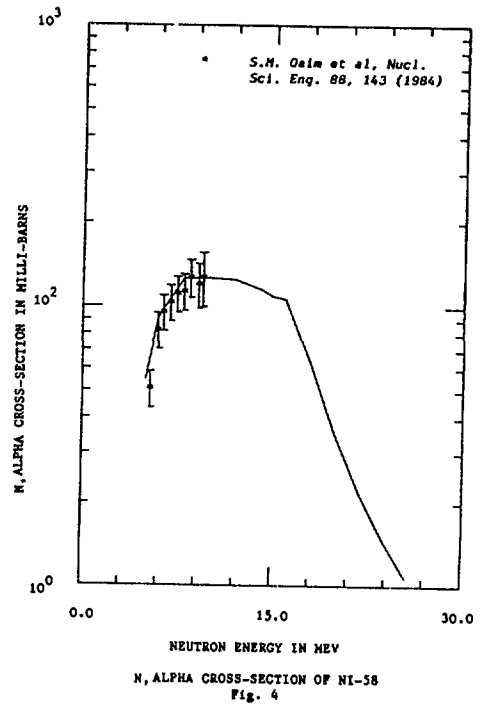


FIG.:2 NUCLIDES PARTICIPATING IN THE DECAY CHAIN OF $n+Ni^{60}$ REACTION



N, ALPHA CROSS-SECTION OF NI-58 Fig. 4

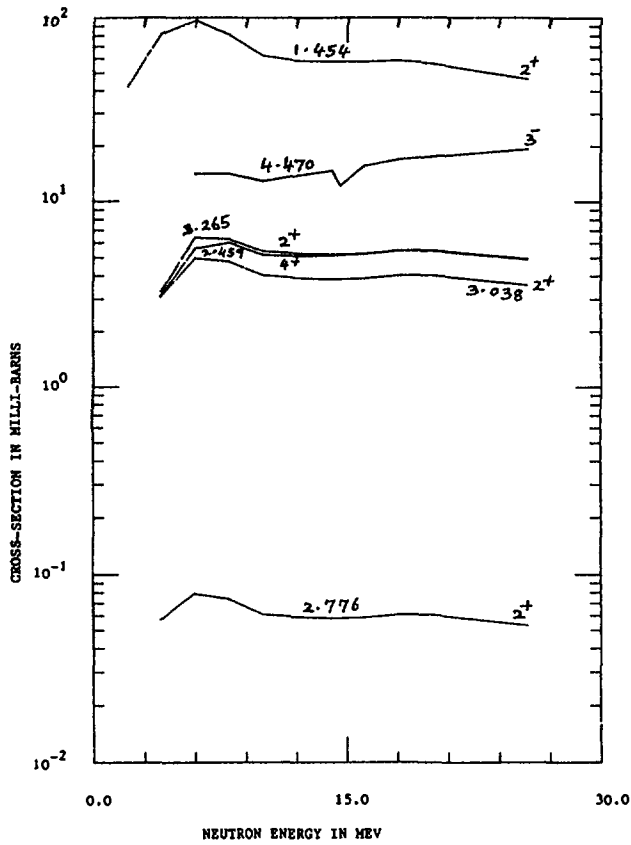
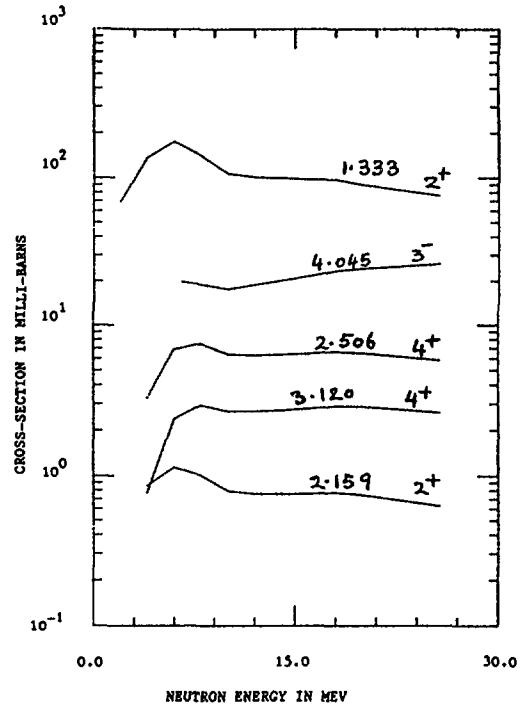


FIG. 5 DIRECT LEVEL EXCITATION CROSS-SECTIONS OF NI-58



DIRECT LEVEL EXCITATION X-SECTIONS OF NI-60
Fig. 6

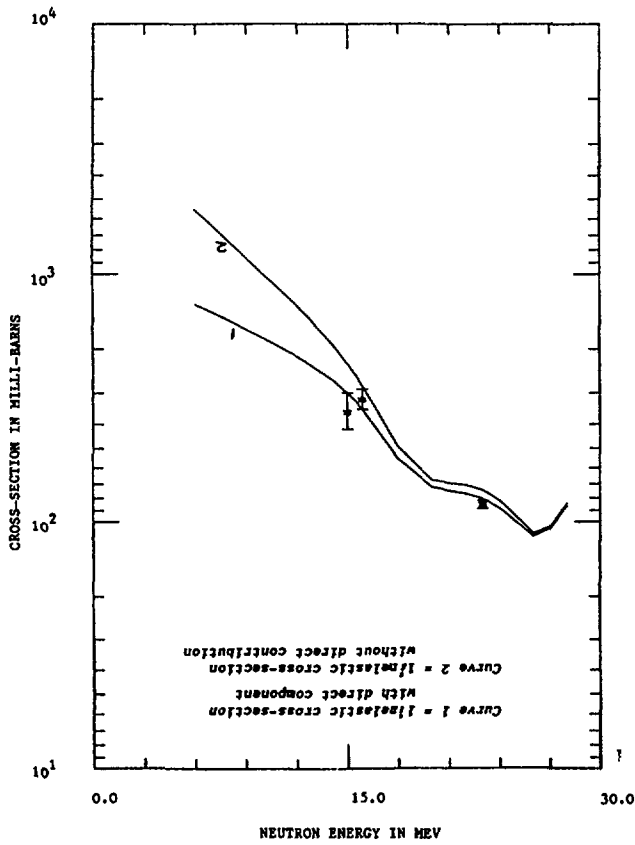


Fig. 7 TOTAL NEUTRON INELASTIC CROSS-SECTIONS OF NI-58 WITH AND WITHOUT DIRECT REACTION COMPONENT

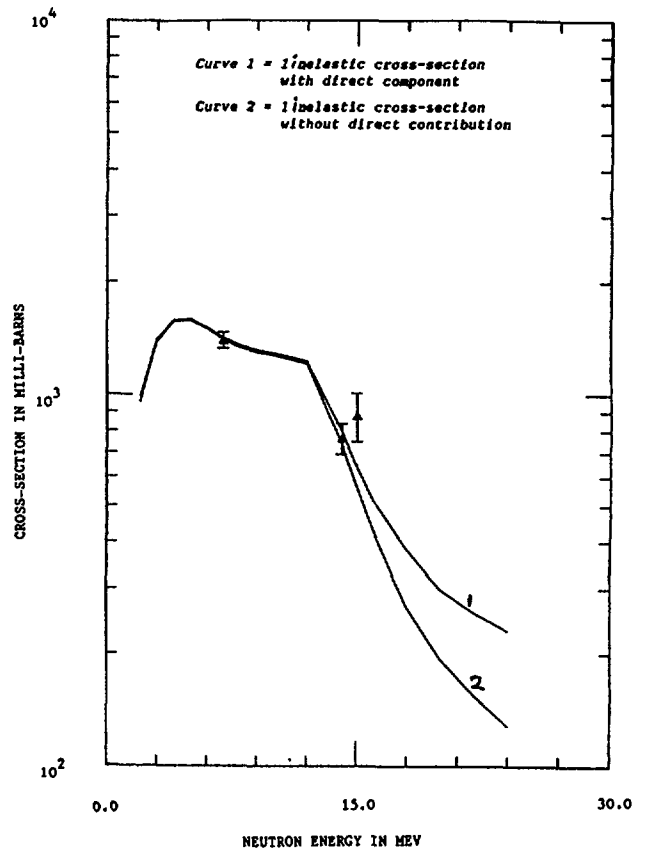


FIG. 8 TOTAL NEUTRON INELASTIC CROSS-SECTION OF NI-60 WITH AND WITHOUT DIRECT COMPONENT

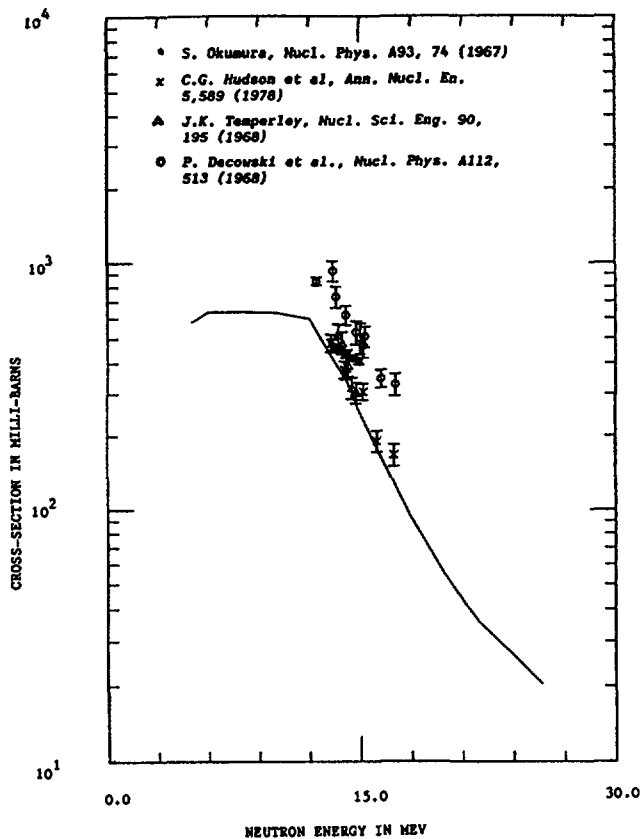


FIG. 9 (N,P) CROSS-SECTIONS FOR NI-58

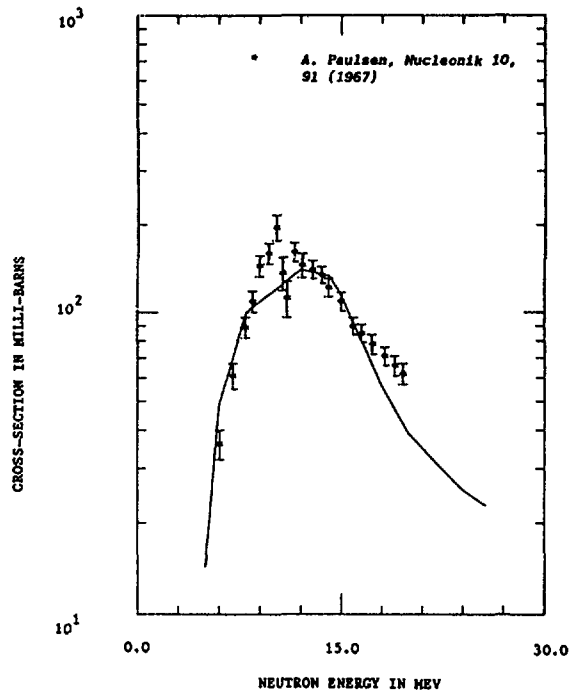


Fig. 10 N,P CROSS-SECTIONS OF NI-60

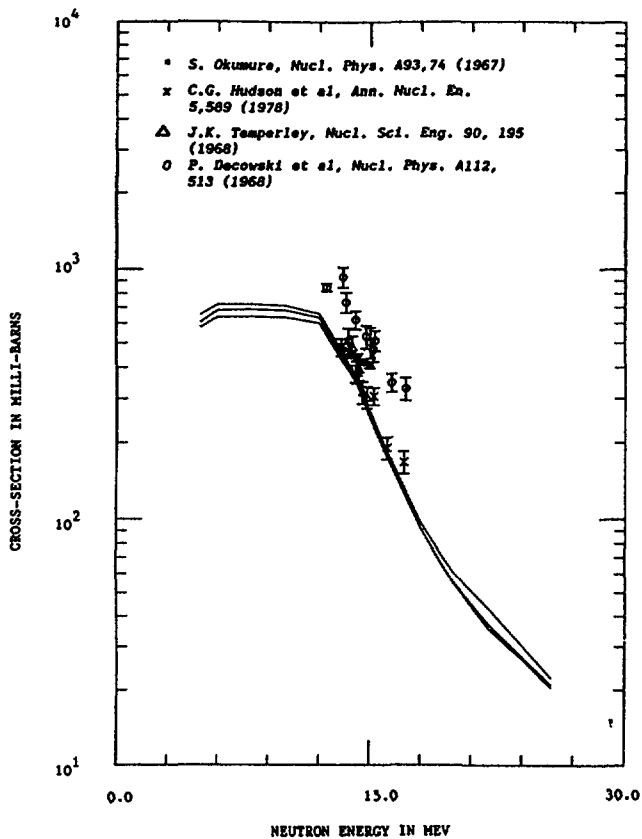
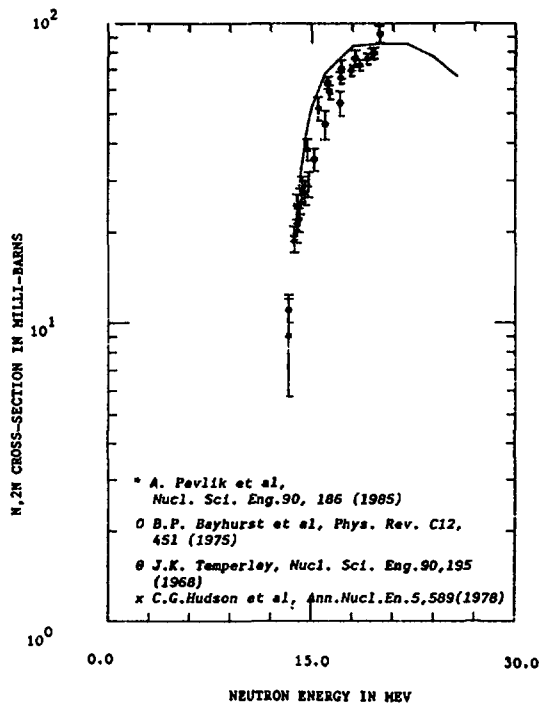


FIG. 11 INTER-COMPARISON OF (N,P) CROSS-SECTIONS OF NI-58 WITH DIFFERENT PROTON POTENTIALS



N,2N CROSS-SECTION OF NI-58
Fig. 12

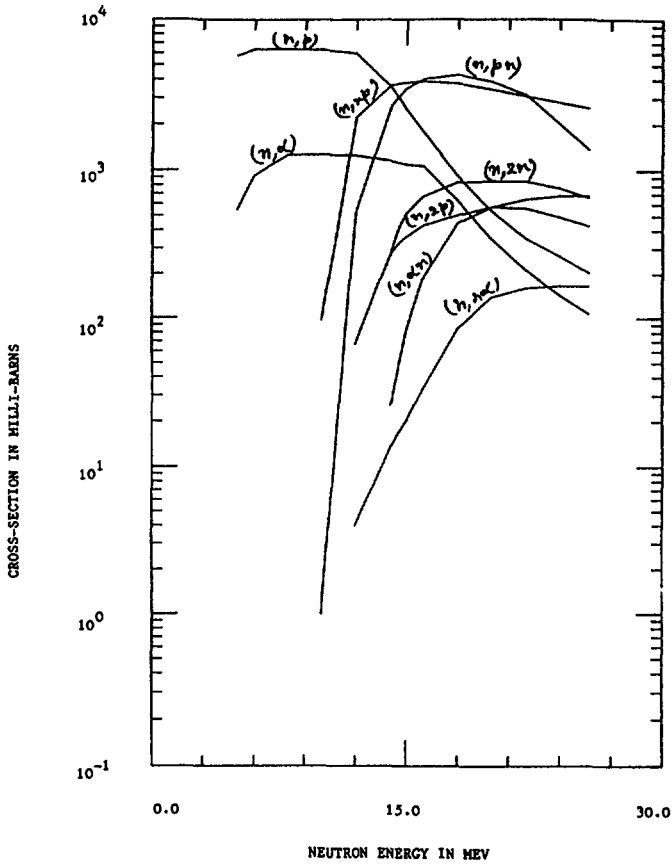
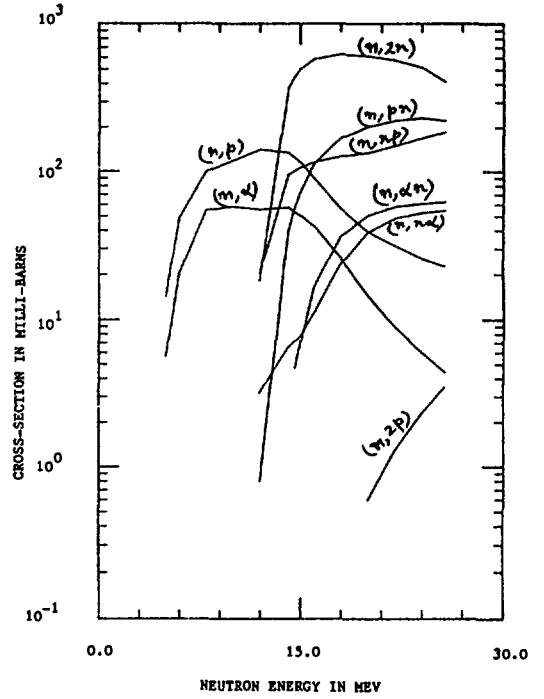
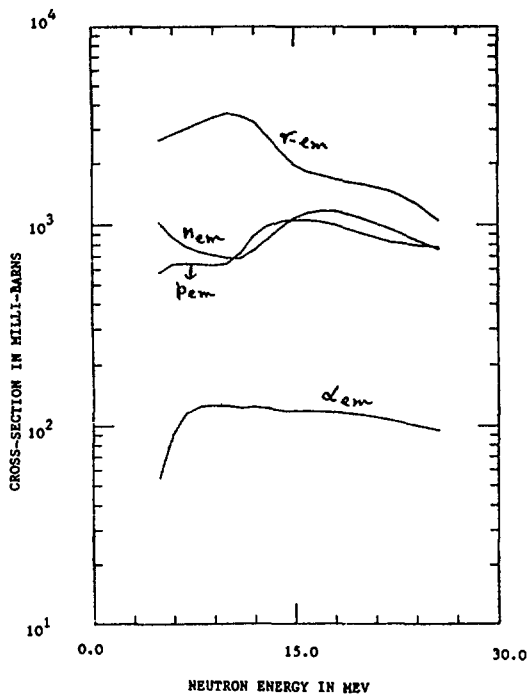


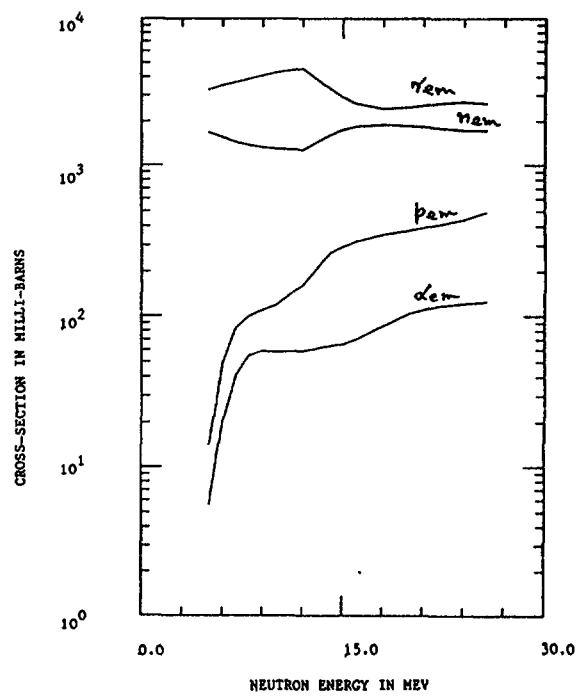
FIG. 13 VARIOUS TYPES OF REACTION CROSS-SECTIONS FOR NI-58



VARIOUS TYPES OF REACTION CROSS-SECTIONS FOR NI-60
Fig. 14



TOTAL EMISSION CROSS-SECTIONS FOR N, P, ALPHA AND GAMMA IN NI-58
Fig. 15



TOTAL EMISSION X-SECTIONS FOR N,P,ALPHA AND GAMMA FOR NI-60
Fig. 16

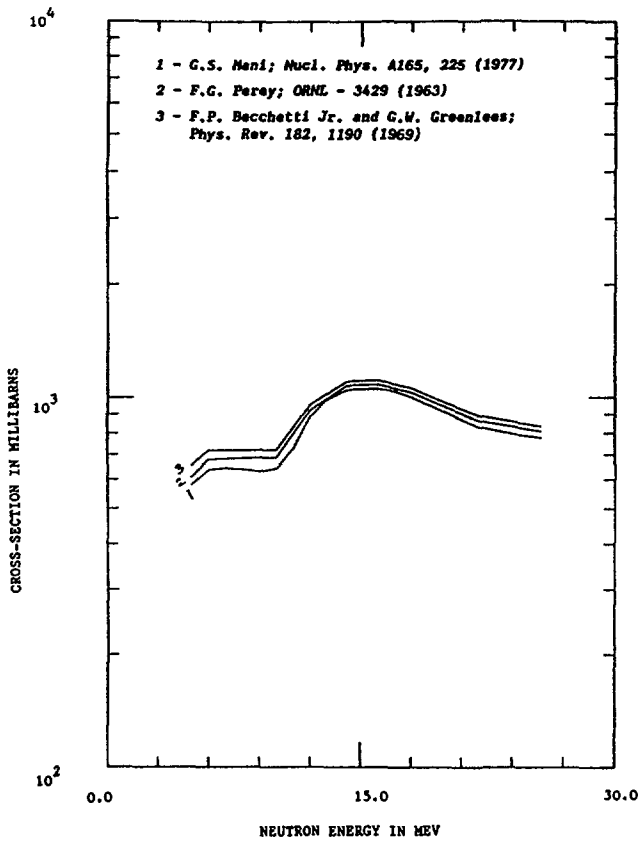
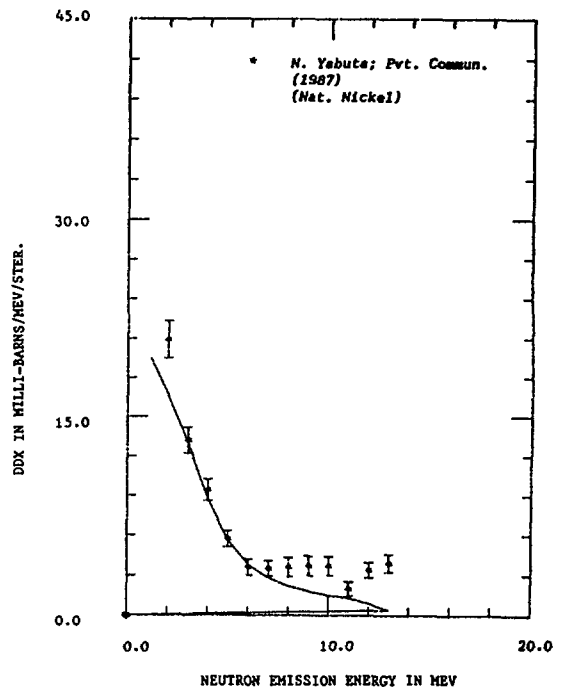
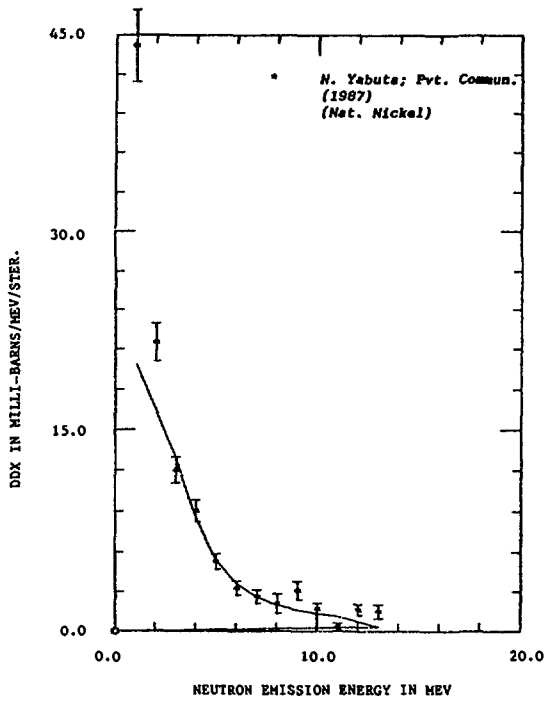


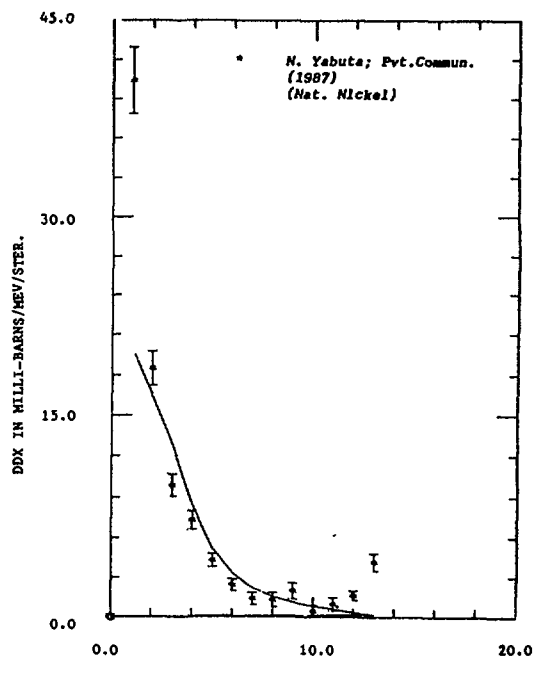
FIG. 17 INTERCOMPARISON OF PROTON EMISSION CROSS-SECTIONS OF NI-58 WITH DIFFERENT PROTON POTENTIALS



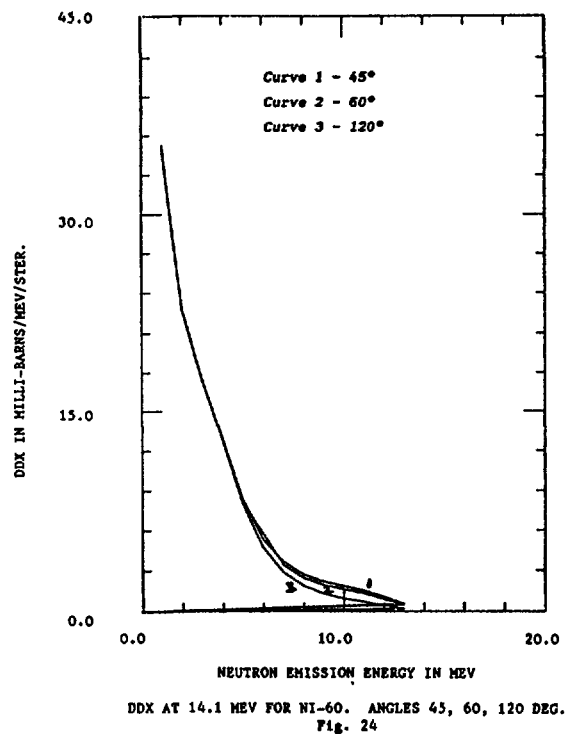
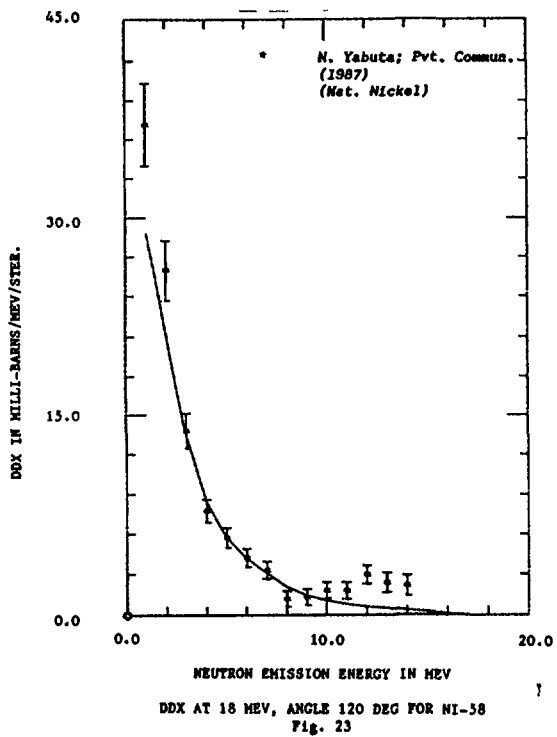
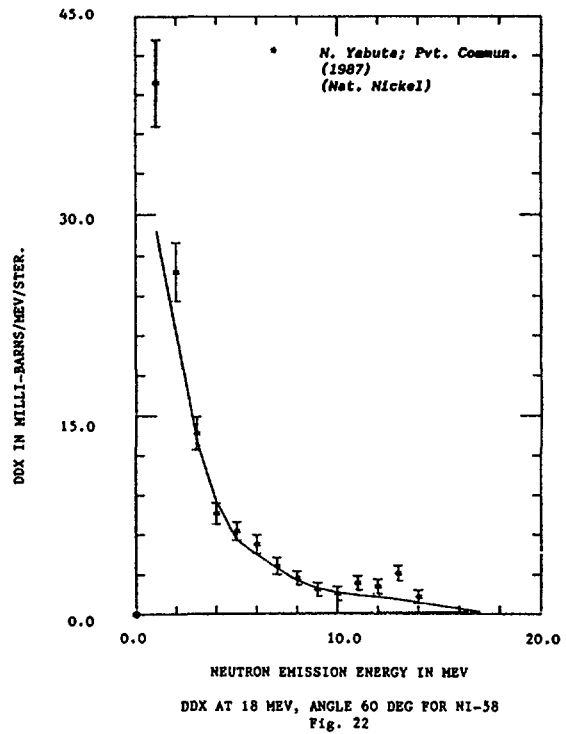
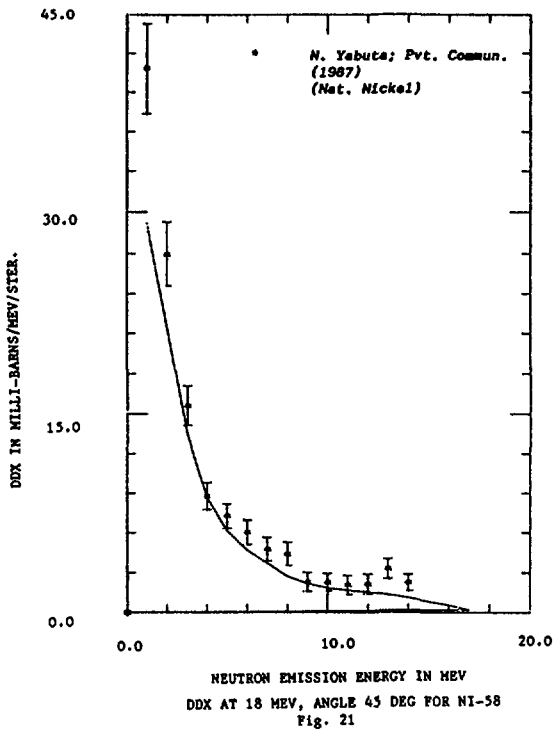
DDX AT 14.1 MEV AND ANGLE 45 DEG. FOR NI-58 Fig. 18

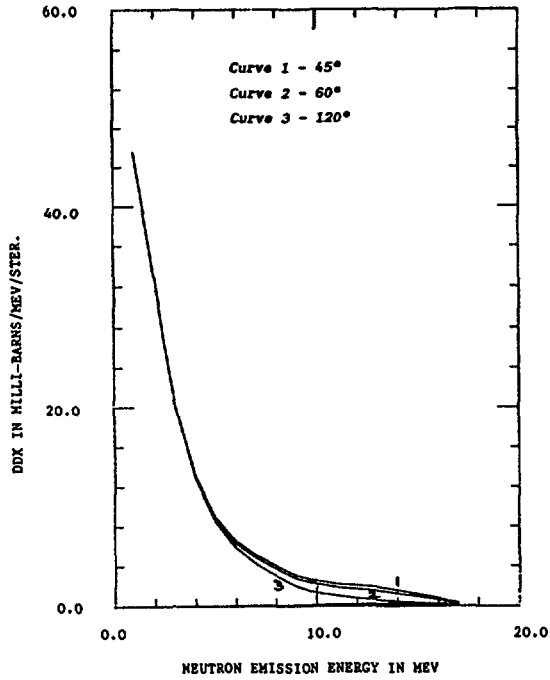


DDX AT 14.1 MEV AND ANGLE 60 DEG FOR NI-58 Fig. 19

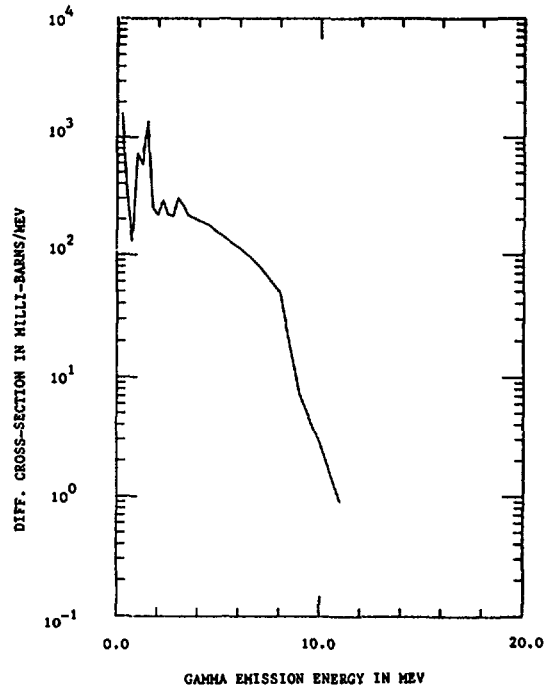


DDX AT 14.1 MEV AND ANGLE 120 DEG FOR NI-58 Fig. 20

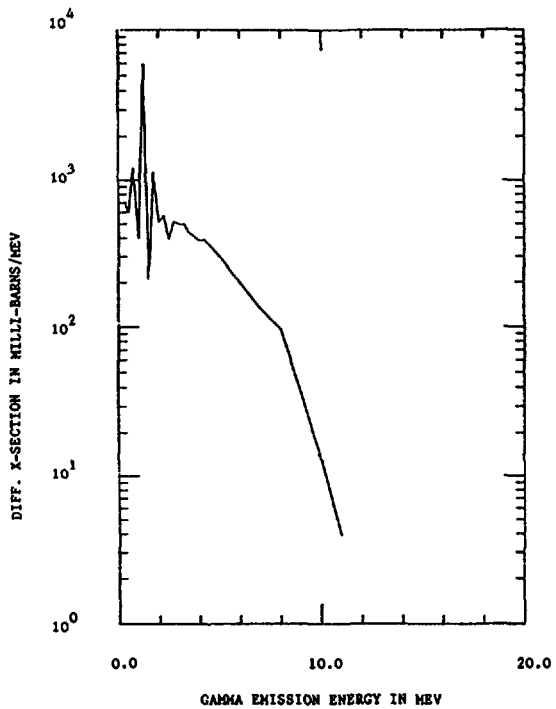




DDX AT 18 MEV FOR NI-60, ANGLES 45, 60, 120 DEG.
Fig. 25



GAMMA EMISSION SPECTRUM AT 14.1 MEV FOR NI-58
Fig. 26



GAMMA EMISSION SPECTRUM AT NEUTRON ENERGY OF 14.1 MEV
FOR NI-60
Fig. 27

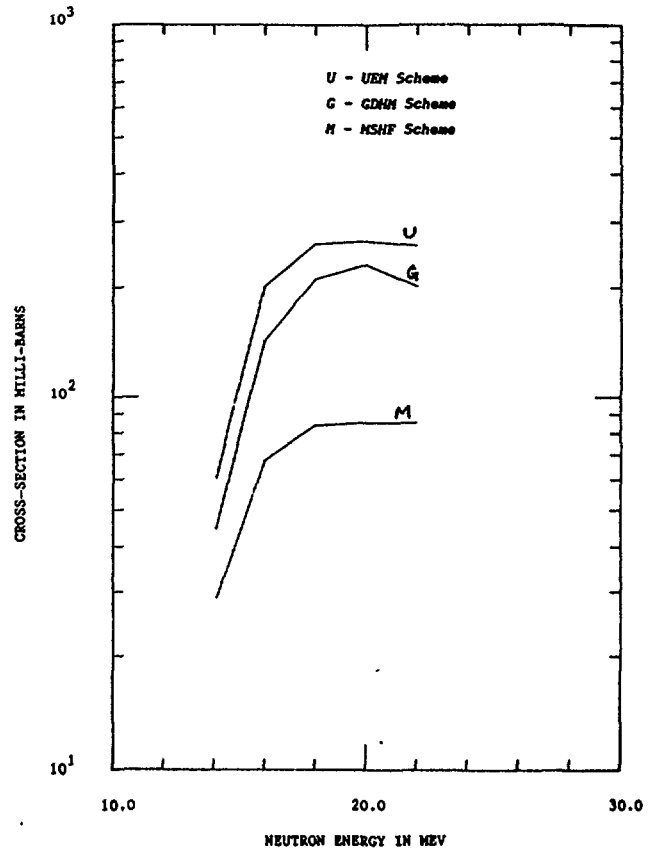


FIG. 28 INTER-COMPARISON OF (N,2N) CROSS-SECTION OF NI-58
IN MSHF, GDHM AND UEM SCHEMES

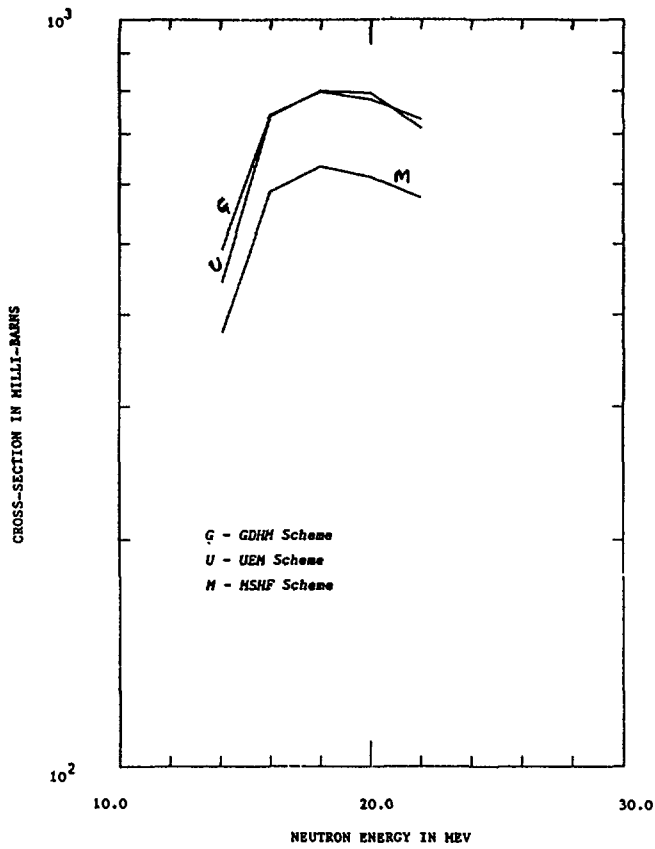


FIG. 29 INTER-COMPARISON OF (N,2N) CROSS-SECTION OF NI-60 IN MSHF, GDHM AND UEH SCHEMES

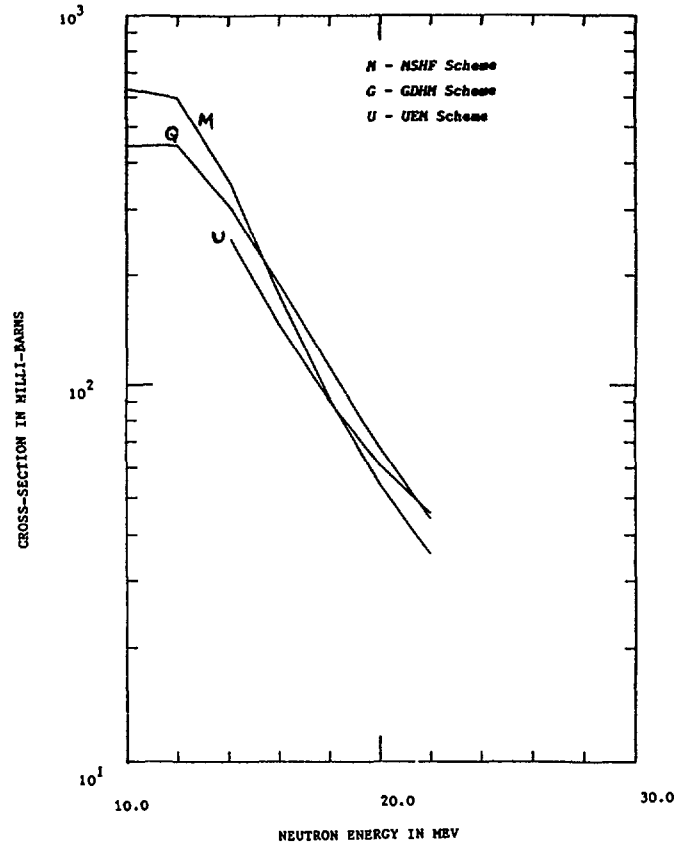


FIG. 30 INTER-COMPARISON OF (N,P) CROSS-SECTION OF NI-58 IN MSHF, GDHM AND UEH SCHEMES

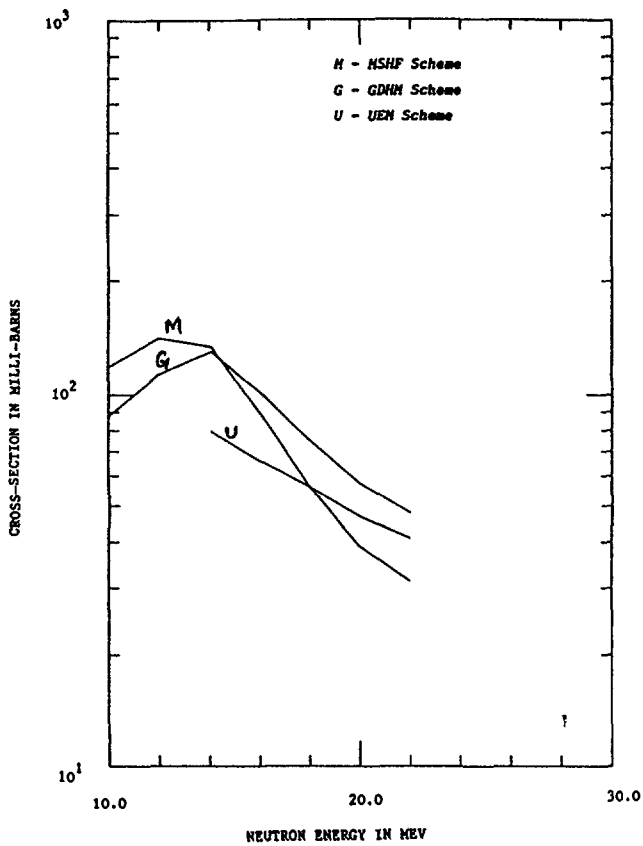


FIG. 31 INTER-COMPARISON OF (N,P) CROSS-SECTION OF NI-60 IN MSHF, GDHM AND UEH SCHEMES

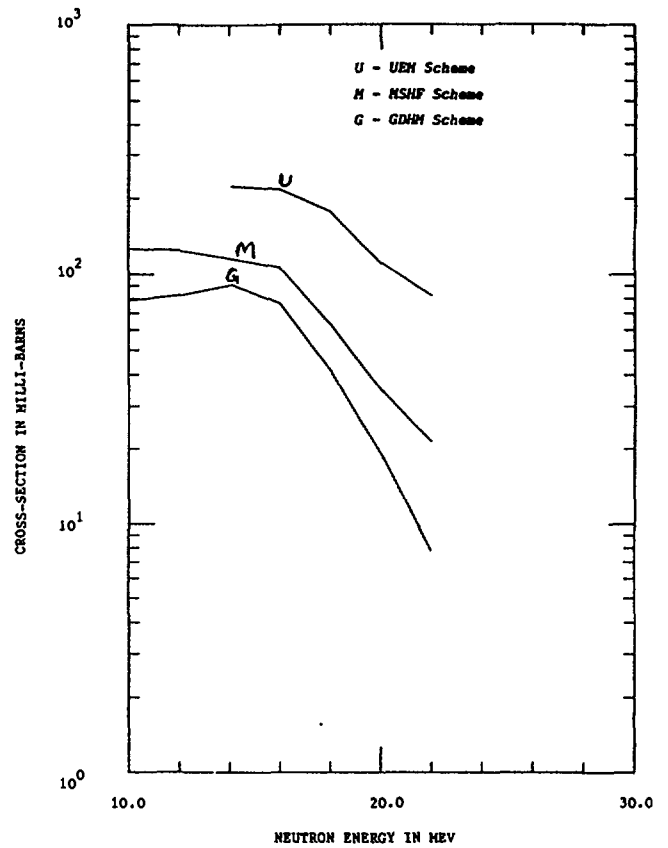


FIG. 32 INTER-COMPARISON OF (N,A) CROSS-SECTION OF NI-58 IN MSHF, GDHM AND UEH SCHEMES

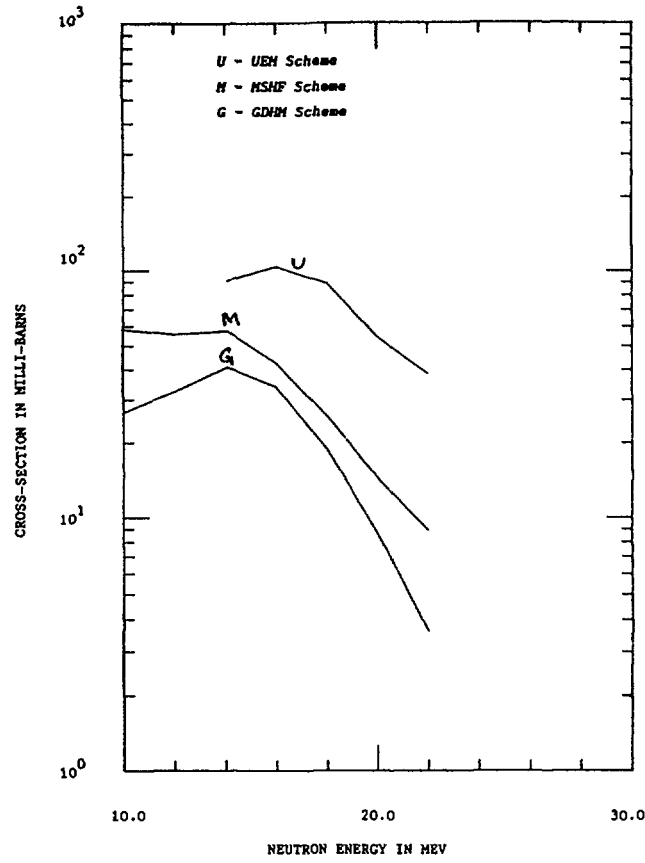
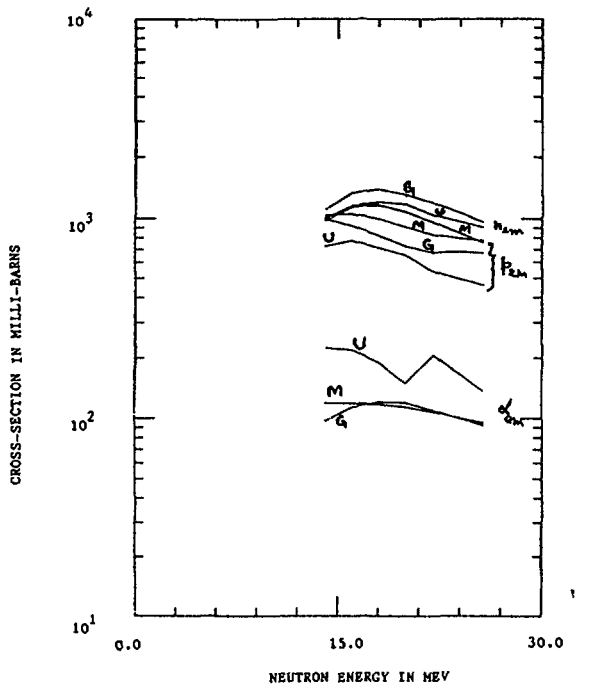
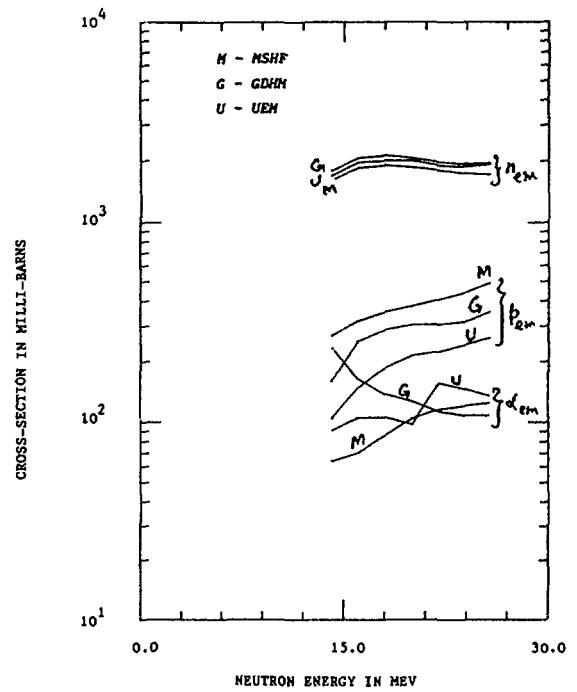


FIG. 33 INTER-COMPARISON OF (N, A) CROSS-SECTION OF NI-60 IN MSHF, GDHM AND UEM SCHEMES



INTERCOMPARISON OF EMISSION X-SECTIONS FOR N, P & ALPHA IN NI-58
Fig. 34



INTERCOMPARISON OF NI-60 CROSS-SECTIONS FOR THE EMISSION OF N, P & ALPHA
Fig. 35

9. CONCLUSIONS

The following conclusions are drawn based on the investigations carried out in this study :

- (i) The multistep Hauser-Feshbach scheme with pre-equilibrium corrections reproduces the measured cross-section data rather well and may be adopted to extrapolate the data to those energy regions where the measurements are lacking.
- (ii) The neutron and proton emission cross-sections predicted by the three schemes are within 15% to 30% of one another. The GDHM scheme being the simplest of the three schemes from computational considerations may provide quick estimates for these reactions and thus may be useful in the planning and design of suitable experiments to measure them.
- (iii) Alpha-emission cross-sections calculated with the three schemes show wide deviations. The MSHF data, however, represent the measured data quite well. This study points out that there is a scope to reexamine and improve the mechanism of alpha-emission in the GDHM and UEM schemes.
- (iv) The proton potentials currently being employed in the proton emission reactions lead to similar results. Perhaps a new look is desired for the proton potentials in the mass region 50-60 based on recent proton induced measurements.
- (v) The GDHM scheme gives a good representation of the angle-energy correlated double differential cross-sections. For reactor oriented applications this scheme may be employed to generate such data.
- (vi) The direct discrete inelastic contributions should be estimated and utilized to obtain the total inelastic cross-section.

10. REFERENCES

1. A. Prince; Nuclear Data for Science and Technology 574 (1983)
2. G.S. Mani; Nuclear Physics. A 165, 225 (1977)
3. B. Strohmaier et al; Paper presented at the IAEA Advisory Group Meeting On Nuclear Data for Radiation Aspects, Vienna (1981)
4. F.G. Perey; ORNL - 3429 (1963)
5. F.D. Becchetti and G.W. Greenlees; Phys. Rev. 182, 1190 (1969)
6. D.M. Brink; Thesis, Oxford University (1955)
P. Axel; Physics Rev. 126, 671 (1972)

7. G. Reffo; Paper Presented at the IAEA Advisory Group Meeting On Structural Materials, Vienna (1983)
8. G.R. Satchler; Nucl. Phys. 55, 1 (1964)
9. W. Hauser and H. Feshbach; Phys. Rev. 87, 366 (1952)
10. D.M. Hetrick et al; ORNL-TM-10219 (1987)
11. O. Bersillon; CEA-N-2227 (1981)
12. P.D. Kunz; Description of the DWBA Code DWUCK4, SMR/108-2 (1984)
13. P.G. Young and E.D. Arthur; LA-6947 (1977), LA-UR-88-382 (1988)
14. M. Blann and H.K. Vonach; Phys. Rev. C 28, 1475 (1983)
15. M. Blann; UCID-20169 (1984) and IAEA-NDS-93 (1988)
16. J.M. Akkermans; ECN-121 (1982)
17. H. Gruppelaar and J.M. Akkermans; ECN-164 (1985)
18. A. Gilbert and A.G.W. Cameron; Can.J.Phys. 43, 1446 (1965)
19. J.L. Cook et al; Aust. J. Phys. 20, 477 (1967)
20. W. Dilg et al; Nucl. Phys. A 217, 269 (1973)
21. F.C. Williams; Nucl. Phys. A 166, 231 (1971)
22. C. Kalbach; Z. Phys. A 287, 319 (1978)

The Use of Dispersion Relations to Construct Unified Nucleon Optical Potentials

P.E. Hodgson

Nuclear Physics Laboratory, Oxford, U.K.

Abstract: The dispersion relations provide a simple and accurate way of parametrising the optical potential for a particular nucleus over a range of energies. A method is proposed for obtaining a global nucleon optical potential incorporating the dispersion relations.

1. Introduction

The optical model is now established as a convenient and accurate way of parametrising a wide range of nucleon scattering of data. Global potentials have been obtained that give good fits to differential elastic scattering cross sections and polarisations for all but the lightest nuclei over a range of energies and these potentials have parameters that are almost the same for all nuclei and have a known energy dependence.

The quality of fit obtained with such global potentials does however vary through the periodic table, due to the effects of nuclear structure. For optimum fits to the data these effects are rather small for the real part of the potential but may be appreciable for the imaginary part of the potential. In particular, if the scattering nucleus has a strongly collective character the coupling between the elastic and inelastic channels affects the elastic scattering and renders inadequate the predictions of a global potential.

There are several ways of tackling this difficulty. One is to use the coupled channels formalism for such nuclei and thus include explicitly the effects of the coupling to inelastic channels. This restores the global quality of the fits but requires a knowledge of the coupling parameters. A further disadvantage is that coupled calculations are lengthy and so most of the simplicity of the model is lost.

Another response is to develop a new global potential valid for nuclei of similar structures, as has been done for the actinide nuclei by Madland and Young (1978). This retains the computational simplicity of the optical model but is useful only for a particular set of nuclei. It is thus necessary to develop a new parametrisation for each set of nuclei with different level structures. For lighter nuclei it may even be necessary to have a different set of parameters for each to achieve sufficient accuracy.

This paper emphasises the usefulness of a third method that makes use of the dispersion relations that connect the real and imaginary parts of the optical potential. As described in recent reviews (Hodgson, 1988, 1989) these dispersion relations automatically take into account the coupling between the elastic and inelastic channels. If we know the imaginary potential then the dispersion relations enable the correction to the real part due to the coupling to be evaluated. It is still necessary, of course, to insert

into the calculation some information concerning the structure of the target nucleus, but hopefully this can be done by a single normalising constant instead of by the many numbers necessary to specify the collectivity in coupled-channels calculations.

It is usual in precise parametrisations of the optical potential to fix the form factor parameters and to allow the real and imaginary potential depths to vary in a way that optimises the fit to the data. However recent work has shown (Finlay *et al*, 1985, Su Zong Di and Hodgson, 1988) that the radius parameter must also be allowed to vary with energy if an optimum fit is to be obtained. This could of course be included in the parametrisation at the cost of more adjustable parameters. The advantage of the dispersion relation method is that the energy variation of the radius of the potential is included automatically, **without** additional parameters. Since it is physically based, the dispersion potentials are likely to retain their validity when the accuracy of the data increases, whereas this is not necessarily the case for an ad hoc parametrisation, however elaborate. Furthermore, it seems possible that the interaction can be described by a global potential, valid for many nuclei, in which the structure of each individual nucleus is represented by just one adjustable parameter.

If these assumptions are correct, then it should be possible to define a global optical potential that when inserted into an optical model code modified to include the dispersion correction gives the elastic scattering cross-section at all energies for all nuclei. All the parameters of this potential are fixed and known, except a single parameter that normalises the imaginary potential and thus takes account of the nuclear structure effects. This parameter has to be determined for each nucleus by an optical model analysis at any one energy; once found the values of this parameter can be tabulated for future use. It is to be expected that the values will be the same for nuclei with similar collective structure like the actinides, and it may prove possible to develop simple rules connecting this parameter with say the deformation parameter for the lowest collective state. Such rules would make possible the prediction of cross-sections for nuclei for which no scattering measurements are available, provided something is known of their low-lying band structures.

An advantage of the dispersion relation analysis is that it unifies the data over a range of energies so that once the parameters are determined it is possible to calculate cross-sections at any required energy.

In this paper, the dispersion relations are described in Section 2, together with the results of some recent analyses. In Section 3 a global method of analysing nucleon data is proposed, and some conclusions are presented in Section 4.

2. Dispersion Relations Analysis

The essential idea is to use the dispersion relations to connect the real and imaginary parts of the potential, instead of treating them as independent of each other. The most useful form is

$$V(E) = V_{HF}(E) + \frac{P}{\pi} \int_{-\infty}^{\infty} \frac{W(E')}{E' - E} dE' \quad (2.1)$$

where $V_{HF}(E)$ is the Hartree-Fock potential that varies linearly with energy and can be represented by a Saxon-Woods radial form

$$V_{HF}(r) = \frac{V_{HF}}{1 + \exp\left(\frac{r-R}{a}\right)} \quad (2.2)$$

The imaginary potential $W(E)$ has volume and surface-peaked components. The volume component gives a volume contribution and so may be absorbed in the Hartree-Fock field, while the surface-peaked component gives a surface-peaked addition to the Hartree-Fock field, thus automatically giving the required energy-dependent radius.

Many analyses of experimental data have now been made using the dispersion relations, and here we present a selection of recent results.

One of the advantages of dispersion relations analyses is that they unify the optical potential over the whole range of energies. This is shown for ^{209}Bi in Figure 1, which

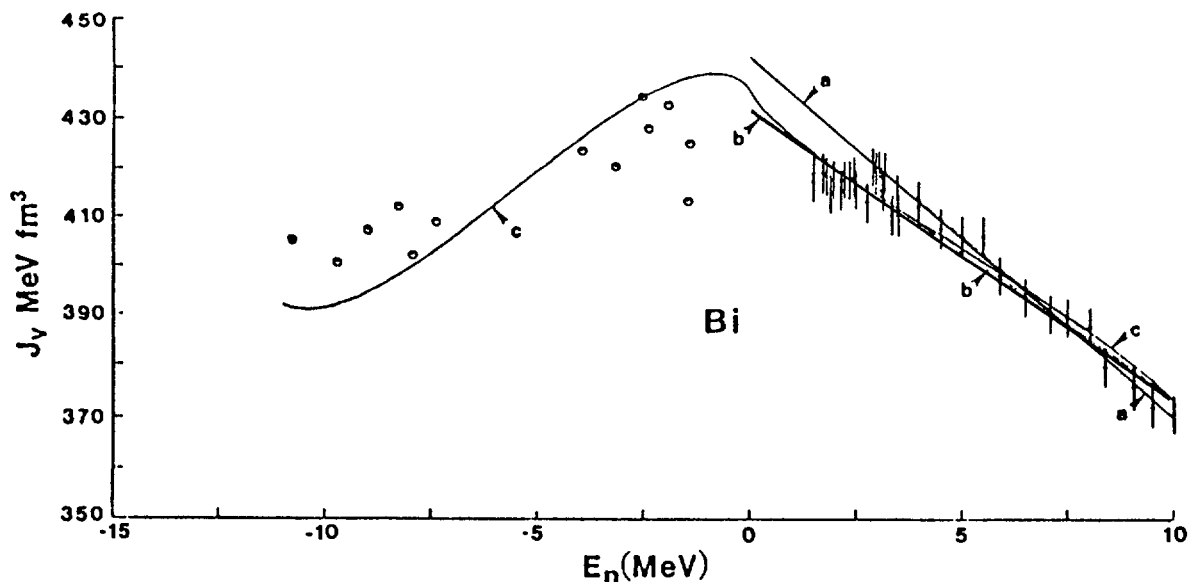


Fig.1 Volume integral per nucleon of the real neutron potential for ^{209}Bi for bound and unbound energies. The points at positive energies are obtained from optical model analyses of elastic scattering data and those at negative energies from the binding energies of particle and hole states. The curves show: a, a linear fit to the scattering data from 4.5 to 10 MeV; b, a linear fit to all scattering data; c, calculated from the dispersion relation (Lawson, Guenther and Smith, 1987).

compares the data for bound and scattering states with the extrapolation made using the dispersion relations. The potentials giving the bound states at their measured energies are given much more accurately than by a simple linear extrapolation of potentials obtained from analyses of scattering data. This is also shown by the energy spectra in Figure 2, where the experimental energies are in much better agreement with those found from a potential with the dispersion correction.

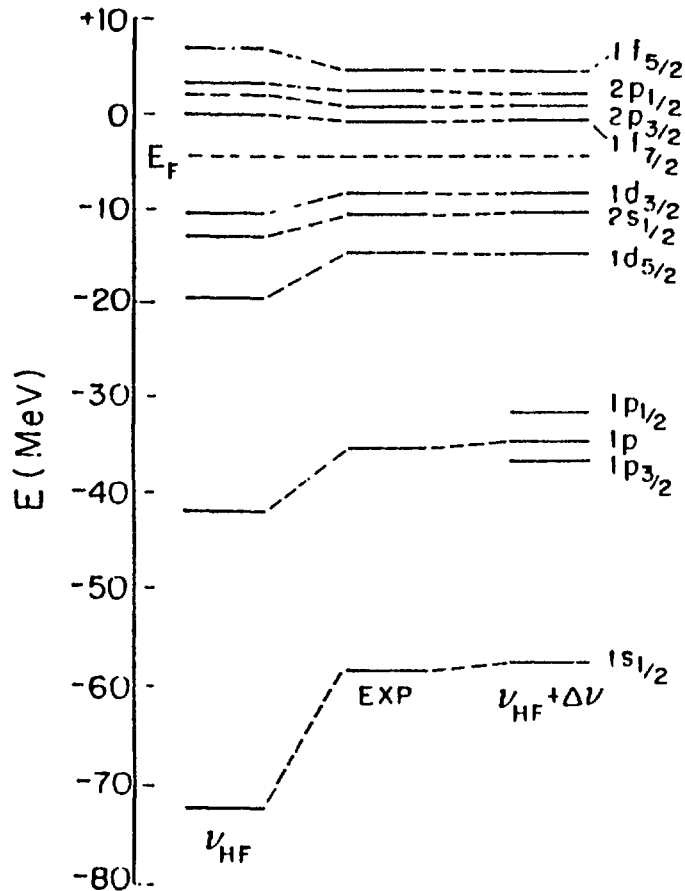


Fig.2 Proton single-particle energies E_{nlj} in ^{40}Ca . The column labelled EXP represents the experimental values. The columns labelled ν_{HF} and $\nu_{HF} + \Delta\nu$ give the energies obtained from the Hartree-Fock potential and from the real part of the full mean field, respectively (Tornow, Chen and Delaroche, 1989).

At positive energies, the dispersion relations have now been used to obtain the analysing powers as well as the differential cross-sections, and a recent example is shown in Figure 3. A very precise analysis of differential cross-sections for the elastic scattering of 4 to 10 MeV neutrons by ^{208}Pb has shown that the differences between the data and the dispersion analyses found by Johnson *et al* (1987) may be attributed to overlapping resonances in that energy range. This shows a limitation on the accuracy of dispersion analyses.

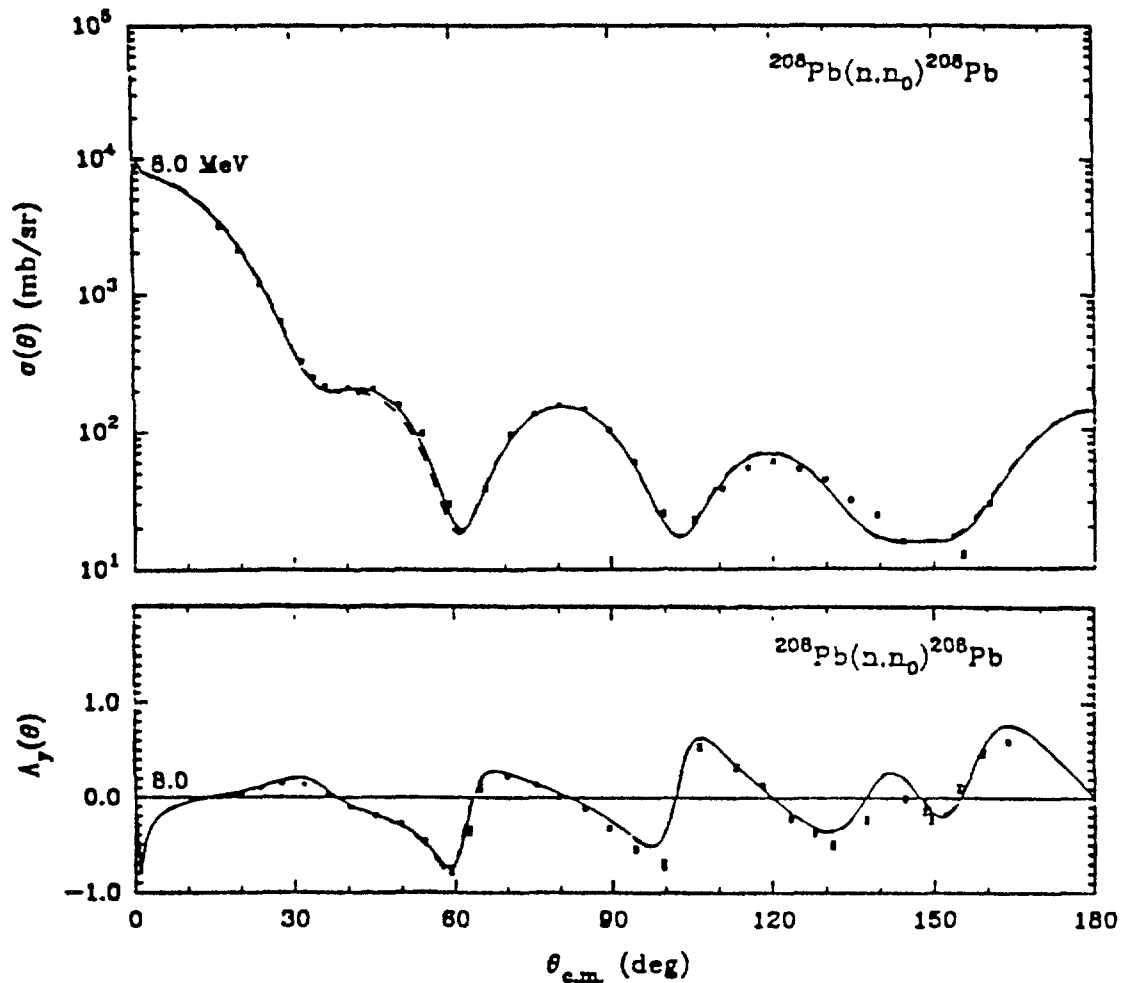


Fig.3 Differential cross-sections and analysing powers for the elastic scattering of 8 MeV neutrons by ^{208}Pb compared with dispersion relation calculations (Roberts *et al*, 1989).

In the case of analyses of neutron data, a particular feature is that the dispersion relations give automatically the increase in radius of the potential at low energies, which produces notable effects on the differential cross-sections (Finlay *et al*, 1985) and on the total cross-sections (Zong Di and Hodgson, 1988). In the past the effects of the increase in radius has been parametrised by using different potentials in different energy regions. The dispersion relations enable the same potential to be used over the whole energy range.

3. Determination of Global Optical Potentials

The success of the dispersion relations analyses of neutron and proton data suggests that it would be useful to use them to obtain global potentials that represent the data to good accuracy over a wide range of nuclei and energies. A method of doing this is described in this section.

The optical model analysis of a set of data for the interaction of nucleons with nuclei over a substantial range of energies can be carried out by a global fitting procedure that differs in several important respects from a standard optical model analysis. The form factor parameters may be fixed to standard average values, and V_{HF} allowed to vary linearly with energy. The main difficulty is that the dispersion relation (2.1) requires the imaginary potential over the whole energy range. The optimum form is suggested by those successfully used in some recent detailed analyses of neutron scattering (Johnson *et al*, 1987; Hicks and McEllistrem, 1988) and specified below. These give simple parametrised expressions for the energy variation of both the real and the imaginary parts of the potential. The same energy variations can be used for other nuclei, with a normalising factor applied to the imaginary part to take account of the structures of the different nuclei. This does however assume that the relative contributions of the volume and surface absorption are the same for all nuclei. The particular feature of these potentials is that the surface imaginary potential falls to zero above a certain energy so that the integral in (2.1) converges.

The two parametrised forms of the imaginary potential already mentioned are:

1. **The straight line segment potentials of Johnson *et al* (1987) for ^{208}Pb**

$$\begin{aligned} &= 0 && \text{for } E < 10 \text{ MeV} \\ W_v(E) &= 0.17(E - 10) && \text{for } 10 < E < 50 \text{ MeV} \\ &= 6.8 && \text{for } E > 50 \text{ MeV} \end{aligned} \quad (3.1)$$

$$\begin{aligned} &= 0.4(E - E_F) && \text{for } -6 < E < 10 \text{ MeV} \\ \text{and } W_s(E) &= -0.103(E - 72) && \text{for } 10 < E < 72 \text{ MeV} \\ &= 0 && \text{for } E > 72 \text{ MeV} \end{aligned} \quad (3.2)$$

(and symmetric expressions for $E < E_f$).

2. **The potentials used by Hicks and McEllistrem (1988) for osmium and platinum**

$$\begin{aligned} &= 0 && \text{for } E < 8 \text{ MeV} \\ W_v(E) &= 2.33(E^{\frac{1}{2}} - 8^{\frac{1}{2}}) && 8 < E < 40 \text{ MeV} \\ &= 2.33(40^{\frac{1}{2}} - 8^{\frac{1}{2}}) \equiv \approx 8.1 \text{ MeV} && \text{for } E > 40 \text{ MeV} \end{aligned} \quad (3.3)$$

$$\text{and } W_s(E) = \frac{a_0 + a_2(E - E_F)^2}{\{E_0^2 + (E - E_F)^2\}^2}$$

(and symmetric expressions for $E < E_F$)

The peak strengths of these potentials are:

	Surface	Volume
Pb	6.4	6.8
Os — Pt	9.2	8.1

It is encouraging that these potentials are very similar in overall shape and absolute and relative magnitudes, with the OsPt potential slightly stronger, as it should be. The difference is quite small, encouraging the hope that all nuclei can be fitted with multiplying factors for W in quite a narrow range. To verify this, it is necessary to fit a wide range of data to find the optimum values of these factors for many nuclei.

4. Conclusions

The dispersion relations potential has several clear advantages over the standard parametrisation. It includes the physically-necessary connection between the real and imaginary parts of the potential and thus automatically includes without additional parameters the energy dependence of the radius that is required by precision analyses. Furthermore, it holds out the hope that it will prove possible to represent the effects of nuclear structure by a single parameter that has a characteristic value for each nucleus.

The extent to which these hopes can be realised can only be evaluated by a series of careful analyses of extensive data sets for several nuclei. The work that has already been done is sufficiently encouraging to suggest that precision optical model analyses should in future be made with the dispersion relations potential.

References

- R.W. Finlay, J.R.M. Annand, J.R. Petler and F.S. Dietrich, *Phys. Lett.* **155B**.313.1985.
S.E. Hicks and M.T. McEllistrem, *Phys. Rev.* **37**.1787.1988.
P.E. Hodgson. Proceedings of the International Atomic Energy Agency Advisory Group Meeting on "Nuclear Theory for Fast Neutron Nuclear Data Evaluation", Beijing, China 12–16 October 1987. IAEA-TECDOC-483.51.1988; Proceedings of the International Conference on Nuclear Reactions, Calcutta, 1989.
C.H. Johnson, D.J. Horen and C. Mahaux, *Phys. Rev.* **C36**.2252.1987.
R.D. Lawson, P.T. Guenther and A.B. Smith, *Phys. Rev.* **C36**.1298.1987.
D.G. Madland and P.G. Young, Proceedings of the International Conference on Neutron Physics and Nuclear Data. OECD Nuclear Energy Agency.349.1978.
M.L. Roberts, Z.M. Chen, P.D. Felsher, D.J. Horen, C.R. Howell, K. Murphy, H.G. Pfützner, W. Tornow and R.L. Walter, TUNL Annual Report XXVIII (1988–1989).80.

Su Zong Di and P.E. Hodgson, J. Phys. G. 14.1485.1988.

W. Tornow, Z.P. Chen and J.P. Delaroche, TUNL Annual Report XXVIII (1988-1989).76.

Global Calculations of (n, p) and (n, α) Cross-sections from 10 to 20 MeV

D. Wilmore

Dairy Flat, Buckland, Faringdon, Oxon SN7 8QR, UK

P.E. Hodgson

Nuclear Physics Laboratory,
University of Oxford,
Keble Road, Oxford OX1 3RH, UK

Abstract

The Weisskopf-Ewing and exciton model theories are combined to give a simple and fast method of calculating the total cross-sections of (n, p) and (n, α) reactions for many nuclei from 10 to 20 MeV.

1. Introduction

It has long been known that the total (n, p) and (n, α) cross-sections at 14 MeV for many nuclei vary rather smoothly with N and Z , and several simple empirical formulae have been proposed to parameterise them. These have recently been compared with an extensive set of experimental data by Forrest (1986).

These formulae are useful for estimating rapidly the cross-sections of many reactions required in the design of fusion reactors, so it is worthwhile considering how they may be improved. Furthermore the latest designs of these reactors also require the cross-sections for a range of lower energies, and these cannot be obtained from the empirical formulae. This energy variation can be obtained from reaction theories, and modern computers enable rapid calculations to be made.

The aim of this work is to develop and test a simple physically-based method of calculating total (n, p) and (n, α) cross-sections. This is done by combining the Weisskopf-Ewing and exciton model theories. The method is described in §2, and compared with the experimental data for (n, p) reactions in §3 and for (n, α) reactions in §4. Some conclusions are given in §5.

2. Method of Calculation

At 14.5 MeV, both compound nucleus and direct reactions contribute to the cross-sections, so theories are required for both these processes. The requirement of simplicity and computational convenience rules out the Hauser-Feshbach

theory (1952), which requires listing the energies and quantum numbers of many states of each nucleus, and also the distorted wave theories that require the calculation of wavefunctions and matrix elements.

For the compound nucleus cross-sections we therefore use the Weisskopf-Ewing theory (1940) which requires only level density parameters, which are extensively tabulated, and transmission coefficients, which can be easily calculated using global optical model parameters. Also required are the Q -values for the reactions, which can be obtained from a table of nuclear masses; it is not sufficiently accurate to use the semi-empirical mass formula. All these parameters for all nuclei are stored in the computer.

For the direct reactions, which are increasingly important for the reactions on heavy nuclei, we investigate the usefulness of (a) a simple empirical formula and (b) the exciton model. We test the results of our calculations by comparing the fit to the data with that obtained by Forrest. Here we encounter a difficulty due to the uncertainties in the measured cross-sections. It is already clear from Forrest's work that many if not most of the discrepancies between his calculations and the experimental data are due to errors in the data. This sets a limit to the sharpness of the test of any proposed method of calculating the cross-sections. Indeed it seems likely that a method which gave perfectly accurate cross-sections would, when compared with the presently available data, give results not much better than the Forrest formulae.

This makes it difficult to develop a method which is clearly better than that of Forrest. However we consider that the attempt is worthwhile for several reasons:

- (a) as the experimental data improves, the advantages of a physically based method of calculation should become increasingly apparent,
- (b) the new method will make it easy to calculate cross-sections over a range of energies if required, whereas the formulae of Forrest refer only to 14.5 MeV,
- (c) the availability of the cross sections as a function of energy makes it possible to identify those cross-sections that are varying rapidly with energy and so are not fitted simply because, for example, they have been measured at 14 MeV, whereas the formulae are fitted to data around 14.5 MeV.

3. The (n, p) Reaction.

Calculations were made for the (n, p) reaction for those nuclei for which experimental data are available, using the Weisskopf-Ewing theory. The absorption cross-sections were obtained by using the optical model with the equivalent non-local potential of Wilmore and Hodgson (1964) for the neutrons and the Perey potential (1963) for the protons. It was found that the results for the heavier nuclei were too low by orders of magnitude, but for light nuclei they were of the right order of magnitude. This is due to the neglect of direct reactions, and since it might be expected that the direct reaction cross-section will

be a smooth function of mass, an attempt was made to fit the experimental cross-sections by adding an estimate of the direct contribution obtained from a simple formula to the compound nucleus results from the Weisskopf-Ewing calculations. It was found by using a least squares fit procedure that a formula of the form

$$(-46.80 + 0.9492A + 0.00178A^2) \exp(2.143S - 116.49S^2) \quad (3.1)$$

where A is the mass number and $S = (N - Z)/A$, gives a fit to the data. For light nuclei the predictions of the Weisskopf-Ewing theory are large enough to explain the data without the addition of a direct component. If these nuclei are neglected, the results of the above procedure, give fits to the data which is about as good as the Forrest formulae.

A simple physically-based model for the direct reactions is the exciton model, and this has been used by Braga-Marcazzan *et al* (1972) to calculate the (n, p) cross-sections for medium and heavy nuclei. They did not include compound nucleus effects and their results are therefore not applicable to light nuclei. We made calculations using the standard value for the single particle energy spacing $g = A/13$, but subsequent work showed that variations in this parameter did not offer much improvement. The exciton formalism described by Jahn (1984) was used with a value of $K = 700 \text{ MeV}^3$, and the exciton master equations were solved numerically until equilibrium was reached. The calculation was then terminated assuming that any further particle emission could be explained by the compound nucleus process. The results of the Weisskopf-Ewing theory were reduced by renormalisation to take account of the loss of flux in the pre-equilibrium process. The results obtained by this procedure are of the correct order of magnitude throughout the periodic table.

To obtain a numerical measure of the overall goodness-of-fit, the value of T/E , where T is the theoretical result and E is the experimental datum, was calculated for each experimental point, and the results are presented in Figures 1-3 for the Forrest formula, the Weisskopf-Ewing theory plus the simple formula, and the Weisskopf-Ewing theory plus the exciton model, respectively. It can be seen that the Forrest formula and the Weisskopf-Ewing theory plus the simple formula, show the best fit to the data, with the Weisskopf-Ewing theory plus the exciton model being somewhat worse. However the fit given by the Weisskopf-Ewing theory plus the exciton model is not too bad when the errors in the data are considered. Both the other two formulae are fitted to the actual data which are presently available, and as better data become available they will have to be altered to maintain the fit. The exciton model is physically based and can be expected to be useful with new data as well as having the advantage that it can be used to extrapolate to other energies where no data are available.

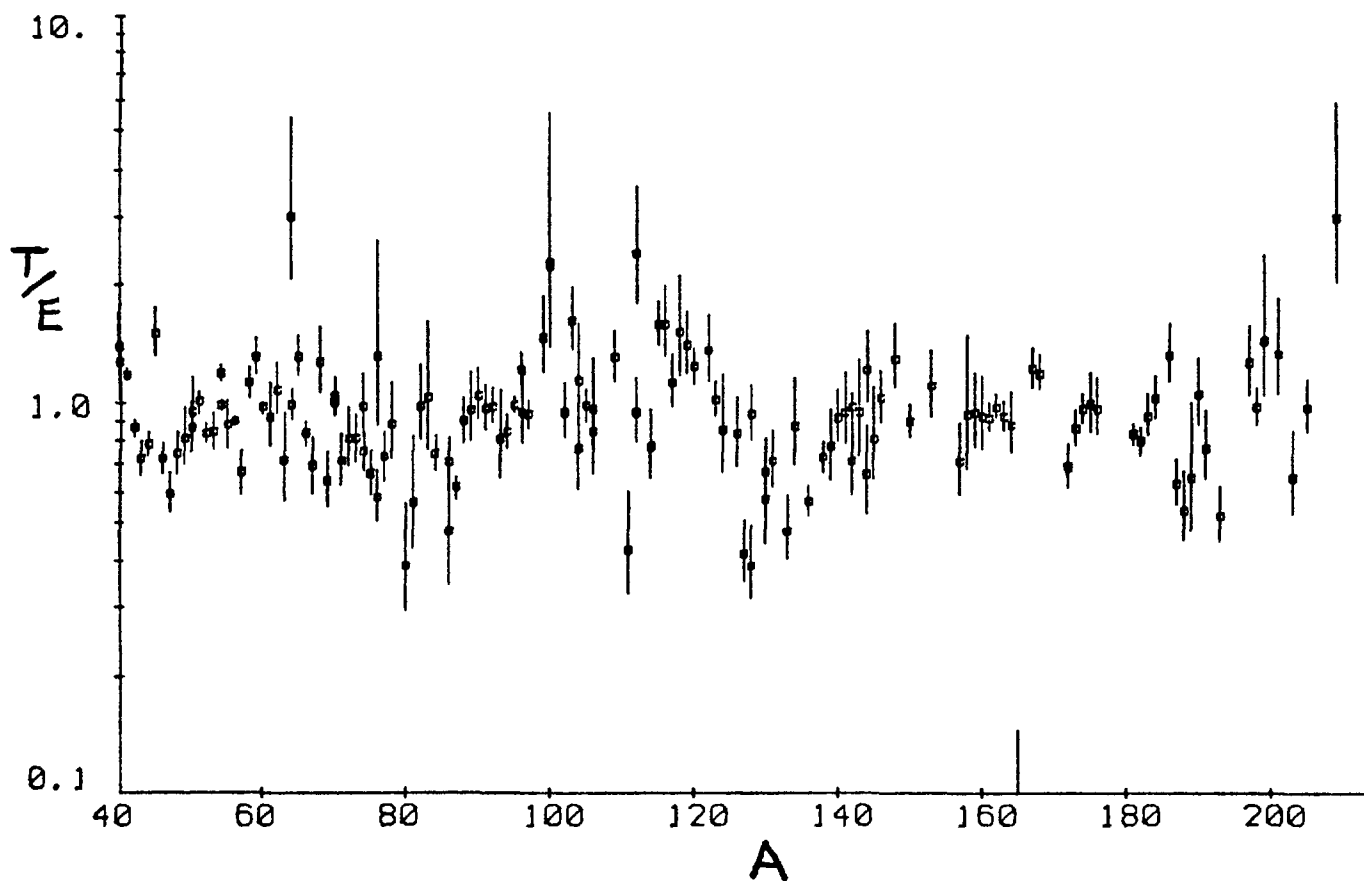


Figure 1. Distribution of T/E for (n,p) reactions at 14.5 MeV for the Forrest formula.

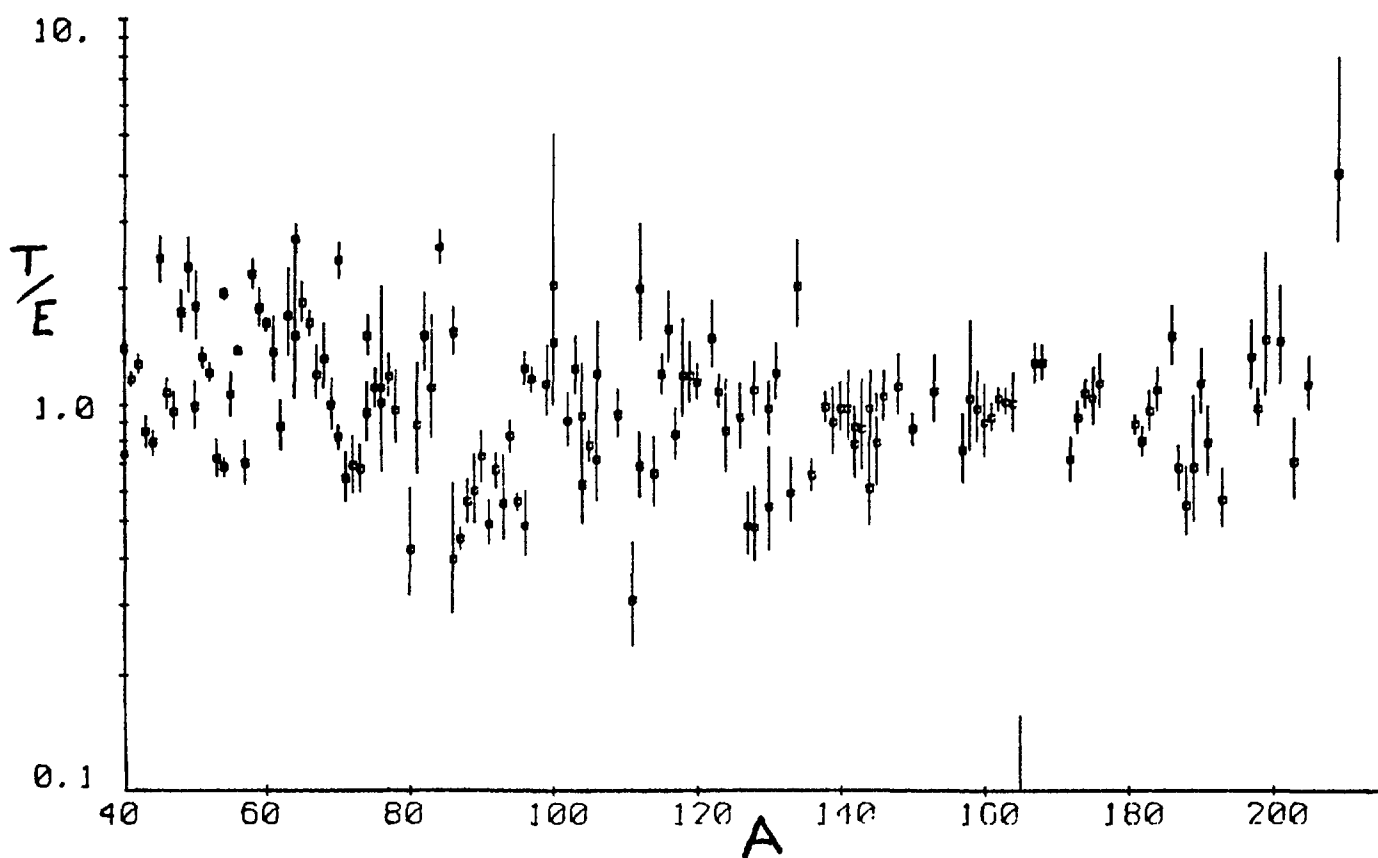


Figure 2. Distribution of T/E for (n,p) reactions at 14.5 MeV for the Weisskopf-Ewing + empirical formula.

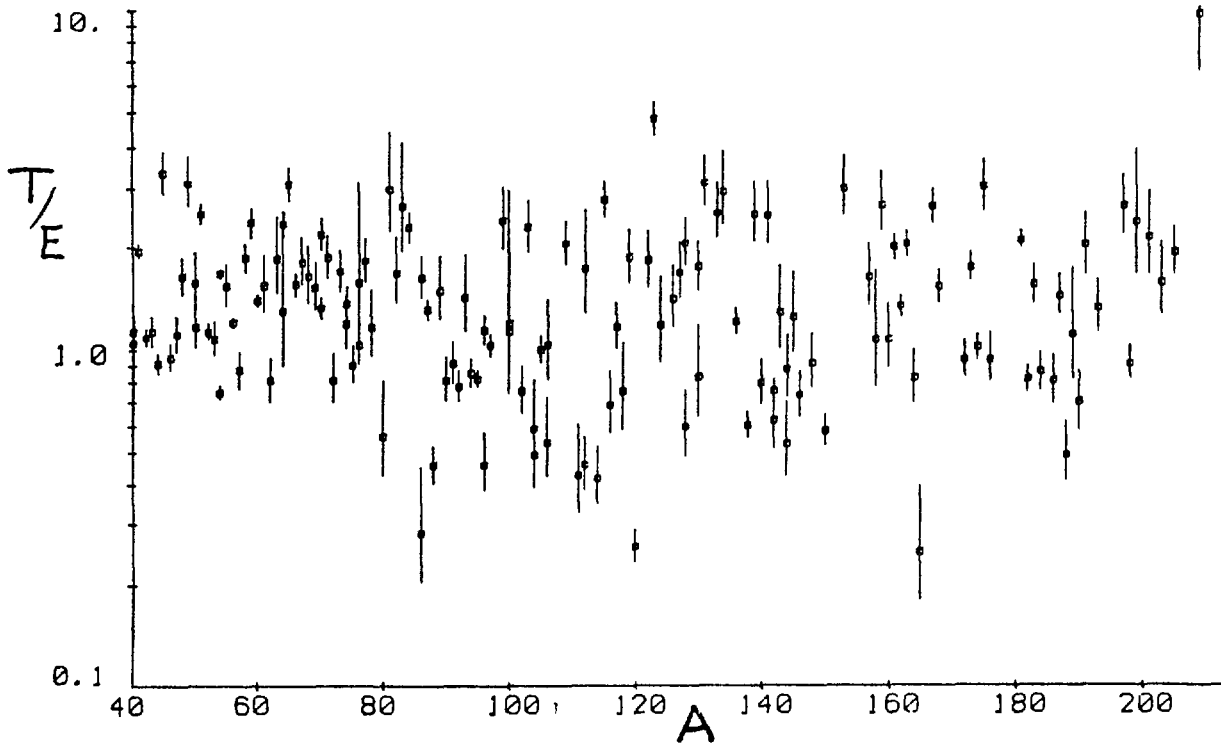


Figure 3. Distribution of T/E for (n,p) reactions at 14.5 MeV for the Weisskopf-Ewing + exciton model.

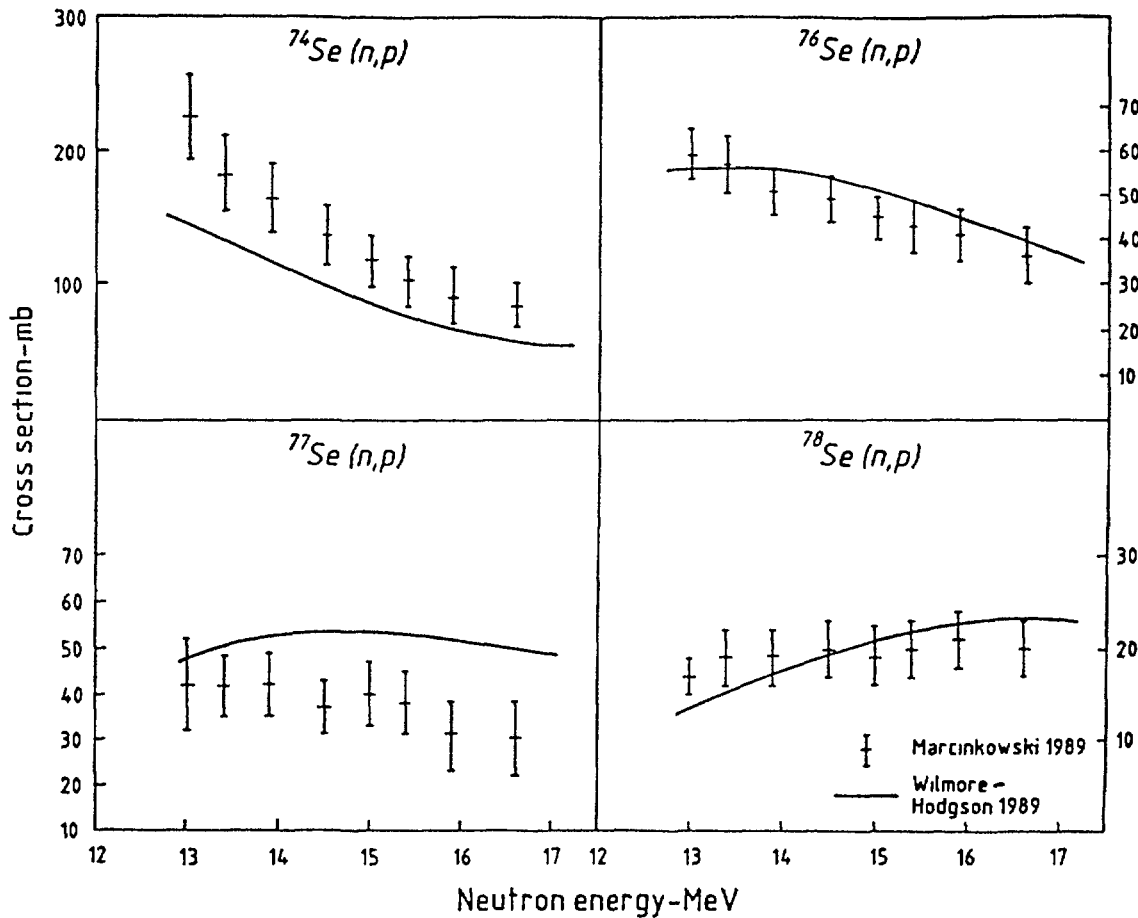


Figure 4. Experimental (n,p) cross-sections for the selenium isotopes compared with Weisskopf Ewing + exciton model calculations.

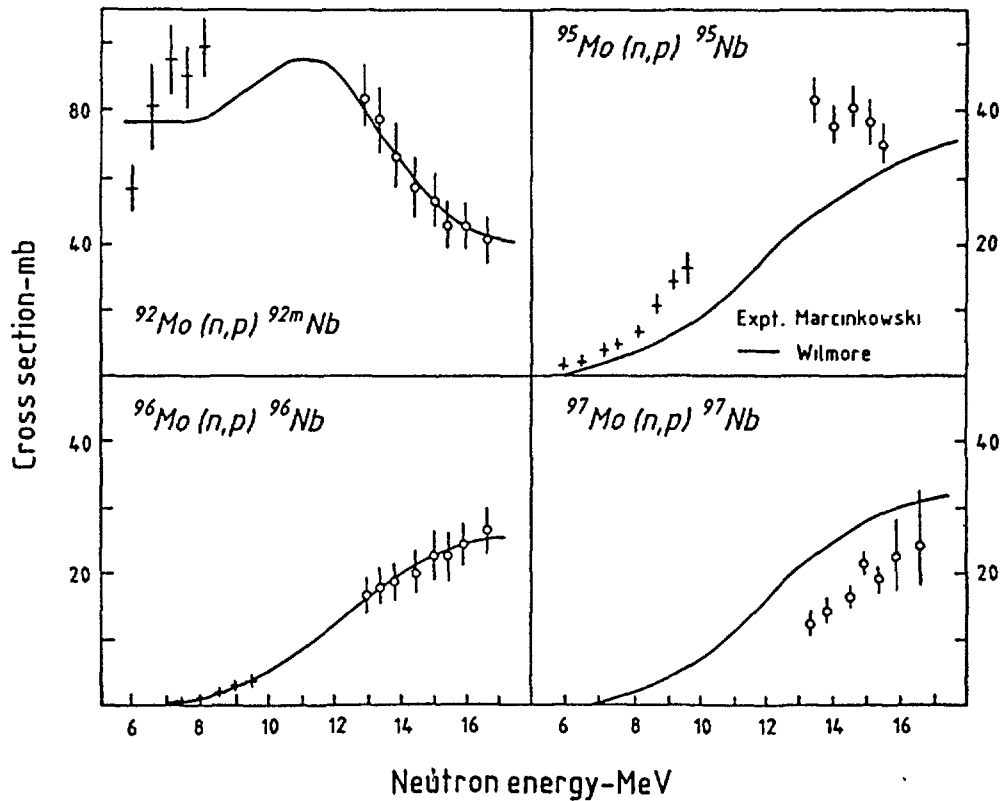


Figure 5. Experimental (n, p) cross-sections for the molybdenum isotopes compared with Weisskopf-Ewing + exciton model calculations.

To see how well this model fits the energy variation of the cross-section, calculations were made for the (n, p) reaction on isotopes of selenium and molybdenum, and the results are shown in Figures 4 and 5. It is apparent that in each case the energy variation is well reproduced by the theory, although as already noted the absolute value may be incorrect by up to a factor of two.

This work shows that it is practicable to make rapid calculations of (n, p) cross-sections using the Weisskopf-Ewing and exciton theories, and that the results are in good overall agreement with the experimental cross-sections and their energy variation.

4. The (n, α) Reaction.

The calculations for the (n, α) reaction were made in a similar way to those for the (n, p) reaction, but encounter two additional difficulties. Firstly there is no reliable global optical potential for alpha-particles, and such a potential would be less accurate than those for nucleons because of the sensitivity of the alpha scattering to the nuclear surface. We adopted the alpha potential with $U = 173.3$, $r_u = 1.49$, $a_u = 0.6$, $W_V = 13.8$, $r_W = 1.49$, $a_W = 0.4$ (Saxon-Woods forms).

The second difficulty is that the exciton model calculations for alpha-particles require the alpha-particles preformation factor. This is not well-known, although several estimates indicate values around 0.1 to 0.2. There is some ev-

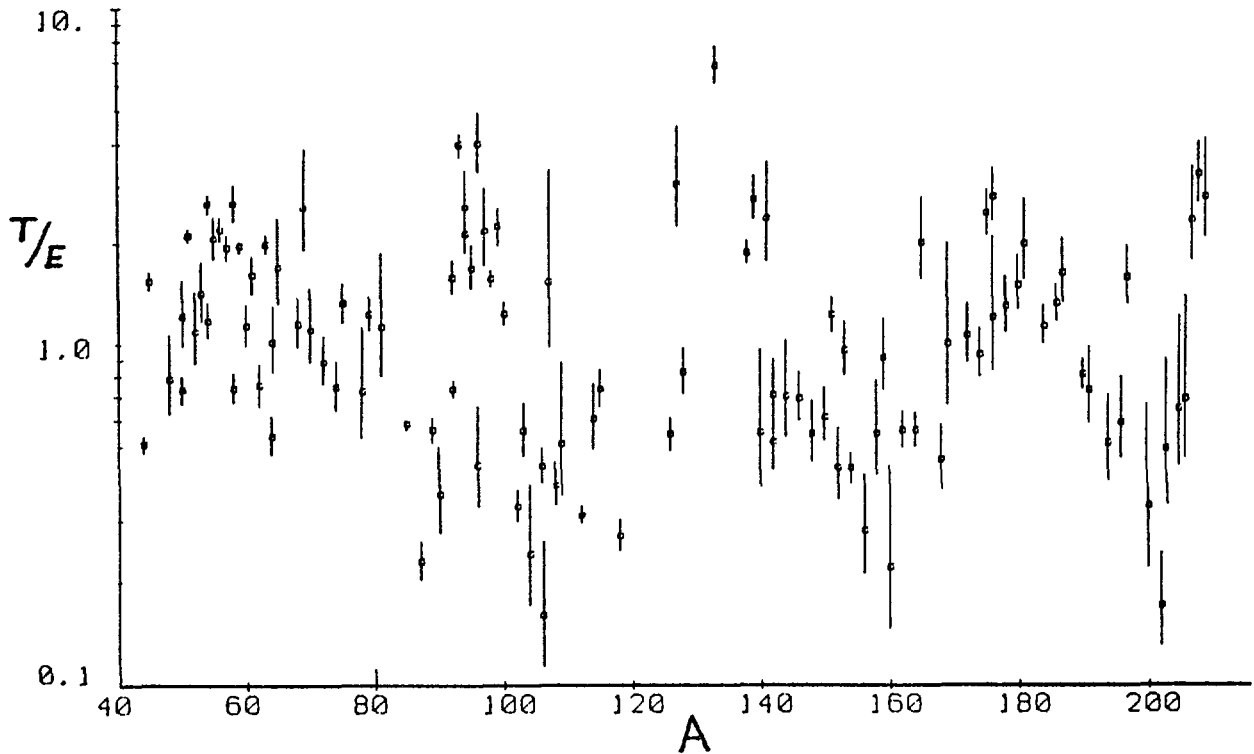


Figure 6. Distribution of T/E for (n, α) reactions at 14.5 MeV using Weisskopf-Ewing + exciton model.

idence for a shell effect in the alpha preformation factors, which is another complication. However since Forrest obtained a good overall fit to (n, α) cross-sections without explicit inclusion of shell effects it seems likely that they are not important.

The exciton model calculations require the alpha particle level density, and this was obtained using the formula of Williams (1971). This gives the level density for n excitons (p particles and n holes) in terms of the single nucleon level density g and energy U :

$$\omega_N = \frac{g^n U^{n-1}}{p! h! (n-1)!} \quad (4.1)$$

This formula does not distinguish between the different types of particles involved, whether they are neutrons, protons or alpha-particles. We assume that the single particle level density for a neutron or proton is given by $g/2$ and for an alpha-particle by $g/4$. Since neutrons and protons are distinguishable the $p!$ in the above formula is replaced by $p_n! p_p! p_\alpha!$ where p_n , p_p and p_α are the numbers of neutrons, protons and alpha-particles. The factor $h!$ similarly becomes $h_n! h_p! h_\alpha!$. Thus for example the expression for one neutron and one alpha-particle with an alpha-particle hole becomes

$$\omega_\alpha = \left(\frac{g}{4}\right)^2 \left(\frac{g}{2}\right) \frac{U^2}{1!1!1!2!} \quad (4.2)$$

This is usually written in terms of Williams' formula by the expression

$$\omega = k_{ph}\omega_N \quad (4.3)$$

Tables of the k_{ph} are listed by Gadioli *et al* (1977).

Several calculations of (n, α) cross-sections at 14.5 MeV were made using (1) the level density of Gilbert and Cameron and $g = A/13$, (2) the same with the Gilbert and Cameron values of g , and (3) the level densities and g of Holmes *et al* (1976). The results are rather similar, and one of them is shown in Figure 6. The spread is appreciably greater than that given by the empirical formula of Forrest. There is some evidence of systematic behaviour but for the reasons already mentioned this is unlikely to be a real effect. In all the calculations the alpha-particle pre-formation factor was fixed at 0.19 (Ferrero *et al*, 1979), independent of A . Three calculations were made of the energy variation of the (n, α) cross-section, and the results are compared with the experimental data in Figures 7–9.

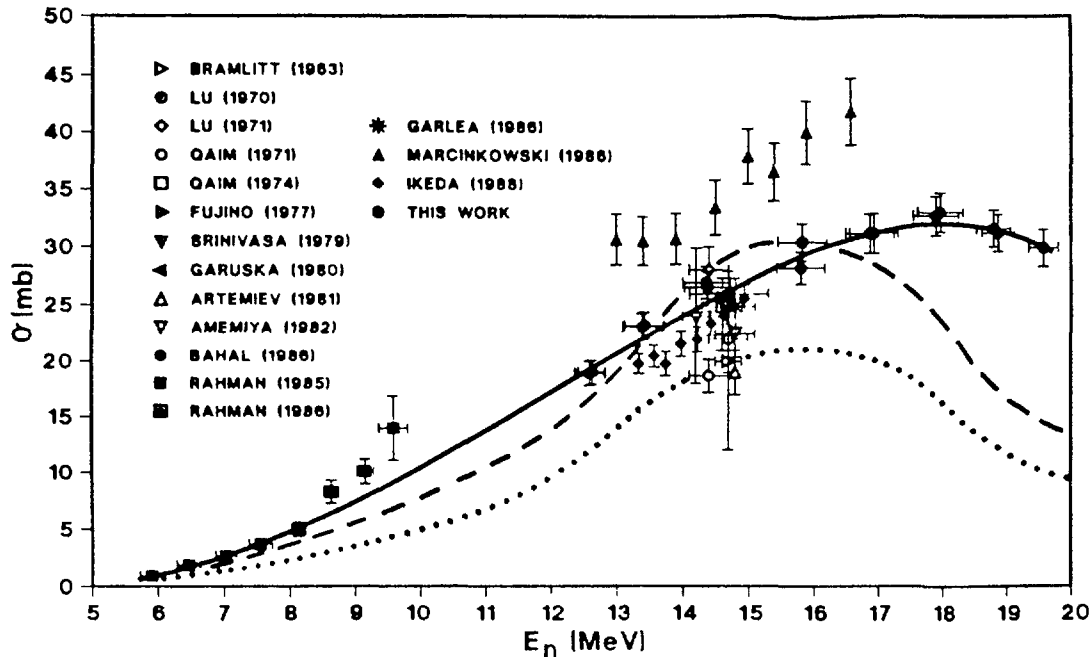


Figure 7. Experimental cross-sections for the $^{92}\text{Mo}(n, \alpha)^{89}\text{Zr}$ reaction (Liskien *et al* 1990) compared with an eye-guide (full curve), the Weisskopf-Ewing + Exciton Model calculations (dotted curve) and the same normalised to the formula of Forrest at 14.5 MeV (dashed curve).

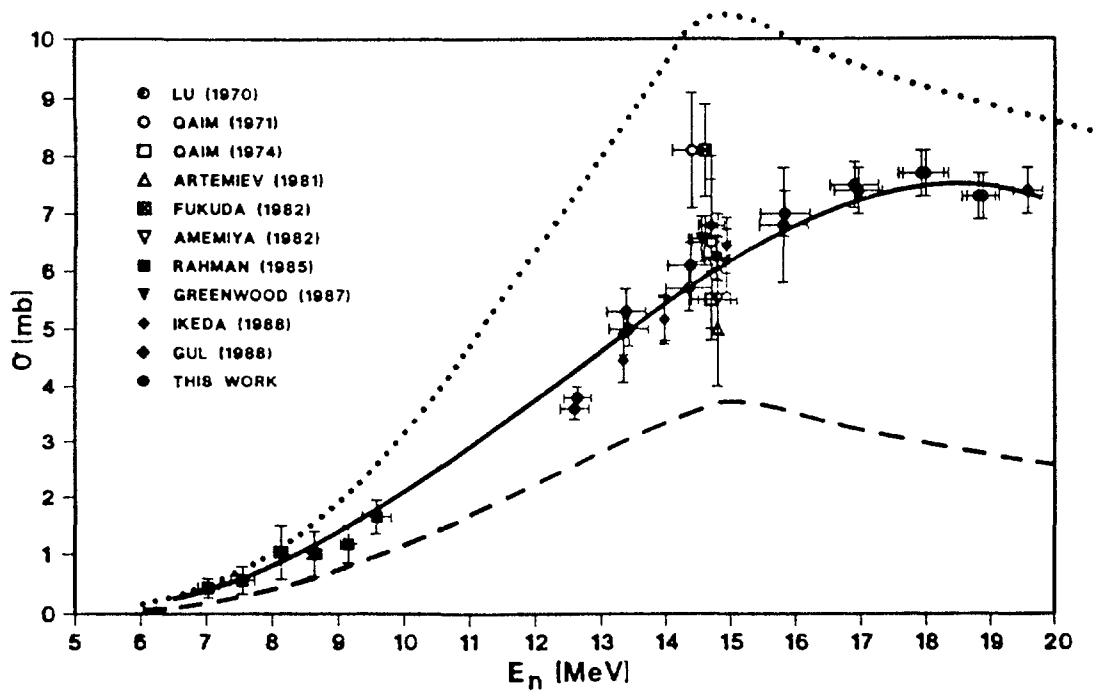


Figure 8. Experimental cross-sections for the $^{98}\text{Mo}(n, \alpha)^{95}\text{Zr}$ reaction (Liskien *et al* 1990) compared with an eye-guide (full curve), the Weisskopf-Ewing + Exciton Model calculations (dotted curve) and the same normalised to the formula of Forrest at 14.5 MeV (dashed curve).

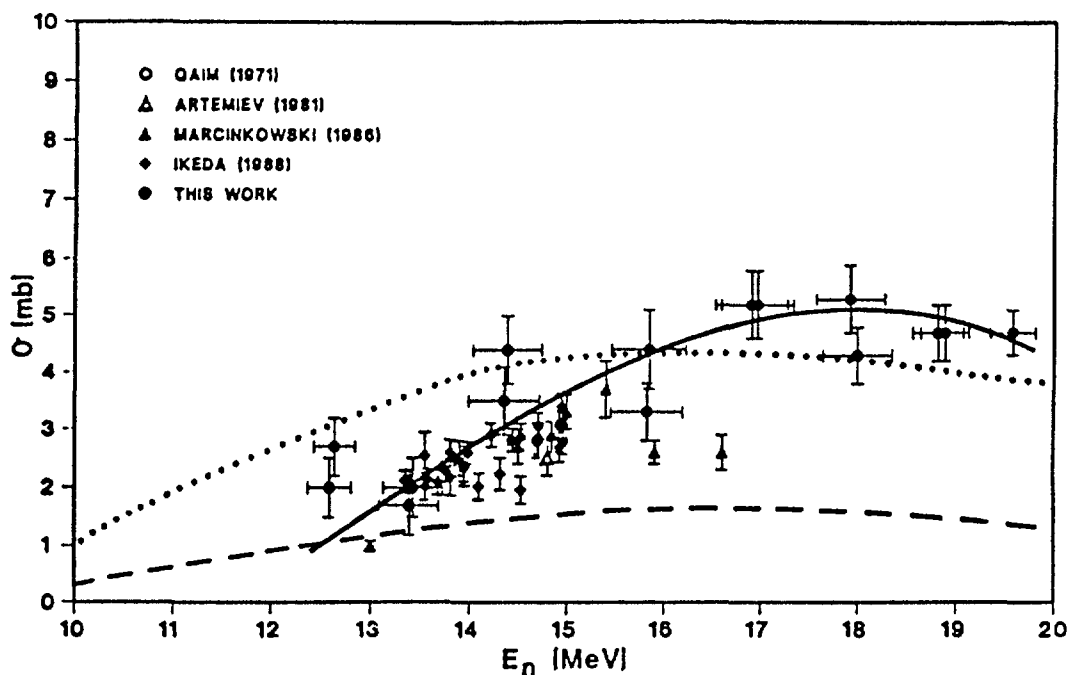


Figure 9. Experimental cross-sections for the $^{100}\text{Mo}(n, \alpha)^{97}\text{Zr}$ reaction (Liskien *et al* 1990) compared with an eye-guide (full curve), the Weisskopf-Ewing + Exciton Model calculations (dotted curve) and the same normalised to the formula of Forrest at 14.5 MeV (dashed curve).

5. Conclusions

The calculations described in the previous sections shown that it is not yet possible to obtain better cross-sections from the physically-based theories than from the Forrest empirical formulae. They do however give the energy variations of the cross-sections, which is not given by Forrest. For practical purposes at present it would seem that the best estimates can be obtained by using the method described here to calculate the energy variation of the cross-sections, and to normalise them to the Forrest values at 14.5 MeV. The results of such calculations are also included in the Figures.

References

- Braga-Marcazzan G M, Gadioli-Erba E, Milazzo-Colli L and Sona P G, 1972 *Phys. Rev.* **C6** 1398
- Ferrero A, Gadioli E, Gadioli-Erba E, Iori I, Molho N and Zetta L, 1979 *Z. Phys.* **A293** 123
- Forrest R A, 1986 *AERE R* 12419
- Gadioli E, Gadioli Erba E and Hogan J J, 1977 *Phys. Rev.* **C16** 1404
- Gilbert A and Cameron A G W, 1965 *Can. J. Phys.* **43** 1446
- Hauser W and Feshbach H, 1952 *Phys. Rev.* **87** 366
- Hoang H M, Garnska U, Marcinkowski A and Zwięgliński B, 1989 *Z. Phys.* **A334** 285
- Holmes J A, Woosley S E, Fowler W A and Zimmerman B A, 1976 *Atomic Data and Nuclear Data Tables* **18** 306
- Jahn H, 1984 *IAEA-SMR-93* 39
- Liskien H, Wölffe R, Widera R and Qaim S M, 1990 *Appl. Radiat. Isot* **41** 83
- Marcinkowski A, 1989 *IAEA-SMR-284* 23 (See also Hoang *et al*, 1989)
- Perey F G, 1963 *Phys. Rev.* **131** 745
- Weisskopf V F and Ewing D H, 1940 *Phys. Rev.* **57** 472 and 935
- Williams F, 1971 *Nucl. Phys.* **A116** 231
- Wilmore D and Hodgson P E, 1964 *Nucl. Phys.* **55** 673

Analyses of Multistep Reaction Cross-Sections with the Feshbach-Kerman-Koonin Theory

P.E. Hodgson

Nuclear Physics Laboratory, Oxford, UK

Abstract: Recent calculations of the cross-sections of multistep compound and multistep direct cross-sections using the Feshbach-Kerman-Koonin theory are reviewed, and their usefulness assessed.

1. Introduction

The Feshbach-Kerman-Koonin (FKK) theory of multistep reactions is now established as a generally useful method of calculating cross-sections for nucleons from 10 to about 100 MeV. More analyses have been made at low energies, especially around 14 MeV, where multistep compound reactions dominate, than at higher energies where the multistep direct reactions account for most of the cross-section.

To evaluate the usefulness of the FKK theory it is necessary to apply it to analyse the cross-sections of many reactions on different nuclei over a range of energies. Many such analyses have been completed recently, and the results are reviewed here.

Analyses at lower energies using the multistep compound theory are discussed in Section 2 and those at higher energies using the multistep direct theory in Section 3. Some conclusions are given in Section 4.

This review is restricted to papers published in 1989 and after.

2. Multistep Compound Reactions

The number of analyses using the multistep compound theory is now sufficient to establish the validity of the theory, and so recent work has concentrated on investigating the importance of possible refinements, extending the analysis over a wider range of reactions, energies and nuclei, and determining the interaction strength to higher accuracy.

In the first of these categories, Chadwick *et al* (1988) showed that taking explicit account of the nucleon spin does not significantly affect the results. It is therefore sufficiently accurate to ignore the nucleon spin. The effect of distinguishing neutrons and protons in the intra-nucleus cascade was studied by Chadwick *et al* (1989) who found that it increases the (n, n') cross-section and decreases the (n, p) cross-section. While the absolute cross-section can be adjusted by an overall normalisation, the ratio of these two cross-sections cannot,

and so this refinement should be included in analyses that include both (n, n') and (n, p) data.

Several (n, n') , (n, p) and (p, n) reactions for a range of nuclei at incident energies from 9 to 18 MeV have been studied by Chadwick *et al* (1989). The (n, p) and (p, n) reactions provide better tests of the theory because there is no contribution from the scattering with excitation of collective states that complicates the analysis of (n, n') reactions. As shown in Figure 1 the (p, n) cross-sections are very well given by the theory. It would be useful to select one of these reactions and study it over a range of energies to find the energy variation of the strength V_0 of the effective interaction potential.

A stringent test of the theory is obtained by analysing at the same time the cross-sections in all the open channels in a consistent way. Many of the parameters used, such as the optical potentials, are applicable to several channels, and the requirements of a consistent overall analysis sets closer limits on other parameters such as the strength of the effective interaction. For similar reasons it is advantageous to analyse neutron and proton data together.

This method of analysis has been applied to the interactions of 14 MeV neutrons with ^{59}Co and ^{93}Nb by Koumdjieva and Hodgson (1989), and the results of their FKK calculations agree well with the experimental data as shown in Tables 1 and 2. In these calculations the Williams formula for the exciton level density was restricted to bound states, so that the particles above the Fermi energy must have energies less than their binding energy in the nucleus and the holes must have energies greater than the depth of the potential. The effective interaction strength V_0 was adjusted to fit the (n, nx) and (n, px) reactions, and also the (p, nx) reaction on both nuclei and the values obtained were closely consistent, ranging from 7.0 to 8.8 MeV. This shows that the FKK theory is able to give a fully consistent account of the more important reaction channels in the interaction of 14 MeV neutrons with ^{59}Co and ^{93}Nb . This supports the conclusions of several previous papers (Field *et al*, 1986; Chadwick *et al*, 1988, 1989) that the FKK theory is able to give reliable (n, nx) and (n, px) cross-sections for neutrons for around 14 MeV on medium weight nuclei. Further work is necessary on the (n, α) reactions, which probably take place mainly by a direct process.

The FKK theory has recently been extended to gamma emission by Obložinský and Chadwick (1990). They calculated the multistep compound gamma emission cross-sections for ^{59}Co , ^{93}Nb and ^{181}Ta using detailed balance and existing parametrisations of photoabsorption cross-sections (Dietrich and Berman 1988). The gamma ray escape widths are shown in Figure 2 as functions of gamma ray energy, together with the r -stage widths calculated assuming that all stages with $N \geq 4$ contribute only to the r -stage. The Figure clearly shows that gamma rays from the early reaction stages are harder than those from the fully equilibrated compound nucleus, so that including multistep compound emission enhances the high energy region of the gamma ray spectrum.

Table 1. Total cross sections of 14 MeV neutron reactions on ^{59}Co .

Reaction	Theory (mb)	Experiment (mb)
(n, nx)	1253	—
(n, px)	82	—
(n, n')	469	402 ± 140^b
(n, 2n)	687	695 ± 23^k
(n, pn)	30	} $\approx (11-60)^c$
(n, np)	97	
(n, p)	52	54 ± 5^k
(n, α)	—	33 ± 1^k
neutron emission	1971	1840 ± 128^a ; 2069 ± 69^b ; 2300 ± 184^j
proton emission	179	108 ± 22^e ; 97 ± 10^d
alpha emission	—	40 ± 3^f ; 33 ± 2^g
total reaction	1368	1370 ± 30^h ; 1430 ± 110^i

^a Hermsdorf *et al* (1974). ^b Grabmayr (1978). ^c Alvar (1972). ^d Colli *et al* (1961).
^e Guenther *et al* (1988). ^f Kneff (1986). ^g Fischer *et al* (1985). ^h MacGregor *et al* (1957).
ⁱ St Pierre *et al* (1959). ^j Degtyarev *et al* (1981). ^k Average from McLane *et al* (1988).

Table 2. Total cross sections of 14 MeV neutron reactions on ^{93}Nb .

Reaction	Theory (mb)	Experiment (mb)
(n, nx)	1692	—
(n, px)	37	—
(n, n')	401	—
(n, 2n)	1285	1350 ± 33^g
(n, pn)	16	—
(n, np)	3	—
(n, p)	21	—
(n, α)	—	9.4^g
(n, $n\alpha$)	3	—
neutron emission	2993	3155 ± 220^a
proton emission	40	39 ± 2^b ; 42.4 ± 2^c ; 42.3 ± 4^d
alpha emission	—	14 ± 3^e ; 14^f
total reaction	1738	—

^a Degtyarev *et al* (1981). ^b Traxler *et al* (1985). ^c Fischer *et al* (1988).
^d Koori *et al* (1984). ^e Kneff (1986) ^f Grimes *et al* (1978). ^g Average from McLane *et al* (1988).

(Koumdjieva and Hodgson, 1989).

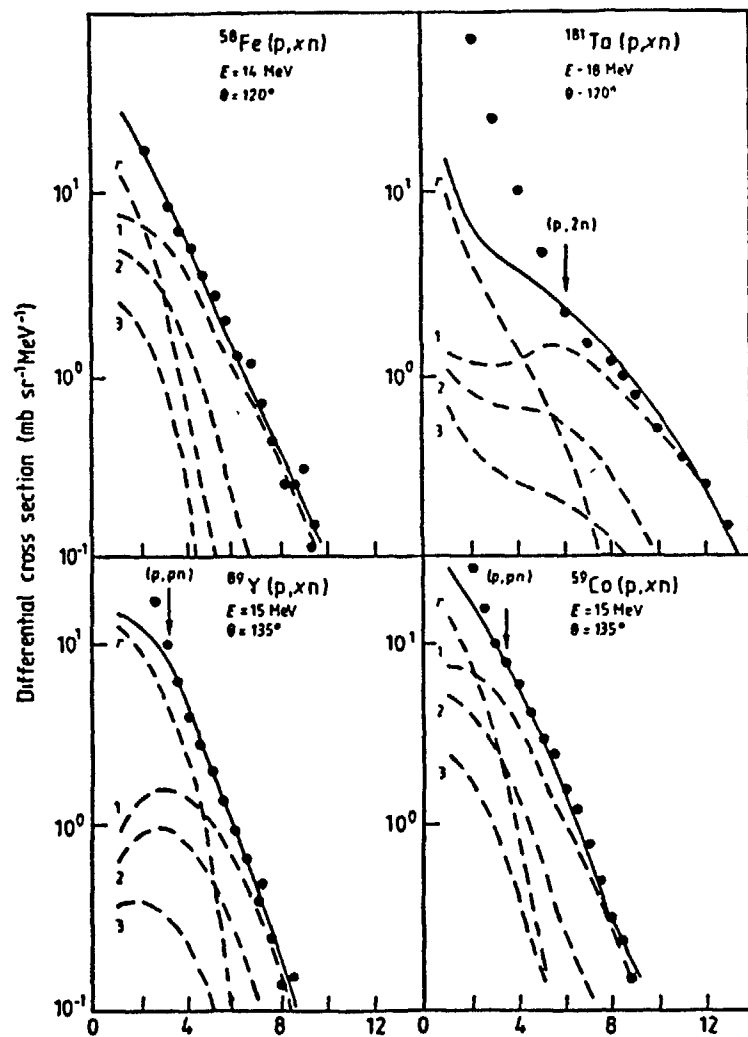


Figure 1. Comparison of the multistep compound theory (—) with data (Grimes *et al* 1971a,b, 1974) for some (p, xn) reactions. The broken curves represent the pre-equilibrium and r th stage contributions to the cross-section (Chadwick *et al*, 1989).

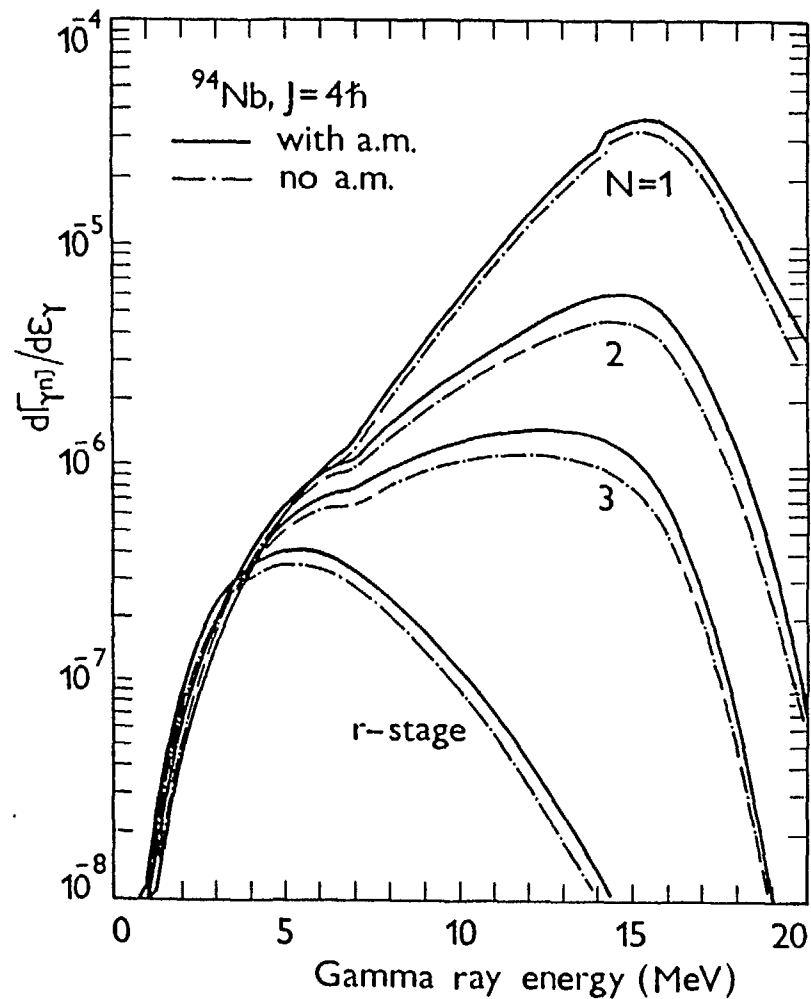


Figure 2. Gamma ray escape widths for the compound nucleus ^{94}Nb at 21.1 MeV with initial spin $J = 4$ as a function of gamma ray energy for stages $N = 1, 2$ and 3 and the r -stage. The full curves are for the calculation with full angular momentum coupling and the dash-dot curves to those that neglect this coupling by assuming constant α -functions (Obložinský and Chadwick).

To calculate the gamma emission cross-sections, Obložinský and Chadwick used the multistep compound formalism as described by Chadwick *et al* (1989) and by Koumdjieva and Hodgson (1989). The effective interaction strength V_0 was determined by equating the r -stage emission widths with those calculated from the equilibrium statistical model; this effectively normalises the multistep compound calculations to the well understood equilibrium spectra at lower emission energies in the equilibrium limit. The results for the (n, γ) cross-sections on ^{93}Nb and ^{181}Ta are compared with the experimental data in Figures 3 and 4. The values of V_0 were 7.9 and 5.3 respectively. The cross-sections for emission from the fully equilibrated compound nucleus are also shown, and these clearly fail to account for the emission at the higher energies. The multistep compound calculations show enhanced emission at the higher energies but still fall short of the experimental data because the cross-sections for multistep direct gamma ray emission have not yet been evaluated.

3. Multistep Direct Reactions

A detailed analysis of the (p, nx) reactions at 26.7 MeV by Holler *et al* (1985) showed that at this energy the reaction for higher emission energies takes place mainly by the multistep direct process. The double-differential cross-sections were very well fitted by FKK multistep direct calculations supplemented by small contributions from the multistep compound process.

Subsequently, multistep direct calculations have been made for (p, n) reactions at energies from 25 to 160 MeV by Mordhorst *et al* (1986), Trabant *et al* (1988, 1989) and Scobel *et al* (1990).

Trabant *et al* analysed the (p, n) reaction on ^{90}Zr and ^{208}Pb at 80 MeV with a Yukawa interaction of range 1 fm and strength $V_0 = 20$ MeV. They obtained good agreement with the angular distributions of the emitted neutrons at various outgoing energies, as shown in Figure 5. Calculations based on the hybrid model of Blann *et al* (1984) were able to fit the angle-integrated neutron spectra to within a factor of two overall, but not the angular distributions at various outgoing energies, particularly in the backward direction. The value of the effective interaction strength at this energy is less than the value $V_0 = 27$ MeV found by Holler *et al* at 26.7 MeV, indicating that it decreases with increasing incident energy.

Subsequently this analysis was extended to (p, n) reactions at 120 and 160 MeV, and the effective interaction strength was again found to decrease with increasing energy (Scobel *et al* 1990). It is notable that for the lower emission energies the reaction is not dominated by the first step, even at the forward angles. This is essential in order to fit the experimental data: the semi-classical pre-compound models overestimate the first step cross-section and so give angular distributions that are too strongly peaked in the forward direction.

Analyses of inelastic scattering have been made by Marcinkowski *et al* (1989) for neutrons and by Cowley *et al* (1991) for protons.

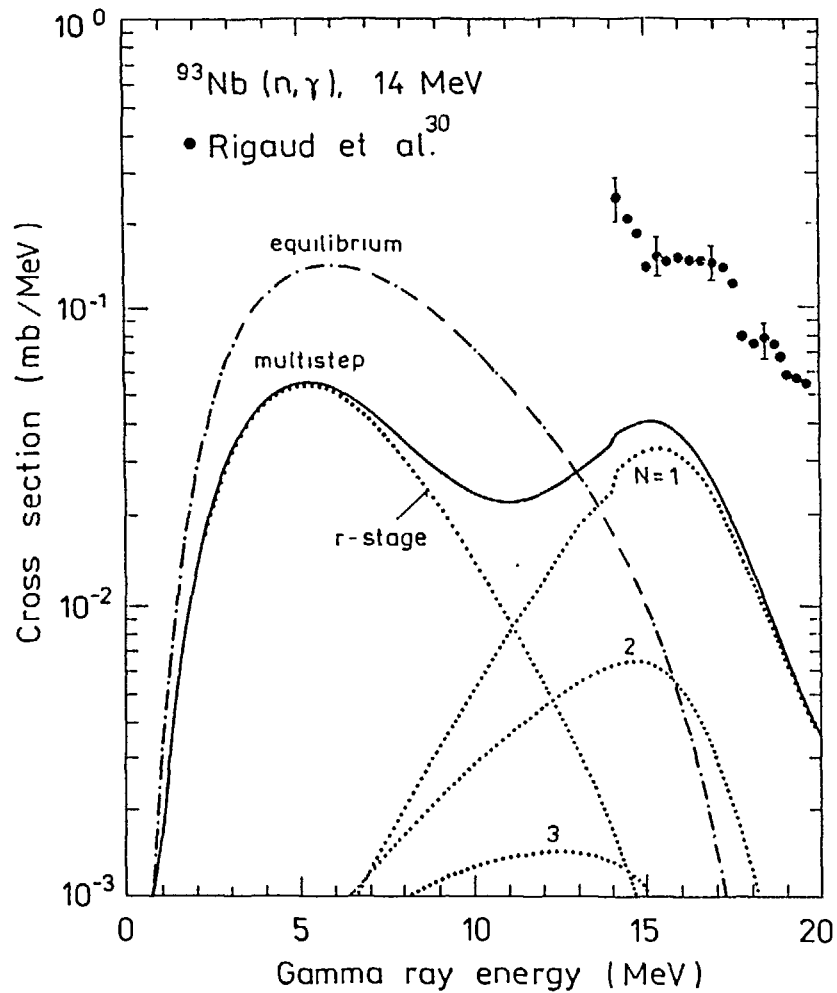


Figure 3. Calculated primary gamma ray emission spectra for 14 MeV neutrons on ^{93}Nb . The full curve shows the multistep compound spectrum and the dotted lines the contributions from the stages with $N = 1, 2$ and 3 , and from the r -stage. The dash-dotted curve is the spectrum calculated from the equilibrium statistical model (Obložinský and Chadwick 1990).

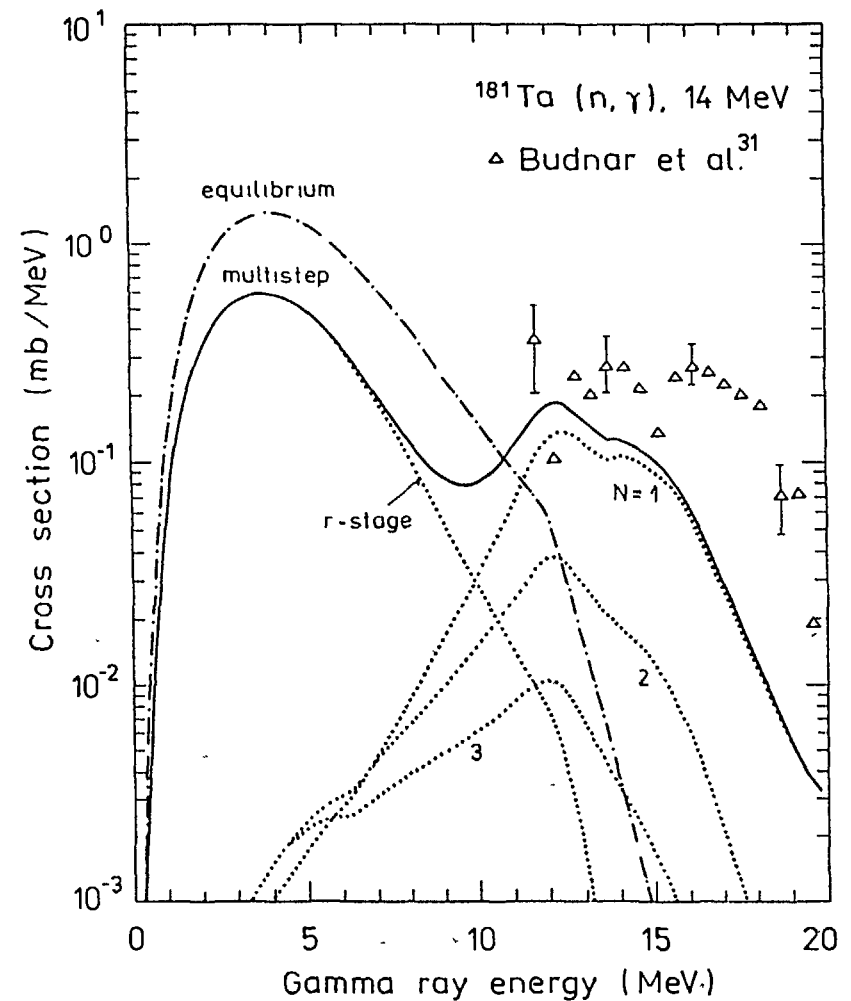


Figure 4. Calculated primary gamma ray emission spectra for 14 MeV neutrons on ^{181}Ta . The full curve shows the multistep compound spectrum and the dotted lines the contributions from the stages with $N = 1, 2$ and 3 , and from the r -stage. The dash-dotted curve shows the spectrum calculated from the equilibrium statistical model (Obložinský and Chadwick 1990).

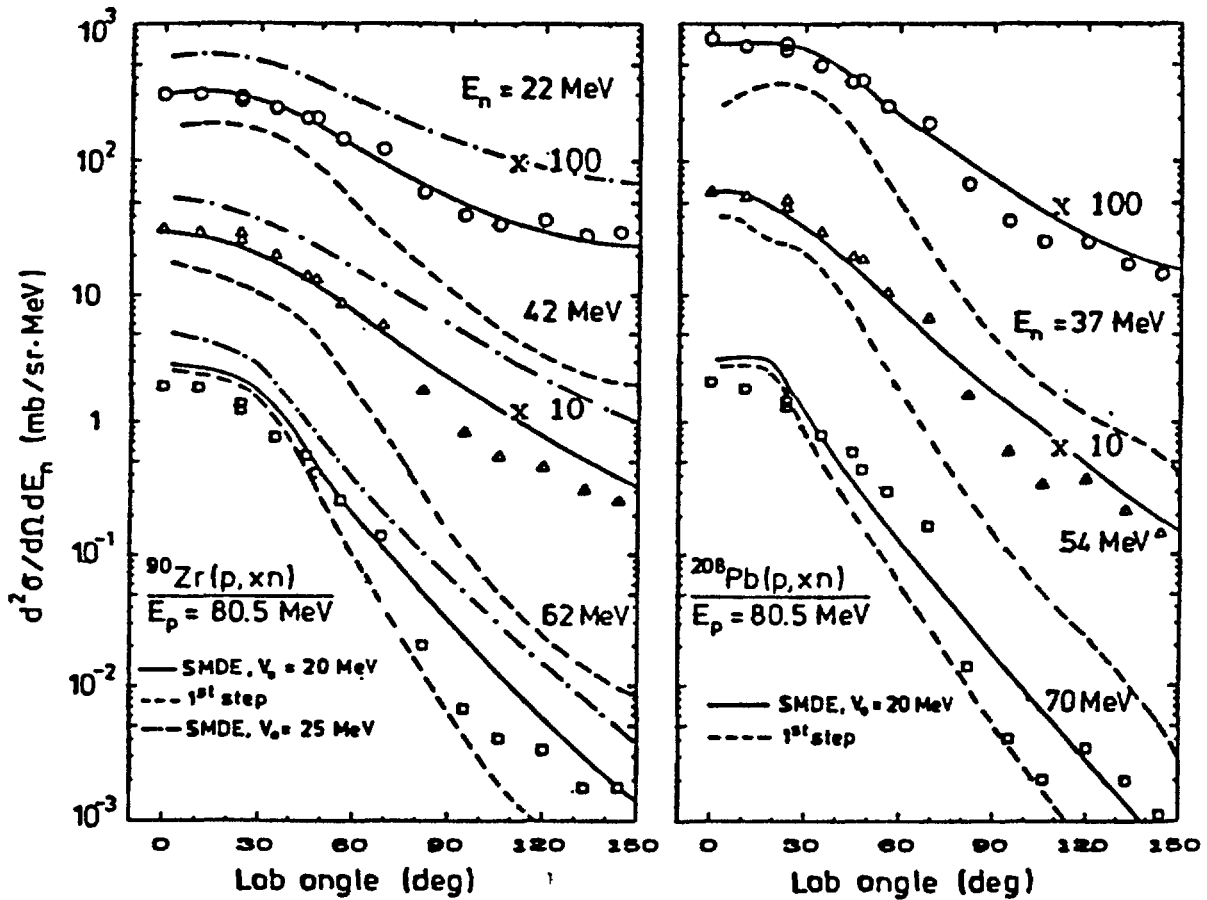


Figure 5. Double differential cross-section for the (p, xn) reaction at 80.5 MeV on ^{90}Zr and ^{208}Pb compared with multistep direct reaction calculations with interaction strengths $V = 20$ and 25 MeV (Trabant *et al*, 1989).

Marcinkowski *et al* (1989) studied the inelastic scattering of 11.5 and 26 MeV neutrons by ^{184}W and found that both the multistep compound and the multistep direct processes contribute substantially to the cross-sections. In the multistep direct calculations, the individual angular distributions for the excitation of sets of particle-hole pairs did not show the striking similarity apparent some earlier work. The average distorted wave differential cross-section thus depends rather strongly on the outgoing neutron energy and also quite significantly on the number of contributing particle-hole pairs. To average out these fluctuations it was found necessary to include up to twelve particle-hole states for each L -value. This implies averaging the calculated cross-sections for the individual particle-hole states over a series of overlapping energy intervals with widths up to 9 MeV. This averaging interval is comparable with the widths of single-particle states measured by $(p, 2p)$ reactions (Jacob and Maris, 1973). The value of the effective interaction strength used in these calculations was $V_0 = 25$ MeV.

The results of these calculations are compared with the experimental data in Figure 6 for several outgoing neutron energies. The angular distributions of the neutrons with lower outgoing energies are well reproduced by the sum of the one-step and two-step multistep direct and the multistep compound calcu-

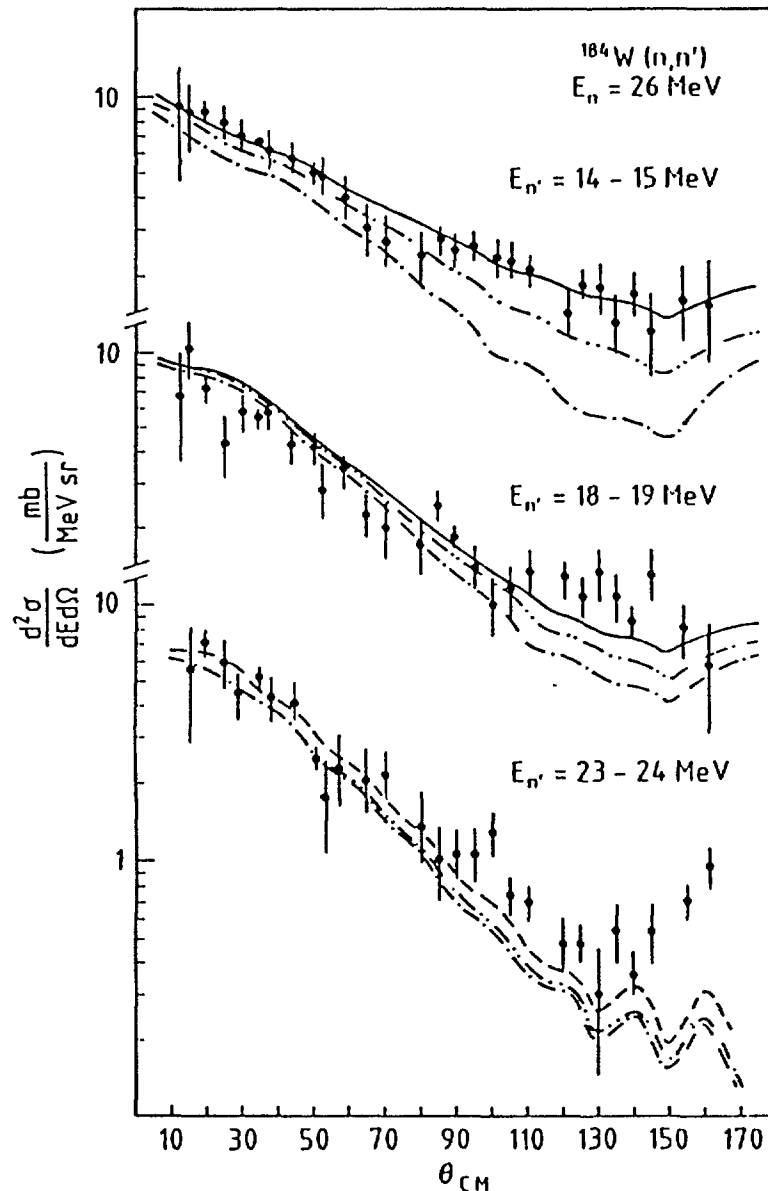


Figure 6. Double differential cross-section for the inelastic scattering of 26 MeV neutrons by ^{184}W compared with one-step direct (dash-dotted curves), plus two-step direct (dash-double dotted curves) plus collective contributions (dashed curve) plus multistep compound (solid curves) (Marcinkowski *et al*, 1989).

lations. At the highest outgoing energies the experimental cross-sections are greater than the calculated ones, and this is attributable to direct processes, in particular to the excitation of low-lying quadrupole and octupole surface vibrations (Marcinkowski *et al*, 1983; Kalka *et al*, 1988). The contribution of such processes was estimated using the energy-weighted sum rule for isoscalar electric transitions, and is also shown in the Figure. Comparison with the experimental data shows that there is still some cross-section unaccounted for at these higher outgoing energies.

Extensive analyses of the (p, p') cross-section have been made by Cowley *et al* (1991) and some of their results are compared with FKK calculations in Figures 7 and 8.

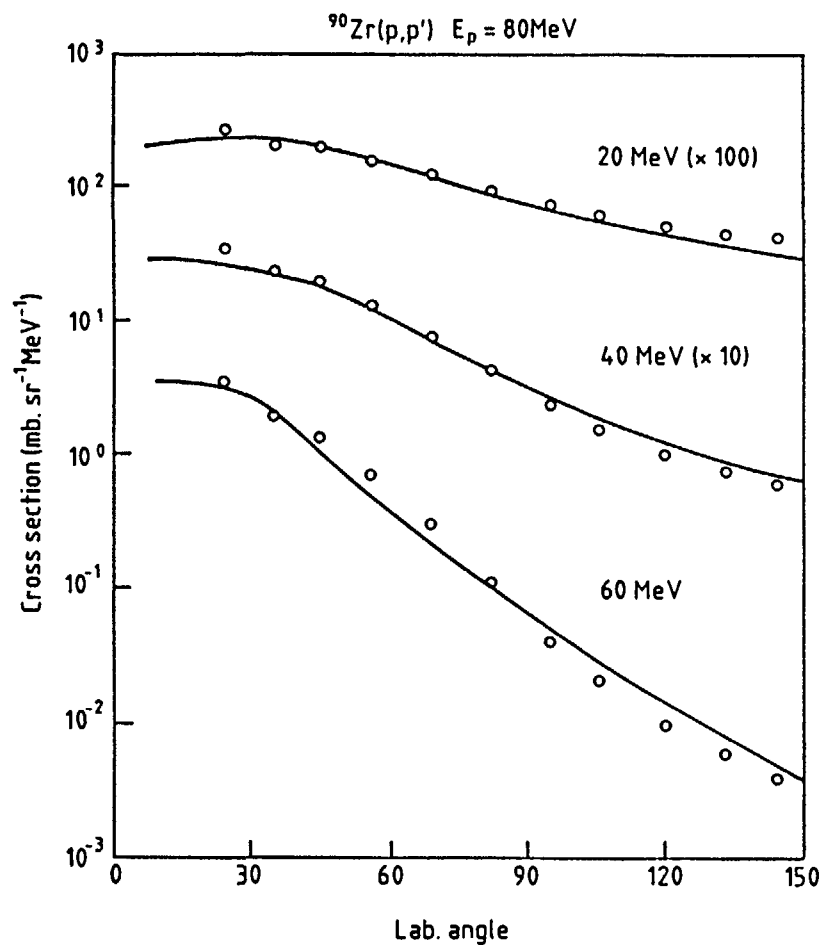


Figure 7. Double differential cross-section for the inelastic scattering of 80 MeV protons by Zr compared with multistep direct calculations with the Feshbach-Kerman-Koonin theory (Cowley *et al*, 1991).

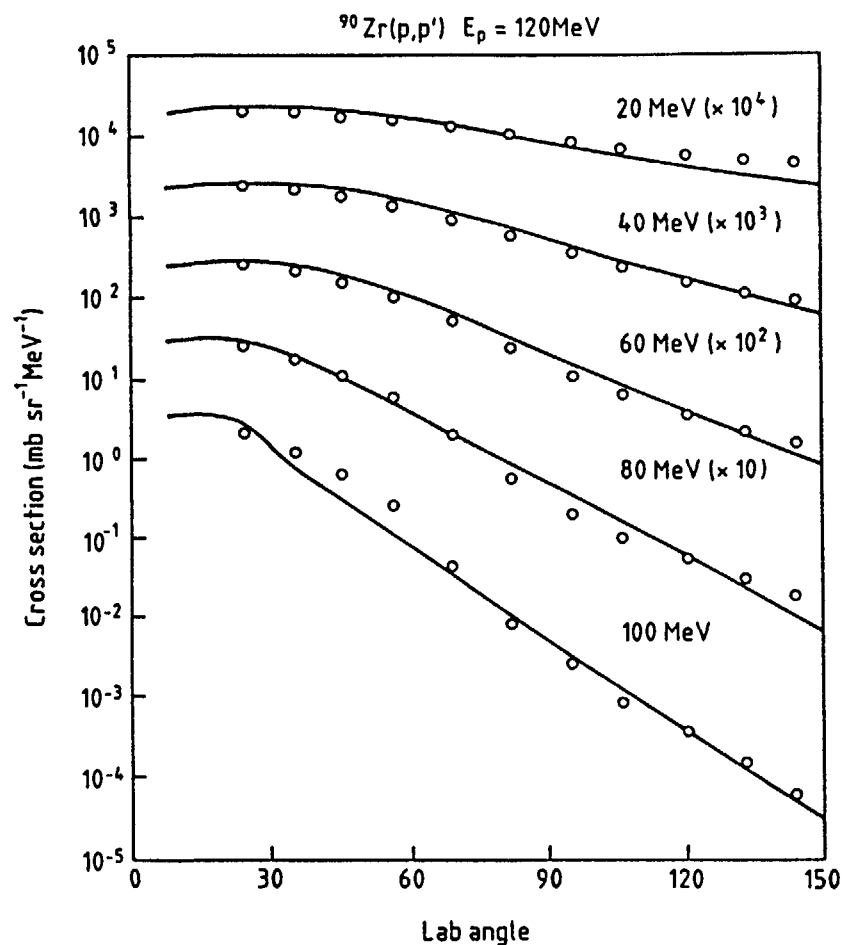


Figure 8. Double differential cross-sections for the inelastic scattering of 120 MeV protons by Zr compared with multistep direct calculations with the Feshbach-Kerman-Koonin theory (Cowley *et al*, 1990).

In all these analyses of multistep direct and multistep compound reactions it is usual to treat the effective interaction strength V_0 as an adjustable parameter and to fix it by fitting the absolute value of the differential cross-section. It is then important to examine the values obtained and see whether they behave in a systematic way that can be connected with other types of analysis. This comparison is however complicated by the progressive improvement in the formulation of the theory, since each improvement affects the value of V_0 obtained. Three main types of analysis have been used, namely (i) using constant wavefunctions inside the nucleus. Such analyses give values of V_0 around 1–2 MeV. Subsequent analyses used the more realistic harmonic oscillator wave functions for the bound nucleons and optical model wavefunctions of the emitted nucleons, with (ii) a delta function two-body interaction, which gives V_0 around 5–10 MeV, and (iii) a Yukawa two-body interaction which gives V_0 around 20–30 MeV. Here we consider only the calculations of type (iii) with realistic wavefunctions.

The results of several analyses are shown in Table 3 and Figure 9. The spread of values of V_0 is due partly to other differences in the analyses and also to the energy dependence of the effective interaction. Thus the multistep direct analysis of Bonetti *et al* (1981) was made using $V = 25$ MeV for the first step and $V = 15$ MeV for subsequent steps, so these values are not included in the Table. Some analyses were made distinguishing between neutrons and protons in the intra-nuclear cascade; this had rather little effect (less than 10%) on the shape of the cross-section but requires an increased V_0 in the case of the more recent analyses of (p, n) reactions.

Table 3. Values of the Effective Strength V_0 of the Yukawa Potential of Range 1 fm for Nucleon Interactions.

Reference	Reaction	V_0 (MeV)
Austin, 1980	(N, N') discrete states	27.9
Holler <i>et al</i> , 1985	(p, n) 26.7 MeV MSC+MSD	27
Mordhorst <i>et al</i> , 1986	(p, n) 25.6 MeV MSC+MSD	25
Marcinkowski <i>et al</i> , 1989	(n, n') 11.25 MeV MSC+MSD	25
Trabant <i>et al</i> , 1988, 1989	(p, n) 80 MeV MSD	20 ± 1
Scobel <i>et al</i> , 1990	(p, n) { 120 MeV MSD	16 ± 1
	{ 160 MeV MSD	12.5 ± 1
Cowley <i>et al</i> , 1991	(p, p) { 80 MSD	23
	{ 120 MSD	17.5

The values of V_0 are found to decrease with increasing incident energy and this is indeed what would be expected from the similar decrease of the real optical potential, which also depends on the strength of the two-body interaction. We can thus estimate the energy variation of V_0 by taking the value $V_0 = 27.9 \pm 3.5$ MeV obtained by Austin (1980) from a survey of the analyses of inelastic proton

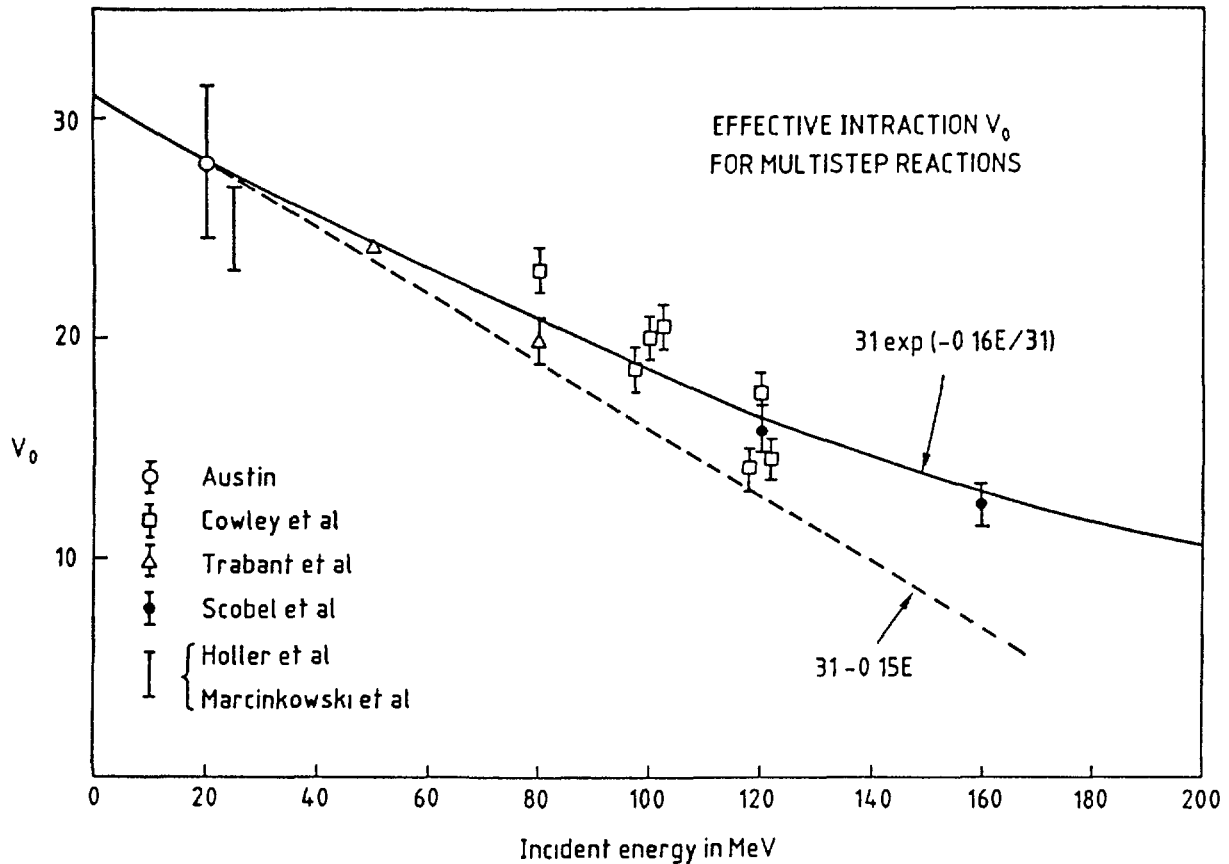


Figure 9. The effective interaction strength V_0 as a function of incident energy for nucleons with the Yukawa form factor with range 1 fm. The use of the delta function effective interaction decreases the value of V_0 by a factor of about three, as determined by calculations on the same reaction with both types of effective interaction (Bonetti and Colombo, 1983). It is also notable that the same value of V_0 is obtained from both the multistep compound and multistep direct analyses of reactions to which both processes contribute substantially (Mordhorst *et al*, 1986). The line $V_0 = 30.8 \exp(-0.16 E/30.8)$ is obtained from the energy dependence of the optical model potential. The references for the data points are given in Table 3.

scattering at around 20 to 50 MeV to discrete final states, and then assume that it has the same energy variation as the real optical potential.

Since the incident particle loses energy as it passes from stage to stage in the multistep process it would be more exact to allow the effective interaction to increase down the chain. It is however simpler to use an averaged value, but this effect should be taken into account when comparing the energy dependence of V_0 with that of the optical potential.

An estimate of the magnitude of the effect can be made by assuming that the incident particle loses about half its energy in the first interaction, and emission from the first and second stages are equally likely (Scobel *et al* 1990). This would reduce the energy-dependent term by about a factor of 3/4. The real optical potential, normalised to the Austin value of V_0 at 20 MeV is

$$V \approx 34 - 0.2E$$

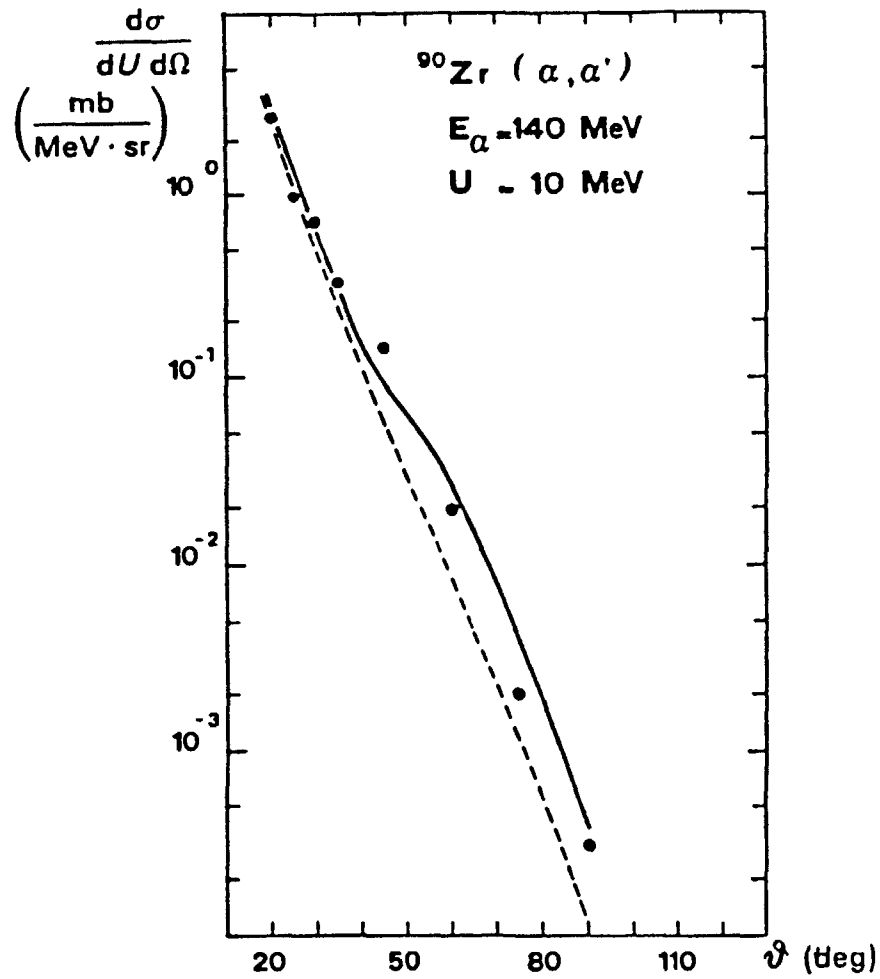


Figure 10. Double differential cross-section for the inelastic scattering of 140 MeV alpha-particles from ^{90}Zr with a final excitation energy of 10 Mev. The dashed curve shows the calculated cross-section obtained with the multistep direct theory assuming interactions with alpha-particles on the nuclear surface and the full curve is obtained by adding the contribution due to interactions with nucleons (Bonetti *et al*, 1984).

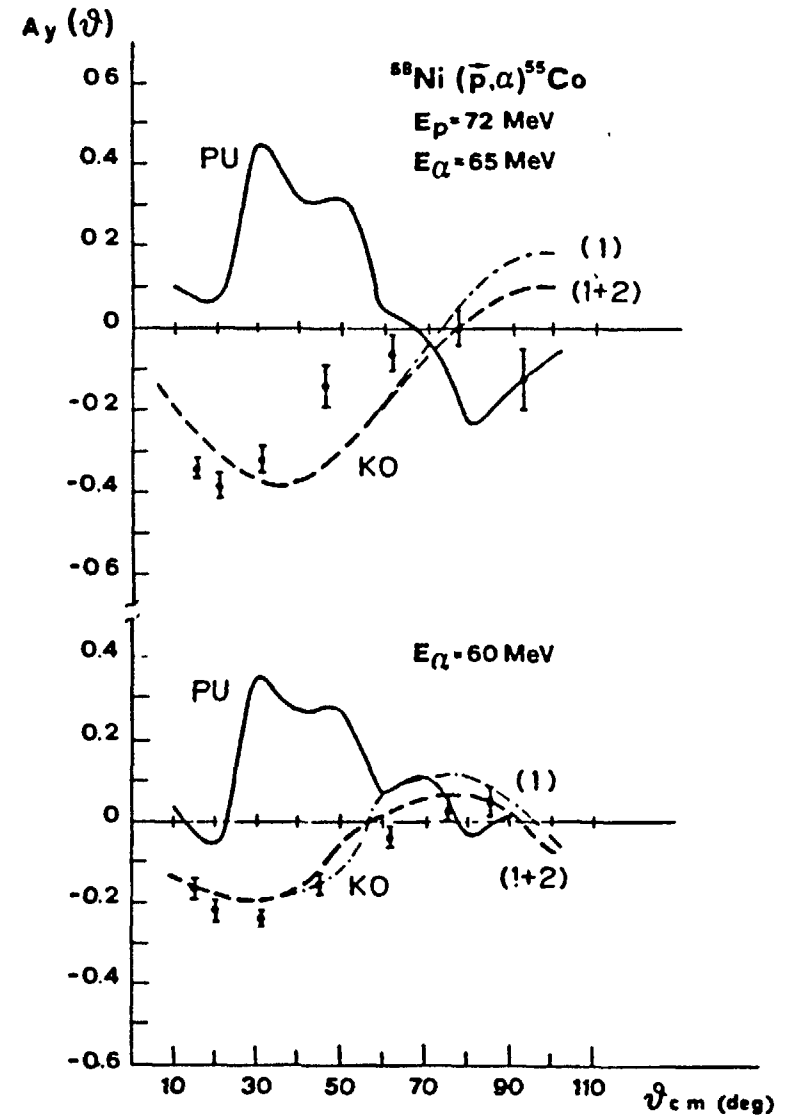


Figure 11. The analysing power of the $^{58}\text{Ni}(p, \alpha)^{55}\text{Co}$ reaction at 72 MeV to the continuum at an excitation energy of 65 Mev compared with multistep direct calculations with the triton pickup (full line) and alpha-particle knockout (dashed line) models. The knockout calculations were made with one step only (1) and with two steps (1 + 2) (Bonetti *et al*, 1989).

Allowing for the increase of V_0 down the chain thus gives

$$V \approx 31 - 0.15E$$

This is plotted in Fig.9 and has an energy dependence similar to the empirical values.

A rather better fit to the overall energy dependence can be obtained using the expression found by Johnson *et al* (1987) for neutrons on lead

$$V = 46.4 \exp(-0.31(E - E_F)/46.4)$$

Taking $E_F = -6$ MeV, normalising and introducing the factor 3/4 as before gives

$$V \approx 30.8 \exp(-0.162E/30.8)$$

which is also compared with the empirical values in Fig.9.

More direct evidence of the energy dependence of the effective interaction is provided by the analysis of the $Zr(p, d)Zr$ reaction at energies from 20 to 120 MeV by Kosugi and Kosugi (1983). In order to obtain energy-independent spectroscopic factors they found it necessary to allow the effective interaction to vary with energy. Normalising their result to that of Austin gives

$$V \approx 31.5 - 0.12E$$

which is very similar to that found above.

The Feshbach-Kerman-Koonin multistep direct theory has also been used to calculate (α, α') and (p, α) cross-sections to continuum states. Bonetti *et al* (1984) analysed the $^{90}Zr(\alpha, \alpha')$ reaction at 140 MeV to the continuum and found that good fits can be obtained to the angular distributions for residual nucleus excitation energies from 10 to 60 MeV by taking account only of the interaction between the incoming alpha-particles and preformed alpha-particles on the surface of the target nucleus. The normalisation of the calculations to the data gave values of the alpha clustering probability around 0.1, in accord with the results of other analyses in that mass region. It was not possible to fit the data with a standard distorted wave Born approximation calculation taking into account only the interaction with the target nucleons. The contributions of these two processes to the angular distribution corresponding to an excitation energy of 10 MeV are shown in Figure 10.

The (p, α) reaction can take place either by the triton pickup or by the alpha knockout processes, and it is difficult to distinguish between them because they often give the same angular distribution. The analysing power sometimes provides more discrimination, and calculations by Bonetti *et al* (1989) using the multistep direct theory showed that at high energies the reaction to the continuum proceeds primarily by the knockout mechanism, as shown in Figure 11.

4. Conclusions

Extensive calculations of (p, n) , (n, p) , (n, n') and (p, p') reactions have now been made at lower energies with the FKK multistep compound theory and at high energies with the multistep direct theory. Satisfactory agreement with the experimental data is found in all cases with consistent values of the effective interaction strength V_0 .

Further work is desirable to extend these analyses over a wider range of nuclei, and to determine the parameters more precisely. It is also important to study in more detail the emission of alpha and other composite particles, and also multiparticle emission at the higher energies.

References

- S.M. Austin, Proceedings of Telluride Conference, 1979.
- M. Blann, W. Scobel and E. Plechety, *Phys. Rev.* **C30**, 1493, 1984.
- R. Bonetti, L. Colombo and K.-I. Kubo, *Nucl. Phys.* **A420**, 109, 1984.
- R. Bonetti, F. Crespi and K.-I. Kubo, *Nucl. Phys.* **A499**, 381, 1989.
- M.B. Chadwick, P.E. Hodgson and A. Marcinkowski, Proceedings of the 5th International Conference on Nuclear Reaction Mechanisms, Varenna. Ed. E. Gadioli, 102, 1988.
- M.B. Chadwick, R. Bonetti and P.E. Hodgson, *J. Phys.* **G15**, 237, 1989.
- A.A. Cowley, A. van Kent, J.J. Lawrie, S.V. Förtsch, D.M. Whittal, J.V. Pilcher, F.D. Smith, W.A. Richter, R. Lindsay, I.J. van Heerden, R. Bonetti and P.E. Hodgson. (In preparation).
- S.S. Dietrich and B.L. Berman, *Atomic Data and Nuclear Data Tables* **38**, 199, 1988.
- G.M. Field, R. Bonetti and P.E. Hodgson, *J. Phys.* **G12**, 93, 1986.
- Y. Holler, A. Kaminsky, R. Langkau, W. Scobel, M. Trabant and R. Bonetti, *Nucl. Phys.* **A442**, 79, 1985.
- G. Jacob and T.A.J. Maris, *Rev. Mod. Phys.* **45**, 6, 1973.
- C.H. Johnson, D.J. Horen and C. Mahaux, *Phys. Rev.* **C36**, 2252, 1987.
- H. Kalka, M. Toryman and D. Seeliger, Semmering Conference, 305, 1988.
- S. Kosugi and T. Kosugi, *Phys. Lett.* **127B**, 389, 1983.
- N. Koumdjieva and P.E. Hodgson, *J. Phys.* **G15**, 1689, 1989.
- A. Marcinkowski, R.W. Finlay, G. Randars-Pehrson, C.E. Brient, R. Kurup, S. Mellema, A. Meigooni and R. Taylor, *Nuc. Sci. Eng.* **83**, 13, 1983.
- A. Marcinkowski, R.W. Finlay, J. Rapaport, P.E. Hodgson and M.B. Chadwick, *Nucl. Phys.* **A501**, 1, 1989.

- E. Mordhorst, M. Trabant, A. Kaminsky, H. Krause, W. Scobel, R. Bonetti and F. Crespi, *Phys. Rev.* **C34**, 103, 1986.
- P. Obložinský and M.B. Chadwick, *Phys. Rev.* (In Press) 1990.
- W. Scobel, M. Trabant, M. Blann, B.A. Pohl, R.A. Remington, R.C. Byrd, C.C. Foster, R. Bonetti, C. Chiesa and S.M. Grimes. (In Press) 1990.
- M. Trabant, H.M. Blann, R. Bonetti, R.C. Boyd, C.C. Foster, S.M. Grimes, B.A. Pohl, B.R. Remington and W. Scobel, Varenna Conference, 52, 1988.
- M. Trabant, W. Scobel, H.M. Blann, B.A. Pohl, R.C. Byrd, C.C. Foster, S.M. Grimes and R. Bonetti, *Phys. Rev.* **C39**, 452, 1989.

Evaluation of Activation Cross Sections of Ni- and Mo-isotopes

Yutaka NAKAJIMA
Department of Physics,
Japan Atomic Energy Research Institute,
Tokai-mura Ibaraki-ken 319-11,

Nobuhiro YAMAMURO
Data Engineering, Inc.,
Midori-ku, Yokohama 226,
Japan

Abstract

The neutron cross sections of Ni- and Mo-isotopes have been evaluated with the system SINCROS-II. The results are compared with experimental data and JENDL-3.

I. Introduction

Evaluation of activation cross sections for the JENDL-activation file started three years ago⁽¹⁾ and more than 1,000 reaction cross sections have been evaluated. The code system SINCROS-II(Nuclear Cross Section Calculation System with Simplified Input-Format, Version II)⁽²⁾ has been developed and used for the evaluation of more than half of them. In this evaluation the unified evaluation method has been employed using the global optical model parameters and the systematical values of level density parameters. Calculated cross sections have never been changed by the normalization. When the calculated cross sections differ significantly from experimental values, the input parameters have been changed. Since we are aiming at accurate evaluation of important reaction cross sections for applications to fission and fusion reactor technologies, the number of the reactions has been reduced. Still many reaction cross sections should be evaluated for the activation file. Review of the evaluated data is being made

by comparing the evaluated data with measured values and with other evaluation. In this paper evaluation procedure of the activation cross sections and the results for Ni- and Mo-isotopes are shown.

II. Evaluation Method

The main part of SINCROS-II consists of the ELIESE⁽³⁾-GNASH⁽⁴⁾ joint program and the simplified-input version of DWUCK⁽⁵⁾.

The system is very convenient for the evaluation of a number of reactions, because the input data have been simplified. The input data consist of discrete level data (level energy, spin, parity and branching ratio of decay channels) which were taken from ENSDF⁽⁶⁾, direct inelastic scattering cross sections calculated with DWUCK and the data designating reaction channels.

The global optical model potentials have been used. For neutrons a modified Walter-Guss potential⁽⁷⁾ was used. The Walter-Guss potential was derived for $A > 53$ and $10 < E_n < 80$ MeV. To apply the potential even below 10 MeV neutron energy, the surface absorption part W_D (in MeV) between 0 and 20 MeV has been changed from

$$W_D = 10.85 - 0.157E - 14.94(N-Z)/A \text{ (Walter - Guss)}$$

to

$$W_D = 7.71 - 14.94(N-Z)/A \text{ MeV.} \quad (1)$$

This was determined so that the calculated nonelastic cross sections of ⁶³Cu, ¹²⁰Sn and Pb agree with the experimental data within about 10 %.

For protons, the Perey potential⁽⁸⁾ was used below 10 MeV proton energy and the Walter-Guss potential was used between 10 and 20 MeV proton energy.

The Lemos set modified by Arthur and Young⁽⁹⁾ was used for α -particles and deuterons. The Becchetti-Greenlees potential⁽¹⁰⁾ was used for tritons and ³He-particles.

The single particle level density constant g is related to the level density parameter a by the formula

$$g = (6/\pi^2)a. \quad (2)$$

In addition to the normalization factor F2 which is equal to the Kalbach constant divided by 100, adjusting factors F3 and F4 were introduced for pick-up and knock-out processes, respectively. The factor F2 and the contribution of the direct inelastic scattering to cross sections were determined so that the calculated neutron emission spectra were in agreement with the high energy part of measured neutron spectra. The values of F2 sometimes were adjusted by using proton emission spectra.

The pick-up factor F3 was determined from α -particle emission spectra. Since the measured α -particle emission spectra could be reproduced with F3 = 0.5 for almost all medium-weight nuclei, F3 was assumed to be 0.5. The factor F4 for the knock-out process was assumed to be 1.0 for the calculation of the cross sections of the Ni- and Mo-isotopes.

The level densities were determined uniquely by the level density parameter a not only in the Fermi gas model but also in the constant temperature model, because the nuclear temperatures were determined automatically from the level density parameter a in the code or by the equation

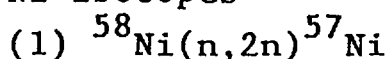
$$T = 7.50 a^{-0.84}. \quad (3)$$

The level density parameter a is plotted against the mass number in Fig. 1 for the nuclei of Ni- and Mo-regions.

Resonance parameters for neutron capture cross sections were taken from the JENDL-3 general purpose file⁽¹¹⁾. The normalization factors were chosen for the evaluated capture cross sections to fit those calculated with the resonance parameters at 100 keV.

III. Results and Discussion

1. Ni-isotopes



The present evaluation deviates a little from measured data below 15 MeV, while JENDL-3 is very close to them, Above 15 MeV there are two kinds of experimental data. The present evaluation is close to the lower data, while JENDL-3

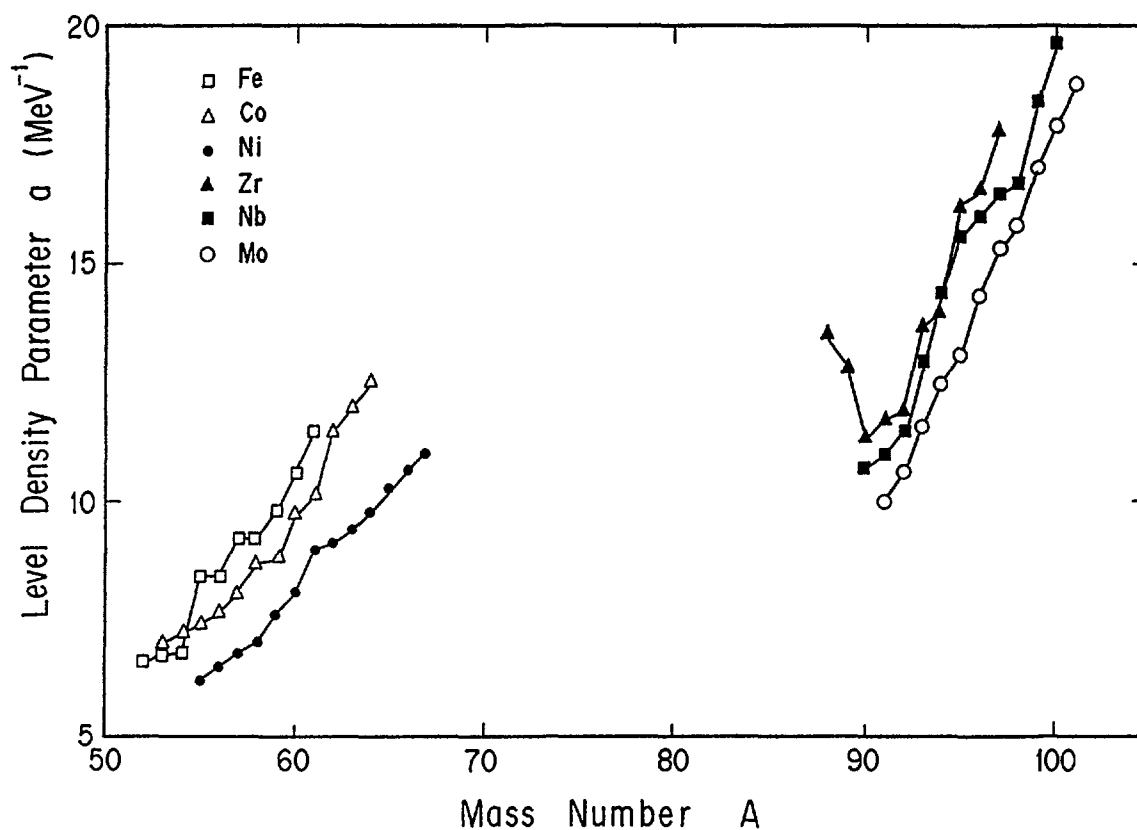
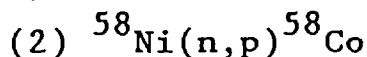
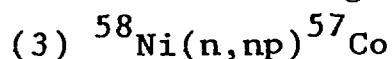


Fig. 1. Level density parameter "a" as a function of mass number for nuclei related to the calculation of the reactions of Ni- and Mo-isotopes.

follows the higher data. Recent measurements support the higher data. JENDL-3 has been evaluated based on experimental data.



JENDL-3 has been evaluated based on experimental data and follows them very well. The present evaluation is in agreement with experimental data only near the threshold and 15 MeV neutron energy, but it reproduces the energy dependence of the Ohio University data (Graham et al. (12)). As the Ohio University data are proton emission cross sections, the agreement can be improved when the present evaluation including (n,np) reaction is compared with them.



The present evaluation is higher than experimental data, while JENDL-3 is lower than those. JENDL-3 is closer to them than the present evaluation. JENDL-3 has been evaluated based on experimental values.

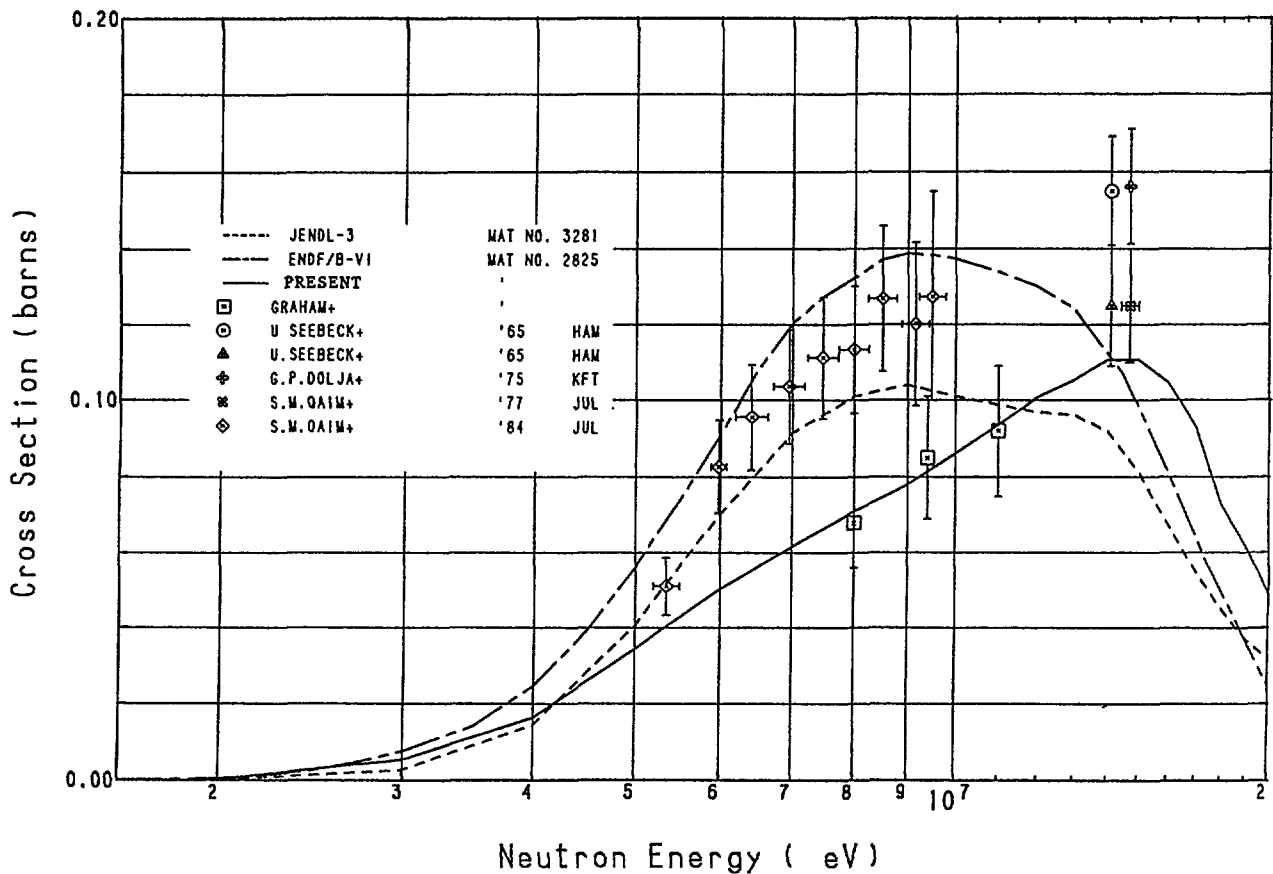


Fig. 2. $^{58}\text{Ni}(n,\alpha)^{55}\text{Fe}$.

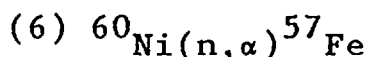
(4) $^{58}\text{Ni}(n,\alpha)^{55}\text{Fe}$

The comparison is shown in Fig.2. The present evaluation has quite a different energy dependence from those of JENDL-3 and ENDF/B-VI. The energy dependence of JENDL-3 is in good agreement with that of ENDF/B-VI, while the normalization is a little different. The average values of JENDL-3 and ENDF/B-VI seem to be in good agreement with experimental data. The present evaluation is in good agreement with the Ohio University data(Graham et al.⁽¹²⁾). JENDL-3 has been evaluated using PEGASUS code⁽¹³⁾ and normalized to experimental data. There are some evaluations which have the same shape as the present evaluation.

(5) $^{60}\text{Ni}(n,p)^{60}\text{Co}$

JENDL-3 has been evaluated based on experimental data. The energy dependence of the present evaluation is quite different from that of JENDL-3. It is impossible to judge which evaluation agrees with measured data. There are some

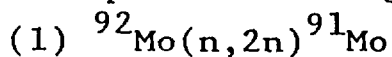
evaluations which have the same shape as the present evaluation.



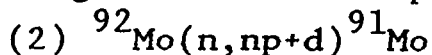
For α emission cross section the present evaluation is in better agreement with the Ohio University data (Grimes et al.⁽¹⁴⁾; Graham et al.⁽¹²⁾) than JENDL-3. The difference among them is not so large. JENDL-3 has been evaluated using PEGASUS code⁽¹³⁾ and normalized to experimental data.

2. Mo-isotopes

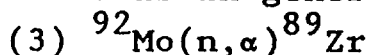
Since the comparison of the present evaluation with experimental data is described in detail elsewhere⁽¹⁵⁾, only brief explanation is given here.



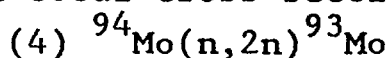
As is shown in Fig. 3, the present evaluation for the ground state, isomeric state and total cross sections is in good agreement with experimental data except a few data.



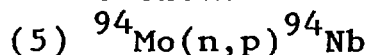
The present evaluation for the isomeric state cross section reproduces the energy dependence of experimental data and is in general agreement with them.



Experimental data for the total (n,α) cross section do not show any definite energy dependence. The present evaluation fairly agrees with Ikeda et al.'s isomeric state and total cross sections⁽¹⁶⁾.



The evaluated values are higher than all experimental values for ground and isomeric state cross sections. The effective threshold energy is different between the present evaluation and the experimental data for the isomeric state cross section.



The present evaluation is in agreement with experimental data for the total cross section but shows a little different excitation function in comparison of that of measured data.

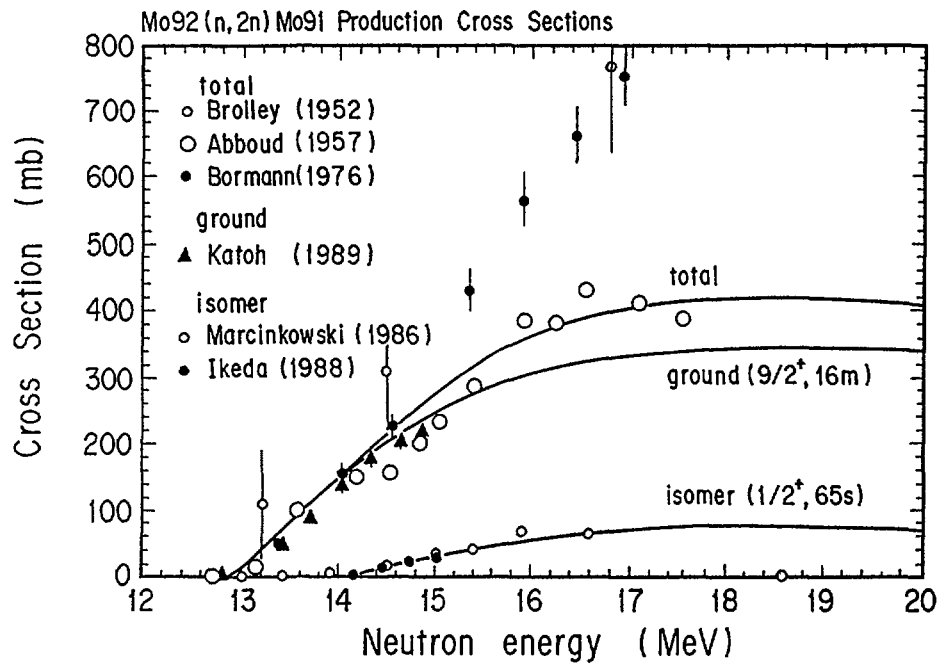


Fig. 3. $^{92}\text{Mo}(n,2n)^{91}\text{Mo}$.

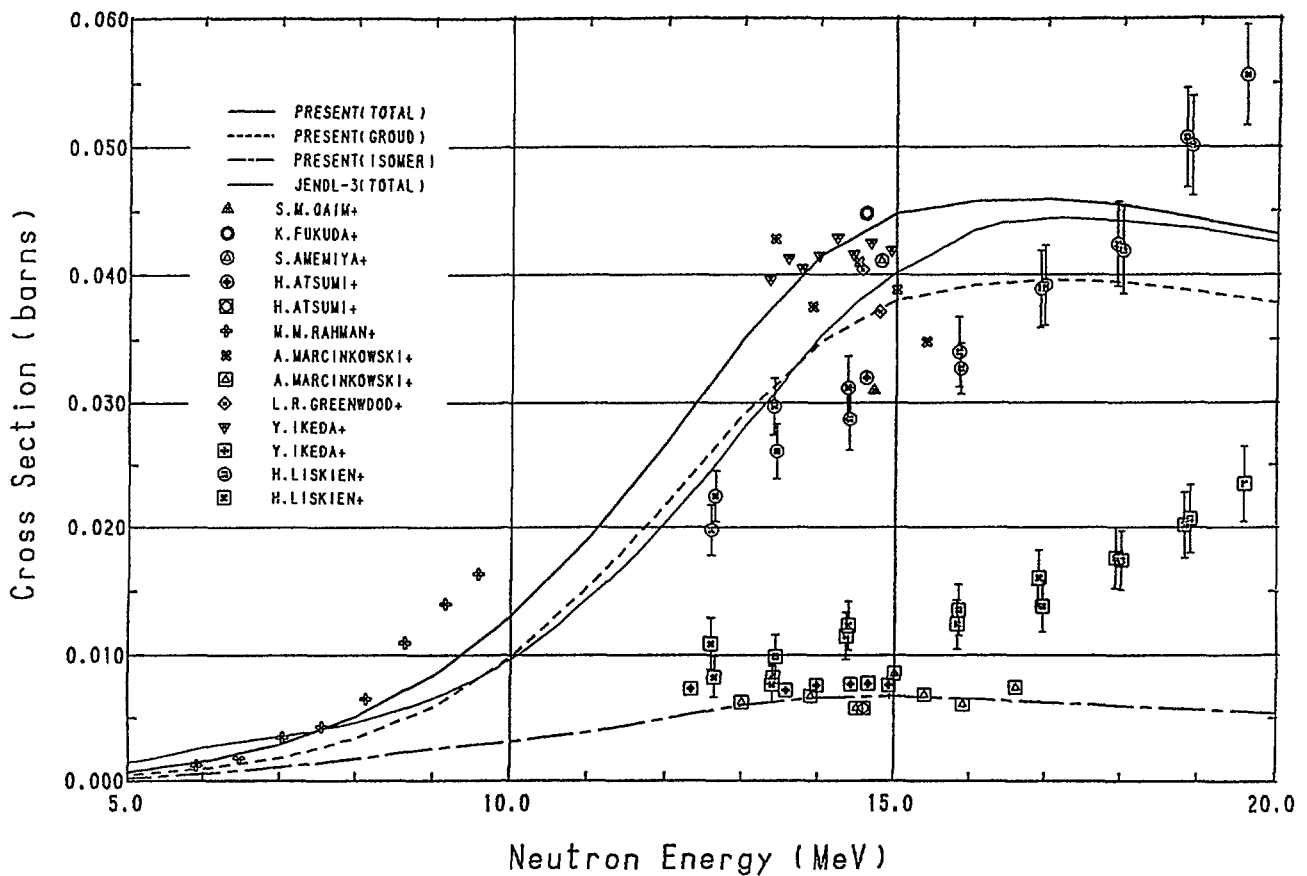
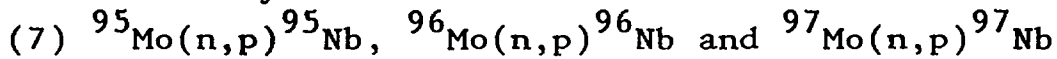


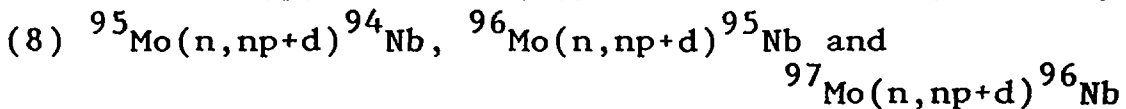
Fig. 4. $^{95}\text{Mo}(n,p)^{95}\text{Nb}$. Symbols enclosed with a circle denote the ground state production cross sections. Symbols enclosed with a square represent the isomeric state production cross sections. Other symbols show the total (n,p) cross sections.



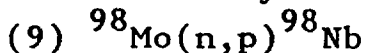
The present evaluation is in good agreement with the data measured by Greenwood and Bowers⁽¹⁷⁾.



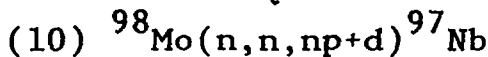
As is shown in Fig. 4, the general agreement between the present evaluation and experimental data is obtained for the ground and isomeric state cross sections except for the data above 16 MeV of Liskien et al.⁽¹⁸⁾, which are higher than the present evaluation. This is due to the contamination of the $^{96}\text{Mo}(n, np+d)$ and $^{98}\text{Mo}(n, np+d)$ reactions into the $^{95}\text{Mo}(n, p)$ and $^{96}\text{Mo}(n, p)$ reactions, respectively.



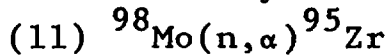
The present evaluation is in good agreement with the data measured by Greenwood et al.⁽¹⁹⁾ Ikeda et al.⁽¹⁶⁾



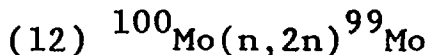
The present evaluation is in good agreement with the data measured by Ikeda et al.⁽¹⁶⁾, Marcinkovski et al.⁽²⁰⁾ and Rhaman and Qaim⁽²¹⁾.



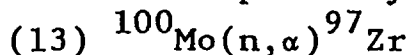
The present evaluation is in good agreement with the data measured by Ikeda et al.⁽¹⁶⁾ and Katoh et al.⁽²²⁾.



Including the excitation function the general agreement between the present evaluation and measured data was obtained.



The present evaluation is in good agreement with measured data of Rhaman and Qaim⁽²¹⁾ and Marcinkovski et al.⁽²⁰⁾ and especially well with Ikeda et al.⁽¹⁶⁾



The general agreement between the present evaluation and measured data was obtained for this reaction.

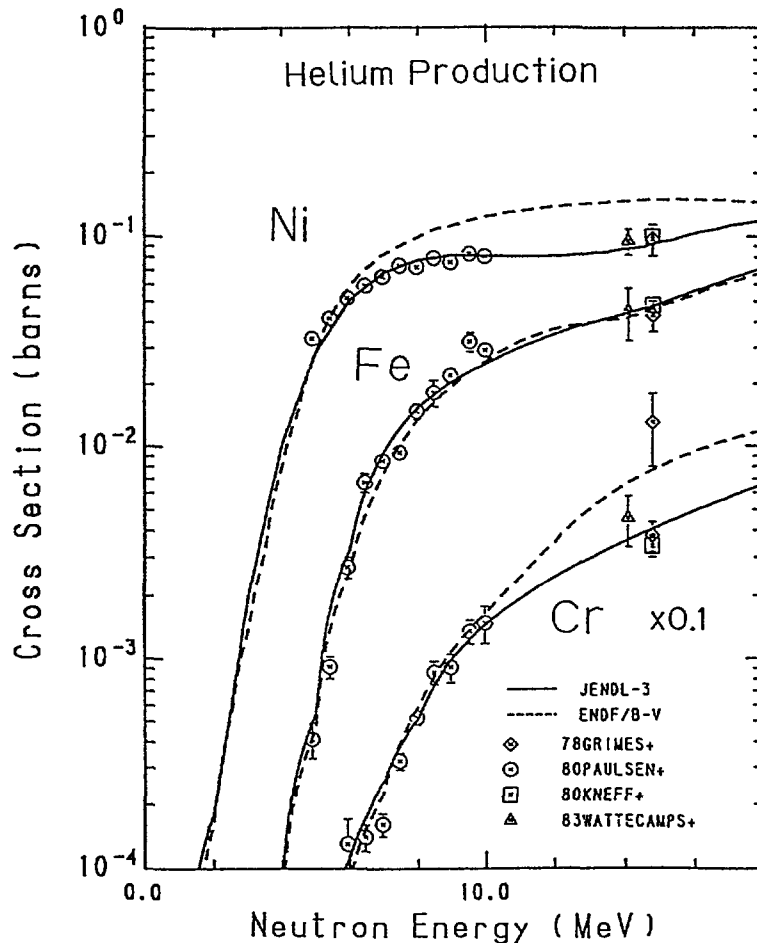


Fig. 5. Helium production cross sections ($n, x\alpha$) for natural Ni, Fe and Cr.

IV. Conclusion

From the comparison with experimental data the present evaluation of the Mo-isotopes is found to reproduce the experimental data better than JENDL-3, while for the Ni-isotopes JENDL-3 follows better the experimental data than the present evaluation. Moreover α production cross sections of natural Ni can be reproduced by JENDL-3 very well as shown in Fig. 5 (Fig. 5 is reproduced from Fig. 2 in Ref.23). The present evaluation on the Mo-isotopes and the evaluation of the Ni-isotopes in JENDL-3 will be adopted for the JENDL activation cross section file.

Acknowledgments

The authors are grateful to Mr. T. Nakagawa and Mr. T. Narita for help of handling of the evaluated data with computers. They are much indebted to the members of the working group on activation cross section data of JNDC.

References

- (1) Y.Nakajima et al., Proc. Specialists' Meeting on Neutron Activation Cross Sections for Fission and Fusion Energy Applications, Sep. 1989, Argonne National Laboratory, NEANDC-259"U", p. 285(1990).
- (2) N.Yamamuro, JAERI-M 90-006(1990).
- (3) S.Igarasi, JAERI 1224(1972).
- (4) P.G.Young and E.G.Arthur, LA-6947(1977).
- (5) P.D.Kunz, "Distorted Wave Code DWUCK4", University Colorado(1974).
- (6) BNL, Evaluated Nuclear Structure Data File.
- (7) R.L.Walter and P.P.Guss, Proc. Int. Conf. Nuclear Data for Basic and Applied Science, Vol. 2, p. 1079, Gordon and Breach(1986).
- (8) F.G.Perey Phys. Rev. 131, 745(1963).
- (9) E.D.Arthur and P.G.Young, LA-8626-MS(1980).
- (10) F.D.Becchetti, Jr. and G.W.Greenlees, "Polarization Phenomena in Nuclear Reactions", the University of Wisconsin Press, p.682(1971).
- (11) K.Shibata et al., JAERI 1319(1990).
- (12) S.L.Graham et al., Nucl. Sci. Eng. 95, 60(1987).
- (13) S.Iijima et al., JAERI-M 97-025, p. 337(1987).
- (14) S.M.Grimes et al., Phys. Rev. C19, 2127(1979).
- (15) N.Yamamuro, "Calculation of Activation Cross Sections for Molybdenum Isotopes", preprint(1990).
- (16) Y.Ikeda et al., JAERI 1312(1988).
- (17) L.R.Greenwood and D.L.Bowers, J. Nucl. Materials 155-157, 585(1988).
- (18) H.Liskien et al., Appl. Radiat. Isot. 41, 83(1990).
- (19) L.R.Greenwood et al., Phys. Rev. C35, 76(1987).
- (20) A.Marcinkovski et al., Z. Phys. A323, 91(1986).
- (21) M.M.Rahman and S.M.Qaim, Nucl. Phys. A435, 43(1985).
- (22) T.Katoh et al., JAERI-M 89-083(1989). In Japanese.
- (23) S.Iijima et al., Proc. Int. Conf. Nuclear Data for Basic and Applied Science, p. 627, Saikon Publishing Co.(1988).

Consequences from Testing Measured and Calculated 14.6 MeV Neutron Inelastic Scattering Cross Sections by Means of Comparison with Results of Fast Proton Inelastic Scattering Using DWBA and GDH*) Approaches

S. Ercakir and H. Jahn**)

Faculty of Physics, University of Karlsruhe

ABSTRACT

In this paper we show that the possibility of calculating double differential inelastic neutron cross sections is considerably improved if we add information from the results of measurements of the inelastic proton scattering cross-sections. With this additional information we obtain a sufficient starting point to calculate rather accurate and unique results for the double differential cross-sections of inelastic neutron scattering at the high energy tail of the secondary energy. This is demonstrated by a few examples of ^{56}Fe . Moreover by applying certain averages to the angle integrated inelastic cross-sections the results of Blann's geometry dependent hybrid model*) are obtained. Consequently this might be a hint to a more rigorous derivation of this model.

1. DISCREPANCIES AND ERRORS OF THE MEASURED FAST (n, n')-CROSS SECTIONS

The investigations of this paper start from the fact that the measured results of the different experimental groups for the 14.6 MeV inelastic neutron cross sections show not only considerable experimental errors in particular in forward direction but also remarkable discrepancies between them must be noted. This is demonstrated in a previous investigation³¹⁾ showing measured and calculated angular distributions of 14.6 MeV (n, n')-cross sections of ^{93}Nb and ^{56}Fe . It can be seen very clearly from the Figures 1a and b of³¹⁾ that the measured results are not accurate enough to enable a decision concerning the validity of the different concepts. The error bar situation in forward direction survives also with the improved measured results of³²⁾.

*) GDH **) Retired from the Institute of Neutron Physics and Reactor Technic, Kernforschungszentrum Karlsruhe

2. RESORT TO CHARGED PARTICLE RESULTS

One way out of this situation can be to resort to the results of measured cross-sections of inelastic scattering of fast protons. The very high resolution obtainable in the proton-channel is presented by the measured results of the inelastic 17,5 MeV proton-cross-section in the work of Peterson¹⁰⁾. Similar results but for inelastically scattered protons with an incident energy of 49,35 MeV also with very high energy resolution of the cross section energy distributions have been considered by Mani¹²⁾. In both cases, for 49,35 MeV incident protons as well as for 17,5 MeV incident protons, the 26 lowest excited states of ⁵⁶Fe are exhibited as the peaks of the very high energy resolved proton-cross section energy distributions. As results of DWBA-analyses of Peterson¹⁰⁾ and Mani¹²⁾ the energies and spins of these states are listed in Tab. 1. These results are obtained from DWBA-calculations according to the formulae

$$\frac{d\sigma_{if_v}^{(x)}(\epsilon_i, \epsilon_{f_v}, \theta)}{d\Omega_{f_v}} = \beta_v^2 \sigma_v^{(x)}(\epsilon_i, \epsilon_{f_v}, 0) \quad (1)$$

with

$$\sigma_v^{(x)}(\epsilon_i, \epsilon_{f_v}, \theta) = \frac{k_{f_v}}{k_i} \left(\frac{m}{2\pi\hbar^2} \right) \frac{R_o^2}{2l_v + 1} \quad (1a)$$

$$\sum_{m_v} \left| \int \chi^{- (x)}(\underline{k}_{f_v}, \underline{r}) \left(\frac{\partial U^{(x)}(r)}{\partial r} \right) Y_{l_v}^{m_v}(\Theta) \chi^{+ (x)}(\underline{k}_i, \underline{r}) d^3 r \right|^2$$

and

$$R_o = r_o A^{1/3}; r_o = 1.25 \cdot 10^{-13} \text{ fm}; U_{(r)}^{(x)} = \text{optical potential} \quad (1b)$$

θ = scattering angle

Ω = space angle of scattering

Θ = projectile coordinate angle

k_i, k_{f_v} = initial and final projectile wave vectors belonging to the incident and final energies ϵ and ϵ_v with the target excitation energy ϵ_v

$\chi^{\pm(x)}$ = optical model scattering states of projectile (x) indicating proton (p) or neutron (n):

$Y_{l_\nu}(\Theta)$	= spherical harmonics
m	= nucleon mass
l_ν	= transferred angular momentum belonging to level ν
m_ν	= component of the angular momentum belonging to level ν

(1) - (1b) represent the DWBA-formulae based on the collective vibrational model. But beyond of this (1) - (1b) have been used by Peterson¹⁰⁾, Mani¹²⁾ and Ignatyuk¹³⁾ also for the phenomenological analysis of any excitation by direct inelastic proton scattering. Then β_ν is a parameter to be chosen to fit the experimental angular distribution. As above the index (x) denotes the type of nucleon (eg. proton or neutron). No index (x) is attached to β_ν because the dependence of β_ν on the type of nucleon can be neglected. But β_ν depends on the target nucleus. Thus β_ν can be obtained by fitting the experimental data for one type of nucleon and can then be used to calculate the angular distribution for the other type of nucleon, for the same target nucleus. Consequently once we have obtained β_ν experimentally from the proton-channel we are able to calculate the scattering for the neutron-channel, in particular for small angles.

3. COMPARISON OF DWBA- AND GDH AVERAGE CROSS SECTION RESULTS

To obtain the appropriate angular distributions of the inelastic neutron cross sections we insert the β_ν -values from the proton channel analysis of Peterson¹⁰⁾ and Mani¹²⁾ shown in Tab. 1 into the expressions of the equations (1) - (1b) together with the scattering states $x^{\pm(n)}$, calculated from the optical model of the neutron channel instead of the scattering states $x^{\pm(p)}$ from the optical model of the proton channel analysis of Peterson and Mani^{10,12)}. Calculations of this type for the neutron channel have been carried out by Kinney and Perey¹⁴⁾, by Penny and Kinney¹⁵⁾ and by Fu¹⁶⁾. Scattering angle dependent neutron cross sections obtained by these authors and can be found on the ENDFB/IV files of the US neutron cross section library.

To proceed with developing our method Fig. 1 may be considered. Fig. 1 shows experimental and theoretical results for the angle-integrated 14,6 MeV in-

⁵⁶Fe STATES

TABLE 1

Energy levels (Mev) and spin values obtained in Ref.12) and Ref.10)

Peak no ν	Ref.12)				Ref.10)			
	ϵ_ν	β_ν	β_ν^2	l_ν	ϵ_ν	β_ν	β_ν^2	l_ν
1	0.849	0.2	0.040	2 ⁺	0.85	0.29	0.0841	2 ⁺
2	2.118			(4 ⁺)	2.08			
3	2.695	0.06	0.0036	2 ⁺	2.65	0.107	0.0115	2 ⁺
	2.968			(0 ⁺)	2.94			
4	2.968	0.02	0.0004	(2 ⁺)	2.96	0.044	0.0019	2 ⁺
5	3.159	0.087	0.0077	4 ⁺	3.12	0.124	0.0154	4 ⁺
6	3.411	0.06	0.0036	2 ⁺	3.37	0.043	0.0011	2 ⁺
	3.411			(6 ⁺)	3.39	0.03	0.0009	6 ⁺
7	3.635	0.05	0.0025	2 ⁺	3.60	0.053	0.0028	2 ⁺
7a					3.75	0.082	0.0067	2 ⁺
8	3.850	0.03	0.0009	2 ⁺	3.83	0.069	0.0048	2 ⁺
					4.04			
9	4.124	0.045	0.0020	4 ⁺	4.10	0.095	0.0090	4 ⁺
					4.40	0.053	0.0028	(4 ⁺)
					4.46	0.074	0.0055	4 ⁺
10	4.512	0.154	0.0237	3 ⁻	4.51	0.198	0.0392	3 ⁻
11	4.660	0.071	0.0050	4 ⁺	4.61	0.055	0.0030	4 ⁺
11a					4.69	0.064	0.0041	4 ⁺
11b					4.73	0.050	0.0025	2 [']
12	4.860	0.039	0.0015	4 ⁺	4.88	0.100	0.0100	4 ⁺
13	5.106	0.041	0.0017	5 ⁻	5.15	0.097	0.0094	(4 ⁺)
14	5.195	0.046	0.0022	(4 ⁻)	5.20	0.078	0.0061	(3 ⁻)
15	5.266	0.050	0.0025	4 ⁺	5.26			
16	5.535	0.050	0.0025	2 ⁺	5.51			
					5.58			
					5.69			
17	5.763	0.03	0.0009	(5 ⁺)	5.73			
18	5.880	0.039	0.0015	4 ⁺	5.90			
19	6.067	0.037	0.0014	4 ⁺	6.00			
20	6.273	0.053	0.0028	4 ⁺	6.30			
21	6.410			(3,4)				
					6.48			2(+)
22	6.635	0.084	0.0071	(3,4)				
23	6.870							
24	6.966	0.05	0.0025	3				
25	7.080	0.046	0.0021	(3,4)				
26	7.189	0.046	0.0021	(3,4)				
27	7.312	0.038	0.0014	(3,4)				
28	7.475	0.051	0.0026	(3 ⁻)				

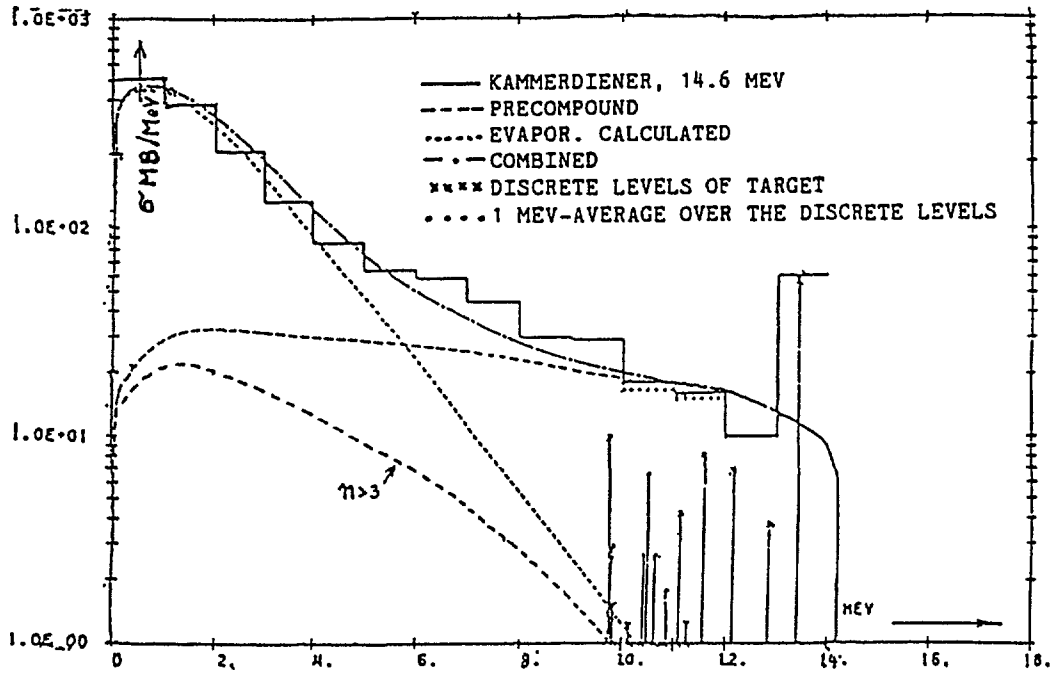


Fig. 1 Neutron emission cross-section of ^{56}Fe ; $E_{\text{in}} = 14.6 \text{ MeV}$

elastic neutron cross section. The step curve of Fig. 1 with 1 MeV interval of the steps is obtained by Hansen et al.¹⁷⁾ from measurements of the neutron leakage spectrum from an assembly of iron. This experimental step curve is in particular at the high-energy tail quite well reproduced by the smooth straight line which is obtained from calculated results⁶⁾ of Blann's geometry-dependent hybrid model (GDH) with optical model option. This approach has no fit-parameters other than those of the usual optical model. This is a remarkable improvement compared to the excitation master equation approach where the internal transition rate between the excitation steps has to be adjusted as an extra fit parameter if the high-energy tail of the secondary energy-dependent inelastic nucleon cross section should be taken into account⁶⁾. On the other hand it can be shown that the experimental step curve of Fig. 1 can quite well be reproduced by average results of the neutron-channel-DWBA-calculations outlined above with β_v taken from the proton-channel as shown in Tab. 1 inserted into the equations (1) - (1b) used to calculate the inelastic neutron cross section. By angle-integrating the results obtained from the equations (1) - (1b) by these equations according to

$$\int d\Omega_{f_v} \left(\frac{d\sigma_{if_v}^{(n)}(\epsilon_i, \epsilon_{f_v}, \theta)}{d\Omega_{f_v}} \right)_{\text{DWBA}} = \left(\sigma_{if_v}^{(n)}(\epsilon_i, \epsilon_{f_v}) \right)_{\text{DWBA}} \quad (2)$$

we obtain on the right hand side of equation (2) cross section results for the single levels which are shown in Fig. 1 by the discrete endpoints of the vertical lines for the first 13 levels obtained by¹⁴⁻¹⁶).

We now turn to reproduce the experimental step curve of Fig. 1 by averaging the measurable angle-integrated secondary energy-dependent inelastic neutron cross section over intervals I being equal to the widths of the steps. Then we obtain

$$\begin{aligned} \overline{\left(\sigma_i^{(n)}(\epsilon_i, \epsilon) \right)} &= \frac{1}{I} \int_{\epsilon-1/2}^{\epsilon+1/2} \left(\frac{d\sigma_i^{(n)}(\epsilon_i, \epsilon')}{d\epsilon'} \right)_{DWBA} d\epsilon' = \\ &= \frac{1}{I} \int_{\epsilon-1/2}^{\epsilon+1/2} \sum_{\nu} \rho_{\nu}(\epsilon', \epsilon_{f\nu}) \sigma_{if\nu}^{(n)}(\epsilon_i, \epsilon')_{DWBA} d\epsilon' = \frac{1}{I} \sum_{\nu CI} \left(\sigma_{if\nu}^{(n)}(\epsilon_i, \epsilon_{f\nu}) \right)_{DWBA} \end{aligned} \quad (3)$$

where the $\rho_{\nu}(\epsilon', \epsilon_{f\nu})$ are the normalized energy distributions around the excitation energies of the single levels and where the single terms in the sum at the most right hand side of eq. (3) and in the integrand of the expression before it are given by the right hand side of eq. (2). Equation (3) expresses that the average angle-integrated inelastic fast-neutron cross section is at the high-energy tail of the secondary energy equal to the sum of the discrete cross section values of Fig. 1 within each averaging interval I.

The results of this summing up for the two intervals 10 - 11 MeV and 11 - 12 MeV are represented in Fig. 1 as horizontal dotted lines which are seen to coincide quite well with the experimental step curve as well as with the $n_0=3$ contribution of the geometry dependent hybrid model. Since the latter is the only calculated contribution of this model to the angle integrated secondary energy dependent neutron cross section at this high energy tail of secondary energy it can be presumed that the $n_0=3$ component of the geometry dependent hybrid model represents a certain average over the direct component of the inelastic nucleon cross section. With the definitions and the results of equations (2) and (3) we therefore conclude

$$\lim_{I \rightarrow 0} \frac{1}{I} \sum_{\substack{\epsilon_j+1/2 \\ \epsilon_{f\nu}=\epsilon_j-1/2}} \left(\sigma_{if\nu}^{(n)}(\epsilon_i, \epsilon_{f\nu}) \right)_{DWBA} = \int_{\epsilon_j-1/2}^{\epsilon_j+1/2} \left(\frac{d\sigma_i^{(n)}(\epsilon_i, \epsilon')}{d\epsilon'} \right)_{n=n_0=3}^{GDH} d\epsilon' \quad (4)$$

The averaging intervals I in equations (3) and (4) do not include very many levels. For instance the interval 10 - 11 MeV includes 6 levels and the inter-

val 11 - 12 MeV includes 5 levels according to Tab. 1. Such a small number of levels is obviously already enough to obtain for the inelastic nucleon cross section at the high-energy tail of the secondary energy an average with a physical meaning in the sense that it can be calculated by a physical model like in this case by Blann's geometry dependent hybrid model. Because of the small number of included levels we conclude that it may not be a statistical average we have to do with in this case. Instead we may have to do here with a summing up in the sense of the well-known sum rules of Satchler¹⁵⁾ and Lane²⁰⁾ (see also Lewis²¹⁾).

If we consider the derivation from equations (1) to (4) then we arrive at the conclusion that it should make sense to introduce the averaged measured angle-dependent differential inelastic fast-neutron cross section at the high-secondary energy tail according to

$$\overline{\left(\frac{d^2\sigma_{ij}^{(n)}(\epsilon_i, \epsilon_j, \theta_j)}{d\epsilon_j d\Omega_j} \right)}_{\text{dir}} = \frac{1}{I} \int_{\epsilon_j-1/2}^{\epsilon_j+1/2} \left(\frac{d^2\sigma_{ij}^{(n)}(\epsilon_i, \epsilon', \theta_j)}{d\epsilon' d\Omega_j} \right)_{\text{dir}} d\epsilon' \quad (5)$$

Corresponding to equation (3) we then obtain

$$\begin{aligned} \overline{\left(\frac{d^2\sigma_{ij}^{(n)}(\epsilon_i, \epsilon_j, \theta_j)}{d\epsilon_j d\Omega_j} \right)}_{\text{dir}} &= \frac{1}{I} \int_{\epsilon_j-1/2}^{\epsilon_j+1/2} \sum_{\nu} \rho_{\nu}(\epsilon', \epsilon'_{f\nu}) \left(\frac{d\sigma_{if\nu}^{(n)}(\epsilon_i, \epsilon', \theta_{f\nu})}{d\Omega_{f\nu}} \right)_{\text{DWBA}} d\epsilon' = \\ &= \frac{1}{I} \sum_{\epsilon'_{f\nu}=\epsilon_j-1/2}^{\epsilon_j+1/2} \nu \left(\frac{d\sigma_{if\nu}^{(n)}(\epsilon_i, \epsilon'_{f\nu}, \theta_{f\nu})}{d\Omega_{f\nu}} \right)_{\text{DWBA}} = \frac{1}{I} \sum_{\nu} \beta_{\nu}^2 \sigma_{\nu}^{(n)}(\epsilon_i, \epsilon_j, \theta_j) \end{aligned} \quad (6)$$

Moreover corresponding to the far right of (6) it follows from (3):

$$\left(\sigma_{if\nu}^{(n)}(\epsilon_i, \epsilon'_{f\nu}) \right)_{\text{DWBA}} = \beta_{\nu}^2 \sigma_{if\nu}^{(n)}(\epsilon_i, \epsilon'_{f\nu}) \quad (7)$$

which corresponds to the structure of (1) - (1b) with the definition

$$\sigma_{if\nu}^{(n)}(\epsilon_i, \epsilon'_{f\nu}) = \int d\Omega \sigma_{\nu}^{(n)}(\epsilon_i, \epsilon'_{f\nu}, \theta) \quad (8)$$

The integrand on the right of (8) is given by (1a).

Equation (7) inserted into (4) yields:

$$\lim_{I \rightarrow I} \frac{1}{I} \sum_{\epsilon'_{f\nu}=\epsilon_j-1/2}^{\epsilon_j+1/2} \beta_{\nu}^2 \sigma_{if\nu}^{(n)}(\epsilon_i, \epsilon'_{f\nu}) = \frac{1}{I} \int_{\epsilon_j-1/2}^{\epsilon_j+1/2} \left(\frac{d\sigma_i^{(n)}(\epsilon_i, \epsilon')}{d\epsilon'} \right)_{n=n_0=3}^{\text{GDH}} d\epsilon' \quad (9)$$

We now take into consideration that the cross section fluctuations with the secondary energy of the inelastic scattering cross sections are predominately given by β_v^2 . Then the slowly varying function (8) can be considered constant within the intervals I and I in (9) according to

$$\sigma_{if_v}^{(n)}(\epsilon_i, \epsilon_{f_v}) \approx \sigma_{ij}^{(n)}(\epsilon_i, \epsilon_j) \quad \text{vcl; } \hat{I} \quad (10)$$

By inserting (10) into (9) we then obtain

$$\frac{1}{\hat{I}} \left(\sum_{\text{vcl}} \beta_v^2 \right) \sigma_{ij}^{(n)}(\epsilon_i, \epsilon_j) = \left(\frac{d\sigma_{ij}^{(n)}(\epsilon_i, \epsilon_j)}{d\epsilon_j} \right)_{n=n_0=3}^{\text{GDH}} \quad (11)$$

and (11) inserting into the far right of (6) yields:

$$\left(\frac{d^2\sigma_{ij}^{(n)}(\epsilon_i, \epsilon_j, \theta_j)}{d\epsilon_j d\Omega_j} \right)_{\text{DWBA}} = \frac{\sum_{\text{vcl}} \beta_v^2 \sigma_{ij}^{(n)}(\epsilon_i, \epsilon_j, \theta_j)}{\left(\sum_{\text{vcl}} \beta_v^2 \right) \sigma_{ij}^{(n)}(\epsilon_i, \epsilon_j)} \left(\frac{d\sigma_{ij}^{(n)}(\epsilon_i, \epsilon_j)}{d\epsilon_j} \right)_{n=n_0=3}^{\text{GDH}} \quad (12)$$

If in the intervals I and \hat{I} only one angular momentum $l_v = \hat{l}$ is contained then (12) reduces to:

$$\left(\frac{d^2\sigma_{ij}^{(n)}(\epsilon_i, \epsilon_j, \theta_j)}{d\epsilon_j d\Omega_j} \right)_{\text{DWBA}} = \frac{\sigma_{\hat{l}}^{(n)}(\epsilon_i, \epsilon_j, \theta_j)}{\sigma_{ij}^{(n)}(\epsilon_i, \epsilon_j)} \left(\frac{d\sigma_{ij}^{(n)}(\epsilon_i, \epsilon_j)}{d\epsilon_j} \right)_{n=n_0=3}^{\text{GDH}} \quad (13)$$

Equation (12) and Equation (13) both fulfill the following relation:

$$\int \left(\frac{d^2\sigma_{ij}^{(n)}(\epsilon_i, \epsilon_j, \theta_j)}{d\epsilon_j d\Omega_j} \right)_{\text{DWBA}} d\Omega_j = \left(\frac{d\sigma_{ij}^{(n)}(\epsilon_i, \epsilon_j)}{d\epsilon_j} \right)_{n=n_0=3}^{\text{GDH}} \quad (14)$$

This conclusion is obtained if attention is paid to the definition of equation (8).

5. SIMPLIFIED DWBA-APPROACH ACCORDING TO KROMINGA AND MCCARTHY

On the right hand sides of the expressions (12) and (13) only the first factor depends of the scattering angle. Any DWBA-approach based on the DWBA-expressions (1) - (1b) may be inserted into this factor. For the sake of simplic-

ity and transparency we introduce here the simplified DWBA-approach of Kromminga and McCarthy²²⁾ which is obtained by introducing into (1) - (1b) as an approximation of the optical model wave function the following 2-parameter Ansatz:

$$X^{(n)\pm}(\underline{k}, \underline{r}) = e^{i(\underline{k}, \underline{r})} \left[e^{\mp \frac{\gamma}{kr}(\underline{k}, \underline{r})} + a \delta\left(\pm \frac{k}{k} R_0 - \underline{r}\right) \right] \quad (15)$$

with

$$k = \frac{\sqrt{2m\epsilon^1}}{\hbar} \quad (16)$$

In (15) the first term in the bracket is caused by the imaginary part of the optical model according to

$$\gamma = \frac{2m}{\hbar} R_0 \frac{W}{2 \sqrt{\epsilon_i - V}} \quad (17)$$

where (16) is approximated by the assumption of a square well potential $U^{(n)} = V + iW$ whilst by the second term in the bracket of (15) the focus effect is taken into account. By inserting (15) into the DWBA-equations (1) - (1b) we obtain with the trapezoid potential as the most simple choice for $U^{(n)}(r)$ according to:

$$\frac{\partial U^{(n)}(r)}{\partial r} = \begin{cases} 0 & \text{für } 0 < r < R_0 - \frac{t}{2} & \text{Bereich I} \\ \frac{U_0^{(n)}}{t} & \text{für } R_0 - \frac{t}{2} < r < R_0 + \frac{t}{2} & \text{Bereich II} \\ 0 & \text{für } R_0 + \frac{t}{2} < r & \text{Bereich III} \end{cases} \quad (18)$$

with the finite surface thickness t and the potential depth U_0 , where (18) has the consequence that only the surface region of the nucleus of thickness t contributes to the integration in the expression (1a) with the substitutions (15) - (18). Thus (15)-(18) inserted into (1) - (1b) yields for our simplified DWBA - approach the result:

$$\frac{1}{2l_v+1} \sum_{m_v} \left| \left| \right. \right|^2 = \left| \frac{U_0}{t} \right|^2 \cdot \frac{1}{(4\pi)^2} \left\{ \left| f_1 \right|^2 \cdot P_{l_v} \left(\frac{\xi_v, \xi_v^*}{\left| \xi_v \right|^2} \right) + \left| f_2 \right|^2 + \left| f_3 \right|^2 + \right. \\ \left. + 2 \operatorname{Re} \left[f_1 f_2^* \cdot P_{l_v} \left(\frac{\xi_v, k_i / \xi_v k_i}{\left| \xi_v \right|^2} \right) + f_1 f_3^* P_{l_v} \left(\frac{-\xi_v, k_{fv} / \xi_v k_{fv}}{\left| \xi_v \right|^2} \right) \right. \right. \\ \left. \left. + f_1 f_3 \cdot P_{l_v} (-\cos \theta) \right] \right\} \quad (19)$$

In (19) the f_1 , f_2 , and f_3 are functions which are given by the following expressions:

$$f_1 = 4\pi(i)^{l_v} \int_{R_0 - \frac{t}{2}}^{R_0 + \frac{t}{2}} j_{l_v}(\xi_v r) r^2 dr = \\ \approx 4\pi(i)^{l_v} \frac{1}{3} \left\{ \left(R_0 + \frac{t}{2} \right)^3 - \left(R_0 - \frac{t}{2} \right)^3 \right\} j_{l_v}(\xi_v R_0) = 4\pi(i)^{l_v} t \left(R_0^2 + \frac{t^2}{12} \right) j_{l_v}(\xi_v R_0) \quad (20)$$

$$f_2 = a R_0^2 e^{i(k_i - k_{fv} \cos \theta) R_0 + \gamma \cos \theta}$$

$$f_3 = a R_0^2 e^{i(k_{fv} - k_i \cos \theta) R_0 + \gamma \cos \theta}$$

In order to be able to calculate f_1 we introduced into the integrand of (20) the value of the Besselfunction $j_{l_v}(\)$ at $r = R_0$ as a constant value. We then obtained the expressions after the last sign of equality of (20) as an approximate result for f_1 . The $P_{l_v}(\)$ in (19) are the Legendre-Polynomials. Finally we have in (19) the komplex vector

$$\xi_v = \frac{k_i}{k_i} - \frac{k_{fv}}{k_{fv}} + i \frac{\gamma}{R_0} \left(\frac{k_i}{k_i} - \frac{k_{fv}}{k_{fv}} \right) \quad (21)$$

with the komplex length

$$\xi_v = \sqrt{(\xi_v, \xi_v)} = \\ = \sqrt{k_i^2 + k_{fv}^2 - 2 k_i k_{fv} \cos \theta - 2 \frac{\gamma^2}{R_0^2} (1 - \cos \theta) + 2 i \frac{\gamma}{R_0} (k_i + k_{fv}) (1 - \cos \theta)}$$

6. RESULTS AND COMPARISONS

Now the GDH yields for the present only angle integrated cross sections as shown in Fig. 1. Therefore first attempts already have been made to attach an angular distribution to the GDH (see^{5,6,23,24}) and³¹⁾). Now the concept of these attempts can be extended by means of the above developed method. In order to proceed this way we make use of the GDH-results of Fig. 1 where the contributions of the excitation steps with $n > 3$ are shown separated. This representation has been presented by Bahm^{24,31)}. Almost only the $n_0 = 3$ -component shows the geometry dependent behaviour. Therefore according to Blann⁴⁾ the $n_0 = 3$ -component should in the main represent the direct processes. Consequently the angular distribution derived above should be normalized with the $n_0 = 3$ -component of the GDH (see Fig. 1), according to (12) and (13). On the right hand sides of (12) and (13) the numerator is given by (1a) with (19), (20) and (21) and the denominator by (8) also with (1a) and with (19), (20) and (21). ϵ_j is the value of the secondary energy being located in the middle of the respective interval like those intervals shown in Fig. 1 and Fig. 2 being attached through the GDH-curve of Fig. 1 and Fig. 2. If an interval of this kind is large enough such that the equation (4)* and with it also equation (14) and the already mentioned equations (12) or (13) respectively with (1a) and with (19), (20) and (21) are valid, then for such an averaging interval of the secondary energy of the inelastically scattered neutrons the angular distribution of the inelastic-neutron-scattering cross section averaged over this interval can be calculated by use of the mentioned equations, but that firstly only as far as the direct component is concerned which according to Fig. 1 is almost the only contribution to the total cross section until down to a secondary energy of roughly 9 MeV. The Figs. 3 and 4 show the results of this kind of calculations for intervals in which according to Tab. 1 2^+ -levels either exclusively or predominantly are represented. Consequently to obtain the calculated results of the Figs. 3 and 4 we inserted $l_\nu = 2$ into the precedingly mentioned equations.

Into those equations different values for the parameters a and γ are introduced. Thus to obtain Fig. 4 $a = 0$ and $\gamma = 0,9$ and to obtain Fig. 3 $a = 1,5$ fm

* see also Avrigeanu et al.²⁹⁾ and Jahn³⁰⁾.

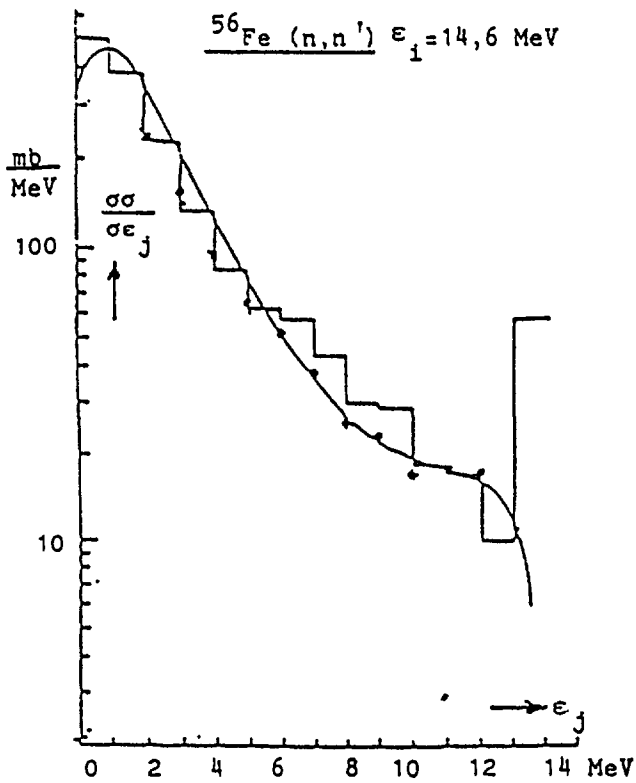


Fig. 2: Stepcurve and GDH-curve of the secondary energy dependent total inelastic scattering cross section of 14,6 MeV neutrons on ^{56}Fe (see Fig. 4)

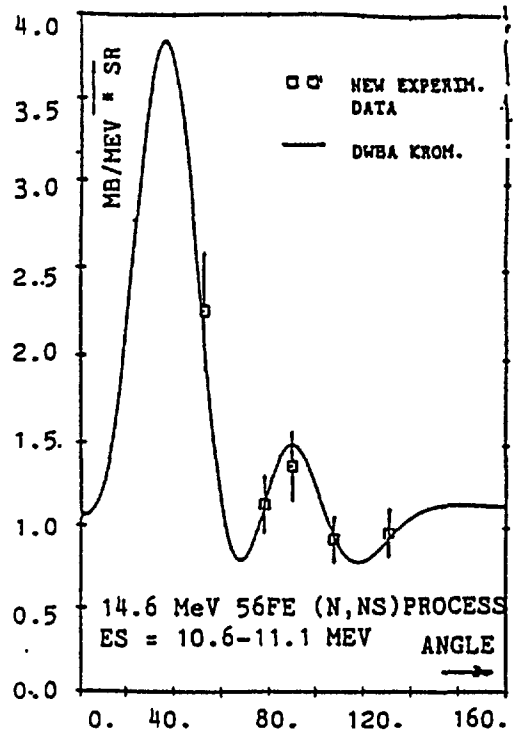


Fig. 3: Angular-distribution of the inelastic-scattering cross section of 14,6 MeV-neutrons on ^{56}Fe averaged over the interval 10,6-11,1 MeV of the secondary neutron energies. Approx. DWBA-curve with $R = 6,5 \text{ fm}$, $t = 2,4 \text{ fm}$, $a = 1,5 \text{ fm u}$, $\gamma = 0.7$

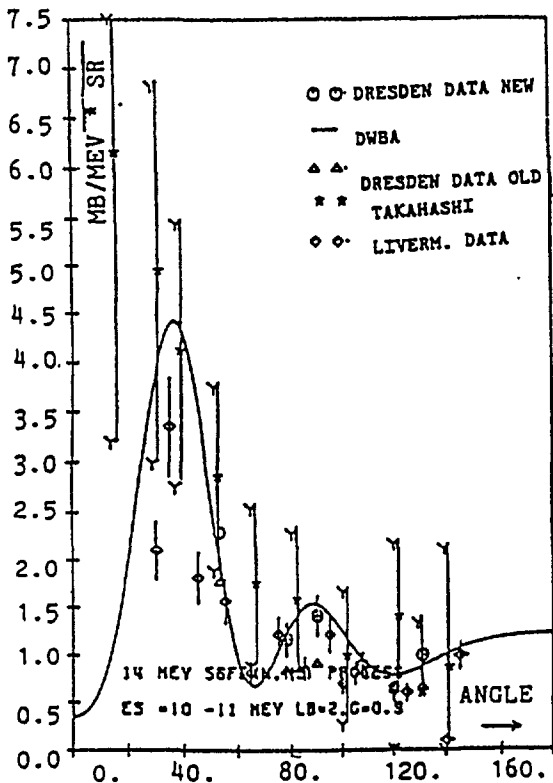


Fig. 4: As Fig. 3 but for the interval 10-11 MeV with $a=0$, $\gamma=0,9$ and with points obtained from the measured results of different experimental groups

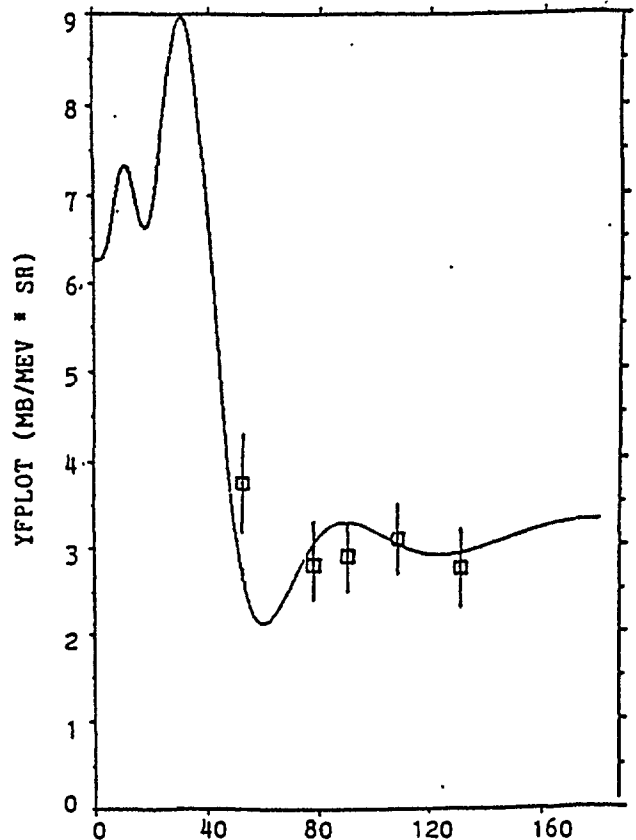


Fig. 5: As Fig. 3 but for the interval 6-7 MeV and with $l_v = 4$

and $\gamma = 0,7$ had to be inserted into equations (19), (20) and (21). This last mentioned γ -value of $\gamma = 0,7$ fits best the formula of Gl. (17) with the values of V and W for the usual optical model of roughly $V = 50$ MeV and $W = 80$ MeV inserted into Gl. (17). Additionally to the curves, calculated as explained in the preceding lines, points are drawn in the Figs. 3 to 5, which are calculated by Bahm²⁴⁾ by averaging the measured results of the respective experimental group over the respective interval of the secondary energy of the inelastically scattered neutrons for the measured scattering angles shown in the Figures. The points shown in the Figures 3 to 5 are obtained from the measured results of the Dresden group⁷⁾. They are quite well compatible with the measured results of Peterson¹⁰⁾ and Mani¹²⁾ for the proton-channels corresponding to Tab. 1. Fig. 4 shows also points which are obtained from the measured results of different groups. It can be seen that those points of Fig. 4 which are obtained from the measured results of the Dresden group⁷⁾ are in much better agreement with the curve calculated using the equations (19), (20) and (21) with the measured results for the proton-channel of Peterson¹⁰⁾ and Mani¹²⁾ as shown in Tab. 1 than the points which are obtained from the other experimental groups.

In order to obtain additional results for the inelastic-scattering cross section of the 14,6 MeV neutrons we consider a region of secondary neutron energies which consist of quite lower secondary neutron energy values than those of Figs. 3 - 4. We select as such a region of lower secondary neutron energies the interval of 6 - 7 MeV which joins the upper limit of the excitation energies of the target nucleus of Tab. 1. Since in this region in the main $l_\nu = 4$ -levels are to be found we insert $l_\nu = 4$ into the expressions (19), (20), (21), (12) and (13) for our angular dependent average cross-section calculations. Moreover we neglect the $n > 3$ precompound components since they yield a contribution of not more than 10 % within the considered interval of secondary neutron energy of 6 - 7 MeV. Finally we add as the compound component the evaporation component shown in Fig. 1 averaged over this interval, whereas the contribution of its angular distribution is assumed to be isotropic. The result as presented in Fig. 5 shows an agreement with the points obtained from the measured results of the Dresden group which is quite satisfactory*. This is also in

* The small angle region still has to be improved.

agreement with the results of an Obninsk group²⁶⁾ which show that the secondary energy dependent angle integrated cross-section for inelastic scattering of 14,6 MeV neutrons on ^{52}Cr can quite well be reproduced by only an addition of the compound plus the direct component without taking into account a precompound contribution. Obviously this neglecting of any precompound component for the sake of reproducing the measured inelastic scattering cross-sections of 14,6 MeV neutrons by theoretical calculations including only the direct plus compound contributions should be valid for a whole group of neighbouring nuclei of structural materials as for instance for ^{51}V till ^{65}Cu provided the direct component is properly averaged.

7. SUMMARY

In this paper a method is described to reduce the uncertainties and inaccuracies of the measured results of the inelastic-scattering cross sections of 14,6 MeV neutrons. This method consists of taking into account informations from the inelastic scattering of fast protons. Measurements of inelastic-fast-proton-scattering cross sections which are appropriate to this purpose are carried through up to now only for ^{56}Fe and for neighbouring nuclei as ^{51}V , ^{52}Cr , and ^{55}Mn . These are investigations by Peterson¹⁰⁾ and Mani¹²⁾ of which the results for ^{56}Fe are discussed and used in the present paper to supplement the partially very unaccurate and discrepant results of the inelastic-scattering cross section measurements for 14,6 MeV neutrons of the various experimental groups. The method carried through in this way in the present paper for ^{56}Fe leads to a preference of the measured results of the Dresden group⁷⁾. Consequently this preference should also be recommended with regard to the measured inelastic-scattering cross section results of 14,6 MeV neutrons on the other nuclei which are mentioned above as ^{51}V , ^{52}Cr and ^{55}Mn as well as on nuclei which are not mentioned above as for instance Co, Ni, Cu, Nb and Pb. These findings are also supported by the measured and calculated results of ref.³²⁾ In contrast to the method of the present paper the procedure of Pavlik and Vonach²⁷⁾ should be mentioned who propose a certain averaging over the measured results of the various experimental groups, while the principle of our method of the present paper is a selection with respect to the relationship between the cross section results of the inelastic neutron and proton scatter-

ing, where data of much higher quality can be obtained for the fast proton case than for the fast neutron case as pointed out in³¹⁾.

It could be indicated in the present papers as well as by the results of the Obninsk group²⁶⁾ that for structural materials as for instance at least for ^{51}V to ^{65}Cu a precompound contribution can be neglected for 14,6 MeV inelastic neutron cross sections, and only direct plus compound contributions have to be taken into account. This yields angular distributions which could be quite different from those of the systematics of Kalbach and Mann⁴⁾ or of the PRANG- or PREANG-codes^{1,28)}. The latter are derived from some precompound formalisms of which the solutions are assumed to cover the whole cross section²⁾. This is in contrast to our just mentioned finding that at least for ^{51}V to ^{65}Cu precompound contributions should be neglected for 14,6 MeV inelastic neutron cross sections and only direct plus compound contributions must be taken into account for those cases. On the other hand the systematics of Kalbach and Mann is obtained from a kind of fitting of inelastic neutron cross sections between 25 MeV and 14,6 MeV⁴⁾. However estimations of internuclear transition rates by Gadioli et al. (see Trieste Cours Contribution of²⁸⁾ and Fig. A6 in⁶⁾) show that there could occur a drastic change in the cross section behaviour at around 14,6 MeV. Thus we should obtain problems by concluding from the cross section behaviour above 14,6 MeV to that one below 14,6 MeV. The measured and calculated results of ref.³²⁾ also contradict ~~to the Kalbach-Mann-systematics.~~ Finally it should be stressed that at the high-energy tail of the secondary energy dependent inelastic-14,6 MeV neutron cross section the angular-distribution as for instance presented in this paper (see Fig. 3) and in ³²⁾ can show a predominance of the Legendre-polynomials of higher order as for instance 10 if analyzed accordingly. In contrast to that Legendre-polynomials up to order only 3 are taken into account by the users of the PREANG- or PRANG-codes or 4 of the systematics of Kalbach and Mann respectively²⁸⁾. This kind of assumption of taking into account only low order Legendre-polynomials has also been applied by Pavlik and Vonach²⁷⁾ in order to obtain their compilation. This also contradicts to the measured and calculated results of ref.³²⁾ for inelastic neutron and proton scattering cross sections.

8. REFERENCES

1. Gruppelaar, H. and Akkermans, I.M., ECN-84, June 1980.
2. Mantzouranis, G., Weidenmüller, H.A., Agassi, B., Z. Physik A276, 145 (1976).
3. Young, P.G. and Arthur, E.D.: GNASH: A Preequilibrium Statistical Nuclear Model Code for Calculations of Cross-Sections and Emission Spectra, Los Alamos report, LA-6947 (1977), about the many applications, Knoxville Conference 1979, Antwerp Conference 1982, Phys. Rev. C16 (1977), 1792.
4. Kalbach, C. PRECO-D2: Program for calculating pre-equilibrium and direct reaction double differential cross sections, Los Alamos National Laboratory Report LA-10248-MS.
5. Broeders, I., Fischer, U., Jahn, H., Wiegner, E., Contribution to the "International Nuclear Model and Code Comparison on Pre-Equilibrium Effects" organized by the NEA DATA BANK 1983/84, Gif-sur-Yvette, France, NEANDC-204 "U", INDC(NEA)6, NEWS LETTER No. 32.
6. Jahn, H., Critical Review of precompound models with consideration of the contribution to the "International Nuclear Model and Code Comparison on Pre-equilibrium Effects", organised by the NEA Data Bank 1983/84, KfK-3646, August 1984.
7. Hermsdorf, D., Meister, A., Sassonov, S., Seeliger, D., Seidel, V. and Shahin, F., Kernenergie 17, 259 (1974) ZfK-277 U.
8. Takahashi, A. et al., Double differential neutron emission cross sections, Numerical tables and figures (1983), A-83-01, Oktavian report, Osaka University, Japan.
9. Sal'nikov, O.A., Inelastic scattering of neutrons, translated by IAEA, INDC(CCP)-233/L, June 1984.
10. Peterson, R.J., An. of Phys. 53, 40 (1969).
11. Kammerdiener, J.L. Report UCRL-51232 (1972).
12. Mani, G.S., Nucl. Phys. A165, 225 (1971).
13. Blokhin, A.I., Ignatyuk, A.V., Lunev, V.P., Pronyaev, V.G., in Materials of the Fourth Kiev Conf. on Neutron Physics, Part II, p. 131, 1977
Blokhin, A.I., Pronyaev, V.G., Yad. Fiz. 30, 1258-1269 (November 1976)
Sov. J. Nucl. Phys. 30 (5), Nov. 1979, Izv. A. N. SSR seriya fiz. 39, 2144 (1975).

14. Kinney, W.E., and Perey, F.G., ORNL-4515 (1970).
15. Penny, S.K. and Kinney, W.E., ORNL-4617 (1971), (ENDF-139).
16. Fu, C.Y., Proceedings of the Conference on Nuclear Cross Sections and Technology, Washington, D.C., March 3 - 7, 1975, 328.
17. Hansen, I.F., Anderson, I.D., Brown, P.S., Howerton, R.I., Kammerdiener, I.L., Logan, C.M., Plechaty, E.F. and Wong, C., Nucl. Sci. Eng. 51, 278 (1973).
18. Satchler, G.R., Nucl. Phys. 55, 1, (1964).
19. Lane, A.M., "Nuclear Theory", W.A. Benjamin Inc. 1964, New York - Amsterdam.
20. Lewis, M.B., Phys. Rev. C9 (1974), 1978.
21. McCarthy, I.E. and Pursey, D.L., "Introduction to Nuclear Theory", John Wiley & Sons, Inc. 1986, New York - Amsterdam.
22. Kromminga, A.J. and McCarthy, I.E., Nucl. 31, 678 (1962), McCarthy, I.E. "Introduction to Nuclear Theorie", John Wiley & Sons, Inc. 1968, New York - Amsterdam.
23. Jahn, H., Broeders, C., Broeders, I., ICTP, Trieste, Jan./Feb. 1978, IAEA-SMR and Proc. Int. Conf. on Nucl. Reaction Mechanism, Varenna, June 13 - 17, 1977, p. 185.
24. Bahm, E., Material zur Karlsruher Diplomarbeit (1985).
25. Blann, M., Ann. Rev. Nucl. Sci. 25, 123 (1975); Nucl. Phys. A213, 570 (1973); Jahn, H. in Nuclear Data Evaluation, Trieste, 1975/76, IAEA-190, Vol. II, p. 315.
26. Simakov, S.P., Lychagin, A.A., Androsenko, A.A., Androsenko, P.A., Zhuravlev, B.V., Zelenekij, A.B., Lunev, V.P., Salnikov, O.A., V. Intern. Symp. on Nucl. Induced Reactions, Smolenic, 1988.
27. Pavlik, A. und Vonach, H., Evaluation of the Secondary Neutron Spectra for the Interaction of 14.1 MeV Neutrons with Cr, Fe, Ni, Cu, Nb, Mo, Ta, W, Pb and Bi, presented at the EFF Evaluators' Meeting Petten, March 1987 by H. Vonach.
28. Gruppelaar, H., Nagel, P., International Nuclear Model and Coe Comparison on Pre-Equilibrium Effects, Newsletter of the NEA Data Bank, No. 32, September 1985, NEANDC-204 "U"; INDC(NEA) 6.
29. Avrigeanu, M., Bucurescu, D., Ivescu, M., Semenescu, G. and Avrigeanu, V., J. Phys. 6: Nucl. Part. Phys. 15 (1989), L241-L247; printed in the UK.

30. Jahn, H., 1978 Proc. Int. Conf. on Neutron Physics and Nuclear Data for Reactors and other Applied Purposes, Harwell, September 1978, p. 502.
31. Bahm, E., and Jahn, H., INDC(NDS)-214/IJ.
32. Mellema, S., Finlay, R.W. and Dietrich, F.S., Phys. Rev. C33 481 (1986).

RECENT DEVELOPMENTS IN THE THEORY OF NUCLEAR LEVEL DENSITIES

A.M. Anzaldo Meneses
Institut für Theoretische Physik
Universität Karlsruhe. D-7500 Karlsruhe
Federal Republic of Germany.

Abstract:

We present here an alternative approach to obtain a better description of nuclear level density, its shell effects and their energy dependency. Our method is statistical, is based on analytical number theory, and considers a system of neutrons and protons in a given single particle spectrum as usual.

1. Introduction.

This work was motivated by the original work of H.A. Bethe (1936/37), N. Bohr (1936), C. Van Lier and G.E. Uhlenbeck (1937), S. Goudsmit (1937) and others over 50 years ago. These authors obtained a formula which showed with very simple analytical relations the most important behaviour of the level density, parametrized by means of quantities with a clear physical meaning. No parameter was introduced in an ad-hoc way to reproduce experimental results. The connection to number theoretical problems was also known. Nevertheless, their results are only a crude approximation which needs to be implemented.

By introducing the shell structure into the single particle spectra, we obtain here new results expressed with simple formulas using as guide calculations from modern analytic number theory (see for example G.E. Andrews, "The Theory of Partitions", Addison-Wesley Publishing Company, London, 1976). In this way it becomes easy to recognize the relevant mathematical quantities which must be related to the physical parameters.

We succeed here to obtain an analytical description throughout, such that only a minimum of numerical computer calculations is needed to carry out the comparison with the experimental results. During the last 30 years, there have been many extensive numerical works under the title "microscopic calculations". But of course they are done without the existence of a consistent fundamental ("microscopic") nuclear theory. It is well known since many years that different spectra lead to the same average results for the level density, there is no unique way to fix the "correct" nuclear Hamiltonian from these considerations. Here we adopt a different point of view. We consider classes of single particle

spectra with common analytic properties. We stress the importance to recognize the most relevant parameters, which must be common to all single particle spectra, whenever they are to reproduce the experimental data. In this way we do not need to limit ourselves to a certain special kind of Hamiltonian and it is also not necessary to diagonalize it. We attempt rather to introduce nuclear structure properties in the form of well founded mathematical quantities. This approach should conduce to the study of invariants associated to heavy nuclei.

2. Starting Equations.

We sketch the method for one kind of nucleons only, the extension to any other number of distinguishable kinds is immediate. The density of excited states of a system of N particles with total energy E is given by $\rho(N,E)$ in the expression:

$$Z(\alpha,\beta) = \prod_{\nu} (1 + \exp(\alpha - \beta \epsilon_{\nu})) = \sum_{N,E} x^N y^E \rho(N,E), \quad \alpha, \beta \in \mathbb{C} \quad (1)$$

with $x=e^{\alpha}$, $y=e^{-\beta}$ and the single particle spectrum $\{\epsilon_{\nu}\}$. Thus, the objective is to obtain a simple expression for $\rho(N,E)$ valid for all energies E in a certain interval. We assume that the excitation energy $U = E - E_0$, where E_0 is the ground state energy, is not large enough to excite the lowest nucleons in the spectrum. This means that we study only "degenerated systems".

The Darwin-Fowler method consists in the evaluation of the contour integral:

$$\rho(N,E) = \frac{1}{(2\pi i)^2} \int_{-i\infty}^{i\infty} d\alpha \int_{-i\infty}^{i\infty} d\beta \exp(\ln Z(\alpha,\beta) + \beta E - \alpha N), \quad (2)$$

The power series in eq.(1) is of course only formal, because it is strongly divergent in general, but we can deform the integration path to evaluate the integrals in eq.(2) by the saddle point method. The well known result is:

$$\rho(N,E) = \frac{\exp S}{2\pi \sqrt{D}}, \quad (3)$$

where S is the "entropy" of the system:

$$S(\alpha,\beta) = \ln Z(\alpha,\beta) + \beta E - \alpha N = 2\sqrt{a(U-\delta)}, \quad (4)$$

a is the so called "a-parameter", δ an energy shift and

$$D = \det \begin{bmatrix} \partial_{\beta\beta} \ln Z & \partial_{\alpha\beta} \ln Z \\ \partial_{\alpha\beta} \ln Z & \partial_{\alpha\alpha} \ln Z \end{bmatrix}, \quad (5)$$

The saddle point is obtained solving the equations:

$$\partial_{\alpha} S(\alpha, \beta) = 0 \quad , \quad \partial_{\beta} S(\alpha, \beta) = 0 \quad , \quad (6)$$

and we must evaluate $\ln Z(\alpha, \beta)$ at the saddle point. The a -parameter, the energy shift δ and the determinant D are all energy dependent in general. From this point on our calculation departs from the usual one. Normally, see for example T.Ericson (1958), the partition function is expressed as an integral over a smooth single particle level density. Different simple Ansätze for such function lead to the well known results (see for example the review by V.S.Ramamurthy (1989)).

3. Formalism of Modern Analytic Number Theory.

We prefer to continue the use of analytic number theoretical functions. The formal series and products as those of equation (1) have a precise analytic meaning restricting the complex variables to a particular region of the complex plane.

We write:

$$\ln Z(\alpha, \beta) = \sum_{k>0} (-1)^{k+1} \frac{1}{k} e^{k\alpha} Z(k\beta) = -\frac{1}{2\pi i} \int_{c-i\infty}^{c+i\infty} dz \frac{\pi e^{\alpha z} Z(\beta z)}{z \sin(\pi z)} \quad , \quad 0 < c < 1 \quad (7)$$

where we defined the function:

$$Z(x) = \sum \exp(-x\varepsilon_n) = \text{Tr } e^{-xH} \quad , \quad \varepsilon_n > 0 \quad , \quad (8)$$

The last integral on the far right hand side of eq.(7) can be shown to be equivalent to the infinite series of that equation using the Laurent series for $1/\sin(\pi z)$ and evaluating the residues at $z=1,2,\dots$.

3a. Introduction of Dirichlet Series.

In general, series of the form

$$\sum a(n)e^{-s\lambda(n)} \quad , \quad s \in \mathbb{C} \quad , \quad \lambda(n) > 0 \quad , \quad a(n) \geq 0 \quad ,$$

are called general Dirichlet series if $\{\lambda(n)\}$ is a strictly increasing sequence of real numbers such that $\lambda(n) \rightarrow \infty$ as $n \rightarrow \infty$. Hence for $Z(x)$ the $a(n)$ give the degeneracy of the corresponding ε_n .

The series is called ordinary Dirichlet series if $\lambda(n) = \ln(n)$. We shall assume that all Dirichlet series we consider are absolutely convergent for the half-plane $s > \delta > 0$. Further we assume that they possess an analytic continuation

in the region $s > -c$, $0 < c < 1$, and that in such a region they are analytic except for a finite number of real simple poles.

The contour in eq.(7) is selected in such a way to allow the interchange of the integration and the summation. We are thus naturally lead to study the function $Z(x)$ in the complex plane. Further, if we express the other factors in the integral in a Laurent series, we recognize that the ordinary Dirichlet series:

$$D(z) = \sum \frac{1}{(\varepsilon_m)^z} = \sum \frac{a_n}{n^z} = \frac{1}{\Gamma(z)} \int_0^\infty dx x^{z-1} Z(x), \quad \varepsilon_m \neq 0, z \neq 0, \quad (9)$$

will play a central role. We have assumed that the ε_m are integer numbers, this can be done by taking a sufficiently small energy unit. The function $D(z)$ will contain all the relevant information of this problem. The most famous and simple case results from $\varepsilon_n \in \mathbb{Z}^+$ leading to the Riemann ζ -function. The integral in eq.(9) is called the Mellin transform of $Z(x)$ (see I.N.Sneddon,"The Use of Integral Transforms",McGraw-Hill Book Company,New York, 1972).

3b. Poles and Residues of the Dirichlet Series.

The function $Z(x)$ can be obtained, once we know $D(x)$ using the integral:

$$Z(x) = \frac{1}{2\pi} \int_{\sigma-i\infty}^{\sigma+i\infty} dz x^{-z} \Gamma(z) D(z), \quad x \in F \subset \mathbb{C}, \quad \sigma > 0, \quad (10)$$

where we assumed that $D(z)$ has only poles, localized to the left of the contour. For simplicity, we will further assume that these poles are simple and are localized at the points $d_0 > d_1 > \dots > d_M > 0$, d_k integer, with residues A_0, A_1 etc., (higher order poles can be easily included). We find:

$$Z(x) = \sum_0^M A_m \Gamma(d_m) x^{-d_m} + \sum_0^\infty (-1)^k x^k D(-k)/k!, \quad x \in F \subset \mathbb{C}, \quad (11)$$

This expression can be interpreted as an asymptotic series for $Z(x)$ as $x \rightarrow +0$.

From relation (11) we see that the quantities to which we have to give a physical interpretation are the residues, the position of the poles and the values at zero, and negative integers of $D(x)$ which determine the analytic structure of the infinite sum. This can be easily seen. By partial summation we notice that if :

$$\sum_{j=1}^{\mu_0} a_n \approx \sum_{m=0}^M \frac{A_m}{d_m} \mu_0^{d_m} + D(0), \quad (12)$$

then, we can approximate $D(s)$ as follows:

$$D(s) \approx \sum A_i \zeta(s - d_i + 1) = \sum A_i 2(2\pi)^{s-d_i} \sin(\pi(s-d_i+1)/2) \Gamma(d_i-s) \zeta(d_i-s), \quad (13)$$

and this means that $D(s)$ has simple poles at $s = d_i$ with residues A_i . The assumption given by eq.(12) can be interpreted on the other hand as a description of the increase of the single particle level density and expresses the total number of particles up to level μ_0 . Equation (13) gives us the analytic continuation of $D(s)$ to the left of the successive poles. Additionally, we can use eq.(13) to obtain $D(-k)$ entirely in terms of the set $\{d_i, A_i\}$. We need only to remember the values: $\zeta(0) = -1/2$, $\zeta(-2m) = 0$ and $\zeta(1-2m) = -B_m/2m$ for $m=1,2,\dots$. Note also that if we naively write $z=-1$ in eq.(9) we obtain an infinite number, the analytic continuation eq.(13) gives the correct answer. This last observation leads to the ζ -function regularization in quantum gravity (see for example S.W.Hawking (1977)).

Conversely, by a formula due to Perron (c.f. T.M.Apostol, "Introd.to Analytic Number Theory", Springer Verlag, N.Y.,1976), we know that:

$$\sum_{n \leq \mu_0}^* \frac{a_n}{n^s} = \frac{1}{2\pi i} \int_{c-i\infty}^{c+i\infty} dz D(z+s) \frac{\mu_0^z}{z}, \quad c > 0, \mu_0 > 0, \text{Re } s > \sigma_a - c,$$

where the last term in the sum must be multiplied by $1/2$ if μ is an integer. From this formula for $s=0$ and if $D(z)$ has only simple poles at d_j with residues A_j , we return to eq.(12).

3c. Expression of the Partition Function by the Poles and Residues.

We need now to solve the saddle point equations whose solution will be then parametrized by the set of constants $\{d_j, A_j\}$. But first we need to insert expression (11) for $Z(x)$ into $Z(\alpha, \beta)$ in eq.(7).

With eq.(11) we have, for a restricted kind of spectrum, a Laurent series for $Z(x)$ which allows a very simple integration of eq.(7), under the condition that the sums are well defined, at least asymptotically.

The integration in eq.(7) has now three different contributions:

- a) The pole at $z=0$ with terms of different multiplicities, resulting from the poles of $D(x)$.
- b) The simple poles of $1/\sin(\pi z)$ for $z < 0$ integer.
- c) The singularities from the function given by the infinite series in eq.(11) with coefficients $D(-k)$.

Let us write these contributions separately as:

$$\ln Z(\alpha, \beta) = I_a + I_b + I_c, \quad (14)$$

We evaluate them now further. First we have from eqs.(7) and (11), expanding $1/\sin x$ in a Laurent series:

$$I_a = \frac{\pi}{2i} \int_{C_0} dz e^{\alpha z} \left(\sum_0^n A_m \Gamma(d_m) z^{-d_m} \beta^{-d_m} + \sum_0^\infty (-1)^{-k} (z\beta)^k D(-k)/k! \right) \cdot \\ \cdot \left[\frac{1}{\pi^2 z^2} + \frac{1}{6} + \frac{7}{360} (\pi z)^2 + \dots + \frac{2(2^{2j}-2-1)}{(2j)!} (\pi z)^{2j-2} B_j + \dots \right], \quad (15)$$

where C_0 is a small contour enclosing the origin and we have expressed the regular part of the cosecant by a power series. The B_j are the Bernoulli numbers. We find after integration:

$$I_a = \pi^2 \sum A_m \Gamma(d_m) \beta^{-d_m} \left[\frac{\alpha^{d_m+1}}{(d_m+1)! \pi^2} + \frac{\alpha^{d_m-1}}{(d_m-1)! 6} + \dots + \frac{2(2^{2j}-2-1) \pi^{2j-2} \alpha^{d_j-2j+1} B_j}{(2j)! (d_j-2j+1)!} \right. \\ \left. + \dots \right] + \alpha D(0) - \beta D(-1), \quad (16)$$

The sum in the bracket is finite and its last term is of order zero in α if d_m is odd and is of order one in α if d_m is even.

For the second integral around the negative integers we obtain from eq.(7), shifting the contour to the left:

$$I_b = \ln Z(-\alpha, -\beta), \quad (17)$$

We shall disregard this term since we consider systems for which α is large. Nevertheless, let us mention that this term is very important for a another reason. It reflects important properties associated with modular forms (see for example H.Rademacher, "Topics in Analytic Number Theory", Springer-Verlag, N.Y., 1973).

Finally, for the last integral we need a similar estimation as for the first case. Since we evaluate the integral in eq.(7) over the imaginary axis (without the origin), we need to know the behaviour of $Z(s+it)$ for $s \rightarrow +0$ and fixed $|t| > 0$. Again, using partial summation and the assumption given by eq.(12) we find:

$$Z(x) \approx \sum \frac{A_k}{d_k} \sum_{n=1}^\infty d_k^{-1} e^{-xn} = \sum \frac{A_k}{d_k} \Gamma(d_k) \sum_{n=-\infty}^\infty \frac{1}{(x+2\pi in)^{d_k}}, \quad d_k = 1, \dots; \quad (18)$$

we see clearly that this function will have for $|\text{Im } x| > 0$ poles of order d_k at $x = \pm 2\pi ni$, $n \neq 0$. We obtain from eqs.(7) and (18):

$$I_c = \sum \frac{A_k \pi}{d_k \beta^{d_k}} \sum_{\substack{n=-\infty \\ n \neq 0}}^{\infty} \left[\frac{e^{\alpha z}}{z \sin(\pi z)} \right]_{z=2\pi ni/\beta}^{(d_k-1)}, \quad (19)$$

where (d_k-1) denotes the (d_k-1) -th derivative and is to be evaluated at $2\pi ni/\beta$.

From eq.(19) we recognize an oscillatory behaviour as function of the "chemical potential" $\mu = \alpha/\beta$ and the "temperature" $1/\beta$. This contribution leads to the energy dependent shell effects which will allow a better description as that given in the current formulae for nuclear level densities.

The saddle point equations can now be readily written using the two contributions for $\ln Z(\alpha, \beta)$ given by equations (16) and (19). The parameter set $\{d_j, A_k\}$ could be selected for protons in a different way as for neutrons.

3d. Explicit Expressions for the Most Relevant Sums.

The partial derivation with respect to β of eq.(16) leads to an "asymptotic" series in positive powers of the chemical potential $\mu = \alpha/\beta$ and the temperature $1/\beta$ plus a constant term :

$$\partial_\beta I_a = - \sum A_m \left[\mu^{d_m+1} \frac{1}{(d_m+1)} + \mu^{d_m-1} \frac{d_m \pi^2}{6\beta^2} + \dots \right] - D(-1), \quad (20)$$

the last term is of order $-(d_m+1)$ in β . This contribution constitutes what is usually called the "smooth part" of the excitation energy. The constant term is a shift of the ground state energy. This is the proper origin of what leads to the so called "back-shifted" formulas of the literature of nuclear level densities. On the other hand, this constant is intimately related to the "dimensions" of the modular forms mentioned after eq.(17).

To interpret the coefficients appearing in eq.(20) we extend the expression (12) somewhat using the formula of Perron and write:

$$\sum n^\kappa a_n \approx \sum \frac{A_m}{(d_m+\kappa)} \mu^{d_m+\kappa} + D(-\kappa), \quad \kappa \text{ positive integer}, \quad (21)$$

For $\kappa=1$ we recognize the first order term of eq.(20). Physically, this is an estimation of the ground state energy for μ equal to the Fermi level, denoted by μ_0 , since a_n is the degeneracy of the level n and we add the corresponding energies up to level μ_0 . For $\kappa=0$ we obtain the number of particles N , as explained before, if $\mu = \mu_0$. Therefore it is natural to define the partial

derivative of N with respect to μ_0 as the "smooth" (or asymptotic) single particle level density:

$$g(\mu) = \sum A_m \mu^{d_m-1} + \sum D(-\kappa) \delta^{(\kappa)}(\mu)/k! , \quad (22)$$

expressed only in terms of the residues and the poles of the Dirichlet series associated with the spectrum. The second sum is added to obtain formally, after integration, eq.(21).

Now we can express all the coefficients of powers of $1/\beta$ by $g(\alpha/\beta)$ and its derivatives, for example:

$$\sum A_m d_m \mu^{d_m-1} = g(\mu) + g'(\mu)\mu ,$$

is the coefficient of $1/\beta^2$ in eq.(20).

The partial derivation of I_a with respect to α is:

$$\partial_\alpha I_a = \sum A_m \left[\mu^{d_m} \frac{1}{d_m} + \mu^{d_m-2} \frac{(d_m-1)\pi^2}{6\beta^2} + \dots \right] + D(0) , \quad (23)$$

where again we can express all coefficients in terms of $g(\alpha/\beta)$ and its derivatives.

If we consider only the contributions given by eqs.(20) and (21) to the saddle point eqs.(6) we obtain a result valid for large excitation energies but without energy dependent shell corrections. Nevertheless, also in such a situation we have a good explanation for the constant shiftings in the excitation energy dependency. We find easily:

$$U + (E_0 - \tilde{E}_0) \approx \frac{\pi^2}{6\beta^2} \sum A_m \mu_0^{d_m-1} ,$$

where U is the excitation energy , E_0 is the ground state energy and \tilde{E}_0 is its estimation given by eq.(21) for $\kappa=1$. In this crude approximation we have disregarded all irregularities of the spectra. Thus, for example the chemical potential μ was approximated by the Fermi level μ_0 . The following calculations will remove these restrictions.

To write down the contributions which lead to the shell effects we introduce the following sums to simplify the notation:

$$\Sigma_0(\mu, t) = \sum_{-\infty}^{\infty} \frac{\sin(2\pi n \mu)}{2\pi n^2 \sinh(2\pi^2 n t)} , \quad t=1/\beta, \quad (24)$$

and its derivatives:

$$\partial_{\mu}\Sigma_0 = \Sigma_1 ; \quad \partial_t\Sigma_0 = -\pi\Sigma_2 ; \quad \partial_{\mu}^2\Sigma_0 = -2\pi\Sigma_3 ; \quad \partial_{t\mu}^2\Sigma_0 = -2\pi^2\Sigma_4 , \quad (25)$$

These sums are directly related with the Jacobi θ -functions (see for example E. Whittaker and G.Watson, 1927: Modern Analysis, Cambridge University Press). Thus we find from eq.(19) for I_c :

$$I_c = \sum \frac{A_k}{d_k} \left[\mu^{d_k-1} \Sigma_1 - (1-d_k)\mu^{d_k-2} \Sigma_0 - \frac{\pi}{\beta}(1-d_k)\mu^{d_k-2} \Sigma_2 \right] + O(\mu^{d_k-3}), \quad (26)$$

and after derivation we find:

$$\partial_{\beta} I_c = \sum \frac{A_k}{d_k} \mu^{d_k-1} \left[(1-d_k)2\Sigma_1 + 2\pi\mu\Sigma_3 + \frac{2\pi^2}{\beta}(2-d_k)\Sigma_4 \right] + O(\mu^{d_k-3}), \quad (27)$$

and:

$$\partial_{\alpha} I_c = \sum \frac{A_k}{\beta d_k} \mu^{d_k-2} \left[-2\pi\mu\Sigma_3 - (1-d_k)\Sigma_1 \right] + O(\mu^{d_k-3}), \quad (28)$$

With these relations we can compute the energy dependent shell corrections to the energy and the entropy for "large" temperature. Unfortunately the series are not always well defined. They have discontinuities and if $1/\beta$ is not large enough they converge only slowly.

To be able to compute the needed sums also for the cases where the temperature is not large enough or near a discontinuity we need to transform the sums in terms of $1/\beta$ into sums in terms of β . This is here possible because of the connections with the θ -function. We obtain:

$$\Sigma_0 = \frac{\beta}{3}y(y^2 - \frac{1}{4}) + \frac{\pi}{3\beta}y - \frac{2}{\beta} \sum_{m=1}^{\infty} \frac{(-1)^m \sinh(my\beta)}{m^2 \sinh(m\beta/2)}, \quad y \in (-1/2, 1/2), \quad (29)$$

where we introduced $y = \mu - [\mu]$, e.g. the chemical potential minus its integral part. For all other sums similar relations follow after derivation.

The calculations sketched above are all what we need to compute the entropy at the saddle point as expressed by equations (4) and (6). We can calculate with the given relations explicitly, in the saddle point approximation, the nuclear level density once we know the analytic properties of a given class of single particle spectra. These properties can be obtained easily using relation (12).

4. Calculations for the Single Particle Spectrum of Kahn and Rosenzweig.

To test the applicability of our results we computed the a -parameter defined in eq.(4) using a periodic spectrum first studied by P.Kahn and N.Rosenzweig (1969) and given by:

$$\varepsilon_k = (k + m(j)) \hbar\omega, \quad k \text{ integer}, \quad j=1, \dots, e; \quad \sum m(j) = 0. \quad (30)$$

where the numbers $m(j)$ give the position of level j in each shell and e is the degeneracy of the shell. The shell width is simply the difference between the largest and the smallest $m(j)$, $W=(m(e) - m(1)) \hbar\omega$ and we assume $W < \hbar\omega$, e. g. non-overlapping shells.

Since the constants $m(j)$ do not depend on k we write:

$$Z(x) = \sum_{n=1}^{\infty} \exp(-xn) \sum_{j=1}^e \exp(-xm(j)), \quad (31)$$

The Dirichlet series corresponding to eq.(31) is expressed easily using the generalized Riemann ζ -function $\zeta(s,m) = \sum (n+m)^{-s}$ which has only one simple pole at $s=1$ with residue one. Thus, here $D(s) = \sum \zeta(s,m(j))$, $A=e$, $d=1$, $D(0)=e/2$, $D(-1)=-e/12 - 1/2 \sum m(j)^2$.

The saddle-point equations lead to:

$$U \approx \frac{\pi^2 e}{6 \hbar\omega \beta^2} + E_{\text{shell}}(\tau) - E_{\text{shell}}(0), \quad (32)$$

where $\tau = 2\pi^2 / \hbar\omega \beta$ and the temperature dependent energy shell correction is:

$$E_{\text{shell}}(\tau) / \hbar\omega = -\frac{e}{2} (x-y)^2 + \sum_{j=1}^e \sum_{k=1}^{\infty} (-1)^k \tau^2 \frac{\cos(2\pi k(y-m(j))) \cosh(k\tau)}{2\pi^2 \sinh^2(k\tau)}, \quad (33)$$

where $y = \mu - [\mu] - 1/2$. For $\tau=0$ we find the well known result of Kahn and Rosenzweig, obtained using the Euler summation formula:

$$E_{\text{shell}}(0) / \hbar\omega = -\frac{e}{24} + \frac{1}{2} x e(1-x) + \sum_{j=1}^{xe} m(j) + \frac{1}{2} \sum_{j=1}^e m(j)^2, \quad (33a)$$

The temperature dependent y is now:

$$x = y + \sum_{j=1}^e \sum_{k=1}^{\infty} \frac{(-1)^k \tau \sin(2\pi k(y-m(j)))}{e\pi \sinh(k\tau)}, \quad (34)$$

For the entropy we find:

$$S \approx \frac{e\tau}{6} + \sum_{j=1}^e \sum_{k=1}^{\infty} \frac{(-1)^k \cos(2\pi k(y-m(j))) \{k\tau \coth(k\tau) - 1\}}{k \sinh(k\tau)}, \quad (35)$$

Kahn and Rosenzweig did not consider the energy dependency of the shell effects given by eq.(33). The temperature dependency of the chemical potential described by eq.(34) was also neglected by them.

It is usually argued that, for relatively large excitation energies, the Fermi level ε_F at zero temperature and the chemical potential μ are practically equal and thus μ is substituted by ε_F in all formulae. This is correct only for terms depending on powers of μ , but it is not necessarily correct for circular functions of μ , since in such case the relevant quantity is the departure of μ from the average energy spacing between shells and not the absolute value of μ . In other words, it is not always correct to substitute y by the shell filling parameter x for relatively large excitation energies. Thus to complete the set of equations that we need in our example, we need also an equation to obtain a good estimation for y when the series in eq.(34) do not converges sufficiently fast. This equation is:

$$x = - \sum_j \left[\sum_{k=1}^{\infty} \frac{(-1)^k \sinh(2\pi^2 k(y-m(j))/\tau)}{e \pi \sinh(\pi^2 k/\tau)} + \sum_j^* \left[\frac{1}{e} + \sum_{k=1}^{\infty} \frac{(-1)^k \sinh(2\pi^2 k(1-y+m(j))/\tau)}{e \sinh(\pi^2 k/\tau)} \right] \right],$$

Here, the sum Σ' runs over $-1/2 < y-m(j) < 1/2$ and the sum Σ^* runs over $1/2 < y-m(j) < 3/2$.

In our calculation we computed the a-parameter for the nuclei reported by T.von Egidy, H.Schmidt and A.Behkami (1988) at the corresponding neutron binding energies. We used the definition contained in eq.(4) for the a-parameter and of course, we considered two kinds of fermions. Thus, we added in the given equations for the excitation energy, the chemical potential and the entropy the corresponding terms for the other kind of nucleons present. The shift δ given in eq.(4) is know: $\delta = E_{\text{shell}}(\tau) - E_{\text{shell}}(0)$, for large excitation energies.

The adopted shell width was fixed for all nuclei belonging to the same shell in a harmonic oscillator type potential. Besides the shell widths and the average spacing between shells fixed by the shell model, we did not adjust any other parameter. We used only the first terms of the corresponding infinite series, depending on the convergency of the series. In figure 1, we show the results of our calculation in comparison with the experimental results compiled by v.Egidy et al. which include also former compilations of G.Rohr et al. The agreement is encouraging. In a forthcoming publication we will show more details of this calculation and the results for the nuclear level density as well as additional developments of theoretical as well as practical interest.

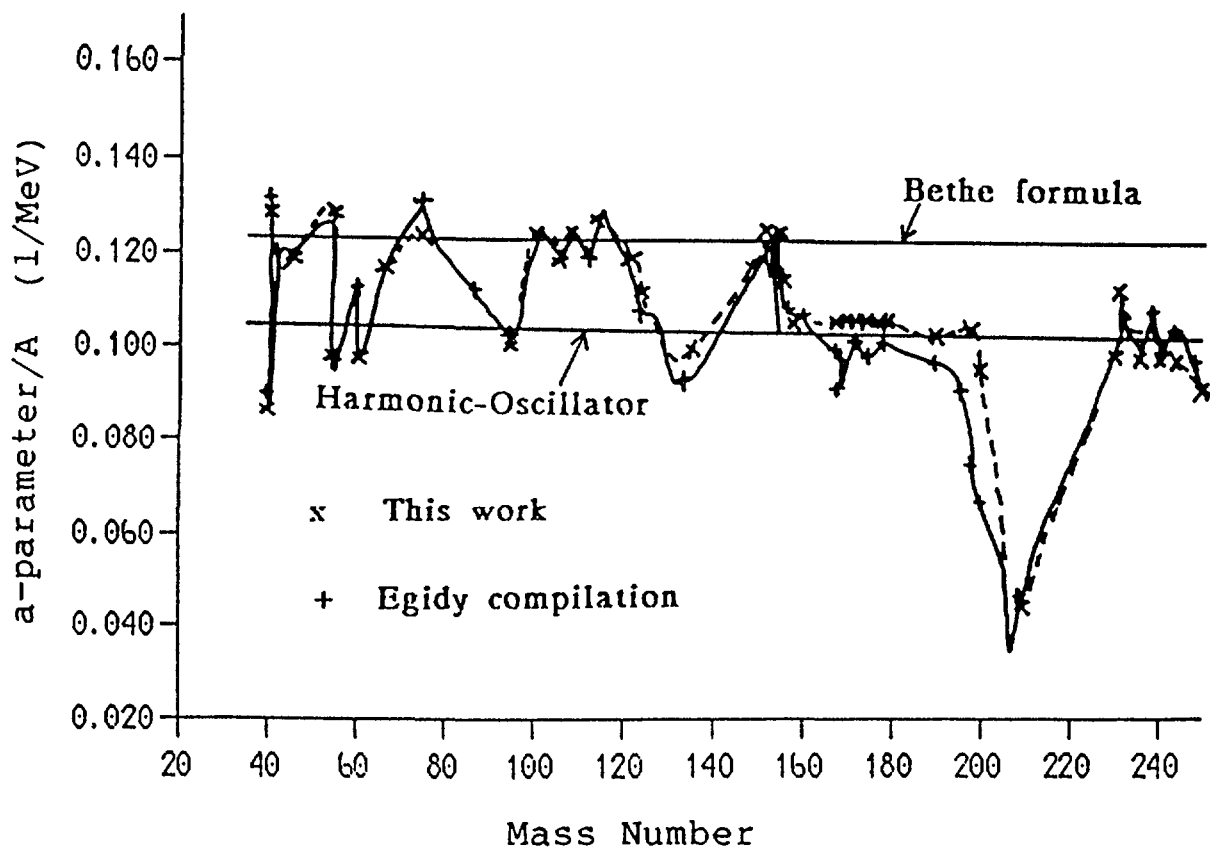


Fig. 1

5. Conclusions.

In conclusion we like to stress the following points:

- 1) We have shown a consistent method to study and include the most relevant characteristics of the adopted single particle spectra. This includes the "smooth" behaviour as well as the shell corrections and their excitation energy dependency.
- 2) Only the consideration of an energy dependent chemical potential can lead to a correct description of the shell effects in the nuclear level density. This follows from the discontinuous character of the infinite sums as a whole. Instead to take only few terms of a given series it is necessary to understand its transformation properties.
- 3) All other analytic attempts in the current literature (to our best knowledge) on nuclear level densities can be seen as particular cases of the presented method. Also those which assume a smooth single particle level density given by a power or a Fourier series.
- 4) The presented method is not only of academic interest but provides us a tool for applications as our calculations showed. The consideration of more "realistic" spectra e.g. of the Nilsson or Woods-Saxon types is also possible without difficulty. In a work to be published we will show further results.

REFERENCES

- Andrews, G.E., "The Theory of Partitions", Addison-Wesley Publishing Company, London, 1976.
- Apostol, T.M., "Intro. to Analytic Number Theory", Springer Verlag, N.Y. 1976.
- Bethe, H.A., Phys. Rev., 50 (1936) 332.
- Bohr N. and Kalckar F., Math.fys.Medd., 14 (1936/1937) 1.
- Egidy, T.von, Behkami, A. and Schmidt, H., Nucl.Phys., A454 (1986) 109.
- Egidy, T.von, Schmidt, H. and Behkami, A., Nucl.Phys., A481 (1988) 198.
- Ericson, T., Nucl.Phys., 8 (1958) 265.
- Goudsmit, S., Phys.Rev., 51(1937) 64.
- Hawking, S.W., Commun.Math.Phys., 55 (1977) 133.
- Kahn P. and Rosenzweig N., Phys. Rev., 187 (1969) 1193.
- Rademacher, H., "Topics in Analytic Number Theory", Springer Verlag, N.Y., 1973.
- Ramamurthy, V.S., in "Workshop on Applied Nuclear Theory and Nuclear Model Model Calculations", ed. by M.K.Metha and J.J.Schmidt, World Scientific Publ., Singapore 1989, pages 280-318.
- Sneddon, I.N., "The Use of Integral Transforms", McGraw-Hill, N.Y., 1972.
- Van Lier, C., Uhlenbeck, G.E., Physica, 4 (1937) 531.
- Whittaker, E. and Watson, G., "Modern Analysis", Cambridge Univ.Press, 1927.

MODELS AND THEORY FOR PRECOMPOUND
ANGULAR DISTRIBUTIONS*

M. Blann, B. A. Pohl and B. A. Remington
Lawrence Livermore National Laboratory
Livermore, CA 94550, USA

W. Scobel and M. Trabandt
I. Institut für Experimentalphysik, Universität Hamburg,
D-2000 Hamburg 50, Fed. Rep. Germany

R. C. Byrd
Los Alamos National Laboratory
Los Alamos, NM 87545, USA

C. C. Foster
Indiana University Cyclotron Facility
Indiana University
Bloomington, IN 47405, USA

R. Bonetti and C. Chiesa
Istituto de Fisica Generale Applicata
dell'Università di Milano, Italy

S. M. Grimes
Ohio University
Athens, Ohio 45701, USA

ABSTRACT

We compare angular distributions calculated by folding nucleon-nucleon scattering kernels, using the theory of Feshbach, Kerman and Koonin, and the systematics of Kalbach, with a wide range of data. The data range from (n, xn) at 14 MeV incident energy to (p, xn) at 160 MeV incident energy. The FKK theory works well with one adjustable parameter, the depth of the nucleon-nucleon interaction potential. The systematics work well when normalized to the hybrid model single differential cross section prediction. The nucleon-nucleon scattering approach seems inadequate.

*Work performed under the auspices of the U. S. Department of Energy by the Lawrence Livermore National Laboratory under contract No. W-7405-ENG-48.

1. INTRODUCTION

The purpose of this brief report is to look somewhat critically at our ability to predict precompound angular distributions. Much of the early work was focussed on data from 14 MeV incident neutron energy; these data had large uncertainties due to experimental difficulties, and were not well suited for testing our ability to predict angular distributions. More recently data sets for (p,n) reactions, spanning a very broad dynamic range of incident energies, have become available. Data on ^{90}Zr have been obtained at 25, 35, 45, 80, 120 and 160 MeV over an angular range of 0-160°. ¹⁻³ Measurements at higher energies are planned. We will use some of these data to see how well different approaches to treating angular distributions work as predictive tools. These will include formulas based on systematics,⁴ on folded nucleon-nucleon scattering kernels,⁵ and on the quantal formulation of Feshbach, Kerman and Koonin (FKK).⁶

2. COMPARISONS OF MEASURED AND CALCULATED ANGULAR DISTRIBUTIONS

In Fig. 1 we show several data sets for the $^{93}\text{Nb}(n,xn)$ angular distributions.^{5,7} These are compared with hybrid model angular distribution calculations involving nucleon-nucleon scattering kernels. The agreement with data seems reasonable, due in part to the large experimental uncertainties.

In Figs. 2-5 we show similar calculations versus data taken at incident proton energies of 25, 45, 80 and 160 MeV. For the 25 MeV incident energy (Fig. 2) for the 9 MeV exit energy one can do a parameter manipulation - called 'refraction' in this application - to force a reasonable back angle 'fit' with data. At the higher exit energy of 14 MeV, not even this parameter game works. An arbitrary isotropic (compound) component would again give the appearance of agreement over the entire range of angles. This is apparently used in some approaches, but is not consistent with statistical theory. As data from higher incident energies are analyzed, the discrepancies between both forward and backward angles becomes

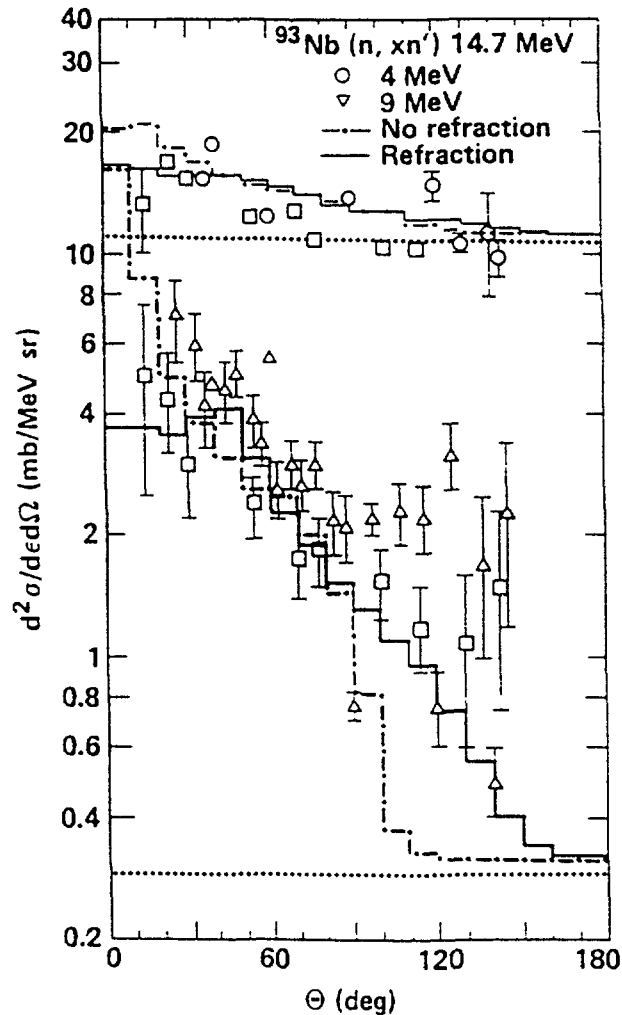


Fig. 1 Experimental and calculated angular distributions for the $^{93}\text{Nb}(n, xn)$ reaction with 14.7 MeV incident neutrons. Results are shown for 4 and 9 MeV emitted neutrons. Data (circles, squares, and triangles) are from Ref. 7. The dotted lines are the calculated equilibrium components which have been added to the histogram results. The dotted-dashed histograms are the results of the semiclassical calculation using the folded N-N scattering result described in the text. The solid histograms are the results of the same calculation but with an additional folding for "refraction" in the entrance channel as described in the text.

more evident (Figs. 3-5). In Figs 4 and 5 no 'refraction' has been used in one example using the nucleon-nucleon scattering calculation. Here the quasi-elastic peak may be seen as the first collision contribution, and the higher order collision contributions may be seen as the component with softer slope extending to higher angles. The data do not show this dichotomy; quantal effects may be expected to reduce it. Adding the 'refraction' folding to these calculated angular distributions

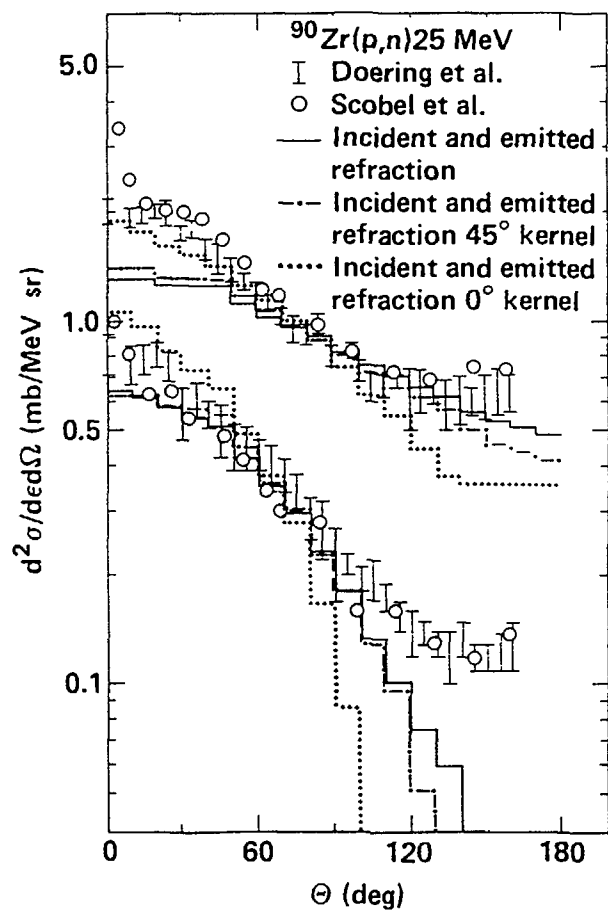


Fig. 2 Results for the $^{90}\text{Zr}(p, n)$ reaction at 25 MeV incident proton energy. Experimental results are from Ref. 1 (horizontal bars) and from Ref. 8 (circles). The data of Ref. 1 are more reliable than those of Ref. 8 at angles forward of 20° . The isotropic (dotted and dashed) components are the calculated evaporation contributions which have been added to the precompound results shown.

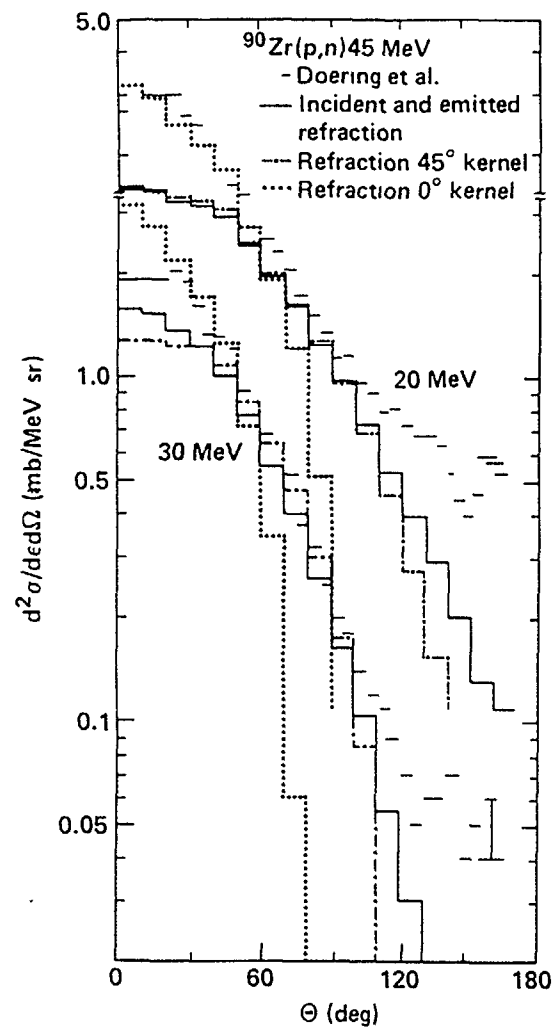


Fig. 3 As in Fig. 2 for an incident proton energy of 45 MeV. Data (horizontal bars) are from Ref. 1.

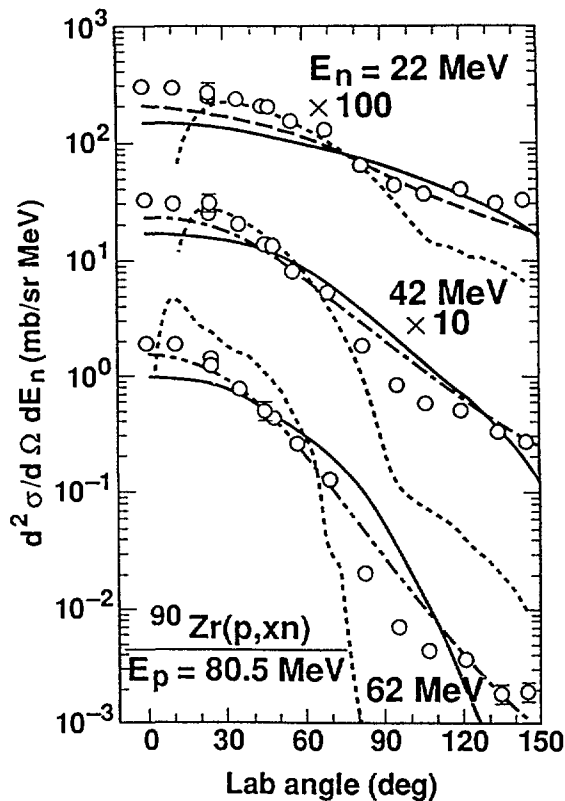


Fig. 4 Angular distributions for $^{90}\text{Zr}(p, xn)$ for 80 MeV proton energy in comparison with the normalized results of Ref. 4 (dot-dash line) and the hybrid model (dashed-short line) using a nucleon-nucleon scattering kernel. The heavy solid curve is the hybrid model with nucleon-nucleon scattering and refraction in entrance and exit channels.

will help to reduce the change in slope noted at around 90° but does not change the inability of the calculated result to fit the data, as may be seen in Figs. 4 and 5.

Kalbach⁴ has recently revised her formulation of angular distributions based on systematics. Results of this formula, normalized to the single differential cross sections predicted by the hybrid model, are shown in Figs. 4 and 5. The agreement is quite good, and the computation exceedingly fast. While there is no gain in knowledge of physics from using this approach, it is fast and it gives good results over a wide range of targets and projectile/ejectile energies.

Finally we investigate the theory of FKK in reproducing angular distributions. In Fig. 6 we show results for $^{65}\text{Cu}(p, xn)$ due to Holler et al. for 26.7 MeV incident proton energy.⁸ In Fig. 7 we show comparisons for incident energies of 120 and 160 MeV for $^{208}\text{Pb}(p, n)$ reactions. In Figs. 8 and 9 we show similar

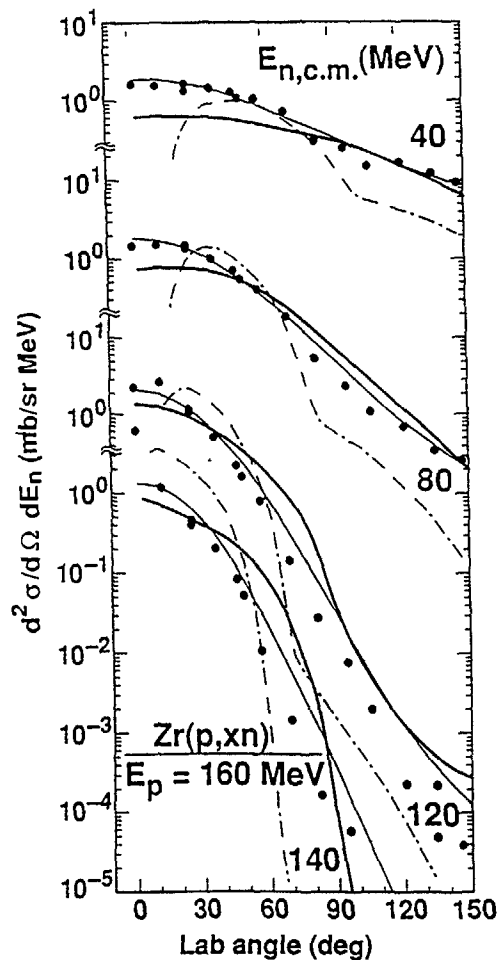


Fig. 5 Experimental (solid points), hybrid model (dashed-dot) and systematics fit (Ref. 4) for the $^{90}\text{Zr}(p, n)$ reaction at 160 MeV incident energy. The exit neutron energies from 40 to 140 MeV are indicated. The hybrid model N-N scattering result is without refraction (dot-dashed line) and with entrance and exit channel refraction. This figure is from Ref. 3.

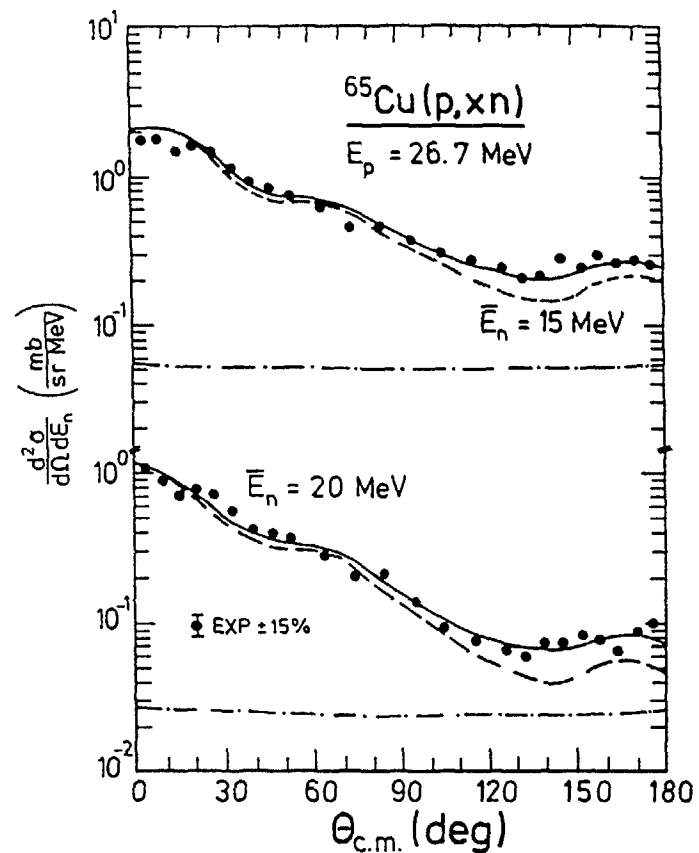


Fig. 6 Experimental and calculated angular distributions for the reaction $^{65}\text{Cu}(p, xn)$ at 26.7 MeV incident proton energy. This figure is from Ref. 8. Solid points are experimental values for 15 and 20 MeV neutron emission energies. The solid line is the result of the FKK theory summed over several scattering terms. The dashed line is the first term only.

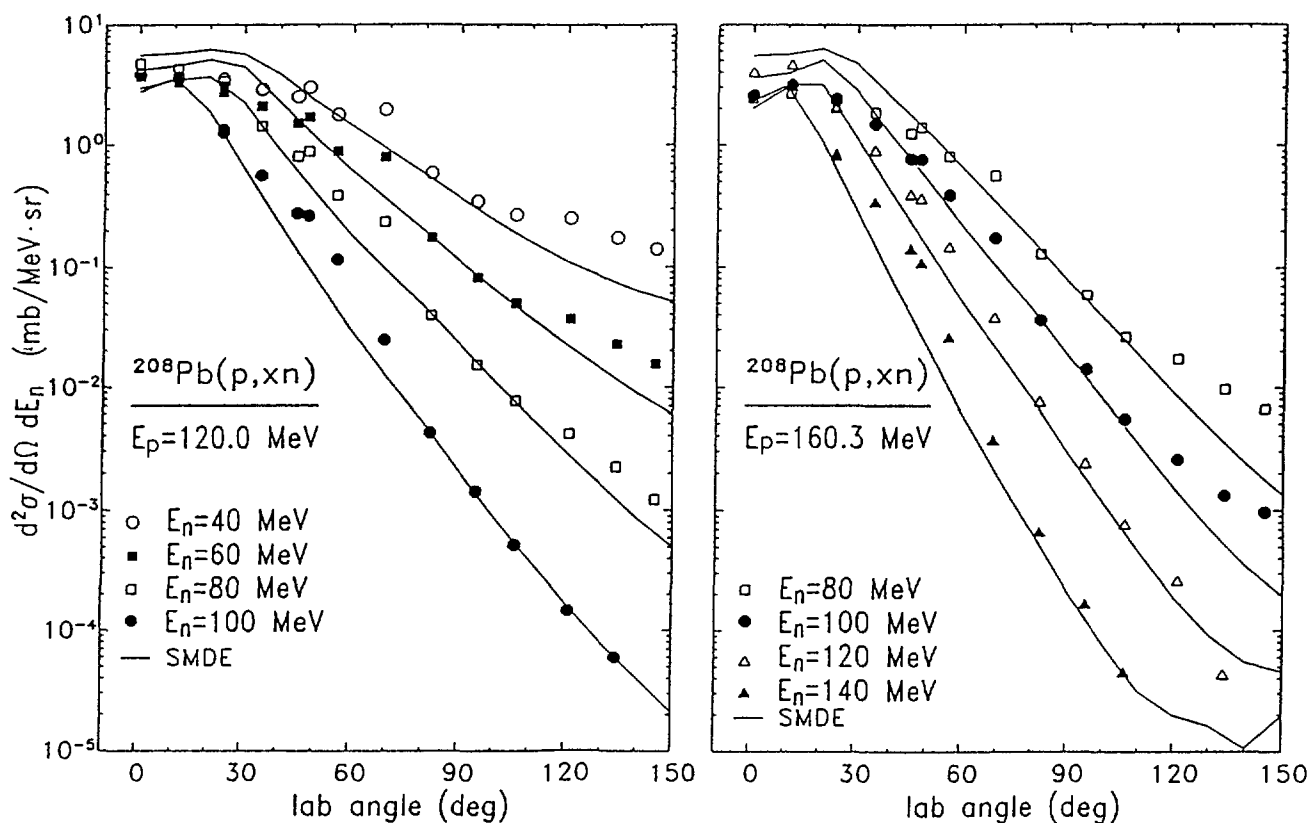


Fig. 7 Experimental angular distributions of neutrons of several c.m. energies for the reactions $p+^{208}\text{Pb}$ in comparison to SMDE calculations with $V_0 = 16$ MeV (for $E_p = 120$ MeV) and $V_0 = 12.5$ MeV (for $E_p = 160$ MeV).

comparisons for $^{90}\text{Zr}(p,xn)$ reactions at 120 and 80 MeV. The FKK theory does very well across the entire range of energies - but there is an adjustable parameter. This is the square of the nucleon-nucleon interaction potential depth, V_0^2 ; it has thus far been selected to force-fit the data. The values used for reactions on ^{90}Zr are shown in Fig. 10. These values seem to be independent of target mass, but strongly dependent on incident energy. Thus far the theory has not been predictive; perhaps Fig. 10 may be used to interpolate values necessary for V_0^2 , making this approach predictive within the range of prior measurements.

4. CONCLUSIONS

Semiclassical/exciton approaches to angular distributions may not be extrapolable with accuracy much beyond the regime of reactions of neutrons of up to 14 MeV. They probably lack an adequate treatment of the physics. The FKK theory

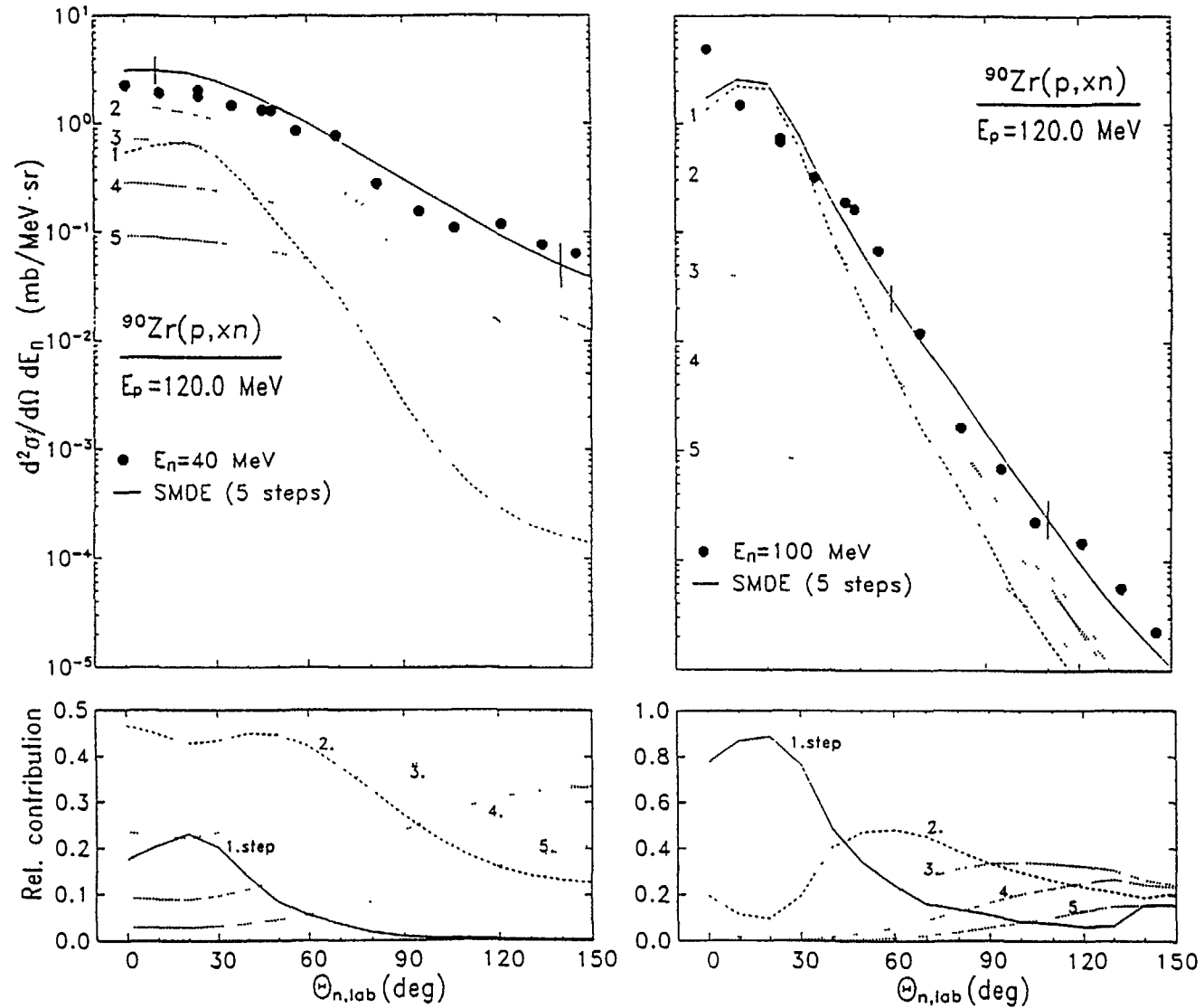


Fig. 8 Absolute (upper panels) and relative contributions of the leading 5 MSDE steps to the angular distribution of 40 and 100 MeV neutrons (c.m.) from $^{90}\text{Zr}(p, n)$ for $E_p = 120$ MeV. The calculations were performed with $V_0 = 16$ MeV; the vertical bars indicate the variation for $\Delta V_0 = \pm 1$ MeV.

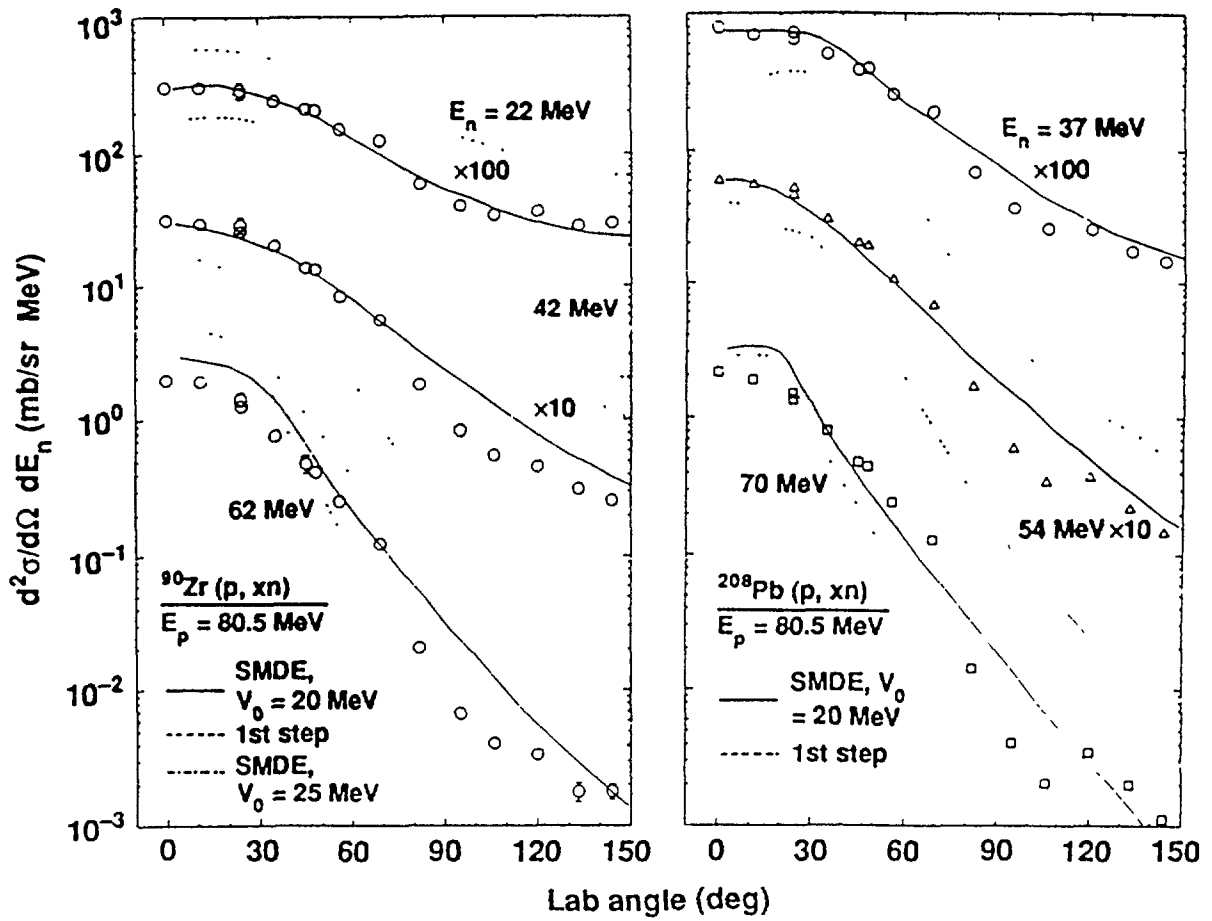


Fig. 9 As in Fig. 7 for $^{90}\text{Zn} + 80$ MeV protons.

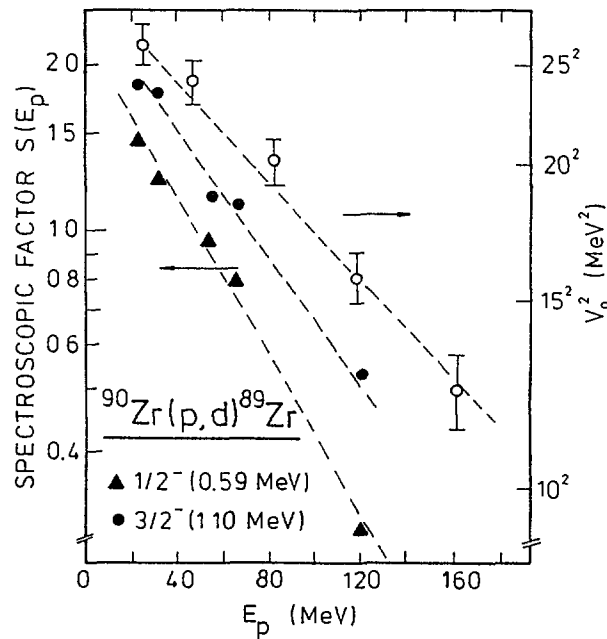


Fig. 10 MSDE best fit values V_0^2 of this work (open circles) and spectroscopic factors for the $^{90}\text{Zr}(p, d)^{89}\text{Zr}$ transition to the excited state indicated.⁹ The dashed lines are drawn to guide the eye.

offers hope of an approach containing the proper physics, but we must understand the variation of V_0^2 with incident energy. We may be able to interpolate this from Fig. 10 for energies within the range where measurements have been made.

Because the exciton model weights higher order terms more heavily than the hybrid model, a thorough investigation should be made of the N-N scattering approach within this (exciton model) formulation.

The systematics of Kalbach provide a very satisfactory means of predicting the shapes of the angular distributions. At present this may be the best approach for applied nuclear data needs.

REFERENCES

1. M. Blann, R. R. Doering, A. Galonsky, D. M. Patterson and F. E. Serr, Nucl. Phys. A257, 15 (1976).
A. Galonsky, R. R. Doering, D. M. Patterson and H. W. Bertini, Phys. Rev. C 14, 748 (1976).
2. M. Trabandt et al., Phys. Rev. C 39, 452 (1989).
3. W. Scobel et al., Phys. Rev. C (May 1990).
4. C. Kalbach, Phys. Rev. C 37, 2350 (1988).
5. M. Blann, W. Scobel and E. Plechaty, Phys. Rev. C 30, 1493 (1984).
6. H. Feshbach, A. Kerman and S. Koonin, Ann. Phys. (N.Y.) 125, 429 (1980).
7. D. Hermsdorf et al., Zentrum für Kernphysik Report ZfK-277, 1974; A. Takahashi et al., Osaka University, Oktavian Report A-83-01, 1983 (unpublished); J. L. Kammerdiener, Lawrence Livermore National Laboratory Report UCRL-51232, 1972 (unpublished).
8. Y. Holler, A. Kaminsky, R. Langhau, W. Scobel, M. Trabandt and R. Bonetti, Nucl. Phys. A442, 79 (1985).
9. R. Bonetti (private communication); R. Bonetti and L. ColliMilazzo, Workshop on Coincident Particle Emission from Continuum States, Bad Honnef, Federal Republic of Germany, 1984).

A REAL PART OF NEUTRON OPTICAL POTENTIALS CONSTRAINED BY RMFA CALCULATIONS

S. Gmuca

Institute of Physics, Slovak Academy of Sciences,
Dubravska cesta 9, CS-842 28 Bratislava, Czechoslovakia

Abstract

We test an applicability of Dirac optical model for neutron elastic scattering at low energies. Real parts of scalar and vector potentials are constrained by a relativistic mean field approach to nuclear structure. We find that by this way we are able to produce a good agreement with experimental data.

1. Introduction

In recent years there has been growing interest in using relativistic approaches in nuclear structure calculations and scattering of nucleons on nuclei. Relativistic quantum field theoretical approaches have been reviewed recently by Celenza and Shakin [1] and Serot and Walecka [2]. The success of the RIA at intermediate energy proton scattering is now well documented [3]. Nuclear optical model studies using the Dirac equation containing large canceling Lorentz scalar and Lorentz four-vector potentials have shown its superiority to the standard Schrödinger equation based phenomenology [4] at higher energies.

Contrary to these previous studies, in this work we present the results of an analysis of neutron-nucleus elastic scattering at low energies. The aim is to test some aspects of relativistic approach at this energy region. In particular, we constrain the real parts of the optical potentials by relativistic mean field calculations. To be consistent with conventional studies and to facilitate the comparison with nonrelativistic analyses we transform the

Work performed under IAEA Research Contract No. 4325/RB

Dirac equation to the Schrödinger-like one with effective central and spin-orbit potentials. The real parts of these potentials are constructed using the aforementioned relativistic fields. The imaginary part of the central potential is then taken to be of conventional surface plus volume terms. The imaginary spin-orbit potential is ignored.

The analysis presented here is made on some spin-zero nuclei at energy region 8-40 MeV. We test the usefulness of the Dirac approach and seek for a possible energy dependence of the potential parameters.

In the next section we describe essentials of the relativistic mean field approach to nuclear structure. Section 3 is devoted to the Dirac optical model and its transformation to the Schrödinger picture. In Sec. 4 we present the results of our analysis and Section 5 gives conclusions of this work.

2. Relativistic Mean Field Approach

We start with the Lagrangian density of the QHD-II theory with scalar selfinteractions [2] which reads

$$\begin{aligned}
 L(\psi, \sigma, \omega, \rho) = & \bar{\psi} \left[i\gamma_{\mu} \partial^{\mu} - (M - g_{\sigma}\sigma) - g_{\omega}\gamma_{\mu}\omega^{\mu} - g_{\rho}\gamma_{\mu}\tau \cdot \rho^{\mu} \right] \psi \\
 & + \frac{1}{2} \left[\partial_{\mu}\sigma\partial^{\mu}\sigma - m_{\sigma}^2\sigma^2 \right] - \frac{1}{3}bM(g_{\sigma}\sigma)^3 - \frac{1}{4}c(g_{\sigma}\sigma)^4 \quad (1) \\
 & - \frac{1}{4}\omega_{\mu\nu}\omega^{\mu\nu} + \frac{1}{2}m_{\omega}^2\omega_{\mu}\omega^{\mu} - \frac{1}{4}\rho_{\mu\nu}\rho^{\mu\nu} + \frac{1}{2}m_{\rho}^2\rho_{\mu}\rho^{\mu}
 \end{aligned}$$

This includes the baryon field (ψ), neutral scalar and vector meson fields (σ, ω) and the charged isovector meson field (ρ) in a renormalizable field theory.

Exact solutions of the field equations given by the Lagrangian density (1) are very complicated. Instead the corresponding Euler-Lagrange equations are usually solved by replacing the meson fields by their mean values (the so called relativistic mean field approach - RMFA).

We restrict ourselves to the spin-zero closed shell nuclei which possess the spherical symmetry. This symmetry greatly simplifies calculations. As a result we obtain the

coupled set of nonlinear differential equations which have to be solved iteratively up to the selfconsistency is reached. The details of this procedure may be found in ref. [2]. In particular, the baryon field ψ is given as a product of single-particle spinors ψ_α (α labels all relevant quantum numbers) which obey the Dirac equations

$$\left[-i\alpha \cdot \nabla + \beta(M - S(r)) + V(r) \right] \psi_\alpha = E_\alpha \psi_\alpha \quad (2)$$

where the scalar potential is simply

$$S(r) = g_\sigma \sigma(r), \quad (3)$$

while the vector potential has more complicated structure

$$V(r) = g_\omega \omega(r) + 1/2 \cdot \tau_3 g_\rho \rho(r) \quad (4)$$

The $\sigma(r)$, $\omega(r)$ and $\rho(r)$ are the scalar σ -meson field, the time-like component of the vector ω -meson field and the time-like part of uncharged component of the isovector-vector ρ -meson field, respectively. These fields obey the second order radial Klein-Gordon equations with an appropriate density as a source term.

At the end of the iterative selfconsistent procedure we obtain:

- single-particle Dirac wave functions,
- single-particle spectra,
- proton and neutron baryon and scalar densities,
- mean meson fields, etc.

These quantities may be then used in other computations which need nuclear structure information.

The Lagrangian (1) has to be considered as an effective Lagrangian and the meson masses and their couplings are to be understood as effective parameters of the theory. Now there are several parameter sets (see ref.[5] for review some of them) which are suitable for the RMFA calculations. In the course of this work we use the RMFA parameters of ref.[6] which have been obtained by fitting the charge density distribution of ^{208}Pb and have been approved also for other closed-shell nuclei.

3. Relativistic Optical Model

3.1 Dirac equation and its transformation

In most relativistic studies of nucleon scattering the Dirac equation containing large Lorentz scalar, $S(r)$, and time-like component of Lorentz four-vector potential, $V(r)$, is used [7]. These potentials are usually static, local and spherically symmetric.

The Dirac equation for nucleon scattering may be written as

$$\left[\alpha \cdot p + \beta[M + S(r)] - [E - V(r)] \right] \psi = 0 \quad (5)$$

This remembers the eq.(2) of RMFA. Now, however, the optical potentials S and V are complex quantities.

Often it is customary to eliminate the small components of the Dirac spinor in eq.(5). One then obtains, without loss of physical insights, the Schrödinger equation with central and spin-orbit potentials. This procedure gives [7]

$$U_{\text{cen}}(r) = \frac{1}{2E} \left[2EV(r) + 2MS(r) - V^2(r) + S^2(r) + \frac{3}{4A(r)} \left(\frac{\partial A}{\partial r} \right)^2 - \frac{1}{2r^2 A(r)} \frac{\partial}{\partial r} \left[r^2 \frac{\partial A}{\partial r} \right] \right] \quad (6)$$

and

$$U_{\text{so}}(r) = - \frac{1}{2EA(r)r} \frac{\partial A}{\partial r} \quad (7)$$

where

$$A(r) = \left[M + S(r) + E - V(r) \right] / (E + M) \quad (8)$$

As one can see the explicit nonlinearities and energy dependencies of the Schrödinger optical potentials U_{cen} and U_{so} do occur in this approach, even if the scalar and vector Dirac potentials S and V are energy independent. In addition, the spin-orbit potential of the conventional model arises naturally from reduction of the Dirac equation to 2-component Schrödinger form.

3.2 Construction of real parts of Dirac potentials by using RMFA fields

To utilize the results of the Sec.2 we assume that the relativistic scalar and vector potentials are given by the bound-state relativistic mean meson fields. However, since the nucleon finite-size effects are neglected in the RMFA, the potentials really entering into the Dirac equation are determined by folding over a suitable single-nucleon form factor $F(r)$. One may write

$$S_R(r) = \int dr' \cdot g_\sigma \sigma(r) \cdot F(|r-r'|) \quad (9)$$

for the real part of scalar potential, and

$$V_R(r) = \int dr' \left[g_\omega \omega(r) + 1/2 \cdot \tau_3 g_\rho \rho(r) \right] \cdot F(|r-r'|) \quad (10)$$

for the real part of vector potential.

The discussion of possible forms of the nucleon form factor F is beyond the scope of this work. The detailed form of $F(r)$ is, however, not very important, as long as the nucleon rms radius is approximated. Now it is almost commonly accepted that the nucleon rms radius (precisely, the baryon rms radius of the nucleon) should be smaller than the typical electromagnetic rms radius of the proton which is 0.85 fm.

In this work we have used the nucleon form factor of a Gaussian form

$$F(r) = \frac{1}{\pi^{3/2} t^3} \exp\{-r^2/t^2\} \quad (11)$$

with a range $t=0.56$ fm. This corresponds to the nucleon rms radius of 0.69 fm. This range parameter has been obtained by fitting the neutron elastic scattering on the ^{40}Ca nucleus at 19 MeV and has been used also for other nuclei and energies.

4. Analysis of Experimental Data

The aim of this work is to test the Dirac approach to the low-energy neutron-nucleus elastic scattering and the usefulness of the RMFA constraints on the real parts of the Dirac optical potentials.

To facilitate the comparison with previous nonrelativistic studies we have transformed the Dirac equation (5) to the Schrödinger form. The real central and spin-orbit potentials have been obtained by eqs. (6) and (7) using the folded RMFA scalar and vector potentials. These were scaled by factors λ_S and λ_V , respectively, to account for a possible energy dependence.

The effective Schrödinger central imaginary potential has been taken as a sum of conventional volume and surface terms

$$U_I(r) = \left[W_V - 4a_I W_D \frac{d}{dr} \right] \cdot f(r_I, a_I) , \quad (12)$$

where the symbols have their usual meaning. The form factor $f(r, a)$ is of the Woods-Saxon type.

The model thus contains a total of six free parameters which were varied to obtain fits to experimental neutron elastic scattering data for each energy and each target.

We considered ^{40}Ca , ^{54}Fe and ^{208}Pb targets at energies from 8 to 40 MeV.

The final values of parameters are listed in Tabs. 1-3. In Figs. 1-3 we show some representative results of neutron elastic scattering on the nuclei considered. As we see the acceptable fits to the data for all nuclei have been found. The quality of fits as measured by χ^2/N is comparable with results obtained by the conventional Schrödinger phenomenology. This indicates that the procedure used for the construction of the real parts of Dirac optical potentials is reasonable.

Our primary concern in the present paper is the behaviour of the scaling factors λ_S and λ_V . We left out, therefore, the discussion of the imaginary optical potential parameters. In Fig. 4 we show the unscaled real parts of vector and scalar potentials for the ^{40}Ca nucleus as

TABLE 1: Optical model parameters for $^{208}\text{Pb} + n$

E_n (MeV)	λ_S	λ_V	W_V (MeV)	W_D (MeV)	r_I (fm)	a_I (fm)	χ^2/N	Exp. data [Ref]
7.75	0.673	0.626	0.00	7.02	1.249	0.440	15.0	[9]
20.0	0.761	0.719	1.18	8.47	1.185	0.456	11.9	[10]
22.0	0.723	0.677	1.30	8.34	1.246	0.476	12.2	[10]
24.0	0.777	0.738	2.04	7.60	1.243	0.441	29.1	[10]
30.3	0.708	0.663	4.28	6.39	1.227	0.475	7.6	[11]
40.0	0.694	0.649	8.50	2.38	1.274	0.470	16.6	[11]

 TABLE 2: Optical model parameters for $^{40}\text{Ca} + n$

E_n (MeV)	λ_S	λ_V	W_V (MeV)	W_D (MeV)	r_I (fm)	a_I (fm)	χ^2/N	Exp. data [Ref]
9.91	0.725	0.673	0.00	10.51	0.827	0.449	1.70	[12]
11.91	0.691	0.632	0.00	5.88	1.151	0.560	0.85	[12]
13.91	0.716	0.655	0.00	9.56	1.282	0.408	0.78	[12]
19.0	0.673	0.629	0.00	10.30	1.106	0.488	5.77	[13]
21.7	0.719	0.669	0.00	8.47	1.187	0.566	8.63	[13]
25.5	0.702	0.653	0.52	9.61	1.161	0.526	4.66	[13]
30.3	0.702	0.651	0.35	8.29	1.198	0.552	2.85	[14]
40.0	0.693	0.663	2.76	4.71	1.256	0.543	11.6	[14]

 TABLE 3: Optical model parameters for $^{54}\text{Fe} + n$

E_n (MeV)	λ_S	λ_V	W_V (MeV)	W_D (MeV)	r_I (fm)	a_I (fm)	χ^2/N	Exp. data [Ref]
7.96	0.704	0.657	0.60	13.20	1.021	0.386	6.62	[15]
13.92	0.711	0.667	2.52	6.38	1.209	0.552	4.18	[15]
20.0	0.687	0.640	2.22	7.20	1.249	0.495	9.20	[16]
26.0	0.706	0.664	1.13	8.35	1.132	0.547	10.30	[16]

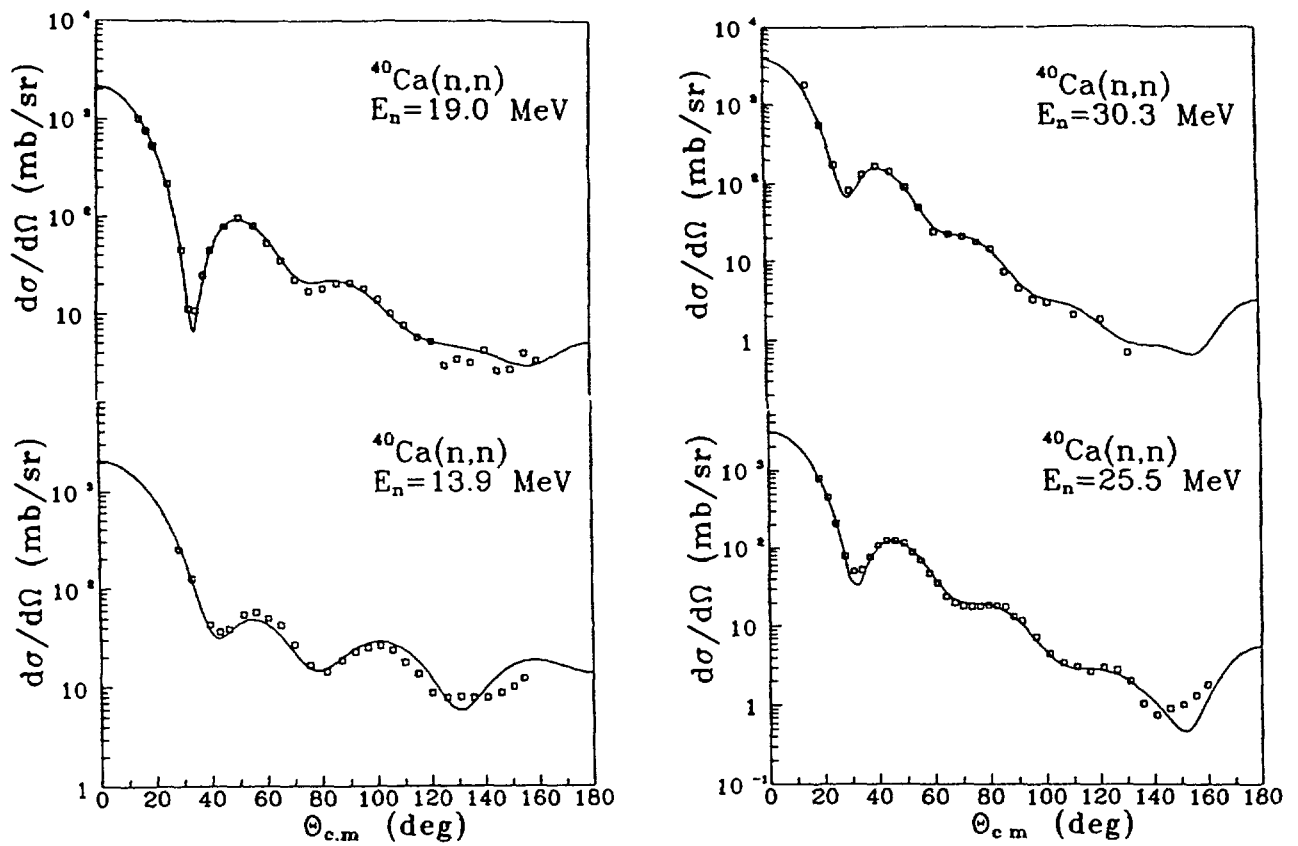


Fig. 1: Best fit differential cross sections on ^{40}Ca using Dirac optical model constrained by RMFA calculations.

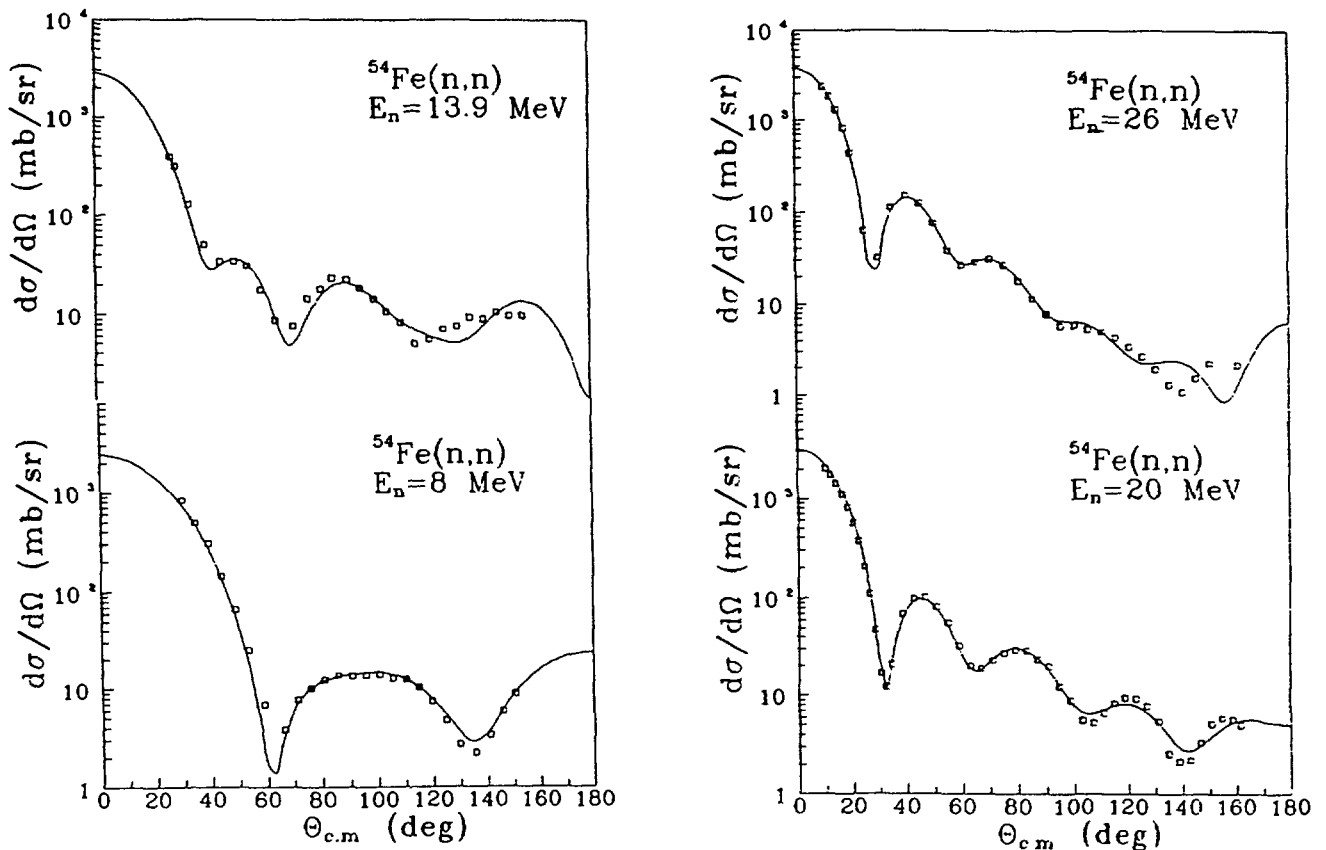


Fig. 2: As in Fig. 1 for ^{54}Fe .

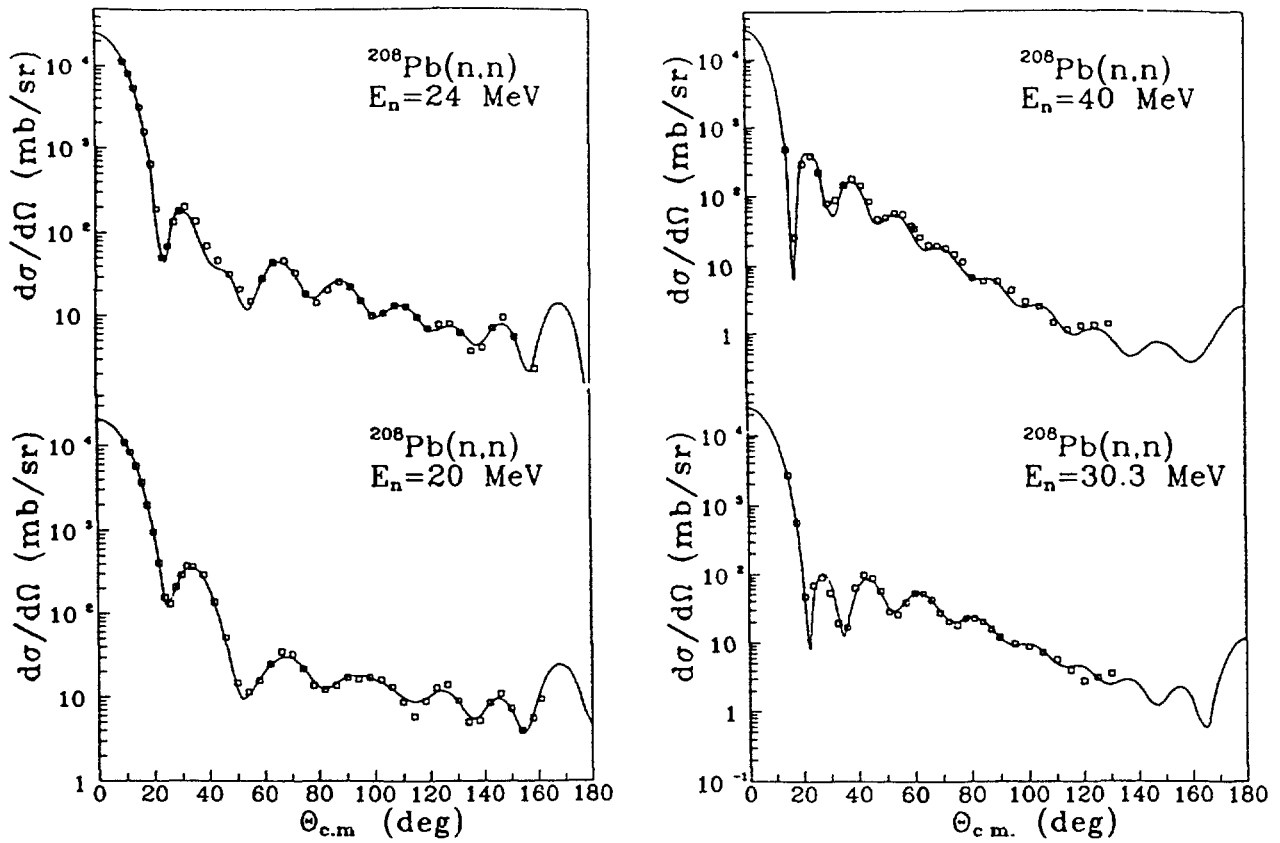


Fig. 3: As in Fig. 1 for ^{208}Pb .

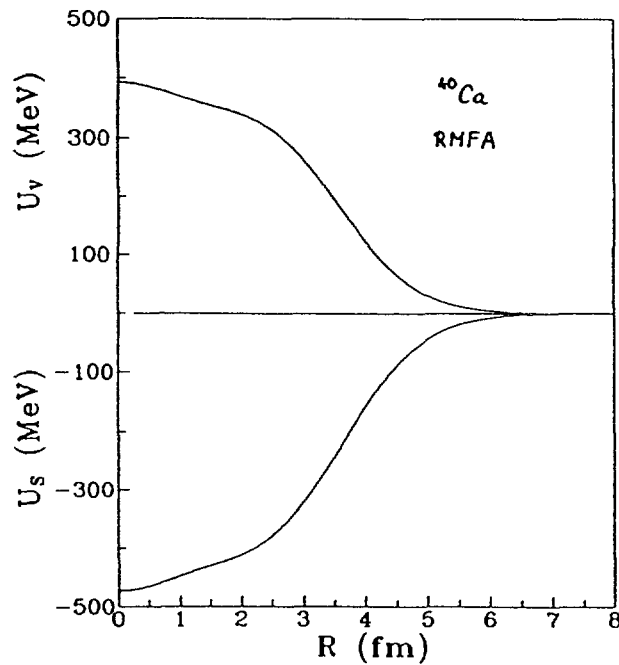


Fig. 4: The RMFA scalar and vector potentials folded with a Gaussian form factor for ^{40}Ca .

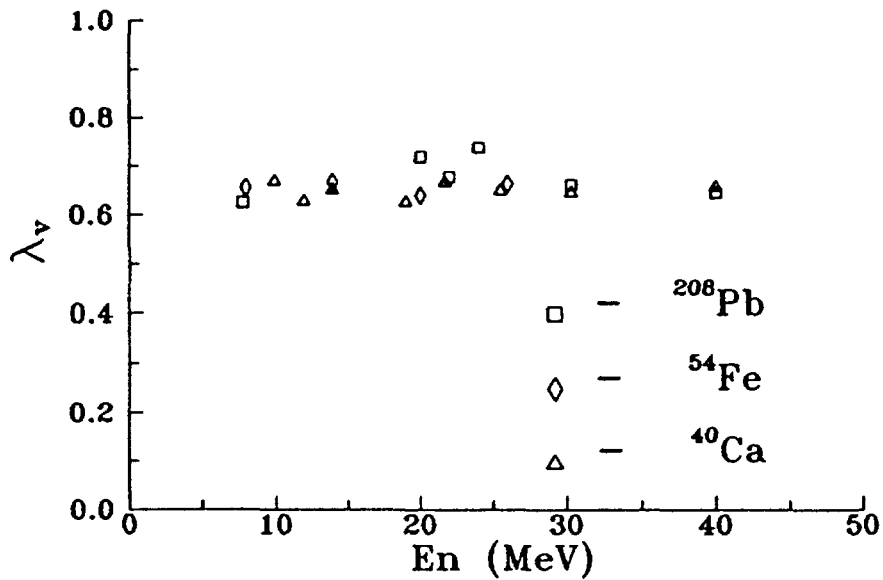


Fig. 5: The energy dependence of the scaling factor for the real vector potential.

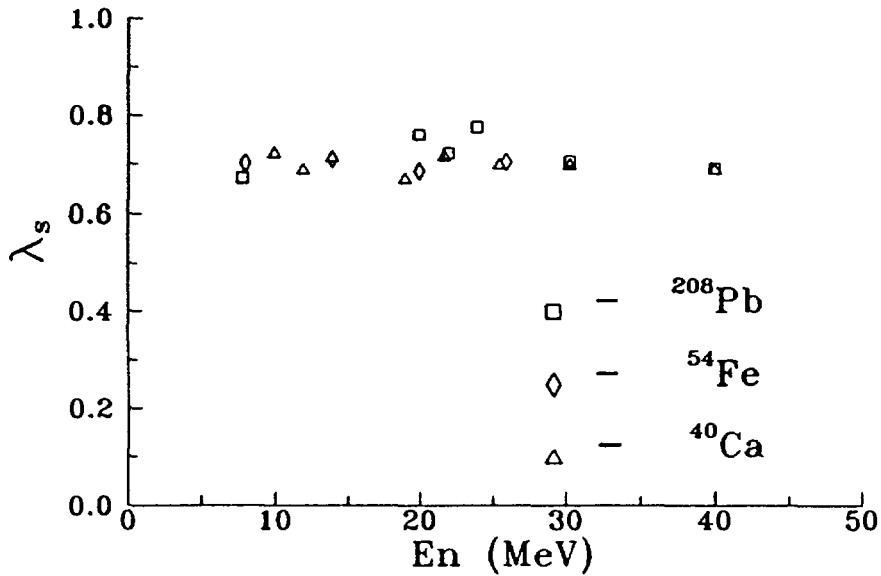


Fig. 6: As in Fig. 5 for the scalar potential.

obtained by folding the RMFA fields with the Gaussian form factors. The results for other nuclei are similar. The dependence of the scaling factors for the scalar and vector potentials on energy are shown in Fig.5 and Fig.6, respectively. We see that these scaling factors show no significant energy dependence. In addition, they seem to be the same also for all three nuclei involved in our analysis. These are very encouraging results. This is an indication that one may construct by this way the reliable global optical potential parameter set (at least for real potentials). The procedure used also provides the link

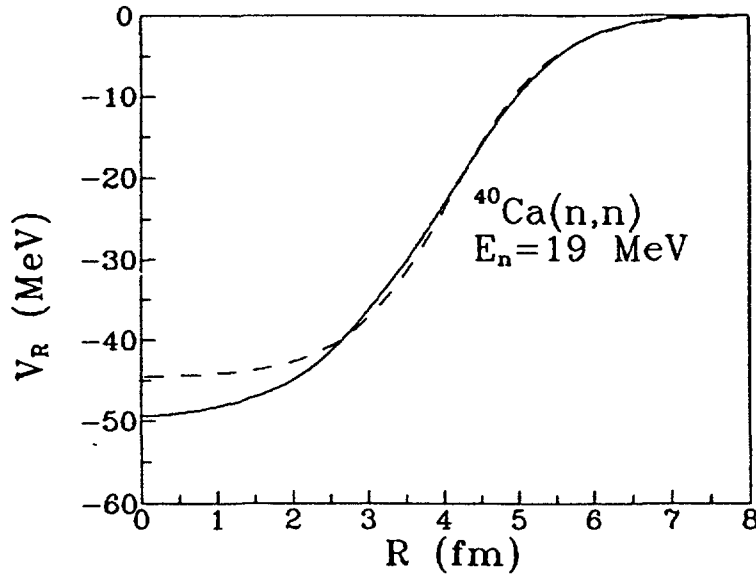


Fig. 7: The effective real central potential (solid line) compared to the phenomenological one (dashed line) for ^{40}Ca .

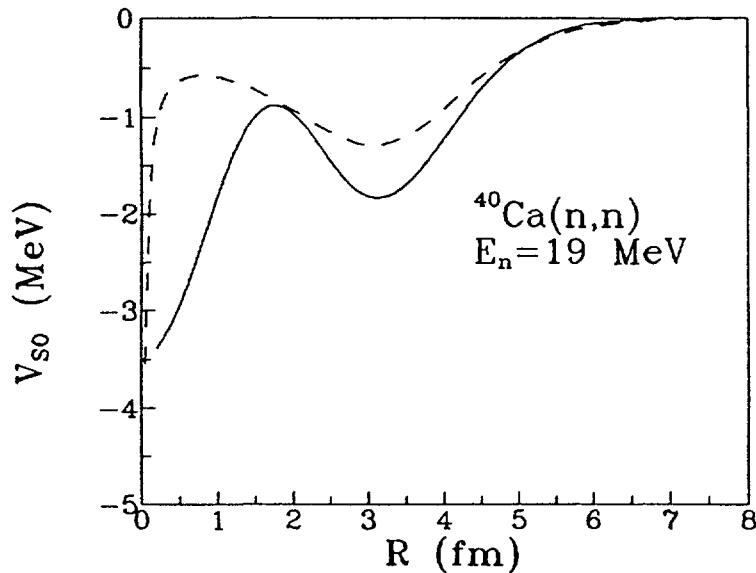


Fig. 8: As in Fig. 7 for the spin-orbit potential.

between the nuclear structure RMFA calculations and the Dirac (Schrödinger) optical model phenomenology.

The average values of the scaling factors λ_S and λ_V are 0.709 and 0.663, respectively. Thus the strengths of the real scalar and vector potentials to be used in the relativistic scattering calculations are damped by about 30% in comparison with the strengths used in the RMFA. These findings agree well with the results of S. Hama et al. [8], where a similar approach has been used to study the proton elastic scattering at intermediate energies. This damping

may be probably resolved by simultaneous fitting of both the ground-state and scattering problems together.

At the end of this section we compare the effective real central and spin-orbit potentials as obtained by the eqs.(6) and (7) with the phenomenological terms obtained by the conventional optical model analysis. This is done in Figs. 7 and 8 for the case of ^{40}Ca at 19 MeV. We see that the effective potentials correctly reproduce the phenomenological terms both in character as well as in absolute values.

5. Summary

We have shown that Dirac optical model potentials, real parts of which are constrained by the relativistic mean field calculations, may be used for reliable description of neutron elastic scattering also at low energies. The model has been tested on ^{40}Ca , ^{54}Fe and ^{208}Pb spin-zero nuclei. The results indicate that scaling factors for real parts of Dirac potentials are essentially energy independent. This opens the possibility to construct a reliable global parameterization of Dirac optical potentials.

References

- [1] L.S. CELENZA and C.M. SHAKIN, Relativistic Nuclear Physics, World Scientific Lectures Notes in Physics, Vol.2, World Scientific Publ. Co., Singapore, 1986
- [2] B.D. SEROT and J.D. WALECKA, The Relativistic Nuclear Many-Body Problem, In: Adv. Nucl. Phys. 16(1986)1
- [3] J.A. NEIL et al., Phys. Rev. Lett. 50(1983)1439
J.R. SHEPARD et al., Phys. Rev. Lett. 50(1983)1443
- [4] L.G. ARNOLD et al., Phys. Rev. C23(1981)1949
B.C. CLARK et al., Phys. Lett. 122B(1983)211
A.M. KOBOS et al., Nucl. Phys. A443(1985) 605
- [5] M. RUFA et al., Phys. Rev. C38(1988)390
- [6] S. GMUCA, In: Proc. Fifth Int. Conf. Nucleon Induced Reactions held in Smolenice, Czechoslovakia, June 20-25,1988, Physics and Applications, Vol.15, VEDA, Bratislava, 1988, p.83
S. GMUCA, Czech. J. Phys. B40(1990)322

- [7] B.C. CLARK et al., AIP Conf. Proc. No. 12, Neutron-Nucleus Collisions, A Probe of Nuclear Structure, eds. J. Rapaport, R.W. Finlay, S.M. Grimes and F.S. Dietrich, AIP Press, New York 1985, p.123
- [8] S. HAMA et al., Phys. Rev. C37(1988)1111
- [9] G. SCHREDER et al., Phys. Rev. C39(1989)1768
Data file EXFOR-22121.013
- [10] R.W. FINLAY et al., Phys. Rev. C30(1984)796
Data file EXFOR-12865.002
- [11] R.P. De VITO, Diss. Abstracts B40(1980)5724
Data file EXFOR-12701.005
- [12] W. TORNOW et al., Nucl. Phys. A385(1982)373
Data file EXFOR-12785.002
- [13] R. ALARCON et al., Nucl. Phys. A462(1987)413
Data file EXFOR-13127.002
- [14] R.P. De VITO et al., Phys. Rev. Lett. 47(1981)628
Data file EXFOR-12724.002
- [15] S.M. EL-KADI et al., Nucl. Phys. A390(1982)509
Data file EXFOR-10958.002
- [16] S. MELLEMA et al., Phys. Rev. C28(1983)2267
Data file EXFOR-12862.002

Acknowledgment: All EXFOR data were received from IAEA Nuclear Data Section, Vienna.

Calculation Uncertainties on Neutron Reaction Cross-Sections,
Particle Emission Spectra and Angular Distributions

V.A. Konshin and O.V. Konshin*
International Atomic Energy Agency
Vienna, Austria

*Byelorussian State University
Minsk, USSR

A B S T R A C T

The significance of uncertainties on the choice of neutron, proton and alpha-particle transmission coefficients and level density models for the calculation of threshold reaction cross-sections, particle emission spectra and angular distributions is analysed with TNG and GNASH-codes taking ^{56}Fe and ^{93}Nb as examples. Both the proton and alpha emission spectra show some sensitivity to level density changes, but these and other minor reaction channels can be rather sensitive to other effects. Optical model parameters for α -particles seem to be not satisfactory and all the relevant experimental information available should be analysed to obtain the respective parameters.

Introduction

One of the tasks to be solved when organizing the International Training Courses on Application of Nuclear Models for Calculation and Prediction of Neutron Cross-Sections is which computer codes should be used for this purpose. At least two criteria can be applied for choosing codes - the reliability (or correctness of physical assumptions used) and general availability of the code. Two codes have been chosen from this point-of-view - GNASH and TNG. These codes were put into operation on PC - TNG in the MS-DOS system and GNASH in OS/2.

The first experience in running these codes will be presented here, with particular emphasis on impact of uncertainties in input parameters on calculated neutron cross-sections, including the uncertainties in optical potential parameters. The unusual energy dependence of neutron optical potential parameters in the low energy region is possibly the most interesting development of the optical model which has been established over the last few decades.

This paper takes the ^{56}Fe and ^{93}Nb -nuclei as an example to investigate the significance of uncertainties in the choice of neutron transmission coefficients for the calculation of threshold reaction cross-sections, particle emission spectra and angular distributions in the incident neutron energy range up to 35 MeV.

From the relatively large number of different exciton models that have proved successful, we have selected Fu's formulation [1], which is attractive because it attempts to give a unified description of the compound and precompound stages of the reaction, with allowance for conservation of angular momentum.

The simplest Fermi gas models [2-5] as well as more systematic approaches [6, 7] were used to calculate the level density.

The Fu method [8, 9] was used to obtain a unified description of level density for both the compound and precompound stages of the reaction.

Two free parameters, a and D , similar to the corresponding parameters in the back-shift Fermi gas model, are used in the state density formula. However, summation for all possible particle-hole states leads naturally to a one-fermion level density formula, whereas the parameters a and D in the systematics of Dilg [4], for example, were obtained from experimental data analysis using a two-fermion level density formula. Traditional level density systematics are therefore not accurate enough for calculation of the parameters a and D .

We have taken the values of a and D from Ref. [10], obtained from systematic analysis of experimental data according to the one-fermion model. For example, we have $a = 5,44$, $D = 1,22$ for ^{56}Fe , instead of the values from Cook's systematics [3] of $a = 5,936$, $D = 0,75$, or from Dilg et al. [4]: $a = 5,998$, $D = 0,749$.

The analysis includes the neutron optical potentials that are most typical and most widely used in practical calculations, i.e. those of Becchetti-Greenlees [11], Wilmore-Hodgson [12] and Rapaport et al. [13], which should by definition be appropriate to describe a wide range of nuclei over a broad energy range. We can compare the results of calculations using such potentials with results obtained from the Arthur-Young potential [14], optimized over a narrow range for the case of ^{56}Fe , and a potential in which the neutron optical potential geometry also takes account of the energy dependence in order to give a consistent description of both weakly bound single-particle states in the shell model, and scattering at low energies [15]: $r_R = 1,315 - 0,0167 E$, $a_R = 0,663$ and all the other

parameters are taken to be as in [13]. The potentials in Refs [11, 16] were used for protons and in [17, 18] for alpha-particles.

If we confine ourselves to the total cross-section (σ_t) data, then there is no need to include an energy dependence of the potential geometry parameters which is unusual for traditional parameterizations - it is sufficient for $E_n < 5$ MeV to increase the depth of the well by $\sim 24\%$ (for example, in the case of ^{56}Ni , to take $V_R = 59,73 - 0,76 E$). However, taking account of a wider range of data (differential elastic and inelastic scattering cross-sections, level excitation functions) makes it necessary to increase the potential well radius with a decrease in the energy of the incident neutron. A modification of traditional parameterizations to take this fact into account solves the problem of extrapolating the parameters of the optical potential to the low energy range. It has been shown that, in the case of the iron group of nuclei, "anomalous" potential geometry shows up in the range $E_n \leq 5-7$ MeV [15]. It would be logical to expect a similar "anomaly" in the threshold reaction cross-section calculations for the (n,2n) and (n,p) reactions and so on, which, as Young has shown [19], are sensitive to the values of neutron transmission coefficients at low energies.

A preequilibrium, statistical nuclear-model code GNASH [29] was used for calculation of reaction and level cross-sections and spectra of neutron, gamma-ray and charge-particles. It became possible to put into operation GNASH, originally developed on CDC 6600 and CRAY 1, on a personal computer PS/2 using the OS/2 system.

Results and Discussion

Figure 1 compares various OP (optical potential) parameterizations for calculations of σ_{n2n} for ^{56}Fe . As we can see, uncertainties in the choice of the OP parameters may lead to an error of $\sim 25\%$ in the final value of σ_{n2n} for $E_n \geq 14$ MeV. Moreover, the potentials that are most reliable in the $E_n > 14$ MeV region, at going to lower energies give values of σ_{n2n} that are too high. At the same time, potentials of the type in Ref. [14], although producing the best results for calculations of σ_{n2n} at $E_n < 14$ MeV, are scarcely suitable at higher energies. It should also be remembered that they are optimized over too narrow a range, which means that there are significant errors in the calculations even for near neighbour nuclei. The situation here is quite similar to what we used to find in calculating $\sigma_{nn'}$, $\frac{d\sigma_n}{d\Omega}$, σ_t [15], and so it would seem natural to

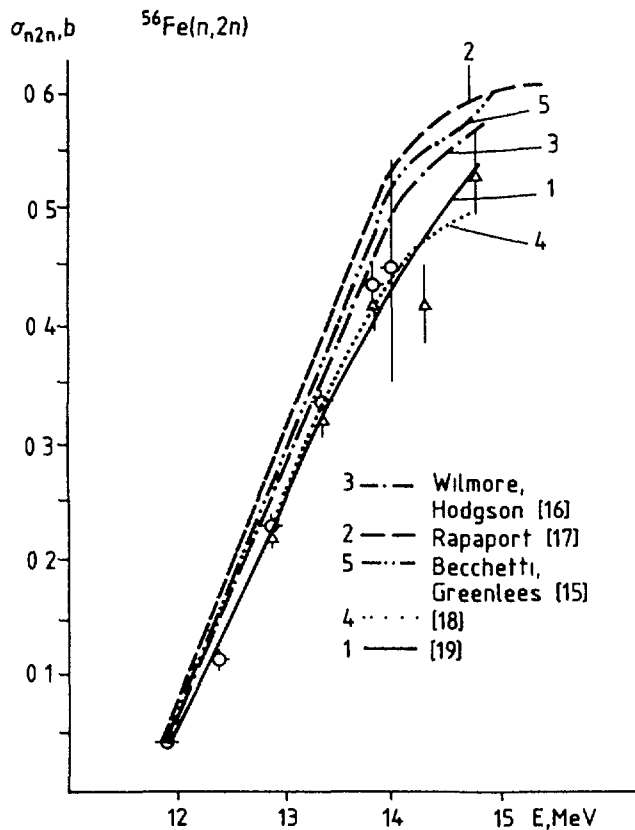


Fig. 1a

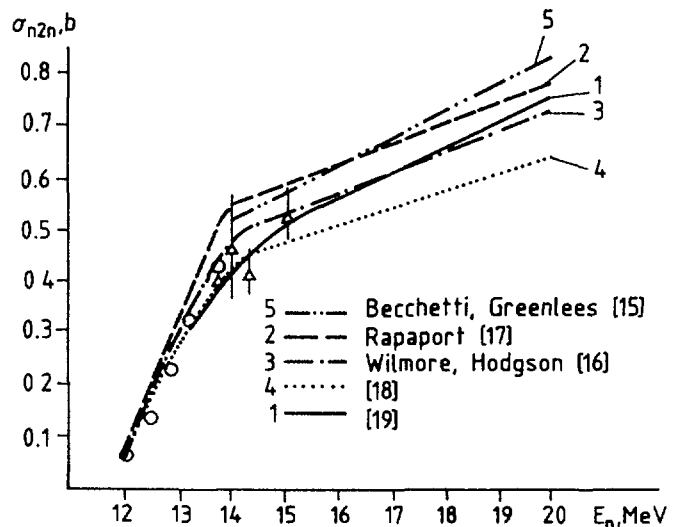


Fig. 1b

Fig. 1(a), (b). A comparison of experimental and theoretical data for σ_{n2n} (^{56}Fe). The neutron OP used are:

- 3 -.- Wilmore-Hodgson [12], 2 --- Rapaport et al. [13],
- 5 -.- Becchetti-Greenlees [11], 4 ... Arthur-Young [14],
- 1 — [15].

adopt the same method for "correcting" the traditional global parameterizations with a view to possible extrapolation to the low energy region. The results look promising (solid curve in Figs. 1(a), (b)).

In this connection it is imperative to recall that in calculating threshold reaction cross-sections, a further problem arises - in addition to the uncertainty in the neutron transmission coefficients - namely the choice of level density parameters.

We can take the neutron optical potential in the form given in Ref. [12] for example, and then see how various approaches to the selection of level density parameters affect the calculation of σ_{n2n} .

Figure 2 shows that the maximum differences do not exceed 10% and that the errors are less than those resulting from an incorrectly chosen optical potential. However, there remains the problem which set of parameters to use.

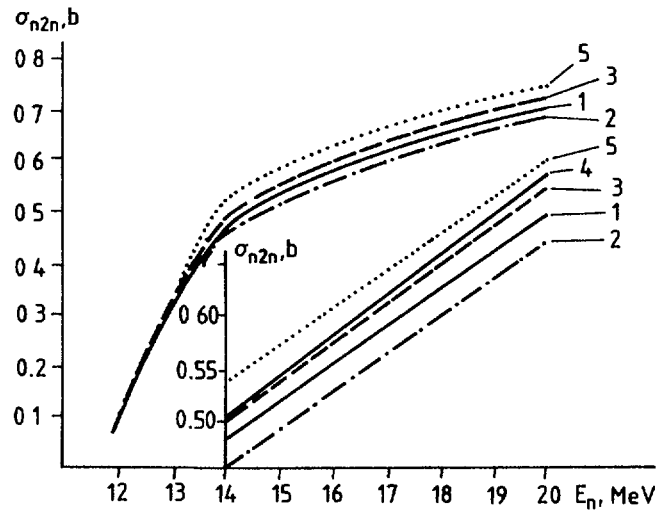


Fig. 2. A comparison of experimental and theoretical data for σ_{n2n} (^{56}Fe). The level density parameters used: 5 ... Gilbert-Cameron [2], 3 --- Cook et al. [3], 4 ___ Su et al. [5], 2 -.- Dilg et al. [4], 1 ____ [7].

No firm conclusion can be drawn from a comparison of calculated and experimental data for σ_{n2n} . The true answer is masked by the additional uncertainty, in the optical potential: the fact is, we are dealing with the combined contributions of two factors which are very difficult to separate.

We shall therefore assume that the traditional Fermi gas model is too crude an approximation, and although in the case of ^{56}Fe the discrepancies between different level density models are small (solid curve in Fig. 2, is obtained using the method by Ignatyuk et al. [6], intermediate value between Cook et al. [3] and Dilg et al. [4]), we have used [6] as a basis for further calculation (all calculations in our paper, including Fig. 1, allow for the energy dependence $a(U)$).

The sensitivity of the neutron emission spectrum (incident neutron energy 14 MeV) to the selection of neutron optical potential parameters is shown in Fig. 3.

In spite of the wide spread of experimental data for the soft (equilibrium) part of the spectrum, one firm conclusion may be drawn: the potentials which give excessively high values of σ_{nn} and σ_{n2n} have a similar effect for the process we are now considering, which is of course simply and easily explained. The situation is less clear for the rigid part of the spectrum - the differences between parameterizations are weaker against a background of broadly scattered experimental data.

In the low energy region we can opt for the potentials in Refs. [14, 15]. The high energy part of the spectrum is determined by rapid

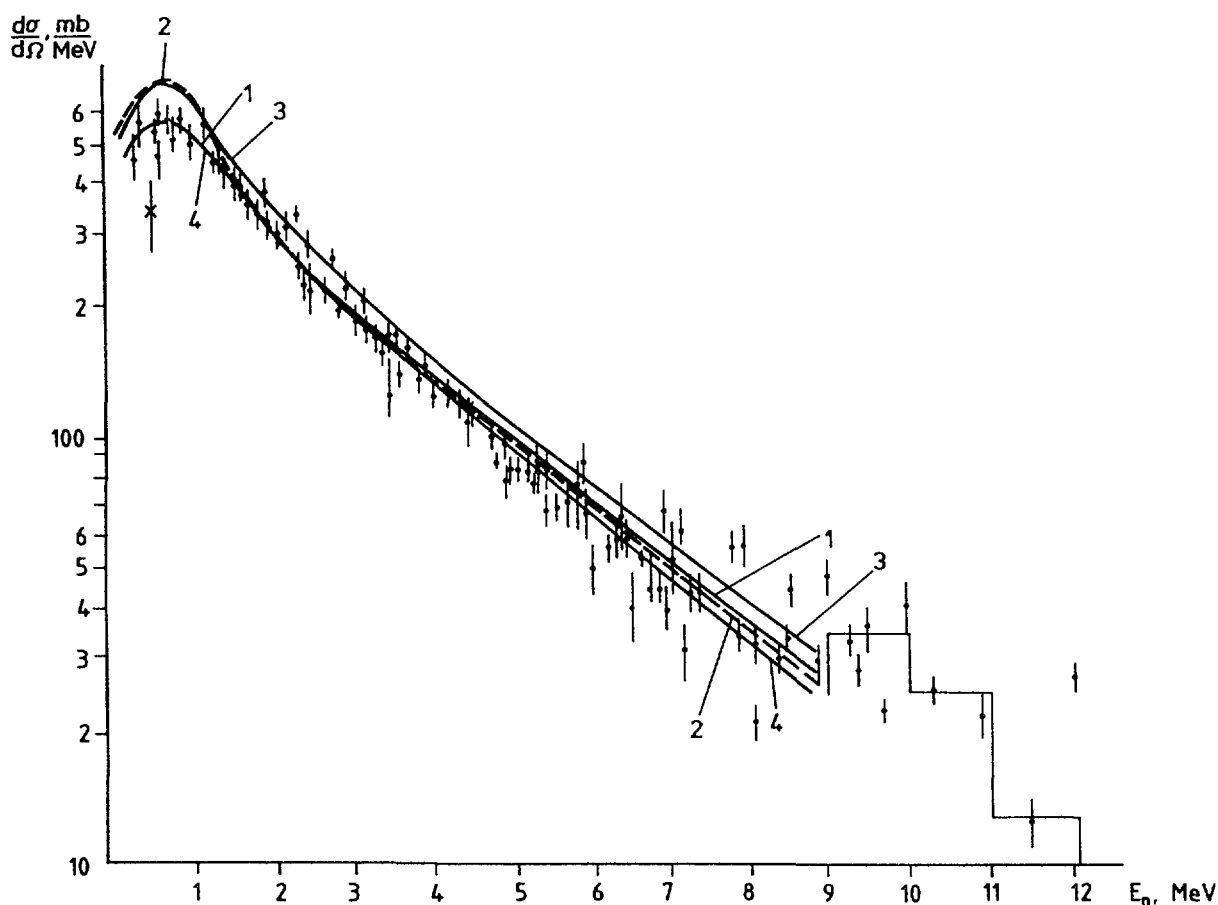


Fig. 3. Neutron emission spectrum for incident neutron energy $E_n = 14$ MeV for ^{56}Fe . The potentials used: 1 [15], 2 [13], 3 [12], 4 [14]. Experimental data from the Vonach compilation.

direct processes at discrete levels. Here we may note the 7–9 MeV range, in particular, where – if we can go by the latest experimental data of Takahashi – there may be a limitation on the validity of the exciton model: here two-phonon excitations of many different multipolarities must be taken into account. However, the exciton model has an arbitrary free parameter K which defines the $1/M^2$ -square of the matrix element for intranuclear transitions. All calculations in Fig. 3 were made with $K = 400 \text{ MeV}^3$.

Figure 4 shows that the rigid part of the spectrum is very sensitive to the value of this parameter, and the choice of a value $K = 200 \text{ MeV}^3$ facilitates agreement with the experimental data over the entire energy interval.

The relationship between K and the approximations used for state density in the exciton model must be considered. Accordingly, the value which we obtained for K is correct only if Fu's method [8, 9] is used for the state

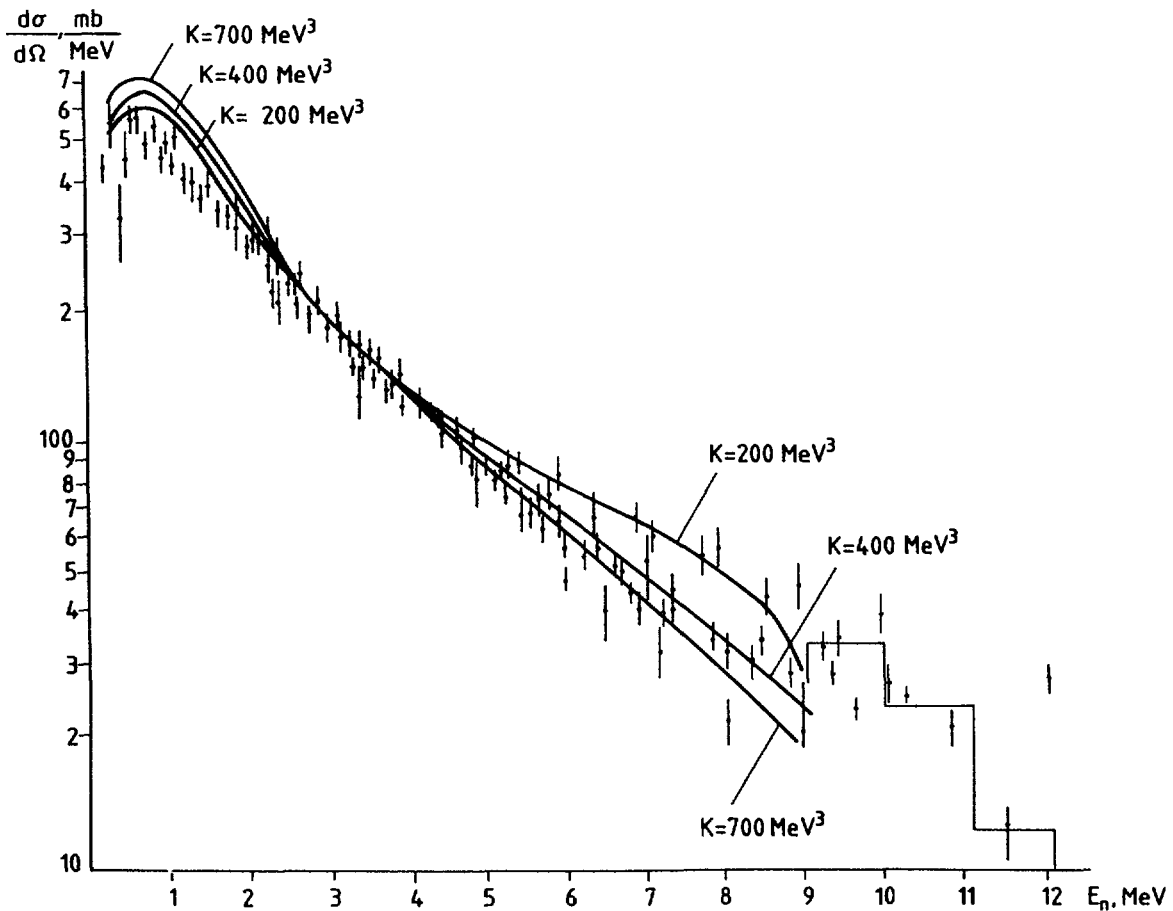


Fig. 4. Neutron emission spectrum for incident neutron energy $E_n = 14$ MeV for ^{56}Fe as a function of $K = 200, 400, 700$ MeV^3 . The neutron optical potential was selected in the form given in Ref. [12].

density calculations to ensure proper consideration of nuclear characteristics. Thus the question whether $K = 200$ MeV^3 can be regarded as a value with universal validity - i.e. applicable to a wide range of nuclei - requires further investigation.

If we consider the substantial contribution of (n, np) and (n, pn) reactions to the total proton yield and the increased sensitivity in the soft part of the calculational spectrum to the choice of neutron optical potential, we may expect the proton emission spectrum to provide much additional, useful information.

Figure 5 shows a calculated proton emission spectrum for an incident neutron energy of $E_n = 14$ MeV (the parameterization from Ref. [14] was used for protons). As we can see, in the proton spectrum, the differences between neutron OPs emerge even more clearly than in the neutron spectrum.

The experimental value for total proton production according to S.M. Grimes et al. [21] is 190 ± 22 mb. The various neutron OP

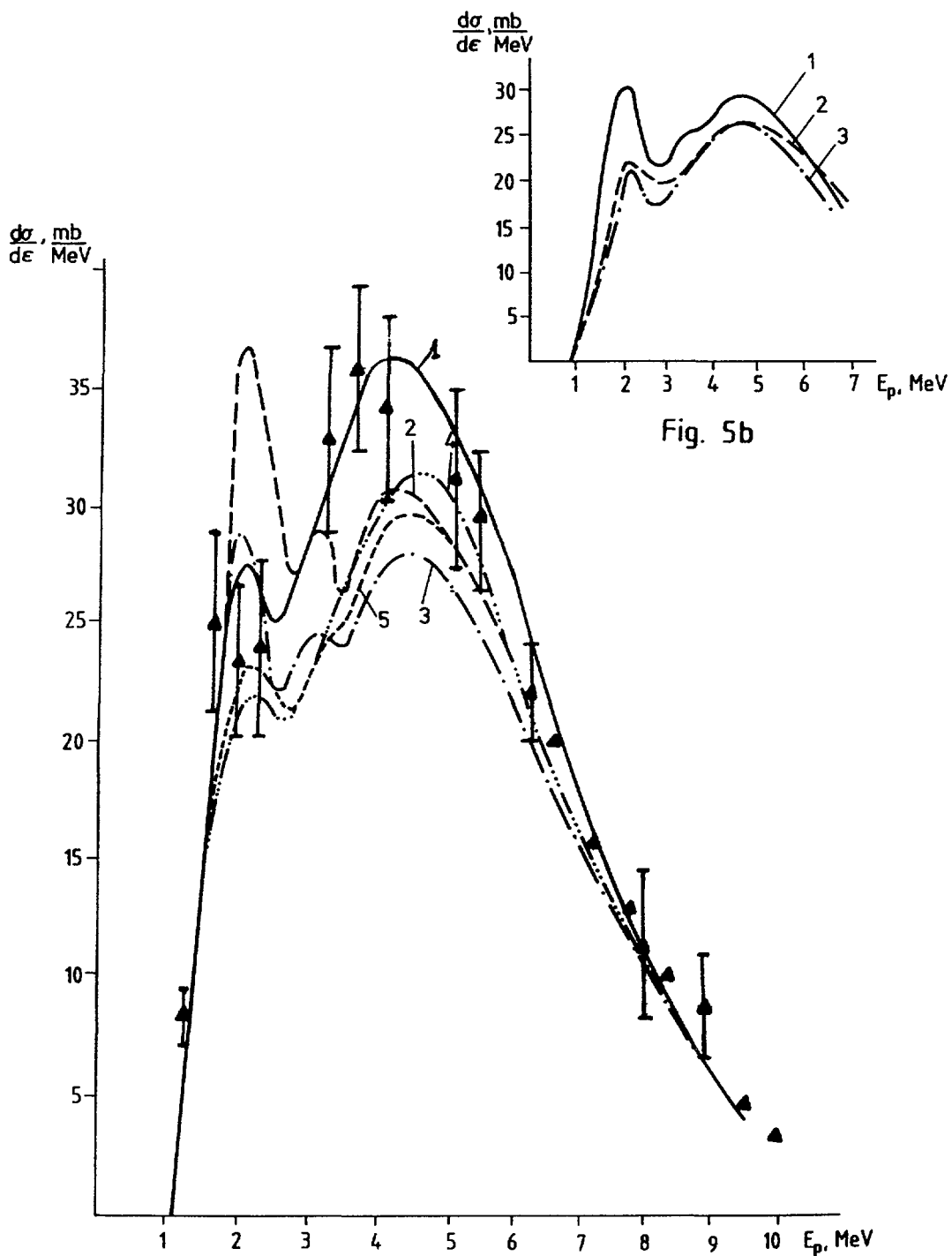


Fig. 5a

- Fig. 5. (a) Proton emission spectrum for incident neutron energy $E_n = 14 \text{ MeV}$ for ^{56}Fe . Neutron OP - 1 [15], 2 [13], 3 [12], 4 [14], 5 [11], proton OP [11].
- (b) 1 - neutron OP [12], proton [11], $K = 400 \text{ MeV}^3$
 2 - neutron OP [12], proton [11], $K = 200 \text{ MeV}^3$
 3 - neutron OP [12], proton [16], $K = 400 \text{ MeV}^3$

parameterizations produce the following values: Wilmore-Hodgson [12]: 158,36; Becchetti-Greenlees [11]: 161,44; Arthur-Young [14]: 164,04; Rapaport et al. [13]: 181,82; [15]: 198,46 mb, for $K = 400 \text{ MeV}^3$. For $K = 200 \text{ MeV}^3$ all the figures shown above should be reduced by approximately 10 mb.

If we compare the results given by the potentials in Refs [14, 15] (for the neutron spectrum they were approximately equal), then those in Ref. [15] are clearly preferable. Let us turn our attention to the main discrepancy in the form of the proton spectrum. Although the potentials in Refs. [15] and [13] differ only slightly from the point of view of the total proton production given (the difference is more significant for the neutron spectrum), the structure of their proton spectra is fundamentally different. Potential parameters from reference [15] give only a small maximum around $E_p = 2 \text{ MeV}$ and a main peak at $E_p = 5 \text{ MeV}$, whereas from Ref. [13] the picture is quite the opposite. S.M. Grimes et al. [21] carried out an experiment with an energy resolution of 500 keV, but a further experiment is needed to establish a physically substantiated energy dependence for the neutron OP parameters. We may note that in the case of the proton spectrum the uncertainty in the selection of the proton optical potential parameters adds to the total error. For example, the use of the Wilmore-Hodgson [12] neutron potential with the Perey-Perey [16] proton potential (instead of the Becchetti-Greenlees proton potential [14]) gives a total proton production of 137.11 mb (see Fig. 5(b)), but even against this background we may conclude that energy dependence of the geometry should be included in the neutron OP.

The calculation of double differential cross-sections

The method of calculating double differential cross-sections suggested by Fu and Plyujko [22, 23] is based on an entirely valid observation: in at least two limiting cases, definite conclusions can be drawn concerning the phases. After a sufficiently large number of collisions within the system, leading to the formation of "holes", a particle forgets its previous history entirely and the random phase approximation becomes valid. In contrast, the second limiting case, $h = 0$, corresponds to fully correlated phases. All really occurring processes are located somewhere between these two limiting cases, and they can be taken into account by introducing a random correlation coefficient C which takes values of $C = 0$ for $h = h$ and $C = 1$ for $h = 0$.

The main problem with the Fu model [24] is how to choose the parameter C . We can take, for example, $C = 0,5$, as in Refs [23, 25]. As we

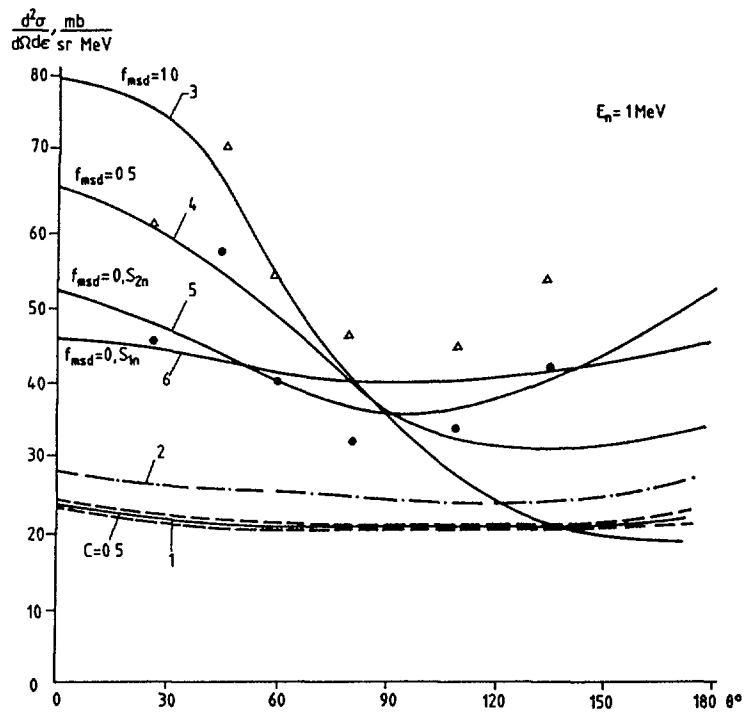


Fig. 6a

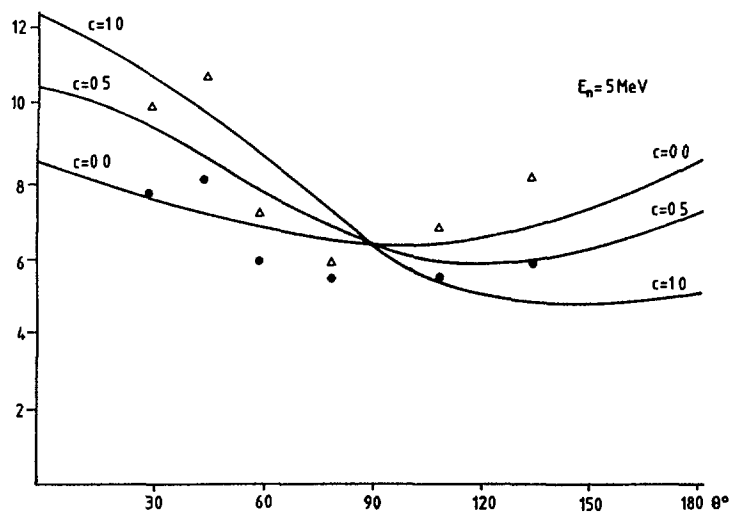
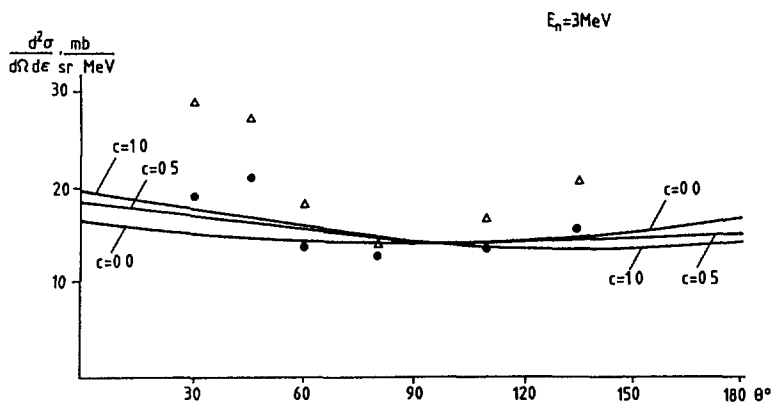


Fig. 6b

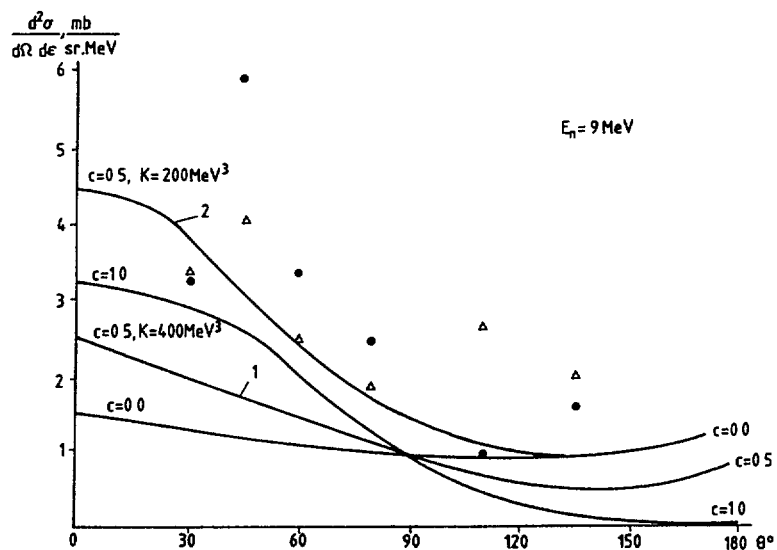


Fig. 6d

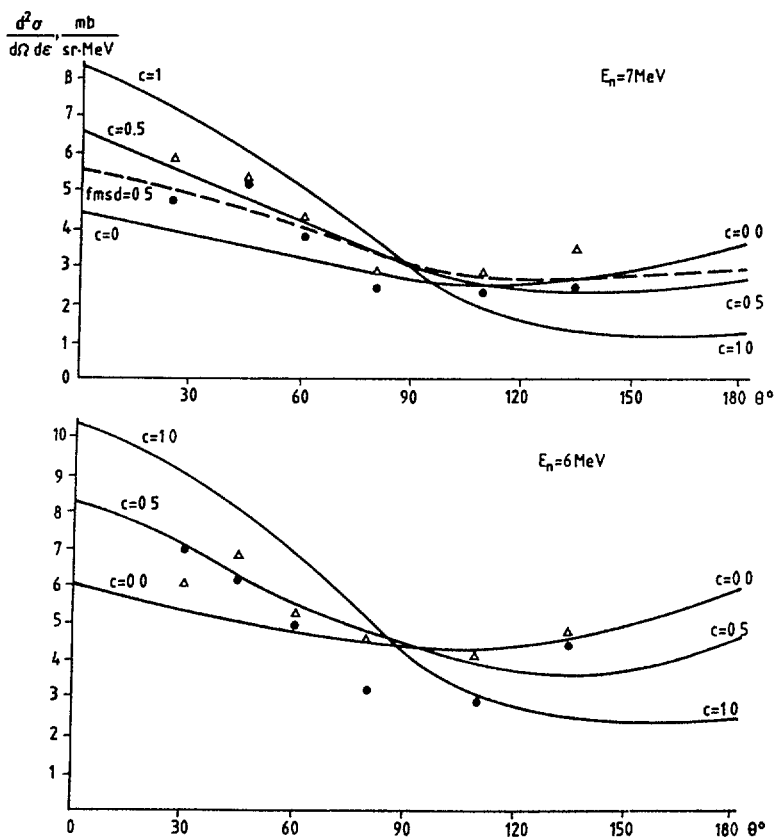


Fig. 6c

Fig. 6.

Angular distributions of neutrons emitted at $E_n = 1, 3, 5, 6, 7$ and 9 MeV for incident neutron energy $E_n = 14$ MeV for ^{56}Fe .

Emission energy $E_n = 1$ MeV: 1 - Fu model, neutron OP [15], solid curve $C = 0.5$, dotted curves $C = 0, C = 1.0$;
 2 - neutron OP [11]; 3, 4, 5, 6 - calculation according to the systematics of G. Kalbach [26], $\left. \frac{d\sigma}{d\epsilon} \right|_{E_n = 1 \text{ MeV}}$,

Fig. 6. calculated with neutron OP [15]; curves: 3-fmsd = 1.0; 4-fmsd = 0.5; 5-fmsd = 0 and the separation energy of two neutrons, S_{2n} , is taken into account; curve 6-fmsd = 0, the separation energy of only one neutron, S_n , is taken into account. The neutron OP from Ref. [15] is used in all calculations.

Neutron emission energy 7 MeV: the dotted line shows the calculation according to Kalbach systematics [26]; fmsd = 0.5, S_{1n} was used.

Neutron emission energy 9 MeV: 1 - Fu model, neutron OP [15], $C = 0.5$, $K = 400 \text{ MeV}^3$; 2 - the same as 1, except that $K = 200 \text{ MeV}^3$.

The experimental data in the figures are taken from Ref. [27]. The signs \bullet and Δ mean, respectively, with and without corrections for multiple scattering.

can see, in the emitted neutron energy interval (4 - 7 MeV) this "universal" value of C gives good agreement with the experimental data. The calculation results are scarcely affected by the various sets of neutron OP parameters. The shape of the angular distribution in this case is midway between full symmetry in relation to 90° (the case of the compound process $C = 0$) and a pronounced peak further ahead ($C = 1, 0$, direct process). At the transition to higher energies it is naturally to be expected that the existing uncertainties would be reflected in the rigid part of the neutron emission spectrum. At 9 MeV we see both forward and backward peaking, as before, in the angular distributions, and the value $C = 0.5$ is therefore acceptable. The value $K = 200 \text{ MeV}^3$, which gives the best description of the rigid part of the spectrum (instead of $K = 400 \text{ MeV}^3$), is also preferable for the description of angular distributions.

The situation is more complicated for $E_n < 4 \text{ MeV}$. Firstly, in this case Takahashi's experimental data reveal an isotropic distribution in relation to 90° ; this corresponds to a purely compound process, and therefore C should be taken as 0. At the same time the sensitivity of the final calculation results to the specific value of C falls off sharply, as we can see. Secondly, it is precisely at low energies that the emission of secondary neutrons becomes significant, and this, by definition, is not considered in Fu's formalism. No variation in the model's free parameters can compensate for this defect. Thus Fu's method requires further development in two areas if

it is to be applied to a wide energy range: the inclusion of secondary neutron emission and parameterization of the constant C as a function of the number of collisions in the system, which would give it a clear physical meaning. Let us compare the results given by the rather complex Fu-Plyujko theory with the predictions of the much simpler systematics of C. Kalbach [26], according to which:

$$\frac{d^2\sigma}{d\epsilon d\Omega} = \frac{1}{4\pi} \left(\frac{d\sigma}{d\epsilon} \right) \frac{a}{\sin h(a)} [\cos h(a \cos \theta) + fmsd \cdot \sin h(a \cos \theta)],$$

where in our case $a = 0,04 la + 1,8 \cdot 10^{-6} (la)^3 + 3,35 \cdot 10^{-7} (la)^4$, $la = E + S_n$, E is the incident neutron energy, S_n is the neutron separation energy, fmsd is the multistep direct (MSD) fraction in relation to the multistep compound (MSC), i.e. the equivalent of the parameter C in the Fu model. In the case where $E_n = 1$ MeV fmsd = 0 naturally gives the best agreement. The

separation energy of two neutrons, $S_{2n} = 20,5$ MeV, should be taken as S_n instead of the separation energy of a single neutron, $S_{1n} = 11,2$ MeV.

In the case of $E_n \sim 7$ MeV, excellent agreement is obtained with $f = 0,5$, and the choice between S_{2n} and S_{1n} is not as important as at low energies; indeed, both lead to angular distributions within the limits of experimental error.

When the Kalbach systematics are used, the uncertainty in the calculation of $\left(\frac{d\sigma}{d\epsilon} \right)_n$ acquires great importance: this uncertainty, as we have shown, is particularly large in the soft and rigid parts of the spectrum, so that a correct choice of neutron OP parameters is clearly important.

Nuclear model calculation of data for neutron-induced reactions on ^{93}Nb in the energy region up to 35 MeV

Test calculations were carried out for ^{93}Nb using the code GNASH. Niobium was selected to make it possible to compare present calculations with a recent revision of previous statistical model calculations made by Strohmaier [28].

The calculations were made for neutron, proton, α -particle and γ -channels. The level density models used were those of Ignatyuk [6] and Gilbert and Cameron [2].

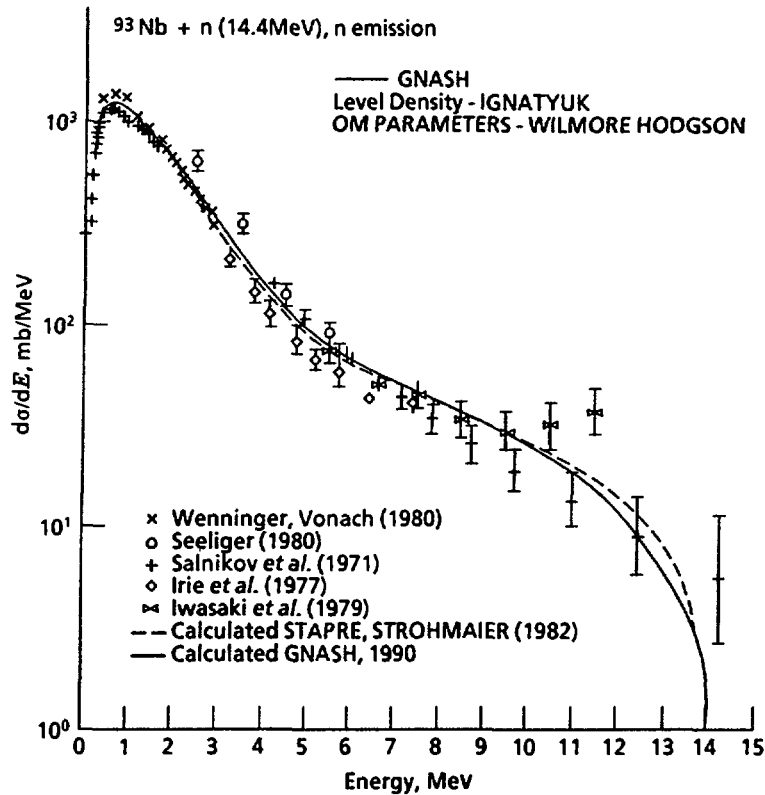


Fig. 7. Comparison of neutron emission spectrum for incident neutron energy $E_n = 14.4$ MeV for ^{93}Nb calculated using GNASH and STAPRE.

The neutron emission spectrum indicates no sensitivity to level density changes (Fig. 7, 8). It is understandable as neutron emission channels dominate the statistical model calculation of both partial and total widths and thus high level density changes produce little impact on this ratio. This was also observed by Arthur [29].

From Fig. 7-10 it can be seen that the neutron channel of the reactions can be described quite well and there is very good agreement between calculations made with STAPRE [28] and GNASH [20]. GNASH calculations support the observation made in [28] that the (n,2n) cross-section data of Frehaut [30] should on average be 8% higher. From Fig. 11 one can see that the Hauser-Feshbach model with the pre-equilibrium correction, such as GNASH, may give results which are very close to those obtained with more unified models for neutron emission spectra [31].

The total gamma-ray emission spectrum can be reasonably reproduced by calculations (Fig. 12) and a similar lack of sensitivity to the chosen level density models up to 10 MeV is displayed in Fig. 13. The difference in gamma-ray spectra in the energy region above 10 MeV is a factor of two in the case where two level density models are used ([2] and [6]).

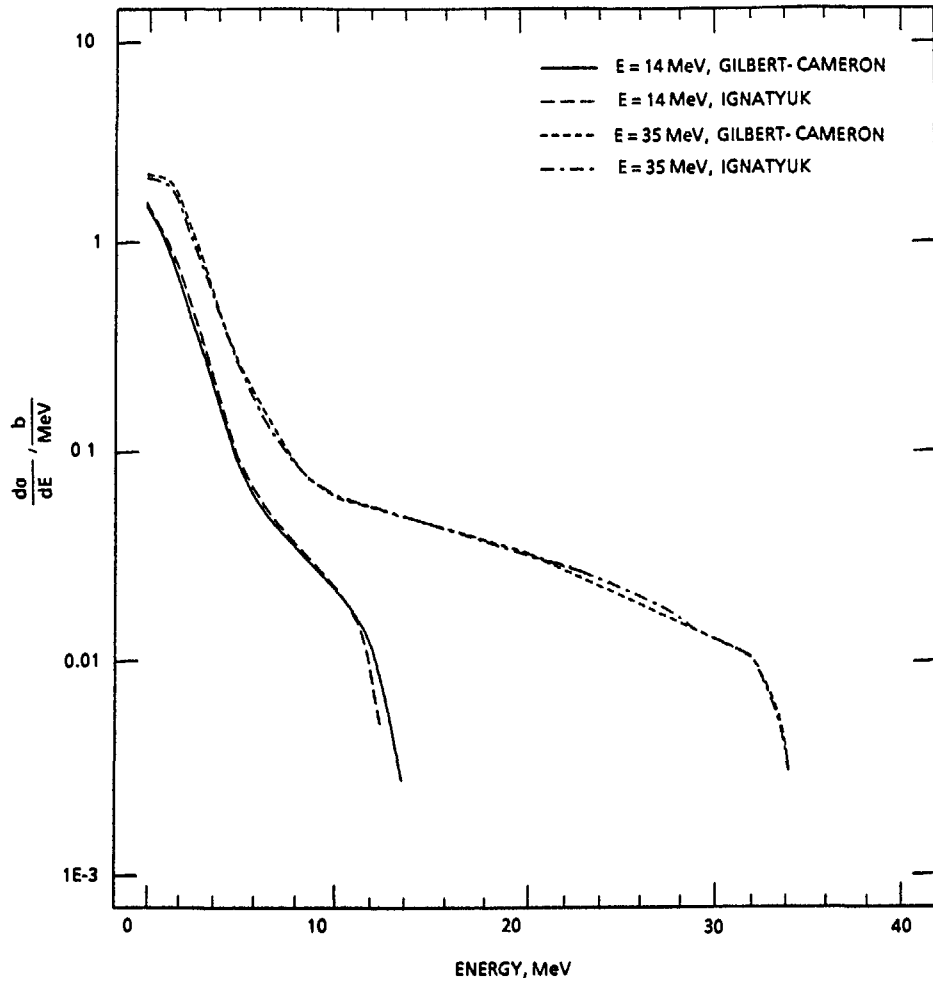


Fig. 8.

Dependence of neutron emission spectra for ^{93}Nb on level density models. Neutron OM parameters used were those of [12].

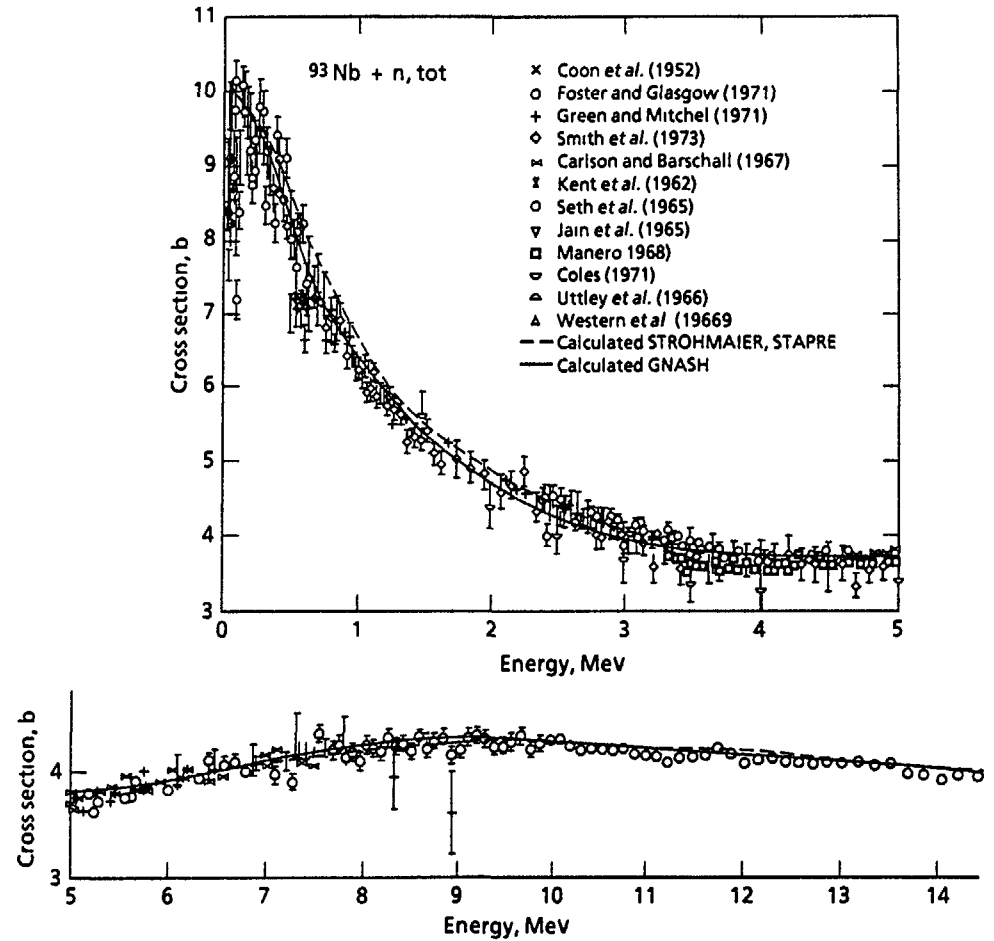


Fig. 9.

Comparison of calculated and experimental total cross-sections for ^{93}Nb - data taken from [28].

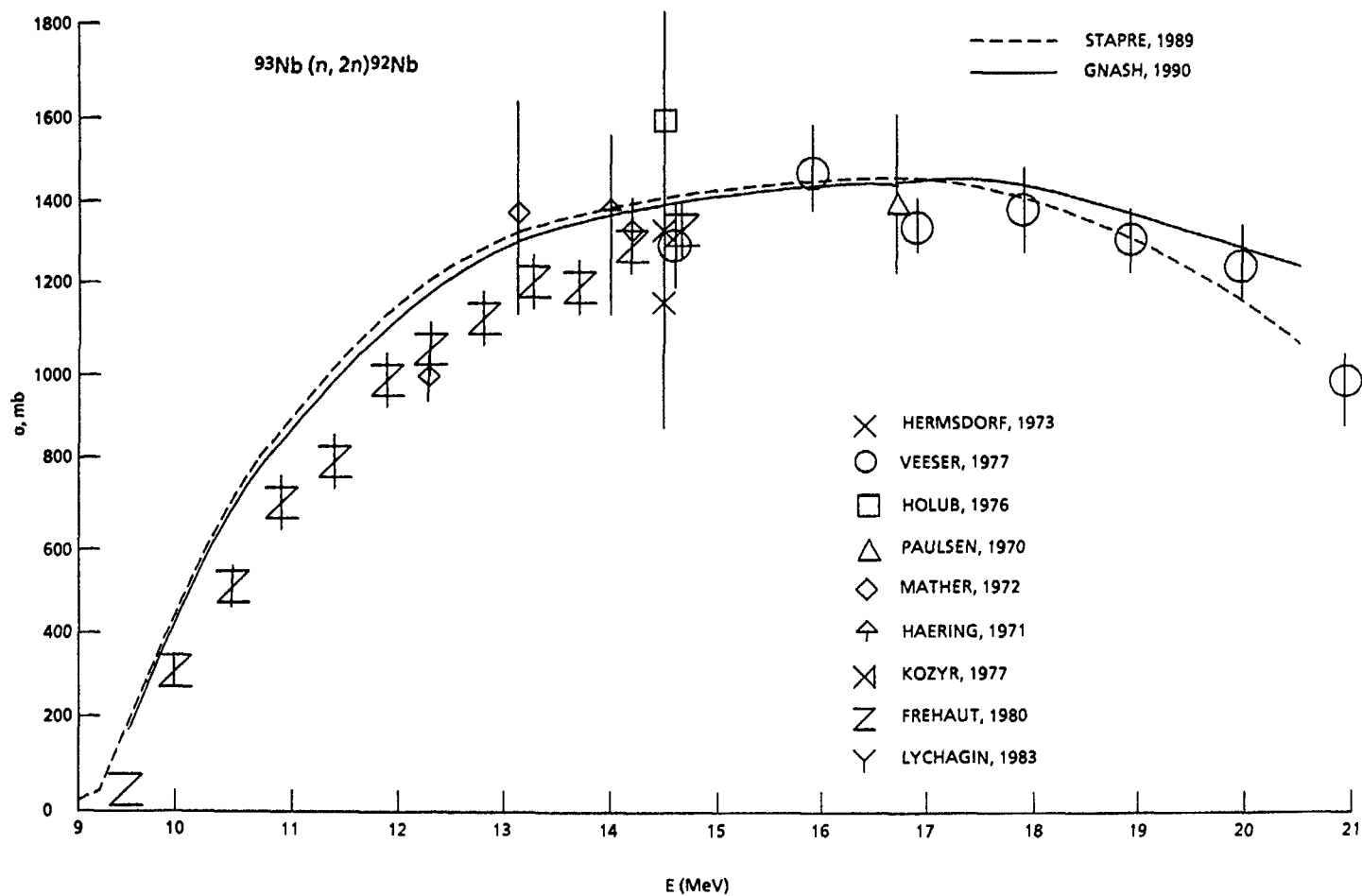


Fig. 10.

Comparison of calculated and experimental (n,2n) cross-sections for ^{93}Nb - data taken from [28].

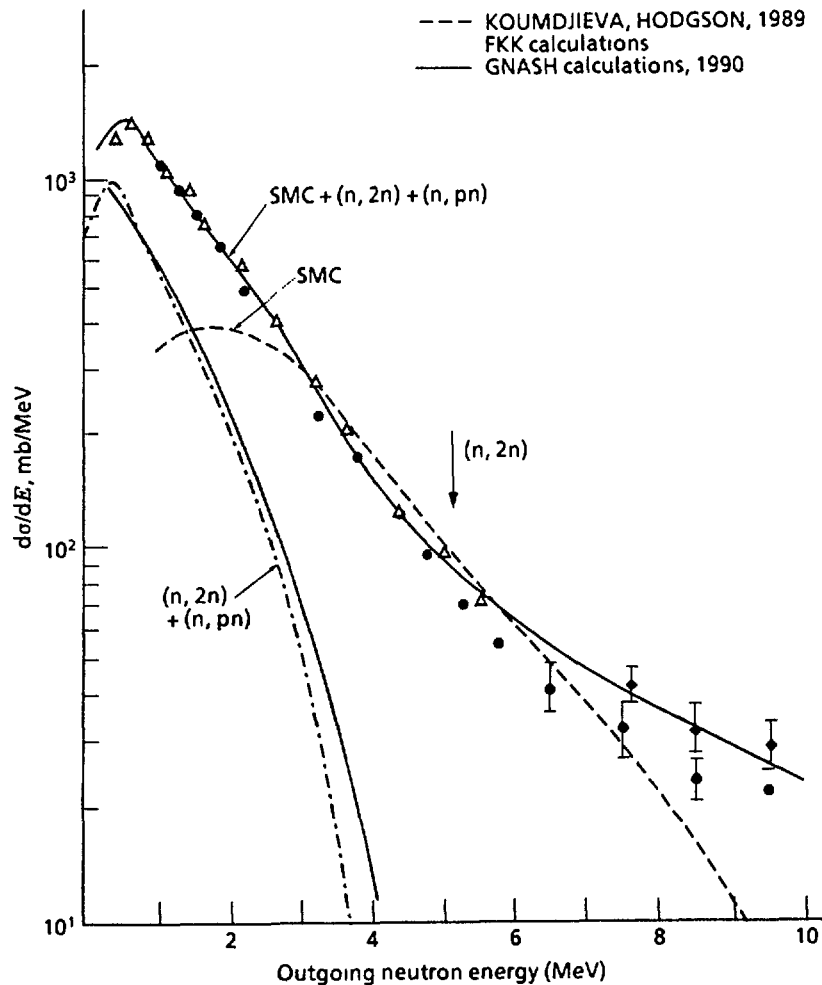


Fig. 11. Comparison of neutron emission spectra for ^{93}Nb calculated by GNASH code with FKK calculations [31].

Results of calculations of proton emission spectra at 14 and 35 MeV neutron incoming energies are shown in Fig. 14-16. A rather high sensitivity of proton emission spectra, in particular in the energy region 4 to 9 MeV, to level density models can be seen. The difference in using Gilbert-Cameron [2] and Ignatyuk [6] models is more than a factor of two. Experimental information on proton emission spectra can be described using the Ignatyuk level density model and proton OM Perey [16]. Parameterization of Becchetti and Greenlees [11]' for the proton OM potential leads to a slightly higher value ($\sim 10\%$) than [16]. The same level of sensitivity to the level density can be seen at 35 MeV neutron energy.

Figures 17-20 give the results of calculations of α -emission spectra and (n, α) cross-sections. It can be seen that both MacFadden et al. [17] and Huizengo and Igo [18] optical potential parameters for α -particles (curves 1 and 5 on Fig. 17) underestimate α -spectra and (n, α) cross-sections by a factor of two (using the Ignatyuk level density model).

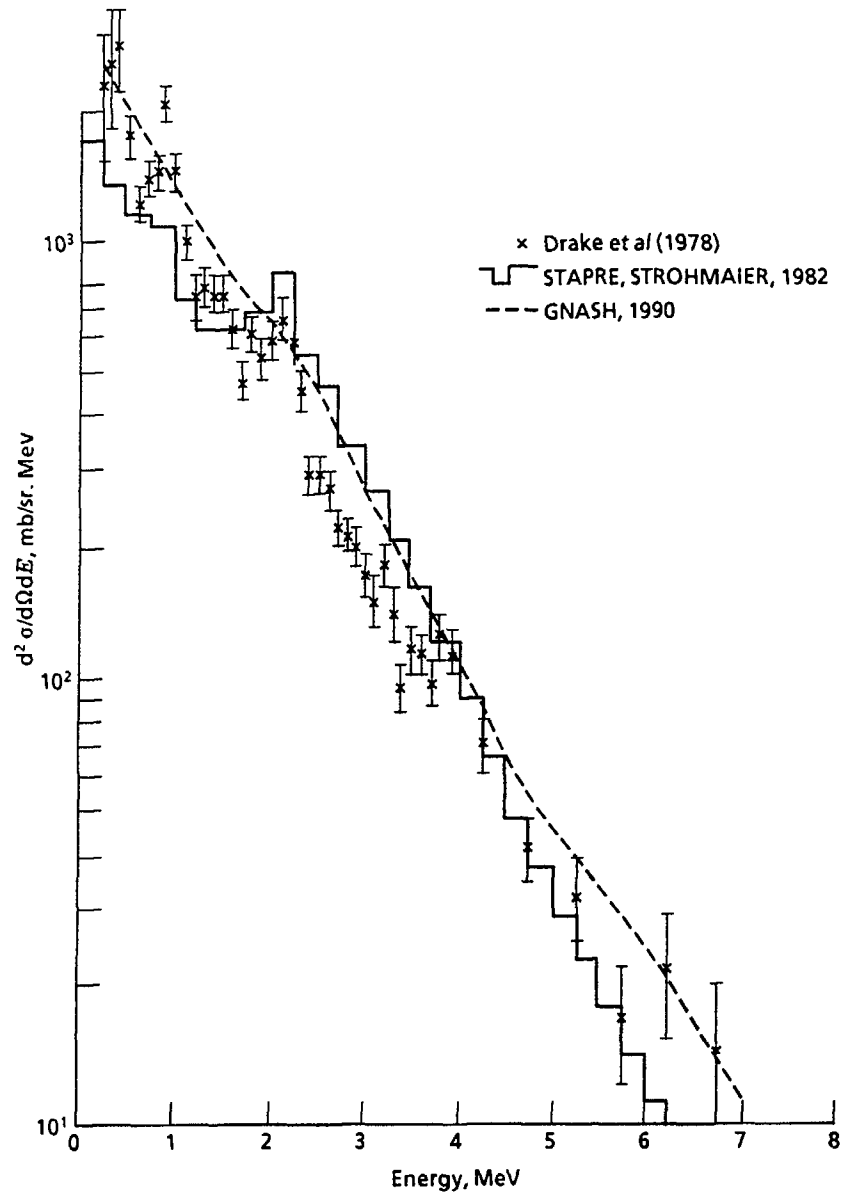


Fig. 12

Comparison of gamma-ray emission spectrum for ^{93}Nb .
 Experimental data are taken from [28].

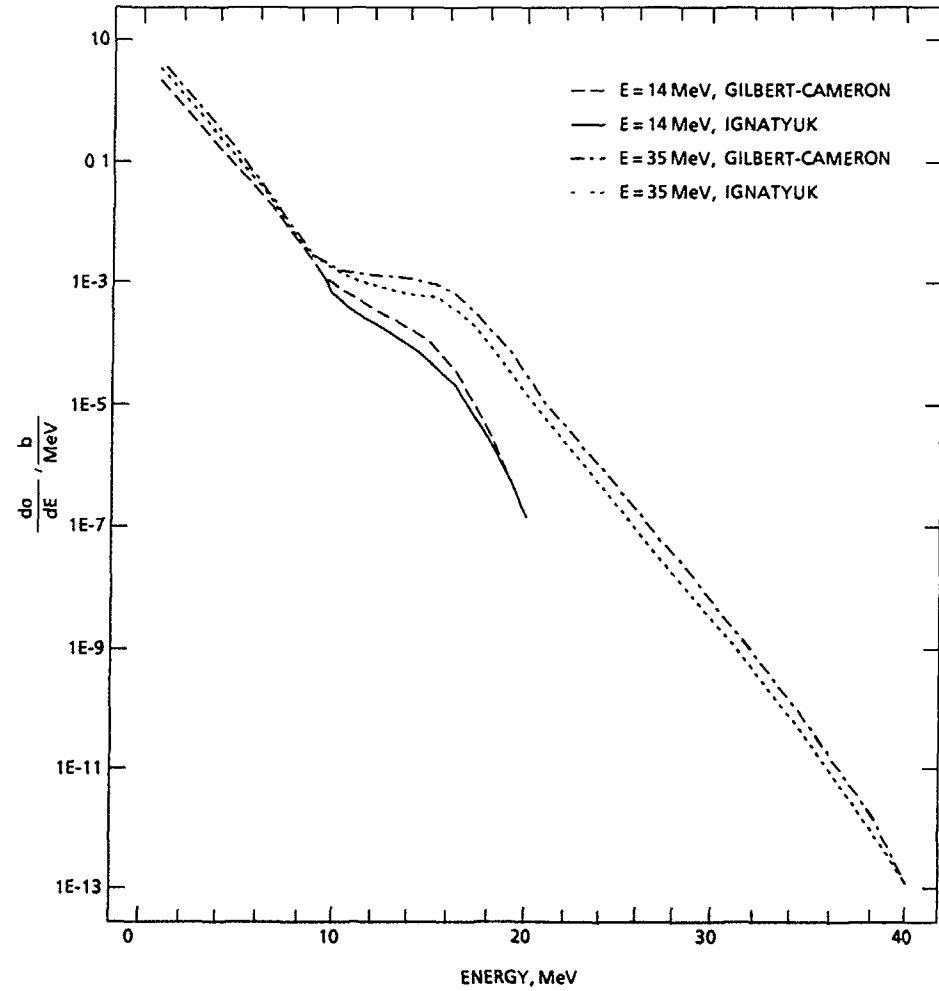


Fig. 13

Dependence of gamma-ray emission spectra for ^{93}Nb on level density models [2] and [6].

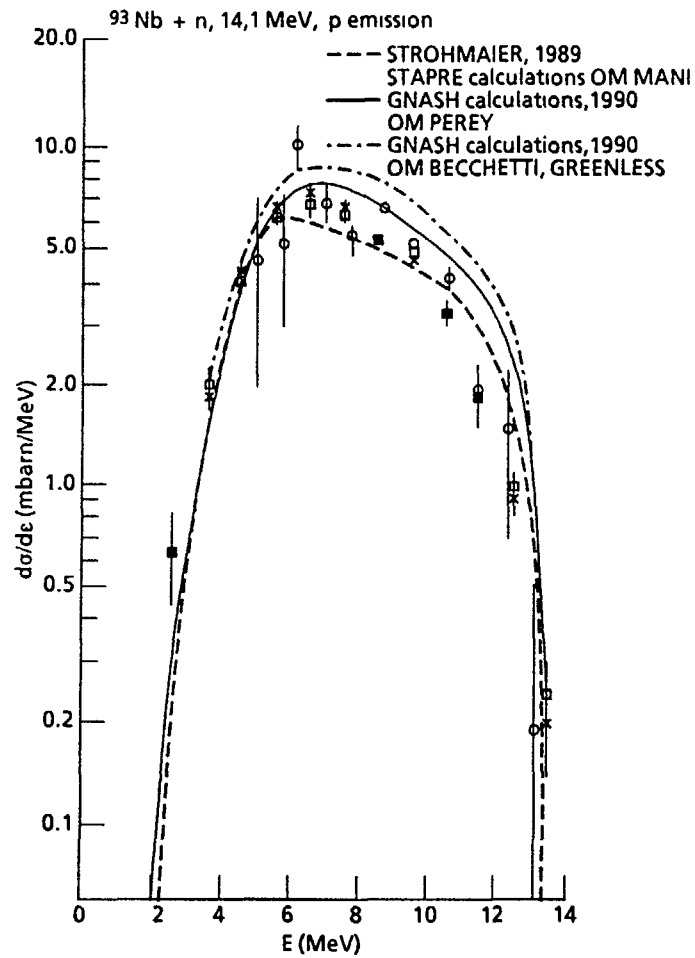


Fig. 14

Calculated proton emission spectra for ^{93}Nb — GNASH calculations, OM Perey [16], LDM - Ignatyuk [6], -.-.- GNASH calculations, OM Becchetti et al. [11], LDM - [6], --- STAPRE calculations [28].

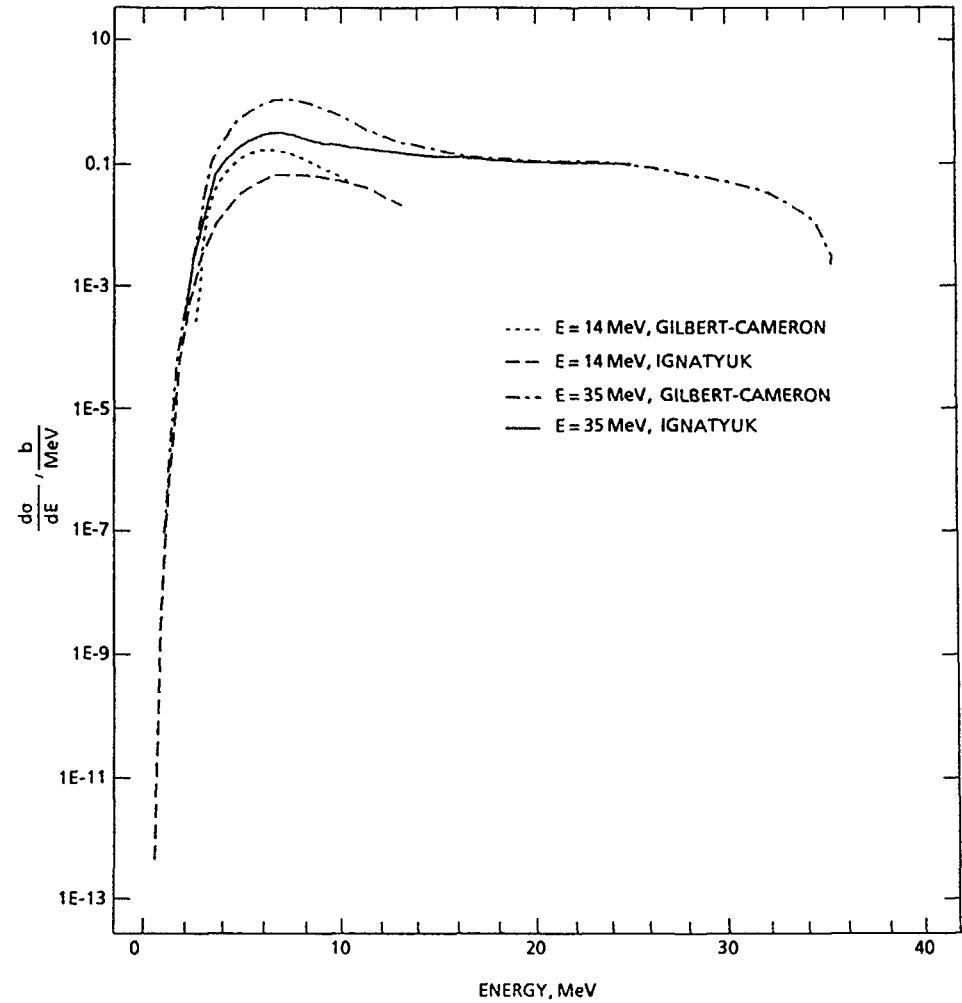


Fig. 15

Dependence of proton emission spectra for ^{93}Nb on level density models [2] and [6].

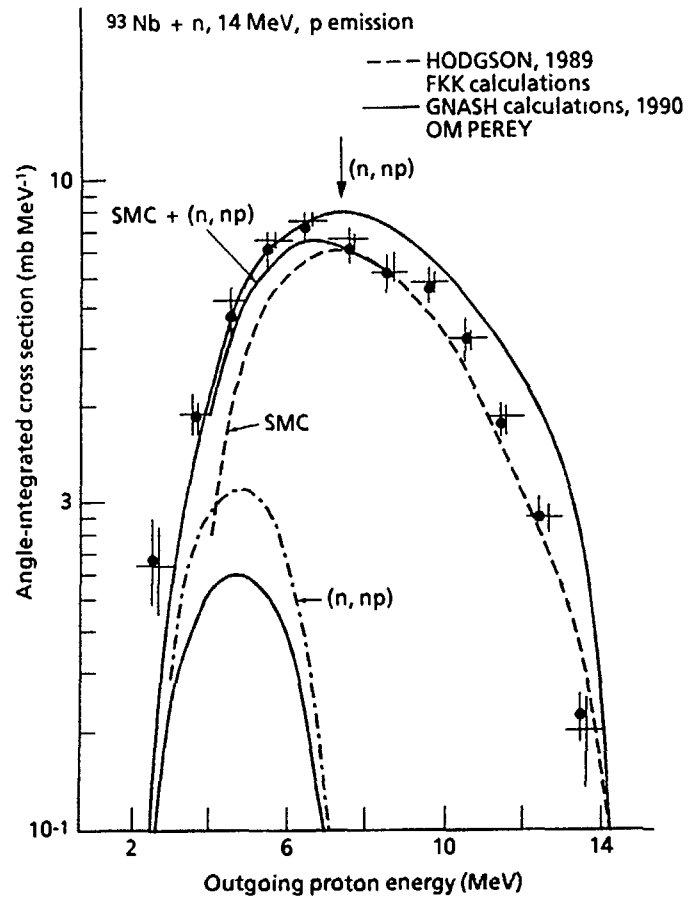


Fig. 16

Comparison of proton emission spectra for ^{93}Nb calculated by GNASH code with FKK calculations [31].

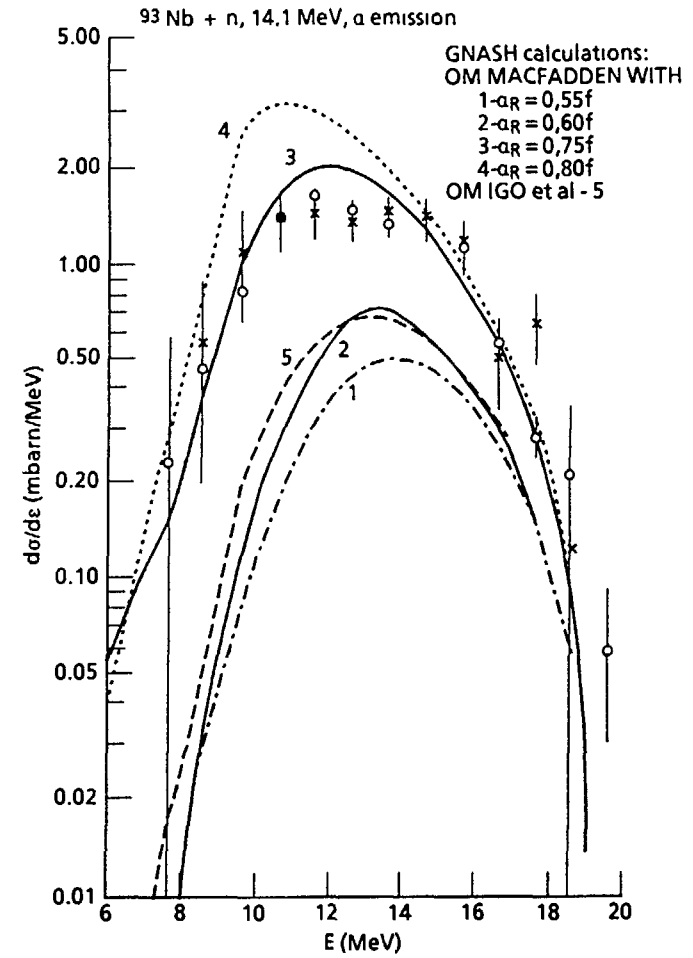


Fig. 17

Alpha emission spectra for ^{93}Nb calculated with OM parameterizations of [18] and [17] with different diffusivity parameters.

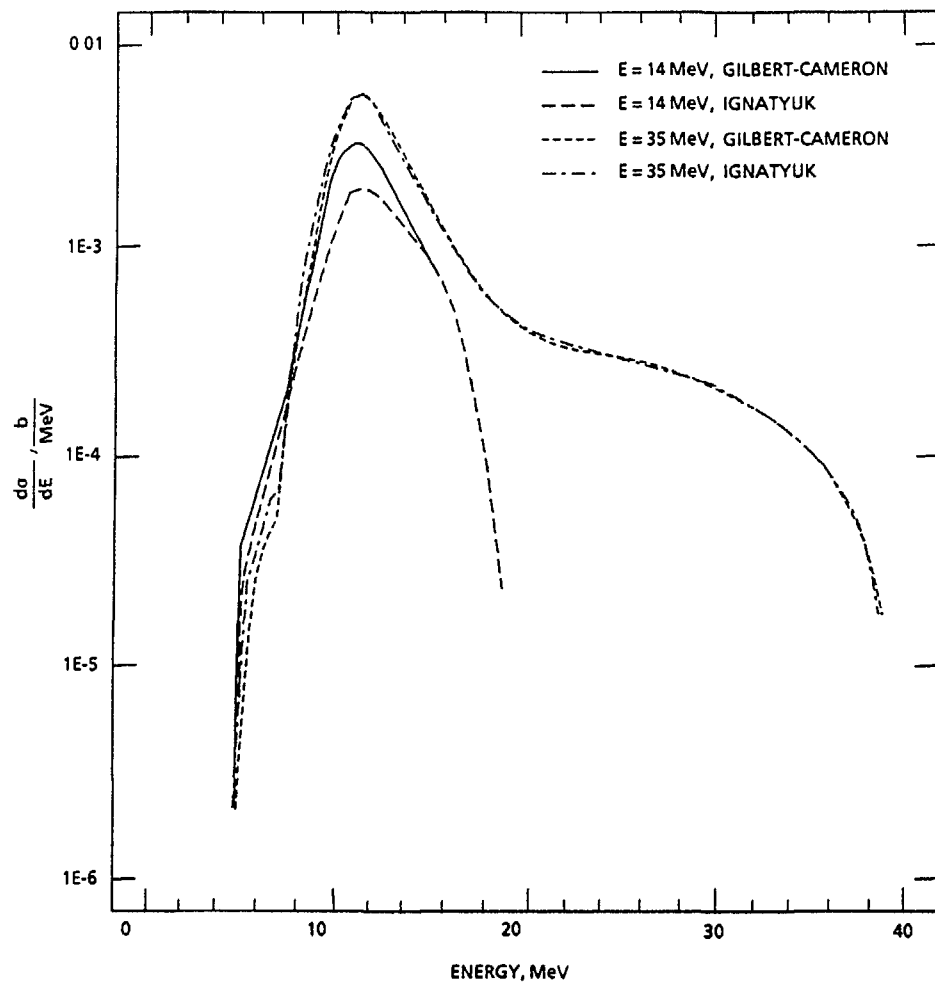


Fig. 18

Dependence of alpha emission spectra for ^{93}Nb on level density models [2] and [6].

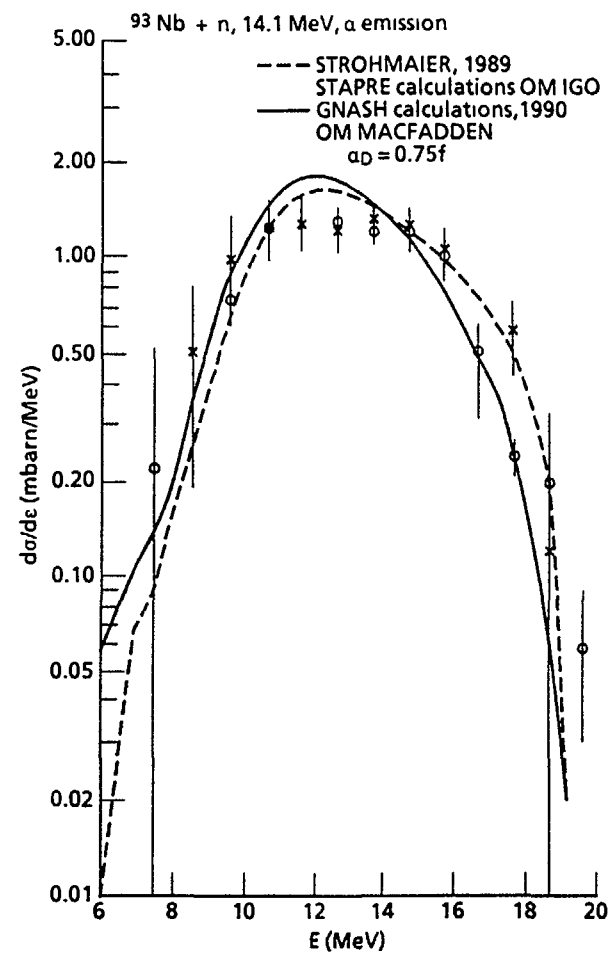


Fig. 19

Comparison of alpha emission spectra for ^{93}Nb calculated by GNASH and STAPRE codes.

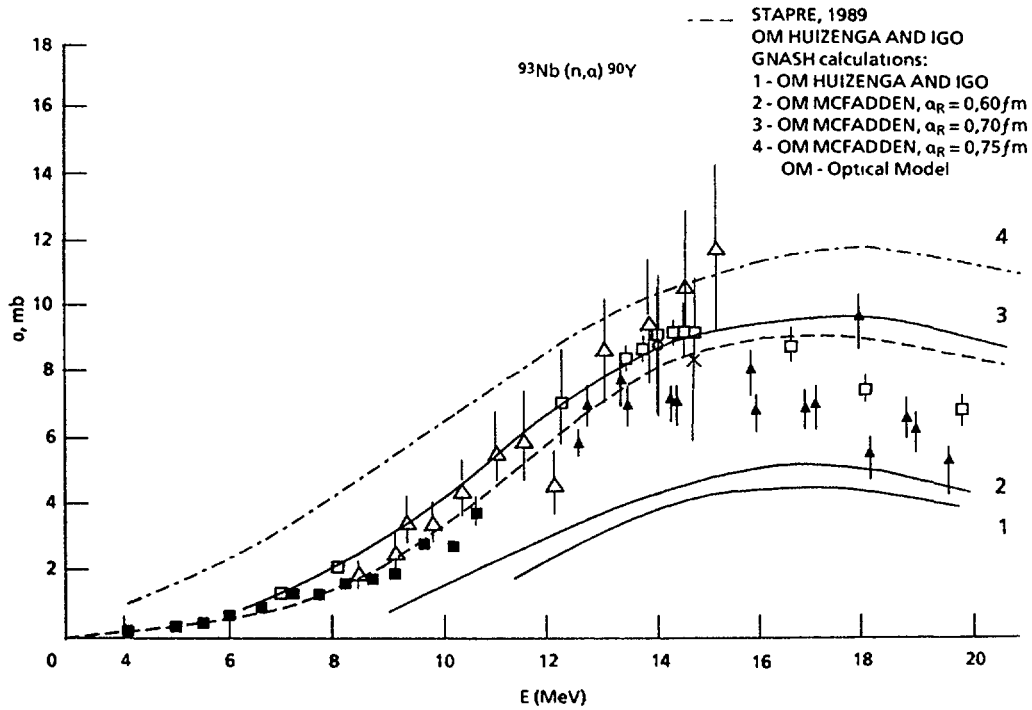


Fig. 20. Results of the (n,α) cross-section for ^{93}Nb calculated with OM parameterizations of [18] and [17] with different diffusivity parameters.

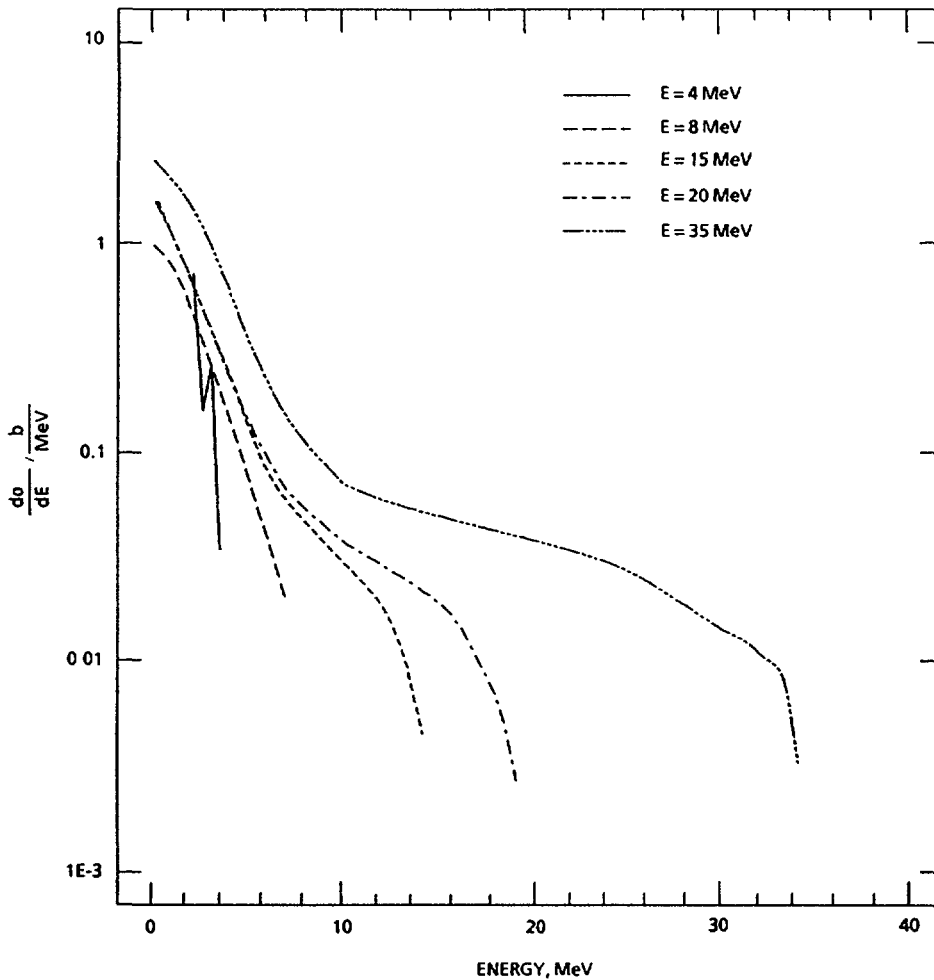


Fig. 21. Dependence of neutron emission spectra on incoming neutron energy for ^{93}Nb .

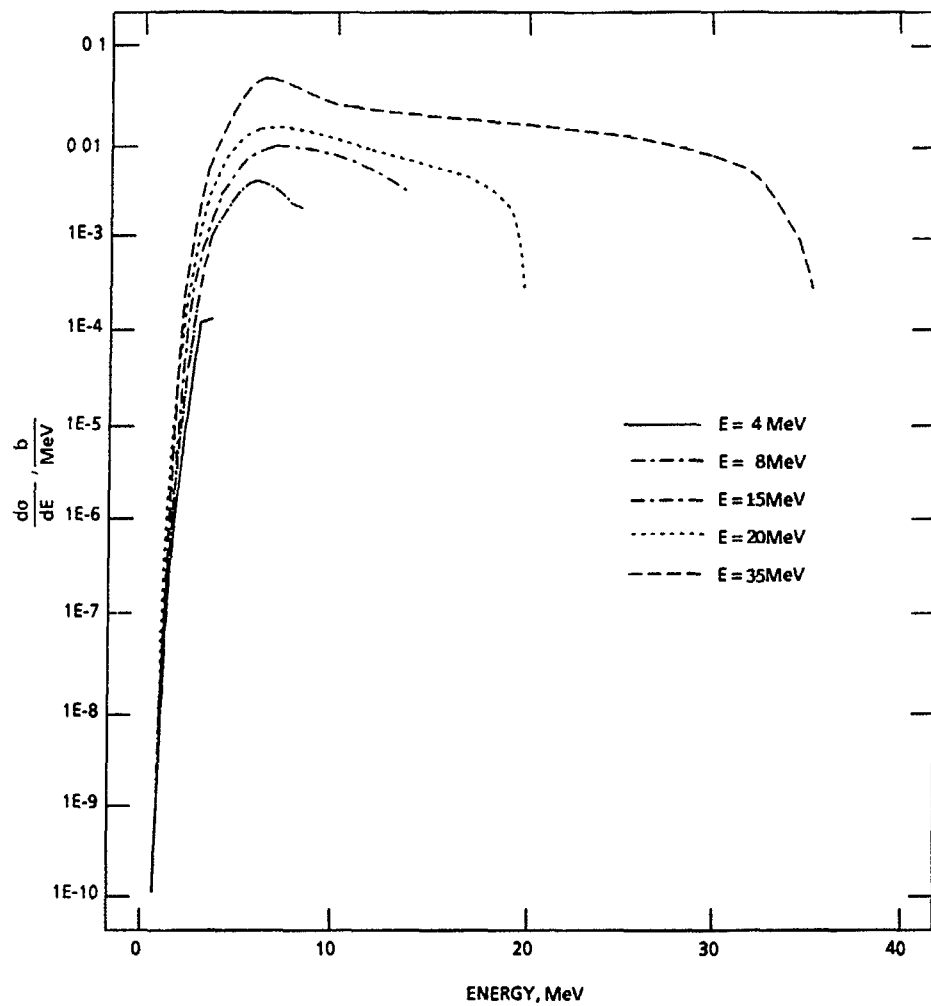


Fig. 22

Dependence of proton emission spectra on incoming neutron energy for ^{93}Nb .

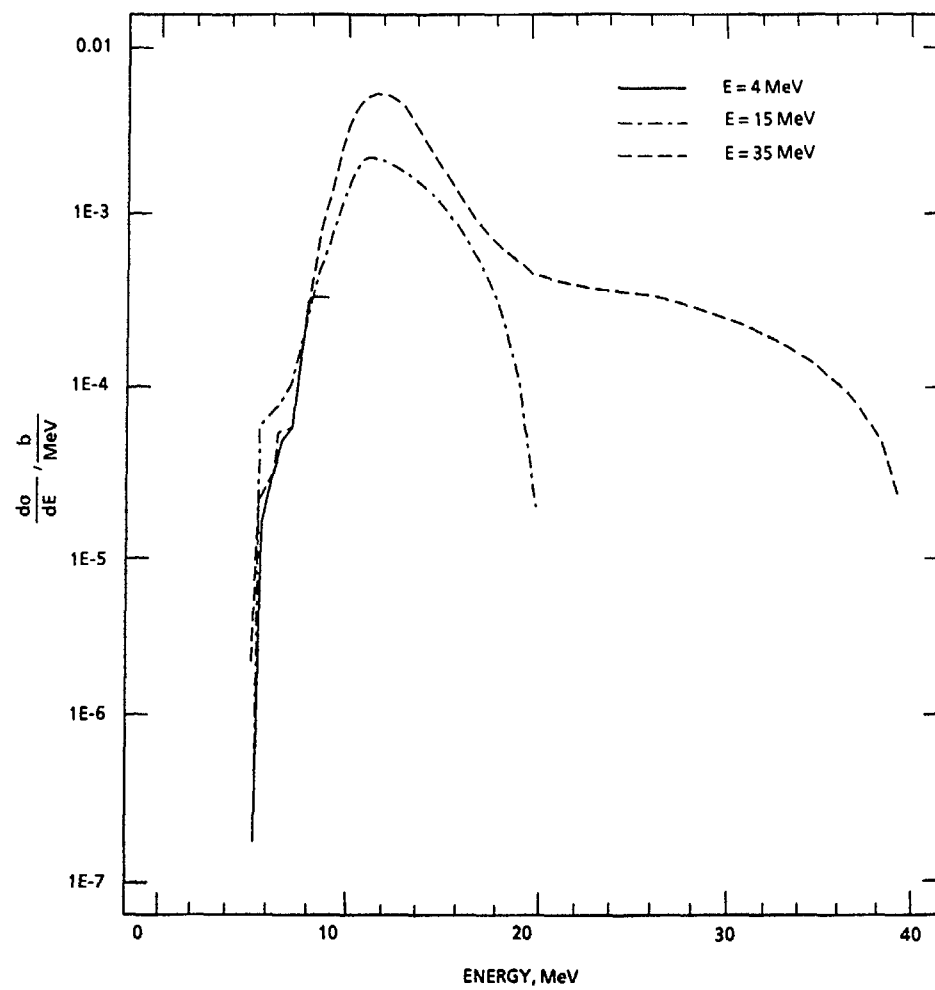


Fig. 23

Dependence of alpha-emission spectra on incoming neutron energy for ^{93}Nb .

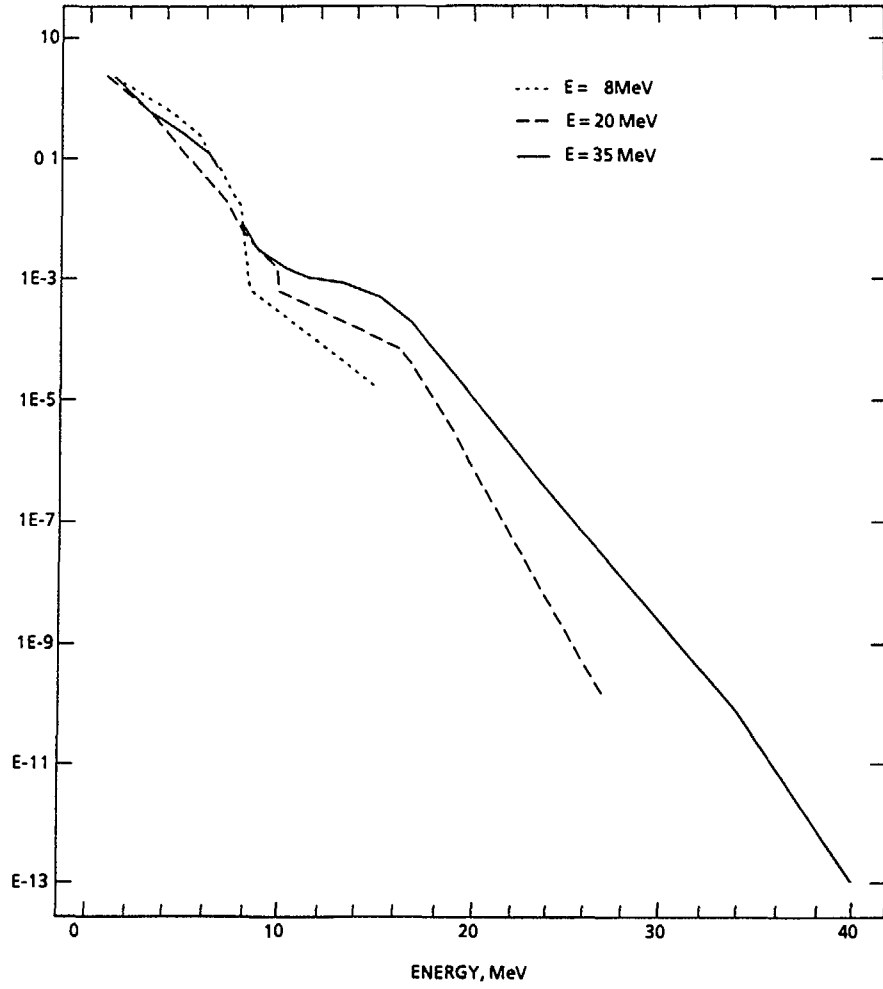


Fig. 24

Dependence of gamma-ray emission spectra on incoming neutron energy for ^{93}Nb .

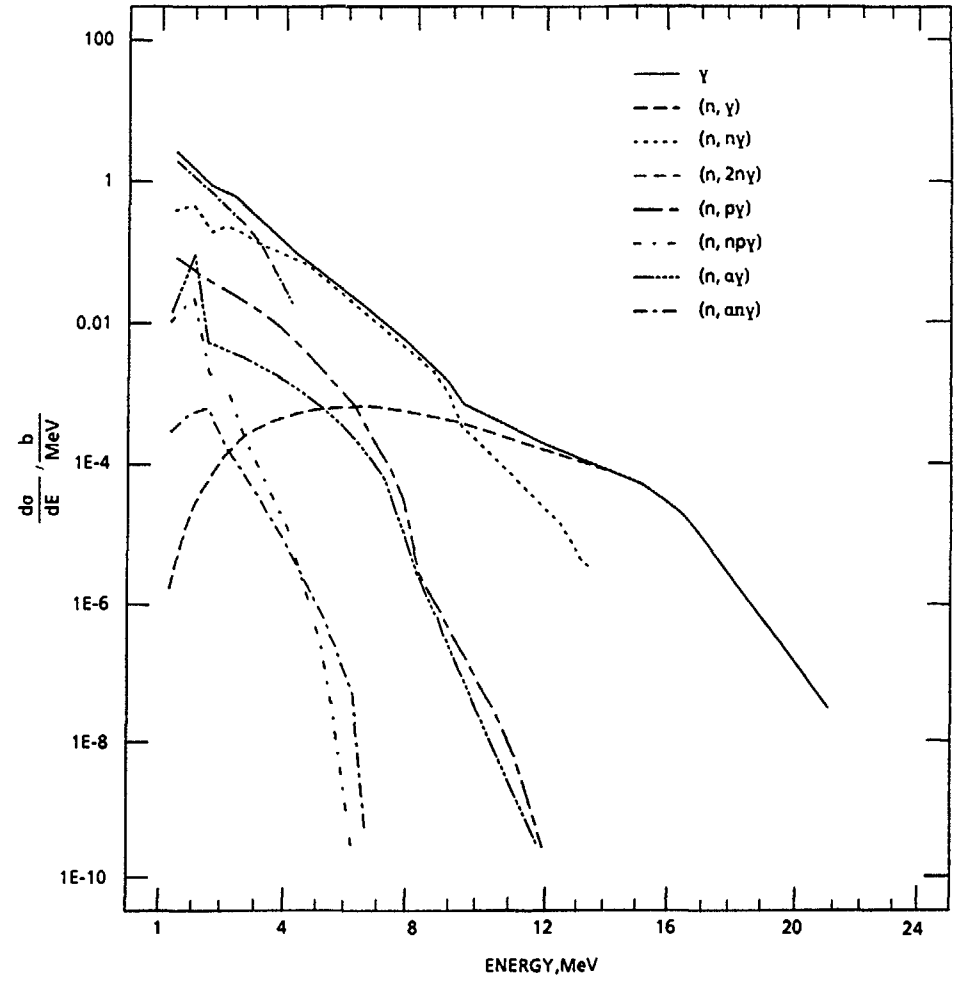


Fig. 25

Contribution of different reactions in gamma-ray spectrum at 14.1 MeV for ^{93}Nb .

Application of the Gilbert-Cameron parameterization [2] may improve the agreement but at 14 MeV only, as at 35 MeV there is practically no sensitivity to level densities. The increase of the diffusibility values (from $a_R = 0.52$ fm to 0.70 fm) has allowed good agreement between the calculated and experimental (n,α) cross-sections and α -emission spectra. But still the problem remains concerning the description of experimental data on the α -particle reaction cross-sections as well as (α,n) -reaction cross-sections as they are greatly overestimated using the diffusibility values adopted for the (n,α) -reaction [32]. The same conclusion on the necessity to increase the diffusibility parameter was reached in [32] ($a_R = 0.64$ fm for Fe) and [33] ($a_R = 0.80$ fm for Fe). The optical model parameters for α -particles do not seem to be satisfactory and all the relevant information available should be analysed to extract the respective parameters.

Dependence of secondary neutrons, protons, alpha- and gamma-spectra on incoming neutron energy is presented in Fig. 21-24. The most significant contribution to the total gamma-spectrum at 14 MeV is due to $(n,2n\gamma)$, $(n,n'\gamma)$ and $(n,p\gamma)$ -reactions to the soft part of the gamma-spectrum and the (n,γ) -reaction to the rigid part.

Conclusions

1. Both the proton and alpha emission spectra show some sensitivity to level density changes, but these and other minor reaction channels can be rather sensitive to other effects resulting from optical model transmission coefficients, pre-equilibrium and direct reaction models, angular momentum transfer, etc.
2. To improve the confidence of cross-section calculations it is necessary to have input from other areas such as higher energy neutron and proton induced reactions.
3. Optical model parameters for α -particles do not seem to be satisfactory and all the relevant experimental information available should be analysed to extract the respective parameters.
4. A phenomenological level density model by Schmidt et al. [34] needs to be included in applied calculations and its predictive power should be tested.

REFERENCES

- [1] Fu, C.Y., A consistent nuclear model for compound and precompound reactions with conservation of angular momentum, ORNL/TM-7042, 1980, 42 p.
- [2] Gilbert, A., Cameron G.W., Canad. J. Phys. 1965, 48, #8, 1446-1496.
- [3] Cook, J.L., Ferguson, M., Musgrove A.R., Aust. J. Phys., 1967, 20, #5, 477-487.
- [4] Dilg, W., Schantl, W., Vonach, H., Nucl. Phys. 1973, A217, #2, 269-298.
- [5] Zongdi Su et al., Proc. of the Intern. Conf. on Nuclear Data for Basic and Applied Science, Santa Fe, 1985; in: Radiation Effects, 1986, 95, 137-140.
- [6] Ignatyuk, A.V., et al., Yad. Fiz. 29 (1978) 875 (in Russian).
- [7] Gruzdevich, O.T., Ignatyuk, A.V., Plyaskin, V.I., in: Neutron Physics, Proc. First International Conference on Neutron Physics, Kiev, 14-18 September 1987, Moscow 2 (1988) 96-101 (in Russian).
- [8] Fu, C.Y., Nuclear Science and Engineering, 1986, 92, 440.
- [9] Fu, C.Y., Nuclear Science and Engineering, 1984, 86, 344.
- [10] Capote, R., et al., in: Neutron Physics, Proc. First International Conference on Neutron Physics, Kiev, 14-18 September 1987, Moscow, 2 (1988) 107-114 (in Russian).
- [11] Becchetti, F.D., Greenlees, G.W., Phys. Rev., 1969, 182, #4, 1190-1209.
- [12] Wilmore, D., Hodgson, P.E., Nucl. Phys., 1964, 55, #4, 673-694.
- [13] Rapaport et al., Nucl. Phys. 1979, A330, #1, 15-28.
- [14] Arthur, E.D., Young, P.G., Rept. LA-8626-MS (ENDF-304) and Proc. Int. Symp. on Neutron Cross-sections from 10 to 50 MeV, Brookhaven, 1980, p. 731.

- [15] Konshin, O.V., Proc. of the Advisory Group Meeting on Nuclear Theory for Fast Neutron Nuclear Data Evaluations, Beijing, 12-16 October 1987, IAEA 1988, p. 85-94.
- [16] Perey, F.G., Phys. Rev. 1963, 131, 745.
- [17] McFadden, L., Satchler, G.R., Nucl. Phys. 1966, 84, 177.
- [18] Huizenga, J.R. and Igo, G., Nucl. Phys., 1962, 29, 462.
- [19] Young, P.G., Proc. of the Meeting on Use of the Optical Model for the Calculation of Neutron Cross-sections below 20 MeV, Paris, 1986, p. 127-145.
- [20] Young, P.G. and Arthur, E.D., LA-6947, 1977.
- [21] Grimes, S.V., et al., Phys. Rev., 1979, C19, 2127.
- [22] Plyujko, V.A., Yad. Fiz. 27 (1978) 1175-1182 (in Russian).
- [23] Fu, C.Y., Proc. of the Specialists' Meeting on Pre-Equilibrium Nuclear Reactions, Semmering, Austria, 10-12 Feb. 1988, p. 285-291.
- [24] Fu, C.Y., Proc of the Symp. on Neutron Cross-sections from 10 to 50 MeV, Report BNL-NCS-51245, BNL, Brookhaven, 1980, Vol. 2, p. 675.
- [25] Fu, C.Y., Nucl. Sci. Eng. 1988 (in press).
- [26] Kalbach, C., "Systematics of Continuum Angular Distributions. Extensions to High Energies", Los Alamos Nat. Lab., LA-UR-87-4139 (1987).
- [27] Takahashi, A., et al., Double and Single Differential Neutron Emission Cross-sections at 14.1 MeV, Vol. 1 and 2, Japan At. En. Commission, 1987.
- [28] Strohmaier, B., Ann. Nucl. Energy, 1989, 16, 461.

- [29] Arthur, E.D., Guenther, P.T., Smith, A.B., Proc. of the NEANDC Meeting on Nuclear Level Density, Bologna, Italy, 15-17 November 1989.
- [30] Frehaut, J., Bovin, A., Bois, R. et al., Proc. Symp. Neutron Cross-Sections from 10 to 50 MeV, Upton, New York 1980, V.1, p.399.
- [31] Koumdjieva, N. and Hodgson, P.E., J. Phys. G.: Nucl. Part. Phys., 1989, 15, 1689.
- [32] Avrigeanu, M., Ivascu, M. and Avrigeanu, V., Z. Phys. A. - Atomic Nuclei, 1990, 335, 299.
- [33] Bychkov, V.M., Zelenetskyi, A.B., Paschenko, A.B., Proc. of the Conference on Neutron Physics, Kiev, 1987, V.2, p.102.
- [34] Schmidt, K.H., Delagrange, H., Dufour, J.P. et al., Z. Phys. A. - Atoms and Nuclei, 1982, 308, 215.

ISOTOPIC EFFECTS AND REACTION MECHANISMS INDUCED BY FAST NEUTRONS

IN THE MASS RANGE $A \approx 50$

M. Avrigeanu and V. Avrigeanu
Institute for Physics and Nuclear Engineering
P.O. Box MG-6, Bucharest, Romania

Abstract

A test of generalized GDH pre-equilibrium emission model and Hauser-Feshbach statistical model predictions across the valley of stability, in the mass region $A \approx 50$, has been performed. Both the absolute cross section values and the "steepness" of the isotope trend have been obtained in good agreement with the experimental data. By using the calculated cross sections, the fast neutron reaction isotope effect has been discussed. The applicability of the generalized Q_{gg} -systematics of deep inelastic collisions between complex nuclei has been extended to fast neutron reactions.

1. Introduction

The significant improvements made in recent years in the prediction and interpretation of non-compound contributions in fast neutron induced reactions as well as the availability of many new experimental data have led to the necessity to perform re-evaluations of fast neutron reaction data for structural elements and isotopes (Fe, Cr, Ni and some others) most important for fission and fusion reactors. The pre-equilibrium and statistical emissions from the composite nuclei formed in these reactions are rigorously described by the master-equation exciton model [1] or the quantum-mechanical theory of Feshbach, et al. [2]. On the other hand, semiclassical pre-equilibrium emission models coupled with the Hauser-Feshbach statistical model have been proved valuable in the analyses of large experimental data bases. The unitary account of a whole body of related experimental data for isotope chains of neighbouring elements (e.g., Cr, Fe and Ni [3]), over a large incident energy range, has increased the predictive capability of these calculations.

Complementary analyses of cross section values at an incident energy of 14.7 MeV are able to provide both: (a) tests of model predictions across the valley of stability [4], a large experimental data base existing at this energy, and (b) unknown cross section prediction with higher accuracies, relative to gross systematics of the isotope effect [5]. These are also goals of this work, following a previous analysis [3] of consistent pre-equilibrium emission and statistical model calculations of (n,p) , (n,α) , and $(n,2n)$ reaction cross sections for $^{50,52,53}\text{Cr}$, $^{54,56}\text{Fe}$ and $^{58,60}\text{Ni}$ isotopes, used to validate a realistic approach for nuclear level densities at excitation energies up to 40 MeV. An attempt for a better understanding of the importance of various reaction mechanisms for these processes, as well as of their parameter systematics, is also performed. Use of more general concepts of nuclear reactions, like the Q_{gg} -systematics of the deep inelastic collisions between complex nuclei [6], has been made in this respect.

The nuclear models used in the reported calculations are briefly reviewed in Sec. 2. A comparison between the calculated and experimental cross sections at an incident energy of 14.7 MeV is given in Sec. 3. A

discussion of the isotope effect for the (n,p), (n, α), (n,2n) and (n,n') reactions is presented in Sec. 4, including the validation of the generalized Q_{gg} -systematics for the fast neutron induced reactions. Conclusions are given in Sec. 5. Preliminary results were given elsewhere [7], while the detailed analysis of the consistent parameter set can be found in [3,8,9].

2. Nuclear Models and Parameters

The Distorted Wave Born Approximation (DWBA) method has been used to describe the neutron direct inelastic scattering on discrete excited nuclear states by means of the code DWUCK4 [10], while the phenomenological pre-equilibrium emission Geometry-Dependent Hybrid (GDH) model [11,12] (included in the computer code STAPRE-H [13], a local version of STAPRE [14]) has been proved able to account for the same process in the continuum [15]. The spherical optical model potential (OMP), used for the calculation of the transmission coefficients within the pre-equilibrium and statistical models, and a conventional collective form factor have been involved. The deformation parameters have been derived from the results of similar macroscopic DWBA analyses of (n,n') and (p,p') data, by imposing the condition of equal deformation lengths. Typical excitation functions of the neutron direct inelastic scattering on the discrete levels for nuclei of interest are shown elsewhere [3], the uncertainties due to uncertainty in the deformation parameter being around 15% [15].

Pre-equilibrium emission has been described by using a generalized version of the GDH model [11,12]. The generalization concerns the inclusion of: (a) angular momentum and parity conservation [8,17] and (b) alpha-particle emission [3]. Moreover, the consistency of the exciton state density, used within the GDH model, and the nuclear level densities involved in the statistical model calculations has been obtained [18]. The pairing and two-fermion system corrections to the exciton state density of Williams [19] have been taken into account in this respect, by using a single set of two-fermion level density parameters.

The multi-step Hauser-Feshbach-Moldauer model calculations were performed by taking into account the neutron, proton, alpha-particle and gamma-ray competition. The input parameters other than the level density at higher excitation energies have been determined by a consistent analysis of various independent experimental data (s-wave neutron strength functions, neutron total cross sections, (p,n) reaction cross sections in the sub-Coulomb energy range and (n,p) reaction data in the first 2-3 MeV of the excitation functions, low-lying discrete levels and s-wave neutron resonance spacings). The particle transmission coefficients and the other OM data were calculated by using the subroutine SCAT2 [20] (also included in STAPRE-H). The same OMPs have been employed in the all three reaction-mechanism models (DWBA, GDH and Hauser-Feshbach). The use of a consistent set of input parameters within consistent pre-equilibrium emission and statistical model calculations finally allowed the establishing of a realistic nuclear level density approach. It was obtained [16] by taking into account the semi-empirical Back-Shifted Fermi Gas (BSFG) model for excitation energies lower than 12 MeV and the realistic analytical formula of Schmidt et al. [21] for higher excitations. The interpolation rule, suggested by microscopic level density calculations, has been obtained through the comparison of the calculated and experimental excitation functions of the (n,p) and (n,2n) reactions on $^{50,52}\text{Cr}$, $^{54,56}\text{Fe}$ and $^{58,60}\text{Ni}$ isotopes [3].

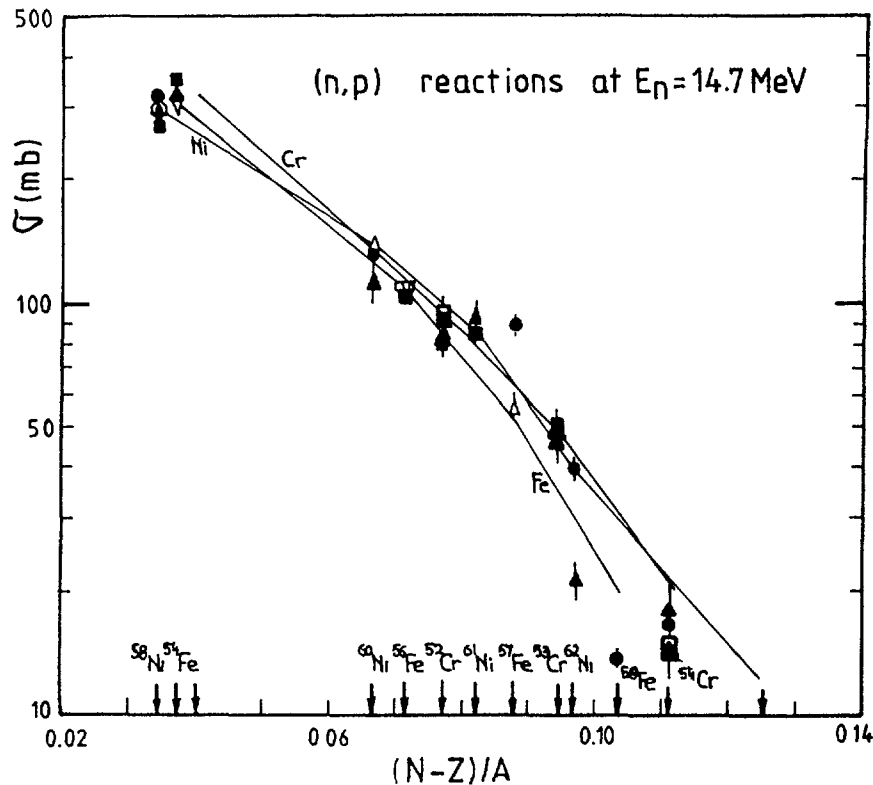


Fig. 1. Comparison between the calculated (solid lines) and experimental cross sections (given in Table I) for (n,p) reaction induced by 14.7 MeV neutrons, versus the asymmetry parameter $(N-Z)/A$ of the target nucleus. The arrows at the bottom of the figure correspond to the asymmetry values for the stable isotopes of Cr, Fe and Ni in included in the present analysis, those for which there are shown experimental data being specified. Experimental data: Δ [31], \square [24], \blacktriangle [5], \square [30], \diamond [34], ∇ [28], \blacksquare [25], \blacktriangle [22], \bullet [27], \blacklozenge [26], \blacklozenge [33].

3. Reaction Cross Sections at 14.7 MeV

First, a good agreement between the calculated and experimental cross sections has been obtained for all types of the available data. Thus, cross sections for (n,p), (n, α), (n,2n) and [(n,n'p)+(n,pn)+(n,d)] reactions measured by the activation technique (Figs. 1-4 and Tables I and II), as well as charged particle emission data (Table I) have been taken into account. It can be emphasized that both the present agreement and the one obtained for the (n,p), (n, α), and (n,2n) excitation-function data [3] have been found with no further change of the model parameters. In conclusion, both the absolute cross section values and the "steepness" of the isotope trend - a very sensitive test of the reaction mechanism model [4,22] - have been given by the present calculation method with no free pre-equilibrium emission parameters.

The second point concerns the accuracy of the predicted reaction cross sections for cases in which experimentally data are missing. In the early 70's Qaim and Molla [5] stated that small-mass-region studies for series of isotopes are able to predict unknown cross sections more accurately than gross isotope-effect systematics. Finally, the difference existing between the present calculated and experimental cross sections, 3-10%, could be claimed as the errors of the predicted values.

Under these circumstances the calculated cross sections, taken as an evaluation, have been used to study the factors affecting the isotope

Table I. Comparison of calculated and experimental^{a)} cross sections for nuclear reactions induced by 14.7 MeV neutrons.

Target nuclide	$\sigma_{(n,p)}$ (mb)			$\sigma_{(n,xp)}$ (mb)			$\sigma_{(n,\alpha)}$ (mb)			$\sigma_{(n,x\alpha)}$ (mb)			$\sigma_{(n,2n)}$ (mb)		
	calc.	exp.	Ref.	calc.	exp. ^{b)}	Ref.	calc.	exp.	Ref.	calc.	exp.	Ref.	calc.	exp. ^{a)}	Ref.
50Cr	326.6			747.6	830(100)		69.3			70.3	121.0(85)	52	21.1	24 (5)	34
											94 (15)	32		21.9 (5)	55
											76.4(9)	53		20.4(11)	51
52Cr	95.4	94(10)	34	167.4	180(25)		39.6			39.8	40.2(36)	52	359	377(31)	56
		80(6)	22								36 (6)	32		361(22)	51
		91(3)	35												
		82(8)	36												
53Cr	48.5	48(7)	22	53.5			43.2			43.6	45.1(37)	52	877		
		50(4)	35												
		46(6)	36												
		47.2(17)	37												
54Cr	20.8	15(4)	34	20.9			16.5	13.4(12)	48	18.0	37.2(30)	52	778		
		18(3)	22					15.0(16)	49						
		14(2)	36												
		16.4(5)	37												
54Fe	306.7	308(11)	38	858.2	900(110)		78.4	84.0(75)	47	79.4	79(13)	32	13.3	11.9(3)	57
		346(22)	35					88 (10)	24					7.9(7)	37
		307(9)	37					88 (6)	37						
56Fe	109.3	107.6(31)	40	172.4	190(22)		43.3			45.9	41 (7)	32	488	519(41)	58
		110.9(14)	41								44 (2)	54		440(40)	22
		104 (6)	35												
57Fe	51.2	55.4(40)	42	59.0			41.7			46.2			1086		
		89 (5)	37												
58Fe	20.1	13.6(7)	37	20.3			18.9	21.5(20)	50	20.1			833		
58Ni	294.4	295 (23)	43	929	1000(120)		111	125(15)	22	122	106(17)	32	36.7	35 (3)	22
		269 (10)	35											37.7(28)	44
		319.5(120)	37											38.6(21)	59
		292.2(54)	44												
60Ni	138.5	112(12)	22	262.8	325(40)		60.5			77.0	76 (12)	32	415		
		134(11)	47								69.6(31)	54			
		131(4)	37												
61Ni	89.1	92(7)	22	121.8			64.1			77.0			1013		
		84(15)	35												
		84(4)	37												
62Ni	39.2	21.0(25)	22	42.0			22.4	20 (3)	22	74.1			769		
		39.4(15)	37					25.8(33)	47						
64Ni	12.1			12.1			5.11	3.7(2)	37	5.18			963		
								4.28(16)	51						

^aThe uncertainty given is in the last significant figures.

^bRef. 32

effects for these reactions, namely the strong dependence of the reaction cross sections on the target asymmetry parameter $(N - Z)/A$.

4. Proton and α -particle Emission Isotope Effects

4.1. Generalized Q_{gg} -Systematics

The isotope effect for the (n,p) reaction cross sections of 14 MeV neutrons was pointed out by Gardner [51,52] as a Q -value effect. In a systematic study of these data, for medium and heavy mass nuclei, Molla and Qaim [37] interpreted the isotope effect in terms of the proton binding energy, which varies as a function of the $(N - Z)/A$ parameter. On the other hand, Pai et al. [53] showed by means of statistical model calculations that the large changes in the total

Table II. Comparison of calculated and experimental activation cross sections for (n,d)+(n,n'p)+(n,pn) reactions induced by 14.7 MeV neutrons.

Target nucleus	$\sigma_{[(n,n'p)+(n,pn)]}$ (mb)	$\sigma_{(n,d)}$ (mb)	Sum (mb)	$\sigma_{[(n,d)+(n,n'p)+(n,pn)]}$		Ref.
	calculated	exp. ^{a)}		syst. ^{b)}	exp.	
50Cr	421.	12(4)	433		405(65)	33
52Cr	72.0	8(3)	80.0	175(85)		33
53Cr	5.04				12(3)	22
54Cr	0.107				3.0(8)	22
54Fe	452	10(4)	562.	490(150)		33
56Fe	63.1	8(3)	71.1	200(90)		33
57Fe	7.78				11.0(24)	22
58Fe	0.192					
58Ni	635	14(6)	649		619(49)	45
					630(27)	46
					520(50)	33
					656(40)	44
					649(34)	44
60Ni	124.3	11(4)	135	225(110)		33
61Ni	32.7					
62Ni	2.79				7.3(14)	33
64Ni	0.010				3.0(4)	33

^aRef. 32

^bRef. 33

proton emission cross sections between neighbouring nuclei are accounted for by an "effective" Q-value, given by

$$Q'_{np} = Q_{np} + \delta_n - \delta_p \quad (1)$$

where δ_n and δ_p are the depressions of the ground state energies of the related nuclei produced by pairing and shell correlations. Subsequently, Pai proved that this quantity is responsible for the exponential decrease of the cross-section ratio $\sigma'_{np}/\sigma'_{nn}$ [54] or $\sigma'_{np}/\sigma_{non}$ [55], where σ'_{np} is the first-proton cross section, that is, $\sigma'_{np} = \sigma(n,p\gamma) + \sigma(n,pn) + \sigma(n,2p)$, σ'_{nn} is the first-neutron cross section, and σ_{non} is the non-elastic cross section.

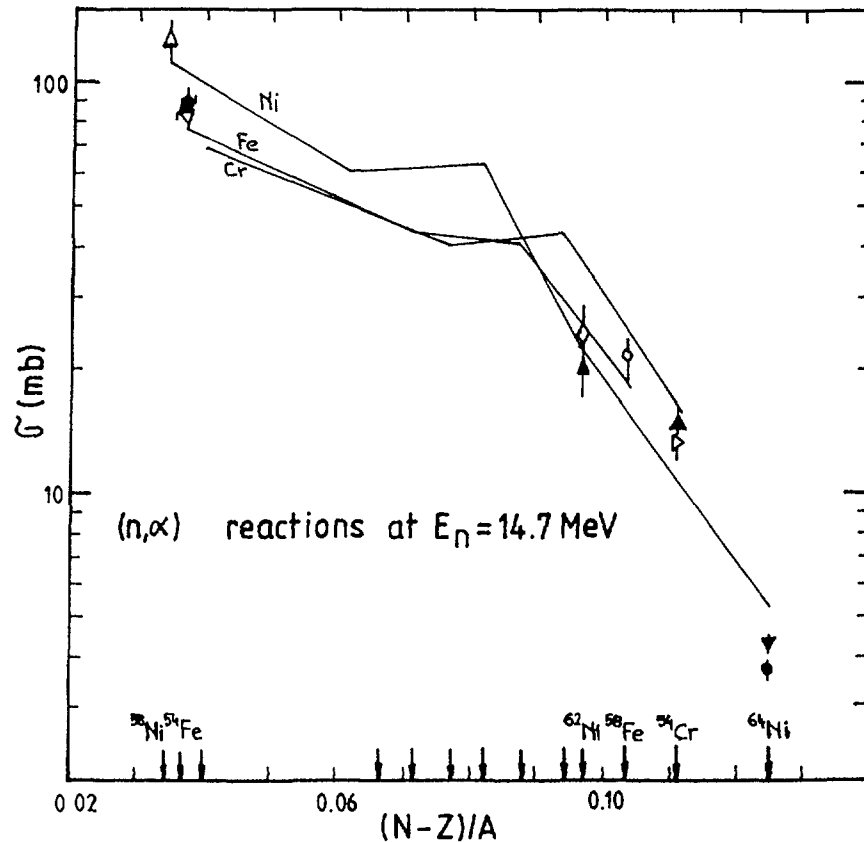


Fig. 2. Same as Fig 1, for the (n,α) reaction Experimental data: \circ [38], \blacktriangle [5], \blacktriangleleft [37], \blacktriangleright [43], \diamond [34], \bullet [27], \blacktriangledown [39].

From a more general point of view, the experimental data for multinucleon transfer reactions in the interaction of heavy ions with nuclei have made evident the role of Q -values even for a complex process. The mechanism of the deep inelastic collisions between two complex nuclei, considered as two-body processes, is associated with the formation of a specific double nuclear system, combining the features of both classical direct processes and compound nucleus decay. An estimation of the production cross sections for individual isotopes and, therefore, determination of the direction in which the double nuclear system evolves, have been allowed by a generalized Q_{gg} -systematics (e.g., [6] and reference therein). This is characterized by the logarithm of the cross sections for the formation of isotopes of a given element lying on straight lines when the abscissa corresponds to the quantity $Q_{gg} - \delta(n) - \delta(p)$, where Q_{gg} is the Q -value of the transfer reaction proceeding as a two-body process with final nuclei in the ground state, and $\delta(n)$ and $\delta(p)$ are non-pairing corrections for the transferred nucleons. Actually, this generalized Q_{gg} -dependence takes into account all the factors effecting the final excitation energy during nucleon transfer. The straight lines corresponding to different final light-product elements have similar slopes, related to a temperature parameter characterizing the partial statistical equilibrium of the double nuclear system.

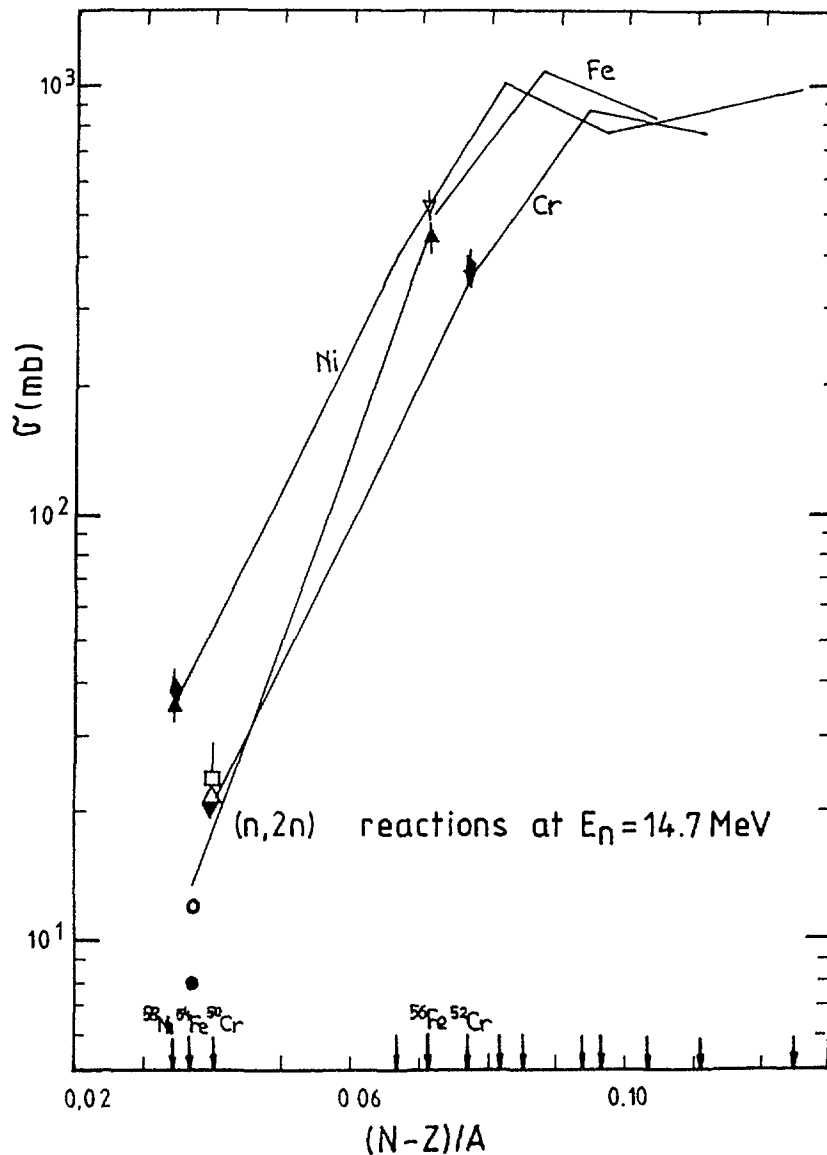


Fig. 3. Same as Fig.1, for the $(n,2n)$ reactions. Experimental data: \triangle [43], ∇ [46], \blacktriangle [5], \circ [45], \blacktriangleright [44], \bullet [27], \blacklozenge [47], \diamond [33], \blacktriangledown [39].

Following the above-mentioned systematics, it seems possible to introduce also for fast neutron induced reactions an empirical effective Q-value given by

$$Q'_{n,x} = Q_{n,x} - \sum_i \Delta_i \quad (2)$$

where the Δ_i are the ground state backshift parameters of the BSFG level density, corresponding to the nuclei reached through the respective x -particle emission. Within the statistical theory the total emission cross section σ'_{nx} for a particle x from a compound nucleus is

$$\sigma'_{nx} = \sigma_{non} \frac{\Gamma_x}{\Gamma_n + \Gamma_p + \Gamma_\alpha} \quad (3)$$

where Γ_n , Γ_p and Γ_α are the partial probabilities for neutron,

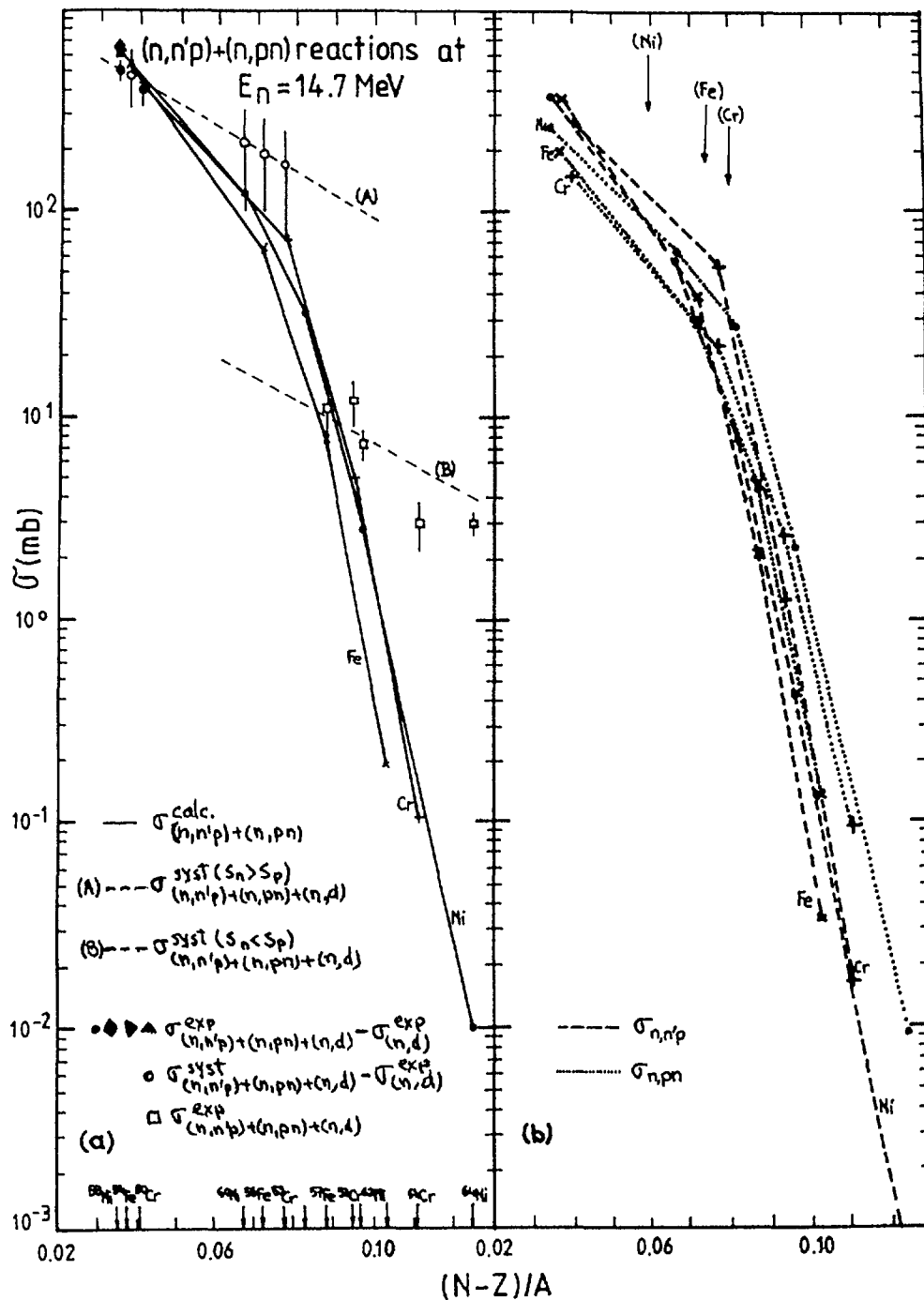


Fig. 4(a). Same as Fig. 1, for $(n,n'p)+(n,pn)$ reactions. The experimental data shown are got by subtracting experimental (n,d) reaction cross sections from the total $[(n,d)+(n,n'p)+(n,pn)]$ reaction cross sections obtained experimentally (full symbols) or based on systematics [33] (open circles). There are also shown total activation cross sections (open squares) when the corresponding experimental (n,d) data are not known. The dashed curves are those established by Qaim [33] as characteristic for the $[(n,d)+(n,n'p)+(n,pn)]$ reaction cross sections of the target nuclei with $S_n > S_p$ (curve A) and, respectively, $S_n < S_p$ (curve B). Experimental data: \bullet [48], \blacktriangle [49], \blacklozenge [30], \blacktriangleright [50]. (b) Calculated cross sections of the $(n,n'p)$ reactions (dashed lines) and (n,pn) reactions (dotted lines) at 14.7 MeV incident energy, for Cr, Fe, and Ni isotopes (+, x, and \bullet symbols, respectively). The arrows at the top of figure indicate the $(N-Z)/A$ values at which the $(n,n'p)$ reaction cross sections become smaller than the correspondent (n,pn) reaction cross sections.

proton, and α -particle emission, respectively; it results [54], by using the constant temperature level density formula,

$$\frac{\sigma'_{nx}}{\sigma'_{nn}} = \frac{\Gamma'_x}{\Gamma'_n} = \exp[(Q'_{n,x} - Q'_{n,n'} - V'_x)/T] \quad (4)$$

where V'_x is an effective Coulomb barrier, and T is a nuclear temperature related to the compound-nucleus evaporating system rather than to a residual nucleus [54]. Thus, the difference $Q'_{np} - Q'_{n,n'}$ of the empirical effective Q -values (2) replaces the former quantity (1), because it represents, in fact, the difference between excitation energy regions or, rather, equal nuclear level densities in the neutron and particle x channels, respectively. The second meaning seems more adequate. Both the reaction Q -values [56] and the difference $Q'_{n,x} - Q'_{n,n'}$ of the effective Q -values for the present (n,p) and (n, α) reactions are shown in Fig. 5. The backshift parameter values have been taken from the previous analysis [3]. There is evidence of correlation between the trends of the reaction cross section logarithm and the effective Q -values difference especially for the (n,p) reactions, with only one exception concerning the neutron-poorest isotope of each element. In this case the (n,pn) reaction cross section has higher values (see below), and thus represents a significant contribution to σ'_{np} .

By using the nuclear model calculation results for the neutron, proton and α -particle total emission cross-sections, one obtains the values of the ratio (4) for protons and α -particles shown in Fig. 6. It could be said that the generalized Q_{gg} -systematics is valid also in the case of fast neutron induced reactions. Unfortunately, even if the effective Q -values (2) can be defined for multiple particle emission reactions, the change of the emitting compound nucleus during the sequential particle emission seems to prevent the extension of these systematics beyond the (n,p) and (n, α) reactions (including most of the respective particle total emission cross sections).

While the above discussion is devoted to the compound nucleus contribution, a special attention has to be paid, in fast neutron reactions, to pre-equilibrium emission. However, taking into account the advanced pairing correction for the exciton-state density calculation [58] within the pre-equilibrium emission model, a significant reduction of this limit is apparent. This pairing correction being exciton configuration dependent, its value P_{n_0} , corresponding to the n_0 initial exciton number (configuration giving the main contribution to the pre-equilibrium emission), is chosen here to estimate the maximum energy $Q - P_{n_0}(x)$ of the pre-equilibrium emitted x particles. The distinct dependence of this revised limit on $(N - Z)/A$, compared to that of the difference $Q'_{n,x} - Q'_{n,n'}$, is also shown in Fig. 5. The relative importance of the systematic variation of these two quantities could be suggested by the presently calculated values of the ratio of the pre-equilibrium to total emission cross sections, for particle x (Fig. 7).

The account of the pre-equilibrium emission on the base of the Q -values may be illustratively used to explain the following point. There is a quite evident difference between the trends of the $\sigma_{n\alpha}$ (Fig. 2) and the $(Q'_{n,\alpha} - Q'_{n,n'})$ -values (Fig. 5b), respectively,

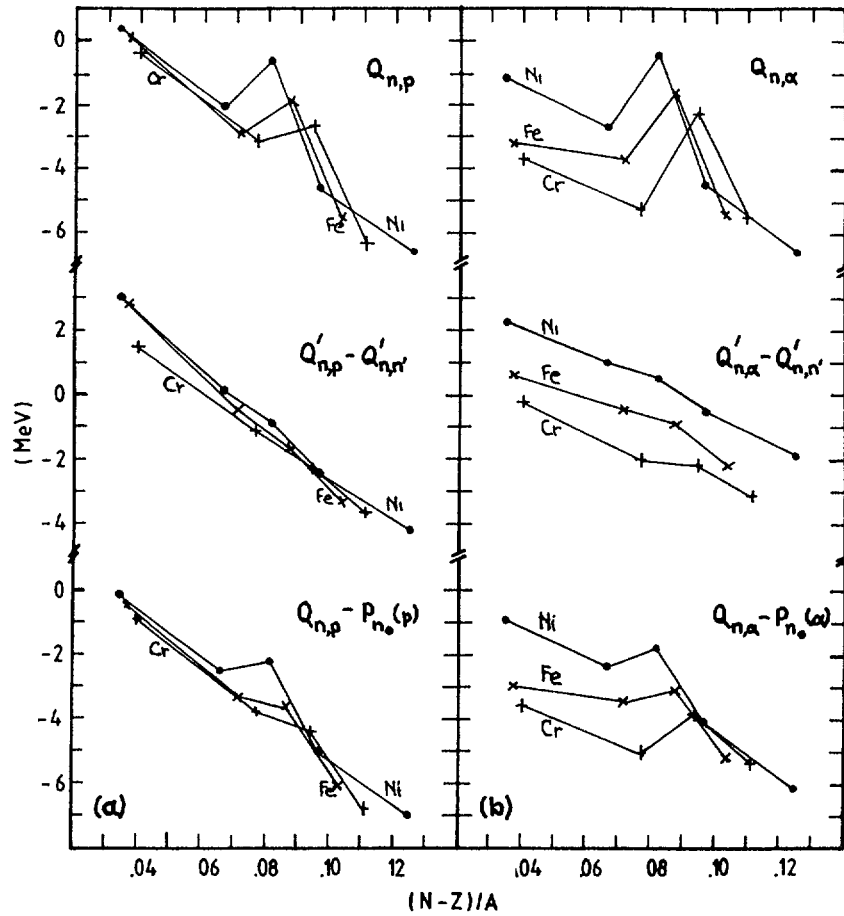


Fig. 5. (a) The dependence on $(N - Z)/A$ parameter of the (n, p) reaction Q - values [56], the difference $Q'_{n,p} - Q'_{n,n'}$ of the effective Q values defined in text, and the maximum energy of the pre-equilibrium emitted protons, for Cr, Fe, and Ni isotopes (+, x, •), $Q_{n,p} - P_{n_0}(p)$. (b) Same as (a), for the (n, α) reaction.

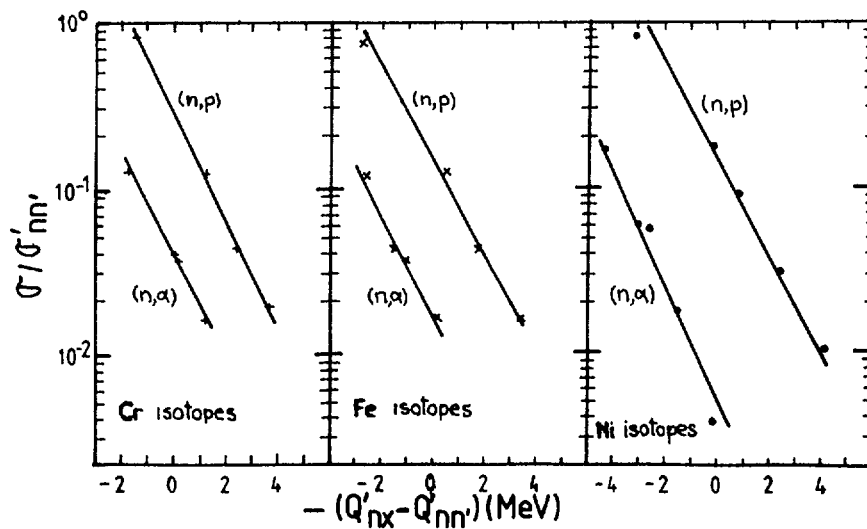


Fig. 6. The dependence of the ratio $\sigma'_{nx}/\sigma'_{nn'}$, at 14.7 MeV incident energy, where $x=n, p$, on the difference $Q'_{n,x} - Q'_{n,p}$ of the effective Q - values defined in text, for Cr, Fe and Ni stable isotopes.

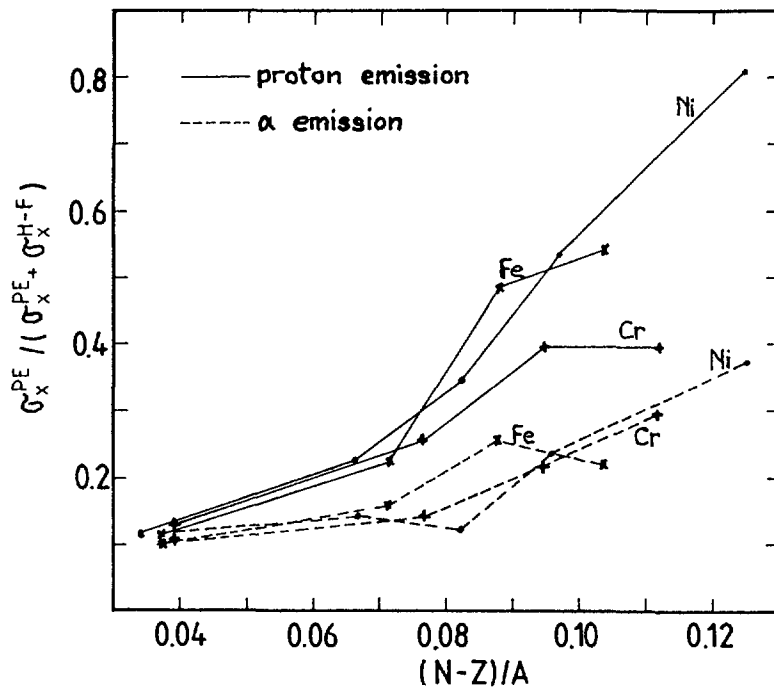


Fig. 7. Ratios of the pre-equilibrium emission to the total "first" particle emission cross sections, for protons and α -particles, in 14.7 MeV neutron induced reactions on the stable isotopes of Cr, Fe and Ni, versus the asymmetry parameter of the target nuclei.

versus $(N - Z)/A$. The reaction cross sections show a local maximum for the odd- A stable isotope of each element, while the Q' -value differences are rather decreasing. However this behaviour could be explained by the corresponding maxima shown by the $(N - Z)/A$ dependence of the pre-equilibrium emission energy limit $Q_{n,\alpha} - P_{n_0}(\alpha)$ (Fig. 5b).

4.2. The $(n, n'p) + (n, pn)$ reactions

A further comment is required by the $(n, n'p)$ reaction analysis. Deuteron emission was not considered within the present pre-equilibrium and statistical model calculations due to its direct main component. The calculated $(n, n'p)$ and (n, pn) reaction cross sections are summed with the experimental (n, d) reaction cross sections [23] and, finally, compared with the experimental or systematic [48] activation cross sections for the $[(n, d) + (n, n'p) + (n, pn)]$ reaction (Table II). Alternatively, to get a sight on the $[(n, n'p) + (n, pn)]$ reaction isotope effect, experimental data are gained by subtracting the (n, d) reaction experimental cross section from the experimental or systematic cross sections of the $[(n, d) + (n, n'p) + (n, pn)]$ processes (Fig. 4a). For some nuclei with higher asymmetry parameters ($^{53,54}\text{Cr}$, ^{57}Fe , $^{62,64}\text{Ni}$), only the total activation cross sections are shown in Fig. 5; (n, d) reaction data are missing. The following supplementary conclusions could be derived, in connection with the exhaustive analysis of the gross trends in (n, p) , (n, d) and $[(n, d) + (n, n'p) + (n, pn)]$ reaction cross sections made by Qaim [48]:

- (a) Unknown cross sections can be predicted by model calculations with accuracies higher than those from gross systematics.

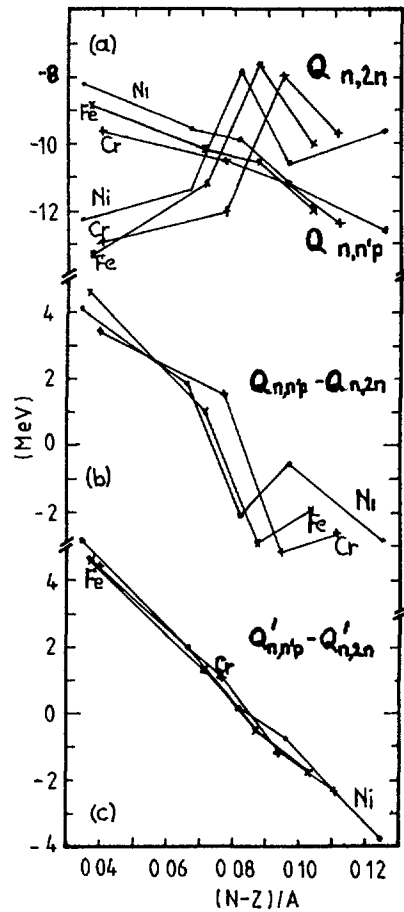


Fig. 8. (a) The $(n,2n)$ and $(n,n'p)$ reaction Q -values versus the asymmetry parameter $(N-Z)/A$ of the target nucleus, for the stable isotopes of Cr, Fe, and Ni; the same dependence for their difference (b), as well as for the difference of the corresponding effective Q -values (c).

- (b) The $[(n,n'p)+(n,pn)]$ reaction cross sections display nearly the same exponential decrease with the asymmetry increase as the (n,p) reaction cross sections. Actually, this behaviour results by summing the two channel contributions with similar trends. Thus, the (n,pn) reaction channel follows the (n,p) reaction channel, the sum of the corresponding cross sections accounting for "first" proton emission which is exponentially decreasing as discussed above. Moreover, the (n,pn) reaction cross section is additionally reduced by the increase of proton binding energy with asymmetry parameter increasing. On the other hand, the $(n,n'p)$ reaction plays a dominant role for the daughter nuclei with $S_n > S_p$ [48]. The separate calculated cross sections of the $(n,n'p)$ and (n,pn) reactions are shown in Fig. 4b. Once the Q -values difference $Q_{n,n'p} - Q_{n,2n}$ becomes lower even than the effective Coulomb barriers (Fig. 8b), the $(n,n'p)$ reaction cross sections are faster decreasing than those of the (n,pn) reactions (Fig. 4b). Further considerations could make use of the effective Q -value difference

$$Q'_{n,n'p} - Q'_{n,2n} = [Q'_{n,p} - Q'_{n,n'}]_{A-1} \quad (5)$$

characterizing the comparative population of the $n'p$ and $2n$

reaction channels. Q-values in the right-hand term refer to the target isotope with one less mass unit. The constant diminishing of this term (Fig. 8c) is well correlated with that of the ratio $\sigma_{n,n'p}/\sigma_{n,2n}$.

- (c) In conclusion, the (n,d) reaction cross section - of the order of 10 mb along the valley of stability [23,48] - is not significant for the lightest isotopes (daughter nuclei with $S_n > S_p$) but the most important one for the neutron-rich isotopes ($S_n < S_p$). Afterwards, it may be considered as mainly responsible for the curve B (Fig. 4) characteristic of the [(n,d)+(n,n'p)+(n,pn)] reaction cross sections for nuclei with $S_n < S_p$.

5. Conclusions

A test of generalized GDH pre-equilibrium emission model and Hauser-Feshbach statistical model predictions across the valley of stability, in the mass region $A \approx 50$, has been performed. Both the absolute cross section values and the "steepness" of the isotope trend have been obtained in good agreement with the experimental data. A distinctive aspect of these calculation methods, relative to other semiclassical pre-equilibrium models, is that no free internal parameter is used for pre-equilibrium emission.

The correlation of the isotope effects of the fast neutron reaction cross sections with the trend of significant quantities for the statistical and pre-equilibrium particle emission has been consequently analyzed, by using calculated cross sections. These isotope effects were largely studied both experimentally (e.g., [5,37,48]) and theoretically [51-55, 59,60]. A new relation is put into evidence in the present work, extending the applicability of the generalized Q_{gg} -systematics [6] from heavy ion induced reactions to fast neutron physics. The possibility to use these systematics to increase the accuracy of the predicted cross sections has to be confirmed by following analyses of an enlarged basis of experimental data.

An analysis of the [(n,n'p)+(n,pn)+(n,d)] reaction cross section, also in connection with the (n,2n) process, has confirmed by means of nuclear model calculations the previously [48] emphasized importance of the (n,n'p) reactions for neutron-poor nuclei. On the other hand, the (n,d) reaction is proved to be mainly responsible for curve B of the Qaim's systematics.

Acknowledgement: The authors are grateful to Prof. M. Ivascu for his continuing interest in this activity and to Prof. M. Petrascu for useful discussions, as well as to IAEA Nuclear Data Section for useful assistance. This work was supported in part by the International Atomic Energy Agency under Research Contract 3802/RB, in the frame of the IAEA Coordinated Research Programme on "Methods for the Calculation of the Fast Neutron Nuclear Data for Structural Materials".

REFERENCES

1. Agassi, A., Weidenmuller, H.A., Mantzouranis, G.: Physics Reports 22C, 147 (1975)
2. Feshbach, H., Kerman, A., Koonin, S.: Ann. Phys. (New York) 125, 429 (1980)
3. Avrigeanu, M., Ivascu, M., Avrigeanu, V.: Z. Phys. A - Atomic Nuclei 335, 299 (1989)
4. Caplar, R.: in "Fast Neutron Physics ", D.Miljanic, B.Antolkovic and G.Paic (Eds.) pp. 37-45. Zagreb: Ruder Boskovic Institute 1986
5. Qaim, S.M., Molla, N.I.: Proceedings of the 9th Symposium on Fusion Technology, Garmisch-Partenkirchen, 1976, pp. 589. Oxford : Pergamon Press 1976
6. Volkov, V.V.: Nukleonika 21, 53 (1976)
7. Avrigeanu, M., Avrigeanu, V.: Report NP-71-1989. Bucharest: IPNE 1989
8. Ivascu, M., Avrigeanu, M., Avrigeanu, V.: Rev. Roum. Phys. 32 , 713 (1987)
9. Avrigeanu, M., Avrigeanu, V., Cata, G., Ivascu, M.: Rev. Roum. Phys. 32, 837 (1987)
10. Kunz, P.D.: DWUCK4 User Manual. Paris: NEA Data Bank 1984
11. Blann, M. : Nucl. Phys. A213, 570 (1973)
12. Blann, M., Vonach, H.K.: Phys.Rev. C28, 1475 (1983)
13. Avrigeanu, M., Ivascu, M., Avrigeanu, V.: Report NP-63-1987/Rev. 1. Bucharest: IPNE 1988
14. Uhl, M , Strohmaier, B.: Report IRK-76/01. Vienna: IRK 1976
15. Avrigeanu, M , Bucurescu, D., Ivascu, M., Semenescu, G., Avrigeanu, V.: J. Phys. G: Nucl. Part. Phys. 15, L241 (1989)
16. Ivascu, M., Avrigeanu, V., Avrigeanu, M.: Rev. Roum. Phys. 32, 697 (1987)
17. Avrigeanu, M., Ivascu, M., Avrigeanu, V.: Z. Phys. A - Atomic Nuclei 329, 177 (1988)
18. Avrigeanu, M., Avrigeanu, V.: J. Phys. G.: Nucl. Part. Phys. 15, L261 (1989)
19. Williams, F.C., Jr.: Nucl. Phys. A 166, 231 (1971)
20. Bersillon, D.: Report CEA-N-2227. Bruyeres-le-Chatel: BRC 1981.
21. Schmidt, K.-H , Delagrangé, H., Dufour, J.P., Carjan, N., Fleury, A.: Z. Phys. A - Atoms and Nuclei 308, 215 (1982)
22. Caplar, R., Udovicic, L., Holub, E., Pocanic, D., Cindro, N.: Z. Phys. A - Atoms and Nuclei 313, 227 (1983)
23. Grimes, S.M., Haight, R.C., Alvar, K.R., Barschall, H.H., Borchers, R.R.: Phys. Rev. C19, 2127 (1979)
24. Valkonen, M.V. : Data File EXFOR-20673, dated 1981-01-16. EXFOR data received from IAEA Nuclear Data Section, Vienna.
25. Viennot, M., Haddou, A., Chiadli, A., Paic, G.: Data File EXFOR-30644, dated 1985-08-26.
26. Hoang Dac Luc : Report INDC(VN)-003(1984). Vienna: IAEA 1984
27. Bahal, B.M., Pepelnik, R.: Raport NEANDC(E)-252/U(1984), p.5.
28. Lu Han-Lin, Li Ji-Zhou, Fan-Guo, Huang Jian-Zhou, Data File EXFOR-30671, dated 1985-03-05.
29. Lim Chi-Chou, Lu Han-Lin, Fan Pei-Kuo, Ma Hung-Chang, Li Yeh-Sha : Data File EXFOR-30483, dated 1979-06-22.
30. Kudo, K.: Report NEANDC(J)-83/U (1982), p.1.
31. Qaim, S.M., Wolfle, R., Stocklin, G.: Proceedings of the International Conference on Chemical Nuclear Data, p. 121, Caterbury 1971
32. Ngoc, P.N., Gmeth, S., Deak, F., Kiss, A.: Data File EXFOR - 30562, dated 1981-11-17.
33. Pavlik, A , Winkler, G., Uhl, M., Paulsen, A., Liskien, H.: Nucl Sci. Eng. 90, 186 (1985)

34. Fukuda, K., Matsuo, K., Shirahama, S., Kumabe, I.: Data File EXFOR-20841, dated 1984-01-05.
35. Sailer, K., Daroczy, D., Raics, P., Nagy, S.: Data File EXFOR - 30438, dated 1978-08-21.
36. Qaim, S.M.: Data File EXFOR-20933, dated 1979-06-28.
37. Molla, N.I., Qaim, S.M.: Nucl. Phys. A283, 269 (1977)
38. Chittenden, D.M., Gardner, D.G., Fink, R.W.: Phys. Rev. 122, 860 (1961)
39. Ribanski, I.: Data File EXFOR-30811, dated 1985-08-23.
40. Dolya, G.P., Bozhko, V.P., Galovnya, Y.Y., Klyuscharev, A.P., Tutubalin, A.I.: Data File EXFOR-40416, dated 1977-12-18.
41. Derndorfer, C., Fisher, R., Hille, P., Vonach, H., Maier-Komor, P.: Z. Phys. A - Atoms and Nuclei 301, 327 (1981)
42. Fischer, R., Traxler, G., Uhl, M., Vonach, H.: Phys. Rev. C30, 72 (1984)
43. Sailer, K., Daroczy, S.: Proceedings of the 4th All Union Conference on Neutron Physics, p. 246, Kiev 1977
44. Molla, N.I., Mizanul Islam, M., Mizanur Rahman, M., Khatun, S.: Report INDC(BAN)-002. Vienna: IAEA 1983
45. Ryves, T.B., Kolkowski, P., Zieba, K.J.: J. Phys. G: 4, 1783 (1978)
46. Frehaut, W., Bertin, H., Bois, R., Jary, J.: Data File EXFOR - 20416, dated 1975-07-28.
47. Ikeda, Y., Miyade, H., Kawade, K., Yamamoto, H.: Data File EXFOR -21945, dated 1985-04-23.
48. Qaim, S.M.: Nucl. Phys. A382, 255 (1982)
49. Hemingway, J.D.: Data File EXFOR-20527, dated 1976-04-21.
50. Raics, P., Paszti, F., Daroczy, S., Nagy, S.: Data File EXFOR-30604, dated 1981-10-21.
51. Gardner, D.G.: Nucl. Phys. 29, 373 (1962)
52. Gardner, D.G., Rosenblum, S.: Nucl. Phys. A96, 121 (1967)
53. Pai, H.L., Clarke, R.L., Cross, W.G.: Nucl. Phys. A164, 526 (1971)
54. Pai, H.L.: Can. J. Phys. 54, 1421 (1976)
55. Pai, H.L., Andrews, D.G.: Can. J. Phys. 56, 944 (1978)
56. Wapstra, A.N., Bos, K.: At. Data Nucl. Data Tables 19, 177(1977)
57. Avrigeanu, M., Ivascu, M., Avrigeanu, V.: Atomkernenergie - Kerntechnik 49, 133 (1987)
58. Fu, C.Y.: Nucl. Sci. Eng. 86, 344 (1984)
59. Bychkov, V.M., Manokhin, V.N., Pashchenko, A.B., Plyaskin, V.I.: Report INDC(CCP)-146/LJ. Vienna: IAEA 1980
60. Bychkov, V.M.: Report IAEA-TECDOC-469 pp. 23-32. Vienna: IAEA 1988.

**ANALYSIS OF EXPERIMENTAL DATA ON NEUTRON INDUCED REACTIONS
AND DEVELOPMENT OF PCROSS CODE FOR THE CALCULATION
OF THE DIFFERENTIAL PREEQUILIBRIUM SPECTRA**

R. Capote, E. Herrera¹⁾, R. Lopez, V. Osorio²⁾, M. Piris¹⁾
Center of Applied Studies for Nuclear Development
P.O. Box 6122, Havana Cuba

1) Institute of Nuclear Science and Technology
Quinta de los Molinos, Havana, Cuba

2) International Atomic Energy Agency
Nuclear Data Section
Vienna, Austria

A B S T R A C T

A new PC code PCROSS for neutron induced reaction calculations up to 25 MeV incident was developed, where the latest theoretical development in the model was employed. A combination of exciton model and multistep direct reaction model parametrization was used in order to describe the high energy part of the spectra. In the PCROSS code several models for level density calculations are available. The code includes a subroutine to generate the input data. In the present paper some calculation results for (n,n') and (n,p) emission spectra in the range of 5 to 25 MeV and for (n,p) and (n,2n) excitation functions up to 20 MeV are shown. A good description of the experimental data was achieved.

INTRODUCTION

Meeting the nuclear data needs of the fission and fusion technologies requires a wide use of theories and phenomenological models. There are now several well-established codes for nuclear data calculations for structural materials involving statistical and preequilibrium models. Our aim was to develop a new PC-based user friendly code for nucleon induced reaction calculations, where the latest theoretical development in the preequilibrium field was employed.

As is well known, for the proper description of the high energy tail of the emission spectra the direct contribution should be taken into account. The combination of the preequilibrium exciton model and direct reaction parameterization should give satisfactory results for the emission spectra and excitation function

calculations. Therefore, we used the exciton model plus SMD parameterization for a theoretical description of the reaction process. In Section I of this paper, we will shortly review the employed theoretical framework. In Section II some test calculations and comparison with experimental data will be shown. Finally, we will give some conclusions and comments about the future work.

I. The exciton model and SMD parameterization

In the PCROSS code a combination of the exciton model[1] and SMD description of the direct interaction of the incident nucleon with the low-lying collective states of the target nucleus was employed. The exciton model used is based on the solution of the master equation[2] in the form proposed by Cline[3] and Ribansky[4]. To obtain the numerical solution of the system of the algebraic equations for $\tau(n)$, we use the algorithm proposed by Akkermans, Gruppelaar and Reffo[5], which produces an exact result for any initial condition of the problem. The preequilibrium and equilibrium spectra can be calculated in the unified form as follows:

$$\frac{d\sigma_{ab}}{d\varepsilon_b}(\varepsilon_b) = \sigma_{ab}^{\text{comp}}(E_{\text{inc}}) D_{ab}(E_{\text{inc}}) \sum_n W_b(E, n, \varepsilon_b) \tau(n) \quad (1)$$

where the usual notation is used, and $D_{ab}(E_{\text{inc}})$ is the depletion factor, which takes into account the flux loss as a result of the direct reaction processes. Using the direct reaction cross section we can calculate the depletion factor in the following way:

$$D_{ab}(E_{\text{inc}}) = 1 - \sigma_{ab}^{\text{dir}} / \sigma_{ab}^{\text{comp}} \quad (2)$$

For the calculation of the direct reaction contribution to the inelastic emission spectra, and therefore, of the σ_{ab}^{dir} the parameterization proposed by Kalka et al.[6] was used. According to this, we can write the direct differential emission cross section as

$$\frac{d\sigma_{ab}^{\text{dir}}}{d\varepsilon_b}(\varepsilon_b) = \delta_{ab} \left[\frac{2\mu}{\hbar^2 \mathcal{E}} \right]^2 \frac{\eta}{(k_a^2 R)^2} \frac{k_b}{k_a} P_a(\varepsilon_a) P_b(\varepsilon_b) v_R^2 \quad (3)$$

$$\sum_{\lambda=2}^3 \frac{\beta_\lambda^2}{(2\lambda+1)} \delta(U - \omega_\lambda)$$

where $\mathcal{V} = (4\pi/3)R^3$, $R = r_0 A^{1/3}$
 $V_R = 48$ MeV is the potential depth
 $\beta_\lambda, \omega_\lambda$ are the deformation parameters and phonon energies
of multipolarity λ
 $P_a(\varepsilon_a)$ is the penetration factor which can be calculated
for neutrons in the following way

$$P_a(\varepsilon_a) = 4k_a K_a / (k_a + K_a) \quad (4)$$

The delta function in the r.h.s. of equation (3) is replaced by a Gaussian with an averaging width according to the experimental data resolution.

For the calculation of the emission rates $W_b(E, n, \varepsilon_b)$ a state density formula is needed. At present, the PCROSS code uses the Williams formula[7] where the Pauli correction is calculated in accordance with Kalbach's method[8]. In addition, one has the option of using the Fu[9] or Kalbach[10] pairing corrections. We must ensure the consistency between equilibrium and preequilibrium emission, as was suggested by Fu[9]. Therefore, the level density parameters tabulated in [11] were employed for all the calculations. The use of these parameters allows us to avoid re-normalization of the particle-hole state densities, thus simplifying the calculation algorithm. Perhaps the D parameter systematics of Ref.[11] doesn't work very well. We should change the D parameter for some nuclei in order to achieve a good description of the threshold excitation functions. Employing the adjusted value of the D parameter from the excitation function an overall good emission spectra description in the whole energy range was achieved.

We want to remark that in the state density calculations we set $\omega(p, h, U)$ equal to zero when the excitation energy U is less than the Pauli energy $(p^2 + h^2)/(2g)$ for a given configuration. Physically, this assumption is clear because you cannot have any configuration with energy less than the Pauli energy by definition!

For the alpha and gamma emission rates the Iwamoto-Harada[12,13] and Akkermans et al.[14,15] formulations were used, respectively.

For the transition rate calculation we use the parameterization proposed by Blann[16]. Using this parameterization Machner[17] deduced the following expressions:

$$\lambda^+(E,n) = \frac{1}{k_{\text{mfp}}} \left[1.4 \times 10^{21} E' - \frac{2}{n+1} 6 \times 10^{18} E'^2 \right] \quad (5)$$

$$\lambda^-(E,n) = \frac{1}{k_{\text{mfp}}} \frac{(n-1)(n-2)ph}{(gE')^2} \left[1.4 \times 10^{21} E' - \frac{2}{n-1} 6 \times 10^{18} E'^2 \right]$$

In the PCROSS code the additional 3/8 factor introduced by Gupta[18] was taken into account in the r.h.s. of equations (5). This factor results from the reduction of a two-component master equation (i.e. with the neutron-proton distinction) to an effective one-component equation[18]. Taking also into account the direct reaction contribution, as has been mentioned above, we obtained an overall value of 1.3 for the mean free path parameter k_{mfp} . The slight increase above unity is possible if we bear in mind that effects such as parity and angular momentum conservation are not considered in the Blann parameterization[14]. These effects taken together would produce an increase of the nucleon mean free path in the nuclear matter. The assumed value of 1.3 is in good agreement with the one employed in the hybrid model calculations. We believe that this is a direct result of the whole correct theoretical approach in the state density and transition rate fields, and also of the account for the direct reaction contribution in the inelastic emission spectra.

According to the research performed by Akkermans and Grupelaar[19,20], in the energy range up to 50 MeV the preequilibrium emission subsequent to primary emission can be neglected. The PCROSS code uses the Weisskopf-Ewing[21] evaporation model in all cases to calculate the secondary emission.

II. Results

The calculations of threshold excitation functions (n,p) and (n,2n) up to 20 MeV incident energy were performed for cobalt and iron isotopes. For $\sigma_{ab}^{\text{comp}}(E)$ the reaction cross section of the global optical potential (Wilmore-Hodgson for neutrons and Bechetti-Greenless for protons) is used in the parameterized form of the

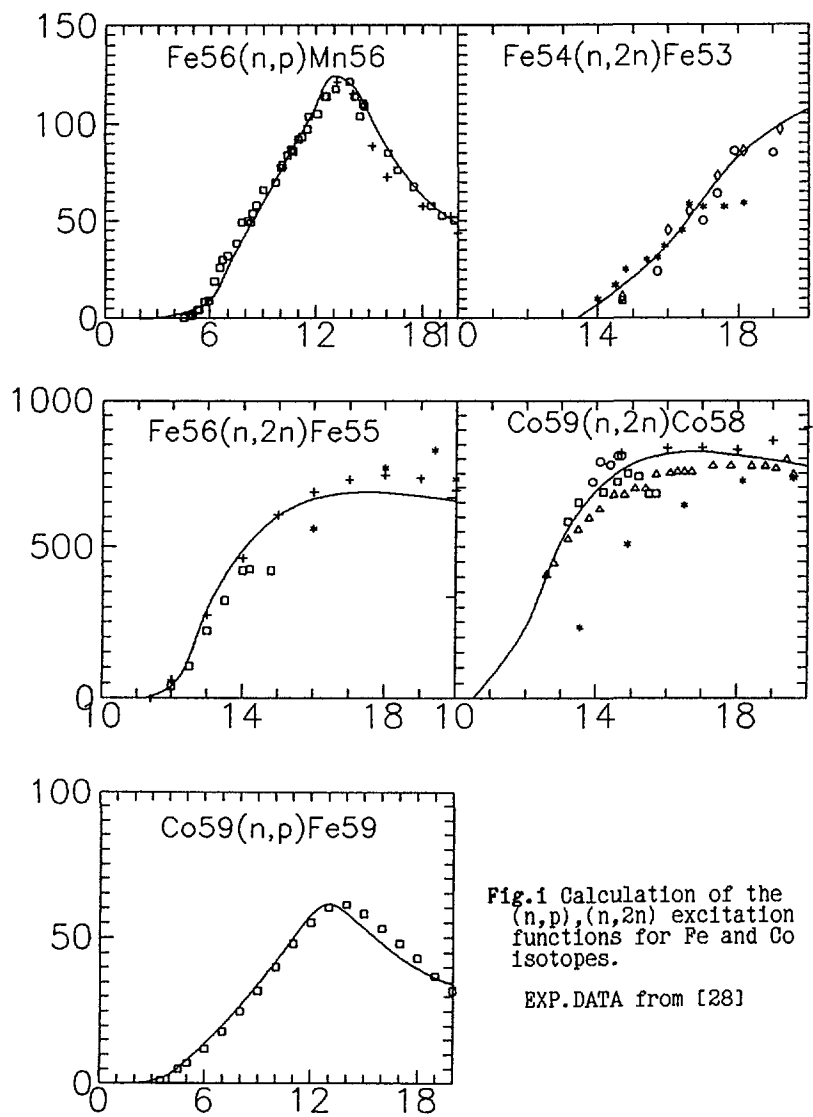


Fig.1 Calculation of the (n,p), (n,2n) excitation functions for Fe and Co isotopes.
EXP.DATA from [28]

Chatterjee et al.[22]. Some adjustment of the D parameters was needed for a correct description of the excitation function. The calculated excitation functions are depicted in Fig.1a-1e. There is a good agreement with experimental data. For the same isotopes the calculated emission spectra in the energy range from 5 to 26 MeV are shown in Fig.2a-2f. In this calculation, the previously fixed values of the D parameter were employed. The obtained description of the experimental data in the neutron and proton channels is good.

Finally, we performed calculations of the emission spectra for indium. The calculation results are shown in Fig.3a-3e. A good agreement with the experimental data is obtained within the whole energy range. In the 14 MeV inelastic emission spectra the SMD contribution is shown. As can be seen direct contribution dominates the high energy tail of the inelastic emission spectra.

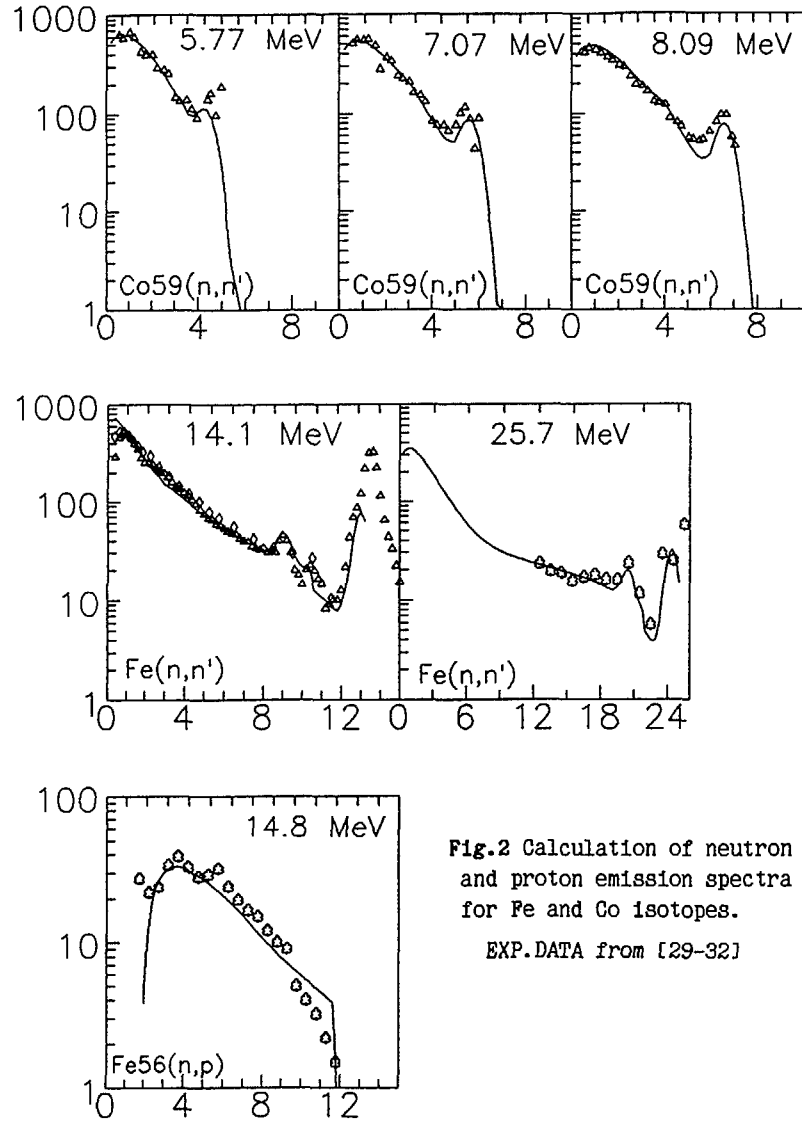


Fig.2 Calculation of neutron and proton emission spectra for Fe and Co isotopes.
 EXP.DATA from [29-32]

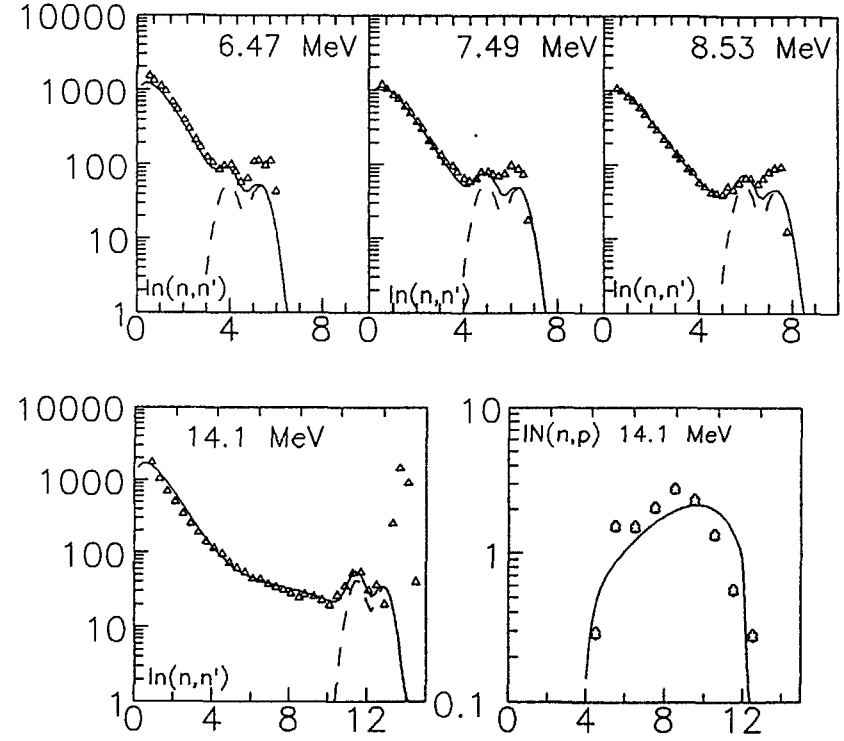


Fig.3 Calculation of neutron and proton emission spectra for indium. The SMD contribution is showed by dashed line.
 EXP.DATA from [29-32]

Conclusions

We have developed the PCROSS program which enables us to use the exciton model+SMD parameterization to calculate the emission spectra and excitation functions for the neutron induced reactions up to 25 MeV incident energy. The program lays particular stress on ensuring that equilibrium and preequilibrium emission are mutually consistent, and on making data input as simple and interactive as possible. The direct excitation of low-lying collective states is taken into account by the simple parameterization of Kalka et al.[6]. Blann's parameterization[16] was used to the calculation of the internal transition rates. An overall good description was obtained using the mean free path parameter equal to 1.3. Some calculations have been performed for (n,n') and (n,p) emission spectra for 5 up to 26 MeV incident energy and for (n,p) and (n,2n) excitation function up to 20 MeV. A good description of the experimental data was achieved. All calculations were carried out at the PC-AT computer and took only few minutes of computer time.

Future development

Recently, an exact formulation of particle-hole state densities taking into account the Pauli and pairing corrections[23] was obtained in our group. The corresponding internal transition rates for the exciton model were also derived[24]. We will try to make some calculations using this new state density formulation to compare with the currently used Williams formulation[7]. The impact of the new state density formulation on the alpha emission will be also studied with the systematic comparison with the new (n, α), (α ,n) experimental data[25].

Acknowledgements

The PCROSS code was developed from Betak's PREEQ program[26] and its modified variant PREANG[27] produced by Gruppelaar and Akkermans. This work was in part supported by the International Atomic Energy Agency Research Contract 5472.

- [1] Griffin J.J. Phys.Rev.Lett.17(1966) 418
- [2] Cline C.K.,Blann M. Nucl.Phys.A172(1971) 225
- [3] Cline C.K. Nucl.Phys.A193(1972) 417
- [4] Ribansky I.,Oblozhinsky P.,
Betak E. Nucl.Phys.A205(1973) 545
- [5] Akkermans J.M.,Gruppelaar H.,
Reffo G. Phys.Rev,C22(1980) 73
- [6] Kalka H., Seeliger D.,
Zhivopistsev F.A. Z.Phys.A329(1988) 331
- [7] Williams F.C. Nucl.Phys.A166(1971) 231
- [8] Kalbach C. in Proc.IAEA Advisory Group Meeting on Basic and
Applied Problems of Nuclear Level Densities, Ed.M.R.Bhat,
Report BNL-NCS-51694(1983),p.113
- [9] Fu C.Y. Nucl.Sc.&Eng.86(1984) 344
- [10] Kalbach C. Nucl.Sc.&Eng.95(1987) 70
- [11] Capote R.,Osorio V.,López R.,Herrera E.,Kabin E.
Proc.XVII Int.Symp.on Nucl.Phys.,nov.1987,Gaussig,GDR,
Ed.D.Seeliger and H.Kalka,Report ZfK-646(1988),p48
- [12] Iwamoto A.,Harada K. Phys.Rev.C26(1982) 1821
- [13] Sato K.,Iwamoto A.,Harada K. Phys.Rev.C28(1983) 1527
- [14] Betak E.,Dobes J. Phys.Lett.84B(1979) 368
- [15] Akkermans J.M.,Gruppelaar H. Phys.Lett.157B(1985) 95
- [16] Blann M., Mignerey A. Nucl.Phys.A186(1972) 245
- [17] Machner H. Z.Phys.A302(1981) 125
- [18] Gupta S.K. Z.Phys.A303(1981) 329
- [19] Akkermans J.M.,Gruppelaar H. Z.Phys.A300(1981) 345
- [20] Akkermans J.M. Z.Phys.A313(1981) 345
- [21] Blatt J., Weisskopf, Theoretical Nuclear Physics
- [22] Chatterjee A.,Murthy K.H.N.,Gupta S.K. Pramana 16(1981) 391
- [23] Bager N.,Capote R.,Pedrosa R. Z.fur Physik A334(1989) 397
- [24] Capote R.,Piris M. "Jornada Científica X Aniversario
de la SEAN",Oct.de 1989, Habana, Cuba, Unpublished.
- [25] "A (p,n),(α ,n) emission spectra",Second CRM,
Vienna 8-10 Feb.1988
- [26] Betak E. Comp.Phys.Comm.9(1975) 92;
Comp.Phys.Comm.10(1975) 71
- [27] Akkermans J.M.,Gruppelaar H. Report ECN-60(1979)

- [28] Handbook on nuclear activation data,
Tech.Rep.Ser.273,IAEA 1987
- [29] Baba M.,Ishikawa M.,Yabuta N.,Kikuchi T.,Wakabayashi H.
and Mirakawa M., Int.Conf."Nucl.Data for Science and
Technology",May-June 1988,Mito,Japan
- [30] Pavlik A.,Vonach H. Report IRK(1988),Vienna, "Evaluation of
the angle integrated neutron emission cross section from the
interaction of 14 MeV neutrons with medium and heavy nuclei"
- [31] Gul K.,Anwar M.,Ahmad M.,Saleem S.M.,Naeem A.Khan
Phys.Rev.C31(1985) 74
- [32] Grimes S.M.,Haight R.C.,Alvar K.R.,Barschall H.,Borchers R.
Phys.Rev.C19(1979) 2127

Efforts in Bologna on Quasiparticle Level Density Systematics and on Comparison and Development of Different Approaches to Preequilibrium Reaction Mechanism

M. Herman, G. Reffo, H.A. Weidenmüller, H. Lenske,
H.H. Wolter, G. Giardina, A. Italiano and
M. Rosetti

A B S T R A C T

We present a summary of activities carried out at E.N.E.A. in Bologna on the development of the preequilibrium emission models. We start with the first application of the Multistep Compound Model in the Heidelberg formulation, which is followed by the Multistep Direct calculations. Next, the comparison between the exciton and Multistep Compound model by Feshbach, Kerman, and Koonin is presented. Finally we discuss energy and isotop dependence of the average single particle level spacing.

1. Precompound reactions in terms of the Heidelberg Multistep-Compound Theory

(M.Herman, G.Reffo, H.A.Weidenmüller)

Modern statistical theories of nuclear reactions¹⁻⁴⁾ distinguish between the multistep-direct and the multistep-compound (MSC) mechanisms, the latter describing the composite system on its way toward formation of an equilibrated compound nucleus. By definition, the MSC mechanism involves only bound configurations embedded in the continuum, yields angular distributions symmetric about 90° c.m., and is expected to be relevant mostly at relatively low (10-20 MeV) incident energies. On the contrary, multistep-direct mechanism treats the evolution of the open configurations, yields forward peaked angular distributions, and is supposed to be dominant at higher incident energies. So far, all MSC calculations⁵⁻¹⁰⁾ have used the theory of Feshbach, Kerman, and Koonin¹ (FKK). In this paper we present the first results obtained in the framework of an alternative approach to MSC processes formulated in Ref.3 to which we refer as NVWY. This theory is based on a well-defined quantum-statistical input and yields precise definitions of emission and internal transition widths.

The average cross section connecting channel a and b via the MSC mechanism has the form

$$\sigma_{ab} = (1 + \delta_{ab}) \sum_{m,n} T_m^a \Pi_{mn} T_n^b. \quad (1)$$

(We have omitted kinematical and angular-momentum dependent factors.) The sums run over all classes (m or n) of particle-hole excitations. T_m^a is the transmission coefficient coupling channel a and class m . It is important to realize that $T^a = \sum T_m^a$ is the usual transmission coefficient in channel a , given by the unitarity deficit of the average S -matrix, and thus available from standard optical-model calculations.

The probability transport matrix Π_{mn} is defined via its inverse,

$$(\Pi^{-1})_{mn} = \delta_{mn}(2\pi\rho_m)(\Gamma_m^{\downarrow} + \Gamma_m^{ex}) - (1 - \delta_{mn})2\pi\rho_m \overline{V_{mn}^2} 2\pi\rho_n. \quad (3)$$

Here, $\overline{V_{mn}^2}$ is the mean squared matrix element coupling states in classes m and n , $\Gamma_m^{\downarrow} = 2\pi \sum \overline{V_{mn}^2} \rho_n$ is the average spreading width of states in class m , and $\Gamma_m^{ex} = (2\pi\rho_m)^{-1} \sum_a T_m^a$ is the average decay width in class m .

To calculate Γ_m^{\downarrow} , we relate it to the imaginary part of the optical-model potential, parametrized in Ref.11 as $W(\epsilon) = c\epsilon^2$ with $c = 0.003 \text{ MeV}^{-1}$, ϵ being the excitation energy of the particle (hole) above (below) the Fermi energy. In calculating Γ_m^{\downarrow} , we average $W(\epsilon)$ over the exciton distribution.

The calculations were performed by means of the statistical model code EMPIRE¹²⁾ which was appropriately modified to allow for the MSC mechanism. In summing Eq.1 over final channels, we took rigorously account⁹⁾ of proper angular-momentum coupling. The calculations were done for the reaction $^{93}\text{Nb}(n, n')$ at a neutron bombarding energy of 14.6 MeV. As input we used binding energies, target spin and parity, global optical-model parameters¹³⁾, and a value $g = A/13$ Mev for the single-particle level density. Allowing for 12 classes, it was possible to calculate equilibrium emission of the first neutron within MSC theory and use the Hauser-Feshbach approach only for the secondary neutrons.

The results of the calculations show a good agreement with the experimental data up to about 8 MeV of the outgoing neutron energy. For higher energies the calculations fell well below the experimental results showing the importance of the multistep-direct processes. Simultaneously, our calculations reproduce also proton spectrum emitted in the $^{93}\text{Nb}(n, p)$ reaction.

We conclude that Heidelberg MSC theory allows for parameter free calculations of the nucleon spectra, consistent with the experimental results.

1. H.Feshbach, A.Kerman and S.Koonin, *Ann.of Phys.* 125,429(1980).
2. T.Tamura, T.Udagawa, and H.Lenske, *Phys. Rev. C*26 379(1982).
3. H.Nishioka, J.J.M.Verbaarschot, and H.A.Weidenmüller, and S.Yoshida, *Ann. Phys.* 172,67(1986).
4. H.Nishioka, H.A.Weidenmüller, and S.Yoshida, *Ann. Phys.* 183,166(1988).
5. R.Bonetti, L.Colli-Milazzo, A.De Rosa, G.Inglima, E.Perillo, M.Sandoli, and F.Shahin, *Phys. Rev. C*21,816(1980).
6. R.Bonetti, L.Colli-Milazzo, and M.Melanotte, *Lett. Nuovo Cimento* 31,33(1981).
7. R.Bonetti, L.Colli-Milazzo, M.Melanotte, A.De Rosa, G.Inglima, E.Perillo, M.Sandoli, V.Russo, N.Saunier, and F.Shahin, *Phys. Rev. C*25,717(1982).
8. R.Bonetti and L.Colombo, *Phys. Rev. C*28,980(1983).
9. M.Herman, A.Marcinkowski, and K.Stankiewicz, *Nucl. Phys. A*430,69(1984).
10. G.M.Field, R.Bonetti, and P.E.Hodgson, *J. Phys. G*12,93(1986).
11. C.Mahaux, P.F.Bortignon, and C.H.Dasso, *Phys. Rep.* 120,1(1985).
12. M.Herman, A.Marcinkowski and K.Stankiewicz, *Comp. Phys. Comm.* 33,373(1984).
13. F.Björklund, S.Fernbach, and M.Shermon, *Phys. Rev.* 109,1295(1958).

2. Multistep-direct Contribution to the $^{93}\text{Nb}(n, n')$ Reaction

(M.Herman, G.Reffo, H.Lenske, H.H.Wolter)

The forward peaked angular distributions and failure of the multistep-compound model to describe the high energy tail of the spectra, provide a clear evidence that more direct processes contribute significantly to this energy region, even at such relatively low incident energies as 14 MeV. These processes may be treated within so called 'multistep-direct' theories, which are an extension of the DWBA method to the continuum transitions and account for multiple interaction of the projectile with the target nucleus. In the present note we report on such calculations performed in terms of the theory formulated by Tamura, Udagawa, and Lenske¹⁾.

We consider $^{93}\text{Nb}(n, n')$ reaction at 14.6 MeV, for which also multistep-compound calculations have been performed (see contribution to this meeting). We allow for 2 reaction steps each of which is assumed to create 1-particle 1-hole configuration in the target nucleus. To calculate transition densities we use single-particle wave functions calculated in Wood-Saxon potential and schematic RPA approach. Strength parameters of the multipole field were chosen to reproduce experimental energies of the first 0^+ , 2^+ , 3^- , and 4^+ states in ^{90}Zn which was considered to play the role of a core. For multipolarity $\lambda = 1$ transitions the field strength was fitted to the GDR energy.

The results of the calculations describe very nicely high energy tail of the experimental spectra at various angles. We note, that also the structure in the spectra is approximately reproduced. The first step dominates at the very end of the spectrum, peaking at outgoing energy of about 12.5 MeV. At energies below 10 MeV the second step becomes overwhelming. It should be stressed, that such

an agreement is only possible if collective effects are taken into account in the transition densities. Neglecting collective correlations yields not only different energy structure of the spectra but results in cross sections which are by an order of magnitude smaller.

We conclude that multistep-direct calculations combined incoherently with the multistep-compound ones provide with a very good description of the neutron induced reactions at low incident energies.

1. T.Tamura, T.Udagawa, and H.Lenske, Phys. Rev. C26 379(1982).

3. Comparison of exciton and multistep compound models

(M.Herman, G.Reffo)

During the last two decades, various preequilibrium models proved to describe processes, that lay between fast direct reactions and slow compound nucleus decay. These essentially classical models, considerably contributed to our understanding of the equilibration process, as well as of the reaction mechanism itself. These models turn out to predict the high energy portion of nucleon spectra surprisingly well, and became an indispensable tool for many basic studies and applications.

The explanation of the preequilibrium model success is, in our opinion, twofold. First of all, we trace it to the fruitful idea describing equilibration of the composite nucleus. On the other hand, experimental data, interpreted with preequilibrium models, do not offer enough information for testing commonly used approaches unambiguously. In fact, all what is available, are parts of spectra and inherent angular distributions, laying between two regions dominated by direct and compound reactions respectively. Both these observables are rather of simple, structureless form, which does not impose sufficient constraints on the theoretical models, used for their interpretation. It seems, that most data may be equally well reproduced in terms of different models by "allowed" adjustment of parameters, that are always involved even in the so called "parameter free" models.

The most popular semiclassical models are the exciton model (EM) /1-10/ and the hybrid model (HM) /11-14/. A detailed analysis of the different physical assumptions underlying EM and HM has been performed recently /15/ and will not be considered here.

To improve classical preequilibrium models better founded quantum mechanical approaches /16-23/ have been introduced.

Here, we attempt to compare the widely used exciton model with the multistep compound (MSC) /17/, the quantum mechanical formulation of preequilibrium decay that has been most frequently applied /24-29/. We will concentrate on the physical ideas underlying both models, and discuss in details the cross section expressions, paying not much attention to the obviously different derivation of both expressions. We shall try to relate the assumptions, that are physically equivalent but differently formulated in the two models. We shall also point out similarities and/or differences in practical calculations using both models.

The basic concept, common to EM and MSC, assumes that the composite nucleus is formed in a relatively simple state and proceeds toward equilibrium through a chain of stages with increasing complexity. Even though, complexity is not specified explicitly in the MSC, it is understood as number of available degrees of freedom, and exciton number is adopted in practical calculations. In both models transitions are mediated by the two-body interaction. This leads to the chaining hypotheses in MSC, or equivalently to the condition regarding the change in exciton number ΔN_2 in EM. There is, however, a well known difference between model space as used in EM and in MSC. While EM makes no restriction regarding model space, the MSC involves only closed configurations (i.e. those built up only with the nucleons placed in the bound shell-model orbitals). This difference has an essential influence on the angular distributions. In the EM /8-10/ the linear momentum in the incoming channel is gradually distributed among excitons, leading eventually to the loss of the direction memory in the compound stage. In the initial stages, however, the projectile direction is still favored, which results in the prediction of forward peaked angular distributions. In

this respect, EM is a classical equivalent of the quantum mechanical models known as multistep direct (MSD) /17,19-23/. The important difference is that the latter consider only open configurations (i.e. those with at least one unbound particle), while EM treats close and open configurations indifferently. As a consequence, one faces a conceptual difficulty in the EM. It is possible to ascribe certain direction to the wave function in the open space. In this case, we deal with a scattering-like wave function containing excited nucleus plus nucleon in the continuum. Such a function extends outside the nucleus and may reveal asymmetry in the configuration space related to the direction of the nucleon in the continuum. Using such a function in the MSD results in asymmetric angular distribution. On the other hand, it is unclear how the same result may be obtained in the case of closed configurations, in which all nucleons occupy bound orbitals, with the wave function vanishing outside the nucleus. Accordingly, MSC process assumes complete loss of the initial direction memory (except of the angular momentum conservation), that results in angular distribution symmetric around 90° . On the contrary, the EM follows the MSD treatment of the linear momentum in the entire model space, including the closed subspace. This should lead to an underestimation of the backward part of the angular distribution, which is in fact usually observed.

In the following discussion, we shall neglect angular distributions and splitting of the model space in closed and open subspaces.

The second important assumption in the EM is the uniform population probability of all accessible nuclear states in the equilibration process. This implies, that particular structure of the initial and final states can be, on the average, neglected so that the decay is governed by the density of states.

A very similar assumption is also found in the MSC model. To assure equal population of the states in the next reaction stage, the average spacings between states in a decaying stage is assumed to be small compared to the width of the states in the next stage. This condition is referred to as "self averaging", and is given in terms of physical quantities, so that its validity may be tested. Alternatively, one could say, that both models are working in a strong coupling limit, so that configurations are expected to be well mixed (see ref.15 in the case of EM).

In addition to the "self averaging", MSC assumes also random distribution of the matrix element phases, that implies vanishing of the interference terms. Such an assumption is not considered in the frame of the EM, because no explicit averaging is performed. It does not mean, however, that this assumption is not implicitly included in the EM.

Formal development of both models is obviously very different. The exciton model employs Pauli master equation to describe the flux flow through different stages. The approach is semiclassical, time dependent, and makes use of the detailed balance to estimate internal transition and escape rates. Derivation of the MSC, instead, consists in the calculation of the averaged value of the squared element of the fluctuating part of the transition matrix. The transition matrix is expressed in terms of the nuclear Hamiltonian and optical model Hamiltonian, which formally account for all the characteristics of the system. In the course of the derivation several averaging procedures are involved. These have been subject to criticisms, as being performed not over matrix elements, for which statistical distributions are well established. The way the averages are performed in MSC is, however, intuitively convincing; at least to the same extent as EM derivation.

Conservation of the flux in MSC is not trivially fulfilled due to the coupling to the open subspace. To ensure the flux conservation, one has to assume weak coupling between closed and open subspaces. Naturally, this problem does not arise in the EM, since entire model space is considered.

Our final remark, concerning general formulation of the two models, regards the "never come back" hypothesis. This assumption is not necessary (but optional) in the EM, because the master equation takes all possible intranuclear transitions into account. Therefore, the EM provides us with a unified model for the description of preequilibrium and equilibrium mechanisms. The multistep compound model makes use of a time independent theory and the "never come back" hypothesis is never invoked. In fact, transition matrix elements contain propagators, which describe the transitions to the compound stage and backwards. However, the MSC cross section formula reveals typical "never come back" structure, that prevents the unified description including equilibrium contribution. The latter is included in the MSC formalism somewhat artificially by setting to

zero spreading width for a sufficiently complicated reaction stage. In order to keep both models as close as possible, we will use the "never come back" version of the EM for our further discussion.

After this general discussion, let us consider the cross section expressions in both models. We take the simplest version of EM neglecting angular distributions., In the case of the MSC we adopt a simplified version, which makes use of the exciton concept to classify stage complexity. It is in fact, the only version of the MSC, that has been applied in practical calculations. To keep our discussion as simple as possible, we also assume that target, projectile, and ejectile have no spin. Accordingly, cross section for the emission of the particle with angular momentum l from the n -th stage of the composite nucleus with spin J , leaving residual nucleus at excitation energy U and spin s , is formally written in the same way in both models

$$\frac{d\sigma_{1J}}{d\varepsilon} = \frac{\Gamma_{nJ}^s(U)}{\Gamma_{nJ}} \prod_{m=1}^{n-1} \frac{\Gamma_{mJ}^l}{\Gamma_{mJ}} \sigma_{1J}, \quad (1)$$

where, Γ_{nJ}^s , Γ_{mJ}^l , and Γ_{nJ} are the averaged emission, spreading, and total widths respectively, and σ_{1J} stands for the formation cross section of a composite nucleus in the stage $n=1$ with specified spin J . Note, that the EM is usually formulated in terms of transition rates λ , which are related to widths by $\Gamma = \hbar\lambda$. In the Eq.1 one may distinguish three factors, with transparent physical meaning. The first one (from the right) is the, above mentioned, formation cross section. The second one is the probability of finding the composite nucleus in the n -th stage, after having survived emissions from the preceding stages (depletion factor). Finally, the third factor is an emission probability from the n -th stage. Eq.1 shows, that EM and MSC, in their versions discussed here, are equivalent to the extent that widths and formation cross sections can be related to each other in both approaches.

Let us consider the formation cross section first. In EM the optical model reaction cross section is usually taken. This can be corrected for the loss of flux due to the direct reactions, either by introducing a multiplicative factor or, more consistently, by using transmission coefficients calculated in the DWBA or coupled channel approaches. In MSC the formation cross section is expressed in terms of the strength function for the formation of the doorway states and is given by

$$\sigma_{1J} = \pi\lambda(2J+1)2\pi \frac{\Gamma_{1J}^{in}}{D_{1J}}, \quad (2)$$

where Γ_{1J}^{in} is the average entrance width for the configurations in the first stage, and D_{1J} is the average spacing of such configurations having spin J . These quantities, essentially, may be calculated directly from the known nuclear Hamiltonian, this being, however, very impractical. Alternatively, the strength function may be obtained using a technique similar to the one employed for the determination of the escape width (see the discussion below). The latter involves, however, unknown strength of the interaction (V_0), and depends strongly on the spacing of the doorway states. It is our feeling, that such a procedure does not meet accuracy required in applications. The third possibility is based on the observation that strength function under discussion is, approximately equal to the suitably averaged strength function for the formation of the compound nucleus /30,31/. Accordingly, predictions of the optical model may be used, and analogy with the EM is recovered. The only difference is, that the reduction has to take into account also multistep direct processes, in addition to the direct ones. Such an approach has been followed in Ref.28.

The remaining difference between EM and MSC may only be contained in the emission and spreading widths, because depletion factor and total width are identically expressed in terms of Γ_{nJ}^l and Γ_{nJ}^s in both models.

Assuming factorization of the spin dependence in the state densities, and using explicit form for the matrix element of the delta-function interaction, the spreading width in the MSC model is written /17/

$$\Gamma_{nJ}^l = X_{nJ}^l Y_n^l(E) |M|^2 \quad (3)$$

where X_{nJ}^l describes angular momentum coupling, and Y_n^l carries all energy dependence. Note that,

as compared to Ref.17, we have separated factor $|M|^2$ from X_{nb} . In the case of the δ -interaction, M factor is proportional to the interaction strength V_o , and to the overlap integral of the radial parts of the wave functions for the nucleons taking part in a transition. Clearly, this factor corresponds to the averaged matrix element in the EM. In Ref.32 it was shown, using identity relation for the Heaviside function, that the factor Y_{nb} corresponds exactly to the accessible density of final states, as used in the EM. Therefore, both quantities are equal when the same state densities are used. The energy dependent part of the spreading widths are, thus, completely equivalent, if the same model space is considered in both cases. The difference is found in the angular momentum structure. The MSC performs the detailed spin coupling of all excitons followed by averaging over initial configurations and by summation over final ones, that results in a complicated X_{nb} factor. Most of the EM formulations disregard angular momentum conservation at all. Only some of them take it into account /33/, but treat it in a much simpler way, including simply spin distributions in the state densities. This may be considered the main difference between MSC and EM as far as the spreading width is concerned. It should be mentioned, however, that the J dependence of the X factor, as calculated in the frame of the MSC, is rather weak /28,34/, therefore is expected not to affect nucleon spectra to a great deal.

An essential conceptual difference concerns treatment of the escape widths in both approaches. The EM assumes that the emission from a given stage occurs with a certain rate, which is proportional to the inverse reaction cross section and to the probability of having the particle with the appropriate channel energy. The latter probability is given as a ratio of the state densities. No intrinsic interaction is involved in the emission process, that reminds similar treatment of the emission in the compound nucleus theory. On the contrary, in the MSC the emission is always mediated by the nucleon-nucleon scattering. This scattering may lead to particle-hole annihilation or creation or it may leave the number of excitons unchanged, thus giving rise to the three so called "exit modes". These resemble the three possible internal transitions in the EM without "never come back" assumption. This way MSC accounts for the $\Delta n = +1, 0, -1$ transitions in the emission. In the result of scattering, one of the nucleons is lifted to the open subspace and is considered to escape the composite nucleus. Due to the scattering, that precedes emission, whole process can be described similarly to the damping transition (Eq.3), using explicit expression for the matrix element of the δ -interaction and accessible state density. Calculating radial overlap integral, we have to keep in mind, that one of the excitons in the final state is described by the wave function belonging to the open subspace. This brings the transmission coefficient into the expression avoiding, however, the danger of using the detailed balance principle. Accessible state densities are calculated in the same way as for the corresponding internal(!) transitions in the exciton model, but having one exciton less in the final configuration. As far as angular momentum is concerned, the appropriate discussion for the spreading width should be here repeated.

In the MSC the escape and spreading widths are both proportional to the interaction strength, which cancels in the cross section expression (Eq.1). It follows, that the MSC can be made independent of the unknown interaction strength, if the formation cross section σ_{IJ} is calculated in the frame of the optical model. This is due to the assumption, that nucleon-nucleon scattering is involved in each emission. On the contrary, all classical preequilibrium models need some estimate for the interaction strength to calculate the ratio between the escape and damping widths.

We have shown that, basic ideas, underlying the EM and MSC, are very similar. Closest correspondence is found between the never come back version of the EM and exciton formulation of the MSC, when neglecting angular and linear momenta considerations. In this case, the main difference concerns treatment of the emission process.

In addition, EM attempts to describe MSC and MSD processes simultaneously. In this respect, the angular distributions, resulting from both models, are very different, since EM is closer to MSD in the treatment of the linear momentum. Disagreement is also found in the way the angular momentum coupling is performed in both models. The approach applied in the MSC is more microscopic, and much more involved.

In the present comparison, we have left apart the most recent approach to the preequilibrium mechanism by the Heidelberg group /18,19/. We mention only, that the latter reveals that "effective

state densities", are involved in place of the ones presently used. So far, the extent of their impact, on the practical calculations, has not yet been clarified. The complete, systematic intercomparison, including Heidelberg model, would be highly desired.

1. J.J.Griffin, Phys. Lett. 17,478(1966).
2. M.Blann, Phys. Rev. Lett. 21,1357(1968)
3. E.Gadioli, E.Gadioli-Erba, and P.G.Sona, Nucl. Phys. A217,589(1973).
4. E.Gadioli and E.Gadioli-Erba, Acta Phys. Slov. 25,126(1975).
5. E.Gadioli, E.Gadioli-Erba, and J.J.Hogan, Phys. Rev. C16,1404(1977).
6. E.Gadioli and L.Milazzo-Colli, in Proceedings of the Europhysics Study Conference on Intermediate Processes in Nuclear Reactions, Yugoslavia, 1973, edited by N.Cindro, P.Kuliscic, and T.Meyer-Kuckuk (Spinger, Heidelberg, 1973).
7. I.Ribansky and P.Oblozinsky, Phys. Lett. 45B,318(1973).
8. G.Mantzouranis, D.Agassi, and H.A.Weidenmuller, Phys. Lett. 57B,220(1975)
9. G.Mantzouranis, H.A.Weidenmuller, and D.Agassi, Z. Phys. A276,145(19 76).
10. J.M.Akkermans, H.Gruppelaar, and G.Reffo, Phys. Rev. C22,73(1980).
11. M.Blann, Phys. Rev. Lett. 27,337(1971).
12. M.Blann and A.Mignerey, Nucl. Phys. A186,245(1972).
13. M.Blann, Phys. Rev. Lett. 28,757(1972).
14. M.Blann, Nucl. Phys. A213,570(1973).
15. J.Bisplinghoff, Phyc.Rev. C33,1569(1986).
16. D.Agassi, H.A.Weidenmuller, and G.Mantzouranis, Phys. Reports 22,145(1975).
17. H.Feshbach, A.Kerman, and S.Koonin, Ann. of Phys. 125,429(1980).
18. H.Nishioka, J.J.M.Verbaarshot, and H.A.Weidenmuller, Ann. Phys. 172,67(1986)
19. H.Nishioka, H.A.Weidenmuller, and S.Yoshida, to be published.
20. T.Tamura and T.Udagawa, Phys. Lett. 71B,273(1977)
21. T.Tamura and T.Udagawa, Phys. Lett. 78B,189(1978)
22. T.Tamura, H.Lenske, and T.Udagawa, Phys. Rev. C23,2769(1981).
23. T.Tamura, H.Lenske, and T.Udagawa, Phys. Rev. C26,379(1982).
24. R.Bonetti, L.Colli-Milazzo, A.De Rosa, G.Inglima, E.Perillo, M.Sandoli, and F.Shahin, Phys. Rev. C21,816(1980).
25. R.Bonetti, L.Colli-Milazzo, and M.Melanotte, Lett. Nuovo Cimento 31,33(1981).
26. R.Bonetti, L.Colli-Milazzo, M.Melanotte, A.De Rosa, G.Inglima, E.Perillo, M.Sandoli, V.Russo, N.Saunier, and F.Shahin, Phys. Rev. C25,717(1982).
27. R.Bonetti and L.Colombo, Phys. Rev. C28,980(1983).
28. M.Herman, A.Marcinkowski, and K.Stankiewicz, Nucl. Phys. A430,69(1984).
29. G.M.Field, R.Bonetti, and P.E.Hodgson, J. Phys. G12,93(1986).

30. B.Block and H.Feshbach, Ann. Phys. 23,47(1963).
31. H.Feshbach, A.K.Kerman, and R.H.Lemmer, Ann. Phys. 41,230(1967).
32. K.Stankiewicz, A.Marcinkowski, and M.Herman, Nucl. Phys. A435,67 (1985).
33. G.Reffo, in Proceedings of the 6-th Soviet Conference on Neutron Physics, Kiev, October 2-6 (1983), available also as ENEA report RT/FI(83)9.
34. P.Oblozinsky, Phys. Rev. C35,407(1987).

4. Systematics in Exciton State Densities

(G.Giardina, M.Herman, A.Italiano, G.Reffo, and M.Rosetti)

In most applications the average spacing of the shell-model hamiltonian eigenvalues is taken to be energy independent and its inverse (density of eigenvalues or density of single particle levels), denoted by g , is taken usually to be proportional to the nuclear mass number A : $g = \frac{A}{c}$ with $c \approx 13$, but such an approach lacks any microscopic foundation and may introduce large errors when used for the determination of dynamical quantities. This has motivated the present investigation of the average dependence of the unperturbed shell-model hamiltonian spacings on the energy, the neutron and the proton numbers. We have analyzed the extensive set of single particle levels, as determined by Nix and Möller. This set contains results for more than 4000 isotopes in the mass range from $A=12$ up to $A=269$ and also covers nuclei far from the stability line, allowing for an investigation of the isotopic effects. We have analyzed a cumulative number of eigenvalues (for particle and hole excitation) as a function of energy above and below the Fermi level.

Observing Fig.1 is evident that above the Fermi level the cumulative number of eigenvalues increases faster than in the case of equidistant distribution (linear energy dependence). A quadratic energy dependence

$$(1) \quad N(E) = a E^2 + b E + c$$

gives a reasonable description (see Fig. 1). In the case of the eigenvalues lying below the Fermi level, the energy increase of the cumulative plot is slower than the one for equidistant levels and may be approximated by

$$(2) \quad E = \tilde{a} (N - 2)^2 + \tilde{b} (N - 2)$$

(the constant 2 appears to ensure two possible hole states at zero energy).

The average density of eigenvalues which appears to be energy dependent:

$$(3) \quad g(E) = \frac{dN(E)}{dE} = 2 a E + b \quad (\text{above the Fermi level})$$

$$(4) \quad \bar{g}(E) = \frac{dN(E)}{dE} = (\bar{b}^2 + 4 \bar{a} E)^{-1/2} \quad (\text{below the Fermi level}).$$

For each isotope, cumulative plots for neutrons and protons were separately fitted with Eqs. 1 and 2 providing values for a , b , c , \bar{a} and \bar{b} parameters.

In Figs. 2 and 3, the parameters a and b are plotted versus the neutron or the proton numbers. The a_ν and a_π determine energy dependence of the average spacing of neutron and proton single particle levels (s.p.l.) above the Fermi energy:

- a_ν (Fig. 2) has a rather well determined dependence on the neutron number N . Some spread of the points in Fig. 2 may be related to the influence of the proton number Z . This effect is explained in Fig. 4.
- a_π (Fig. 3) shows slightly different systematics. It increases linearly for small Z , peaks at $Z=55$ and eventually decreases. For $Z > 40$ one observes a pronounced isotopic effect, which is manifested by a large spread of the points. This effect is pointed out in Fig. 5.
- a_ν and a_π do not show pronounced shell effects.

This is qualitatively understood, since these parameters account for the decrease of spacings between high lying single particle levels, being therefore rather insensitive to the region close to the Fermi level.

Now we consider the constant term in Eq. 4.

- b_ν (for neutrons) appears to be, on the average, an increasing function of N (Fig. 2). Close to the Fermi level this parameter mainly determines eigenvalue spacing. It is, therefore, expected that it should carry on the effects of the shell closure (discontinuities at $N=50$, $N=82$ and at $N=126$ confirm that this is actually the case).

For light nuclei, usually far from the stability line, one occasionally finds negative values of b_ν (see Fig. 2). In terms of Eq. 3 it means that g acquires a physical (positive) value only above certain energies, at which the energy dependent term becomes greater than b_ν . Such cases are related to the large gap between the Fermi level and a first s.p.l. above it. A very wide spread of b_ν around the mean value (see Fig. 2) indicates a strong

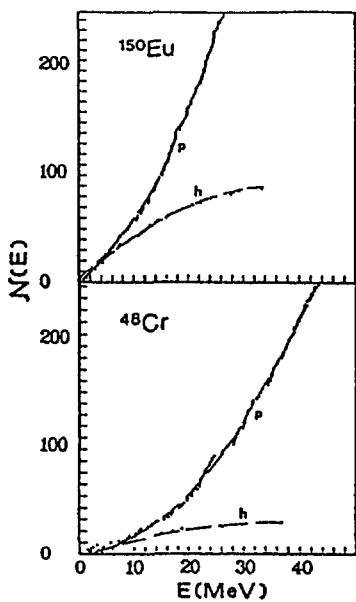


FIG. 1. Cumulative number of eigenvalues *above* (*p*) and *below* (*h*) the Fermi level for ^{150}Eu and ^{48}Cr . Energy is calculated with respect to the Fermi level.

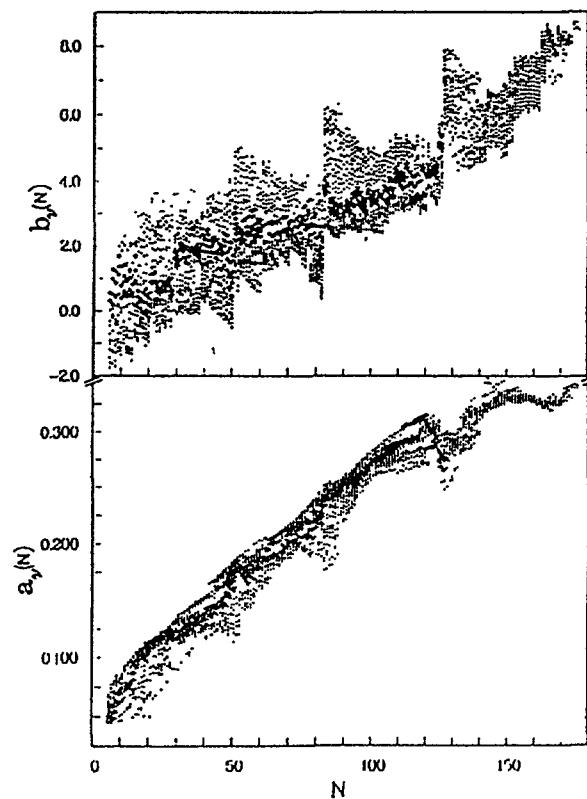


FIG. 2. Parameters *a*, and *b*, determining average spacing of neutron eigenvalues *above* the Fermi level in function of neutron number *N*. Heavy points refer to stable or nearly stable nuclei.

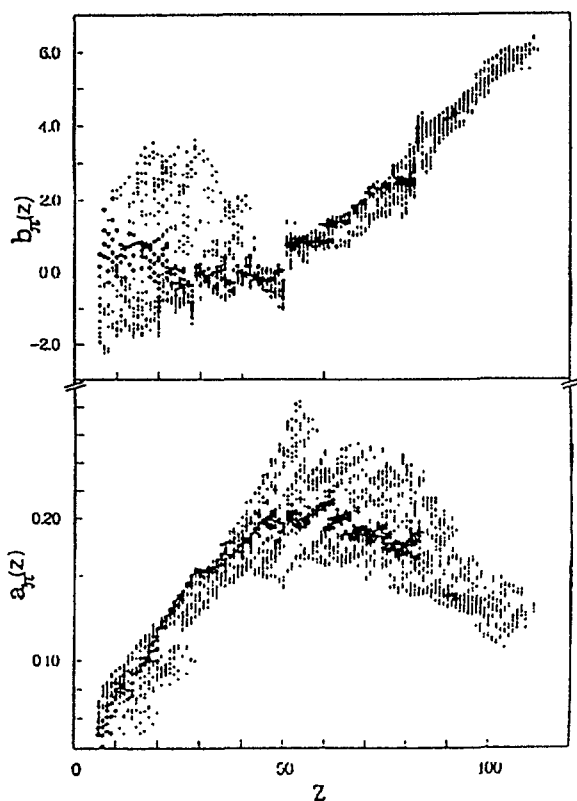


FIG. 3. Parameters *a_p* and *b_p* determining average spacing of proton eigenvalues *above* the Fermi level in function of proton number. Heavy points refer to stable or stable-neighboring nuclei.

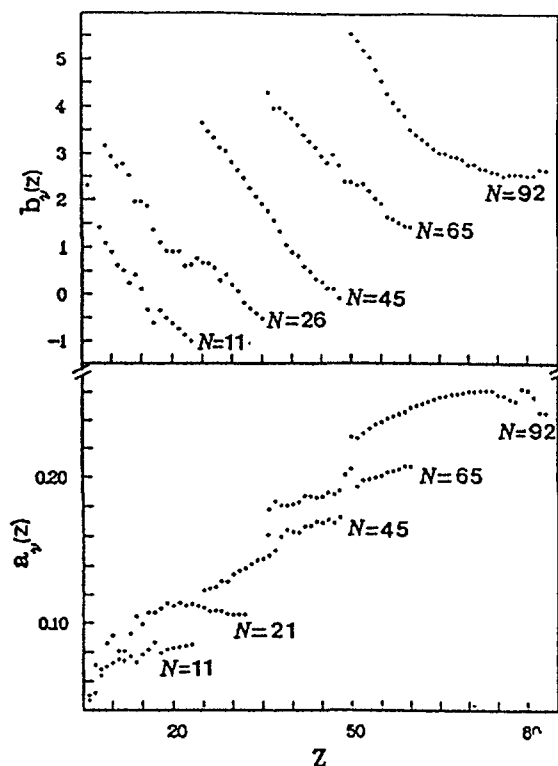


FIG. 4. Proton number dependence of *a_p* and *b_p* parameters for several fixed values of *N*.

isotonic effect, that is pointed out in Fig. 4, where the b_ν values are plotted versus Z for several fixed values of N . Clearly b_ν is a smooth and strongly decreasing function of Z . If only stable, or nearly stable, nuclei (heavy points in Fig. 2) are taken into account, the spread is considerably reduced.

- b_π (for protons) is remarkably constant (usually negative) for $Z=20\div 50$ and increases linearly for higher Z . In this case, the shell closures manifest themselves as discontinuities. Strong isotopic effects are only observed for light nuclei, and are strongly suppressed for nuclei with $Z>40$. Neutron number dependence of b_π for several fixed Z is presented in Fig. 5.

The treatment of the *s.p.l.* spacings below the Fermi level appears to be difficult. Figs. 6 and 7 show that the \tilde{a} and \tilde{b} parameters of Eq. 4 for neutrons (or protons) decrease rapidly with increasing N (or Z), varying by two orders of magnitude between very light and heavy nuclei. One can observe extremely strong shell effects, which show up not only at main shell closures, but also when certain more pronounced sub-shells are filled. Therefore, we can only predict the very general behaviour of the \tilde{a} and \tilde{b} parameters.

In Fig. 8 densities of single particle levels for neutrons and protons are shown as a function of energy above (or below) the Fermi level. These densities were calculated from the values of a , b , \tilde{a} and \tilde{b} parameters for ^{198}Au and ^{78}Rb obtained in the fit. In the case of ^{198}Au , the density for holes appears, at very low energies, much higher than the density of states available for particles. At higher excitation energies, however, the density of particle states becomes much larger, thus particle contribution to p - \hbar state density is overwhelming. From Fig. 8 one may conclude that an assumption of equal single particle state densities and holes is a crude approximation at low excitation energies, and does not hold at all when single particle levels far from the Fermi level are involved.

The g parameter plays an important role in the determination of the state densities within the independent particle model. If the spectrum of *s.p.l.* is assumed to be equidistant the expressions for partial (n -exciton in Ericson's and Williams's formulae) and total (formula type Bethe) state densities are

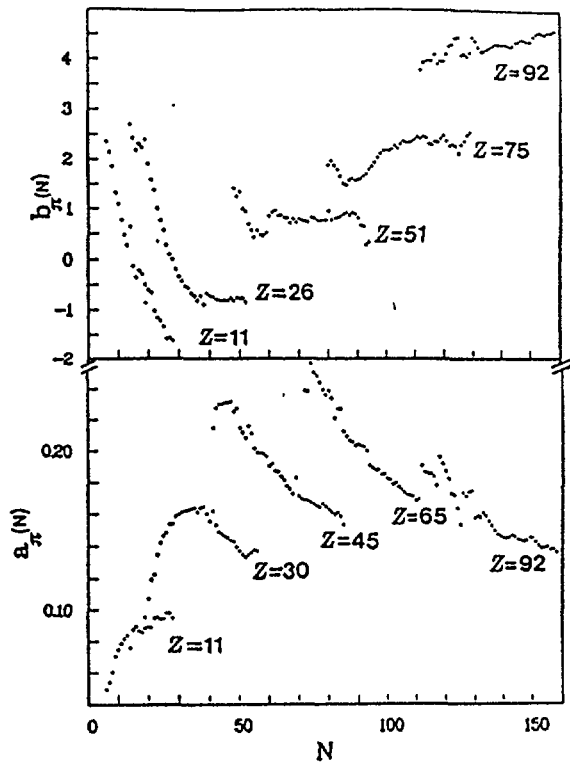


FIG. 5. Neutron number dependence of a_n and b_n parameters for several fixed values of Z .

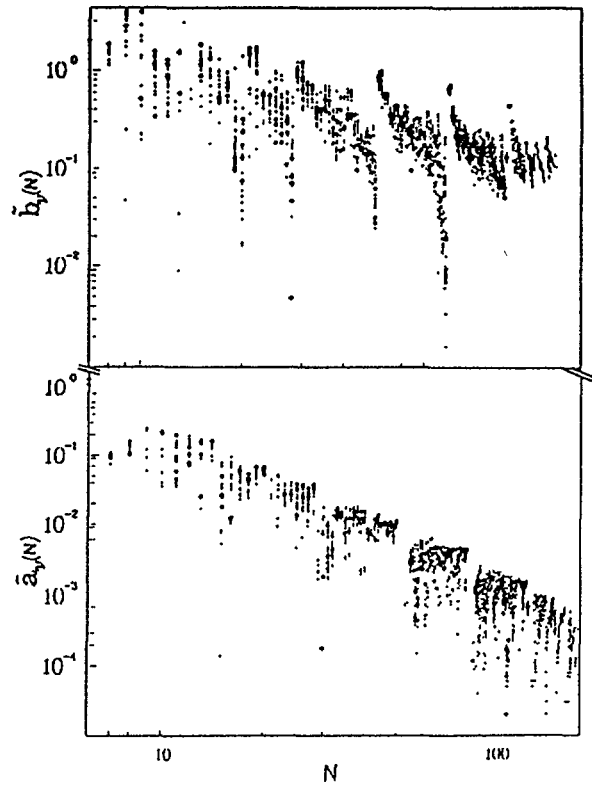


FIG. 6. Parameters \bar{a}_n and \bar{b}_n determining average spacing of neutron eigenvalues *below* the Fermi level in function of neutron number N . Heavy points refer to stable or stable-neighboring nuclei.

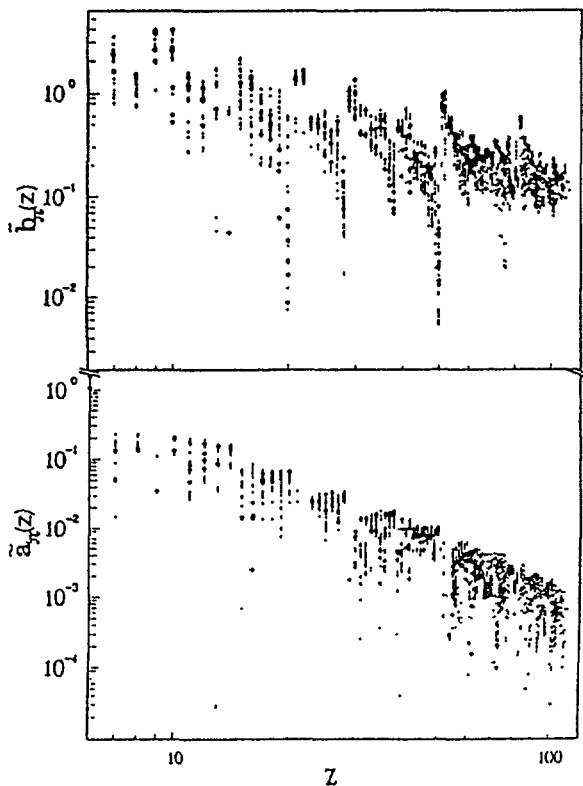


FIG. 7. Parameters \bar{a}_p and \bar{b}_p determining average spacing of proton eigenvalues *below* the Fermi level in function of proton number Z . Heavy points refer to stable or stable-neighboring nuclei.

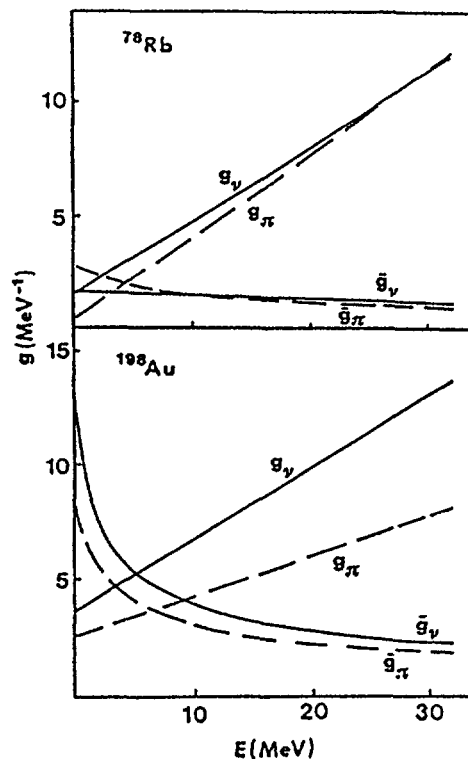


FIG. 8. Average eigenvalue densities *above* (g) and *below* (\bar{g}) Fermi level calculated with Eqs. (4) and (5) using a and b parameters obtained from the fit for ^{198}Au and ^{78}Rb nuclei. Energy is calculated with respect to the Fermi level.

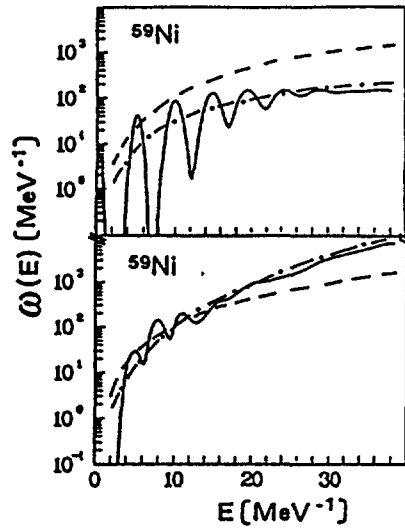


FIG. 9. State density for $3h$ (upper part) and $3p$ (lower part) neutron configurations in ^{59}Ni . Solid line represents result of the microscopic calculation. Dashed line stands for the prediction of Eq. (8) with $G=N/13$ and dash-dotted line represents the same Eq. (8) in which effective G , given by formula 12 or 13 respectively, is used.

derived. Our previous analysis proves that this assumption does not hold. Therefore we attempt to work out the method of calculating state density when the equidistant restriction is relaxed. One of these methods consists of the convolution of an $n-1$ exciton state density with an 1-exciton state density, to obtain the n -exciton state density:

$$(5) \quad \omega(n,E) = \frac{1}{n!} \int_0^E \omega(n-1,E-\epsilon) \omega(1,\epsilon) d\epsilon$$

with eigenvalue spacing given by Eqs.3 and 4.

Considering pure p -particle configurations and noting that

$$(6) \quad \omega(1,\epsilon) = g(\epsilon) = 2a\epsilon + b,$$

the following recursive expression for $\omega(p,E)$ is obtained:

$$(7) \quad \omega(p,E) = \frac{1}{p!} \sum_{i=1}^{p+1} c_i^p (2a)^{p-i+1} b^{i-1} E^{2p-i}$$

The same approach is unpractical in the case of hole configurations, because the analytical form of $\tilde{g}(\epsilon)$ does not provide a reasonably simple expression after several convolutions have been performed, therefore we propose an approximate solution of the problem. Instead of deriving an exact p - h state density formula, taking energy dependence of g explicitly

into account, we propose to retain the standard form given by

$$(8) \quad \omega(p_\nu, h_\nu, p_\pi, h_\pi, E) = \frac{G_\nu^{p_\nu} \tilde{G}_\nu^{h_\nu} G_\pi^{p_\pi} \tilde{G}_\pi^{h_\pi} E^{n-1}}{p_\nu! h_\nu! p_\pi! h_\pi! (n-1)!}$$

in which G stands for the effective density of eigenvalues defined as the average over excitation energy, weighted with the probability of finding an exciton at a given energy (exciton distribution):

$$(9) \quad G(n, E) = \int_0^E P(n, \epsilon) g(\epsilon) d\epsilon = \frac{(n-1)}{E^{n-1}} \int_0^E (E-\epsilon)^{n-2} g(\epsilon) d\epsilon$$

where $P(n, \epsilon)$ is defined by:

$$(10) \quad P(n, \epsilon) d\epsilon = k \frac{\omega(n-1, E-\epsilon)}{\omega(n, E)} d\epsilon$$

and k is a normalization factor.

Using Eq. 3 and considering the case of neutron particle levels, we get

$$(11) \quad G_\nu(n, E) = b_\nu + \frac{2 a_\nu}{n} E$$

and the corresponding expression for protons is obtained by exchanging ν with π .

The same procedure applied to neutron holes yields a more complicated recursive relation:

$$(12) \quad \tilde{G}_\nu(n, E) = \frac{(n-1)}{2 \tilde{a}_\nu (2n-3) E} [(4 \tilde{a}_\nu E + \tilde{b}_\nu^2) \tilde{G}_\nu(n-1, E) - \tilde{b}_\nu]$$

in which $\tilde{G}_\nu(1, E) = \tilde{g}_\nu(E)$.

The analogous expression for protons is obtained by the exchange of subscripts. We note that the effective density G becomes energy and exciton number dependent. In Fig. 9 predictions of Eq. 8 for 3-exciton state densities in ⁵⁹Ni are compared with the exact counting of states.

A closed formula (Eq. 8) was evaluated using common choice $G=N/13$ and using effective G determined from Eqs. 12 and 13, with a_ν , b_ν , \tilde{a}_ν , and \tilde{b}_ν parameters obtained from the fit of the cumulative number of levels. It is

evident that the Williams formula with $G=N/13$ greatly underestimates the exact density of particle configurations and overestimates the density of the hole ones. Use of the effective G in Eq. 8 results, in both cases, in a net improvement regarding the magnitude and slope of the state density.

CALCULATION OF $(n,x\gamma)$ CROSS SECTIONS BETWEEN THRESHOLD AND 100 MeV FOR Fe AND Pb ISOTOPES: COMPARISONS WITH EXPERIMENTAL DATA*

P. G. Young, R. C. Haight, R. O. Nelson, S. A. Wender, C. M. Laymon, G. L. Morgan,
D. M. Drake, and M. Drosg
LOS ALAMOS NATIONAL LABORATORY

H. Vonach, A. Pavlik, and S. Tagesen
UNIVERSITY OF VIENNA

D. C. Larson
OAK RIDGE NATIONAL LABORATORY

D. S. Dale
UNIVERSITY OF ILLINOIS

ABSTRACT

An experimental program is in progress at the Los Alamos National Laboratory WNR/LAMPF facility to perform high-resolution measurements of $(n,x\gamma)$ cross sections for individual lines up to incident neutron energies in the medium-energy range for a variety of target materials. Part of the purpose of these measurements is to provide a data base for testing the details of nuclear models in this energy range, with the goal of facilitating model improvements. In this paper initial calculations using the GNASH nuclear theory code and the level density models of Gilbert-Cameron and Ignatyuk are described. The results are compared to the existing experimental data base for $^{204,206,207,208}\text{Pb}$ isotopes at lower energies and to preliminary data from the WNR/LAMPF measurements on ^{nat}Fe and ^{208}Pb up to $E_n = 100$ MeV.

I. INTRODUCTION

An experimental program is in progress at the Los Alamos National Laboratory WNR/LAMPF facility to perform high-resolution measurements of $(n,x\gamma)$ cross sections for individual lines up to incident neutron energies in the medium-energy range for a variety of target materials. These measurements utilize the white neutron source at WNR and make use of high resolution germanium detectors to provide signatures of individual (n,xn) reactions. Preliminary measurements of gamma rays from a ^{nat}Fe target, corresponding to (n,n') , $(n,2n)$, $(n,3n)$, (n,np) , and (n,α) reactions, were reported by Nelson et al.¹ in 1989. More recently, preliminary results from $(n,xn\gamma)$ reactions on separated targets of ^{204}Pb , ^{206}Pb , ^{207}Pb and ^{208}Pb over the range $1 \leq x \leq 11$ have been described by Haight et al.² for neutron energies to over 100 MeV. In addition to providing data useful for programmatic activities such as accelerator shielding, an important goal of these measurements is to develop a data base that will permit testing of the details of nuclear models that are presently used in this energy range and to thereby facilitate improvements in the underlying nuclear theories.

Over the past several years Los Alamos National Laboratory has been involved in extending the capabilities of nuclear models for more reliable calculations in the incident nucleon energy range of 20-100 MeV.³ Much of this work has focussed on development of the GNASH nuclear theory code.⁴ Recently, an initial set of transport data libraries was completed for incident neutrons and protons up to 100 MeV on 10 target materials, with the library based mainly on calculations with the GNASH code.⁵ The new experimental program at WNR/LAMPF offers a unique opportunity to validate and improve the nuclear models used in nuclear theory codes such as GNASH.

* This work is supported by the U.S. Department of Energy.

In the present paper initial calculations of a small sampling of preliminary data from the new experiments is described. The calculations make use of two existing level density representations, namely, the standard level density parameterization of Gilbert and Cameron⁶ that has been used in many lower energy calculations, and the model of Ignatyuk et al.,⁷ which utilizes an energy-dependent level density parameter that is more appropriate for higher energies.

Most of this paper deals with calculations of neutron-induced reactions on ²⁰⁴Pb, ²⁰⁶Pb, ²⁰⁷Pb, and ²⁰⁸Pb. These calculations are described in Section II, and the results are presented in Section III with comparisons to experimental data. In Section IV, similar calculations for n + ⁵⁶Fe reactions are described, making use of parameters from an earlier analysis of ^{54,56}Fe up to 40 MeV⁸ but including the Ignatyuk et al. level density model as well as that of Gilbert and Cameron. Finally, conclusions and observations from the comparisons are presented in Section V.

II. DESCRIPTION OF THE CALCULATIONS

A. General Description

The GNASH nuclear theory code⁴ is based on Hauser-Feshbach statistical theory with full conservation of angular momentum. Preequilibrium corrections are calculated using the exciton model of Kalbach,⁹ and width fluctuation corrections are obtained from the COMNUC code¹⁰ using the approach of Moldauer.¹¹ Transmission coefficients for neutrons and charged particles are calculated using an optical model, and gamma-ray transmission coefficients are obtained from a simple giant dipole resonance approximation,¹² making use of detailed balance. The level structure for each residual nucleus in a calculation is divided into discrete and continuum regions, with the former obtained from experimental compilations and the latter from phenomenological level density representations.

Except as noted below for radiative capture cross sections, the calculations for n + ^{204,206,207,208}Pb reactions were performed using the default parameters in the GNASH code with no optimization for either the old or new experimental data under consideration. This procedure was followed in order to provide a set of base calculations, against which future improvements can be compared.

B. Optical Model

The spherical optical model potential resulting from the analysis by Finlay et al.¹³ of n + ²⁰⁸Pb experimental data in the range $7 \leq E_n \leq 50$ MeV was used for all the present calculations below 75 MeV. At higher energies the global phenomenological optical potential of Madland,¹⁴ developed for the energy range $50 \text{ MeV} \leq E_{n,p} \leq 400$ MeV and the mass range $24 \leq A \leq 208$, was utilized. Neutron transmission coefficients were computed to 100 MeV using the SCAT2 code by Bersillion.¹⁵

The neutron total cross section calculated from the optical model for ²⁰⁸Pb is compared with the available experimental data¹⁶ for ^{nat}Pb up to 100 MeV in Fig. 1. A similar comparison is given in Fig. 2 for the nonelastic cross section. While the nonelastic curve depends on the GNASH compound nucleus calculations at lower energies, above a few MeV it corresponds essentially to the optical model reaction cross section. The total and reaction cross sections that result from the Finlay et al. and Madland optical model parameterizations are seen in Figs. 1 and 2 to be consistent with the experimental data base. Slight mismatches occur near 80 MeV in the neutron total and nonelastic cross sections computed from the two potentials but the effect on the present calculations is small.

C. Gamma-Ray Transmission Coefficients

Transmission coefficients for gamma-ray transitions were obtained using detailed balance and exploiting the inverse photo-absorption process. The Brink-Axel hypothesis¹² is utilized, permit-

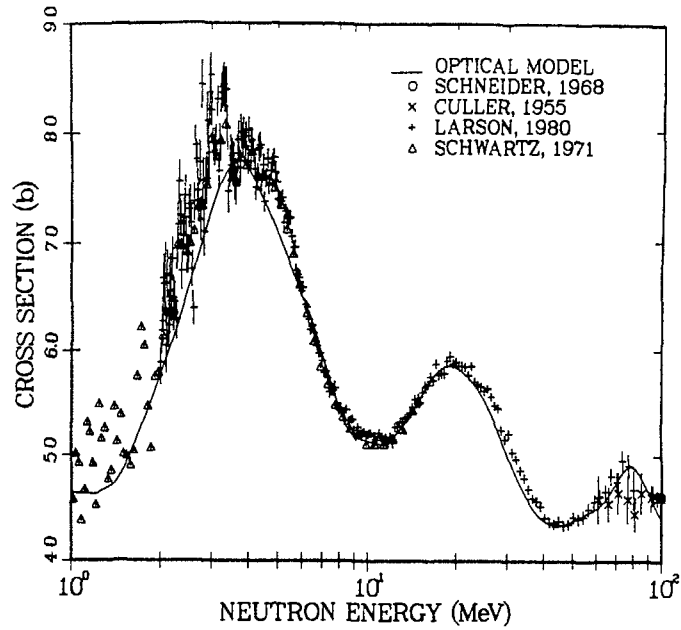


Fig. 1. Comparison of neutron total cross section measurements¹⁶ for ^{nat}Pb with optical model calculations for $n + ^{208}\text{Pb}$ interactions.

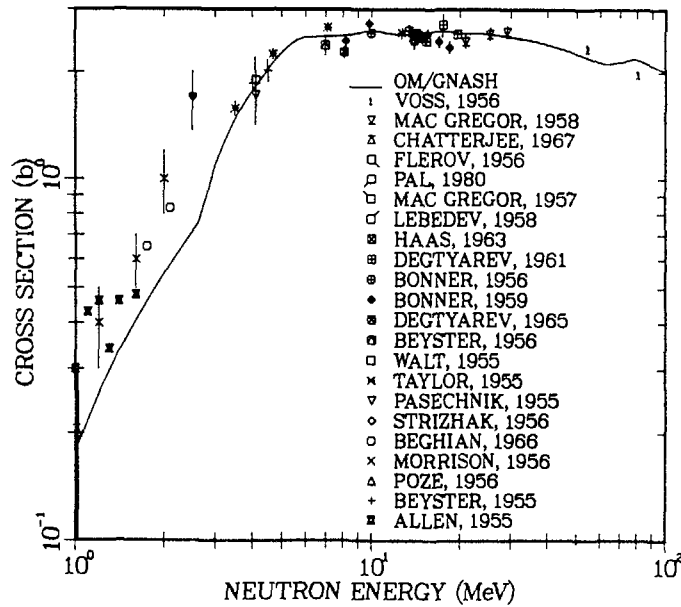


Fig. 2. Calculated and measured¹⁶ nonelastic cross section for neutron reactions on ^{nat}Pb

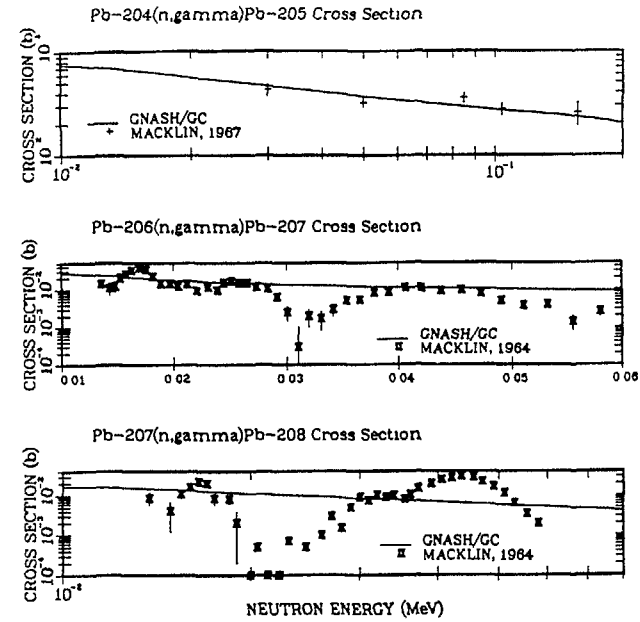


Fig. 3. Calculated and measured radiative capture cross sections for neutron reactions on ^{204}Pb , ^{206}Pb , and ^{207}Pb . The normalization of the gamma-ray transmission coefficients were determined by matching to these data,¹⁶ as described in the text.

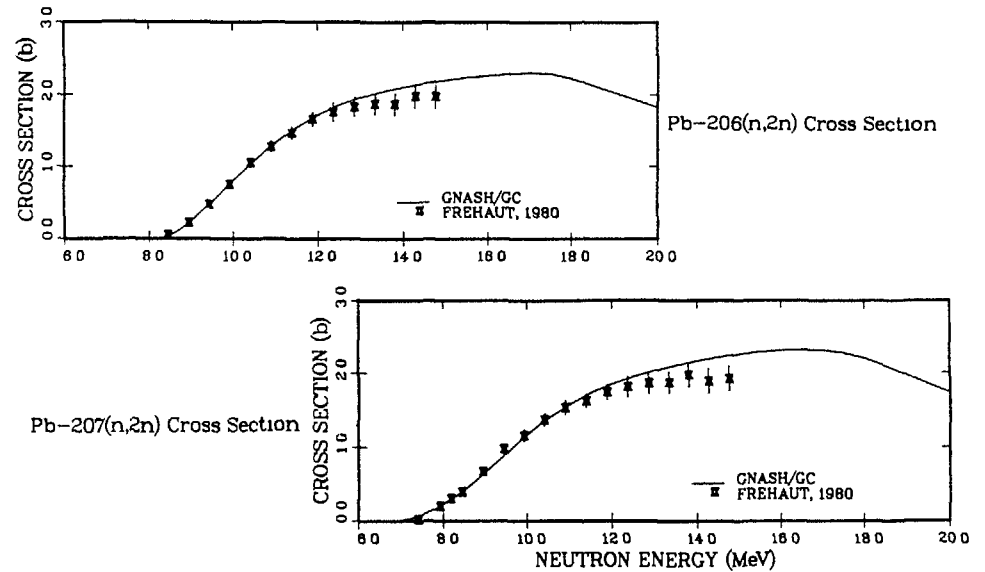


Fig. 4. Comparisons of the $^{206}\text{Pb}(n,2n)^{205}\text{Pb}$ and $^{207}\text{Pb}(n,2n)^{206}\text{Pb}$ cross sections calculated with the Gilbert and Cameron⁶ level density formulation to experimental data.¹⁶

ting the cross section for photo-absorption on an excited state to be equated with that on the ground state. The gamma-ray transmission coefficients for E1 decay are determined from the expression

$$T^{E1}(\epsilon_\gamma) = K (0.013A) \frac{2}{\pi(\hbar c)^2} \frac{\epsilon_\gamma^4 \Gamma}{(E^2 - \epsilon_\gamma^2) + (\epsilon_\gamma \Gamma)^2}. \quad (1)$$

where ϵ_γ is the gamma-ray energy and A is the atomic mass number. The Lorentzian parameters of the giant-dipole resonance, E and Γ , are taken from the tables of Dietrich and Berman.¹⁷

We usually obtain the normalization constant, K , by matching the theoretical gamma-ray strength function for s-wave neutrons to experimental values compiled by Mughabghab.¹⁸ Because of the lack of such data for the Pb isotopes, however, in this case we determined a normalization constant by roughly matching our calculations to measurements of the radiative capture cross sections for the Pb isotopes at neutron energies below 1 MeV. Comparisons are given in Fig. 3 of the calculated (n,γ) cross sections (after determination of K) for ^{204}Pb , ^{206}Pb , and ^{207}Pb . Essentially the same value of K was used in the calculations for all the lead isotopes

D. Level Density Models

A base set of Hauser-Feshbach calculations was performed for each of the Pb isotopes using the level density model of Gilbert and Cameron.⁶ At high excitation energies this model utilizes a Fermi-gas form for the level density, which is matched to a constant temperature form at lower excitation energies. For the full angular momentum calculations, a Gaussian distribution of spin states is taken to describe the angular momentum of levels at given excitation energies, E ,

$$\rho(E, J, \pi) = \frac{1}{2} \frac{(2J+1)}{2\sigma^2} \exp\left[\frac{-(J+\frac{1}{2})^2}{2\sigma^2}\right] \rho(U), \quad (2)$$

where $U = E - \Delta$ (Δ is the pairing energy) and σ^2 is the spin cutoff parameter which is determined via

$$\sigma^2 = 0.146\sqrt{aU} A^{\frac{2}{3}}, \quad (3)$$

for the Fermi-gas region. The spin-cutoff factor is determined empirically in the discrete level region from the spins of the measured levels and is then linearly interpolated in the constant temperature region to the value given by Eq. 3 at the lower energy limit of the Fermi-gas region.

The Fermi-gas expression for $\rho(U)$ used in the higher excitation energy region is given by

$$\rho(U) = \frac{\sqrt{\pi}}{12} \frac{1}{\sqrt{2\pi} \sigma} \frac{\exp(2\sqrt{aU})}{(aU^5)^{1/4}}, \quad (4)$$

and at lower energies the constant temperature form is given by

$$\rho(E) = \frac{1}{T} \exp\left[\frac{(E - E_0)}{T}\right]. \quad (5)$$

The pairing energies and shell corrections were obtained from the Cook parameter set.¹⁹ The level density parameter, a , was taken from the empirical expression in Gilbert and Cameron.⁶ The temperature T , the parameter E_0 , and the matching energy E_m that separates the constant temperature and Fermi-gas regions were obtained by requiring that ρ and $d\rho/dE$ from Eqs. 4 and 5 be continuous, while at the same time requiring the integral of Eq. 5 to match the cumulative number

of levels in the discrete or measured region. The spin- and parity-dependent level densities used in the GNASH calculations then come from Eq. 2.

The Gilbert and Cameron level density formulation (and others such as the back-shifted Fermi gas model of Dilg et al.²⁰) utilizes an energy-independent level density parameter, a , which somewhat restricts flexibility at higher energies. This difficulty is compounded by the effects of shell closures on the Fermi gas level density parameter and on their propagation to higher energies. To address these problems in the present calculations, we carried out a second set of base calculations (^{204}Pb and ^{208}Pb only) using the phenomenological level density model developed by Ignatyuk et al.⁷ In this model the Fermi gas parameter is assumed to be energy dependent and is given as a function of excitation energy U by the expression

$$a(U) = \alpha [1 + f(U) \delta W/U], \quad (6)$$

where α is the asymptotic value occurring at high energies. Shell effects are included in the term δW which is determined via $\delta W = M_{\text{exp}}(Z,A) - M_{\text{ld}}(Z,A,\beta)$. In our calculations we determined the experimental masses, $M_{\text{exp}}(Z,A)$, through use of a preliminary version of the 1988 Wapstra et al. mass compilation,²¹ and calculated $M_{\text{ld}}(Z,A,\beta)$ through use of standard liquid drop expressions evaluated at a deformation β . Additional energy dependence in $a(U)$ occurs via the term $f(U)$ which is given by

$$f(U) = 1 - \exp(-\gamma U) \quad (7)$$

where $\gamma = 0.05 \text{ MeV}^{-1}$ was determined by Ignatyuk et al.

Thus, this model permits shell effects to be included at low excitation energies while at high energies such effects disappear as $a(U)$ reaches the asymptotic value α . This form is in better agreement with results from microscopic Fermi gas models than the assumption of energy independence for a . The asymptotic value of $a(U) \rightarrow \alpha$ is given by Ignatyuk et al. as a function of mass by the expression

$$\frac{\alpha}{A} = \eta + \beta A \quad (8)$$

with $\eta = 0.154$ and $\beta = 6.3 \times 10^{-5}$, and with α in units of MeV^{-1} and A in amu. In the initial calculations described here, however, we utilize Arthur's parameterization⁵ of Eq. 8, which is based on fits to s -wave resonance data¹⁸ and which resulted in the parameters $\eta = 0.1375$ and $\beta = -8.36 \times 10^{-5}$.

The Ignatyuk et al. level density model is implemented in the GNASH code using exactly the same Fermi gas and constant temperature formulas as are applied with the Gilbert and Cameron representation, that is, Eqs. 2-5 above, and the continuum matching and matching to the discrete levels is done in the same manner. The only difference is the energy dependence of the level density parameter, $a(U)$, as specified in Eqs. 6-8.

III. RESULTS OF THE Pb CALCULATIONS

GNASH calculations were made with the Gilbert and Cameron (GC) level density representation to a neutron energy of 80 MeV for ^{204}Pb , 60 MeV for ^{206}Pb , 40 MeV for ^{207}Pb , and 100 MeV for ^{208}Pb . The calculations with the Ignatyuk et al. (IG) level density model were carried out over the same energy ranges but thus far only for ^{204}Pb and ^{208}Pb .

A. Comparison with the Existing Neutron Data Base

The calculations with the GC level densities of the total $(n,2n)$ cross sections for ^{206}Pb and ^{207}Pb are illustrated in Fig. 4 with the experimental data of Frehaut et al.²² The agreement is reasonable although there is a tendency to overpredict Frehaut's higher energy values. The

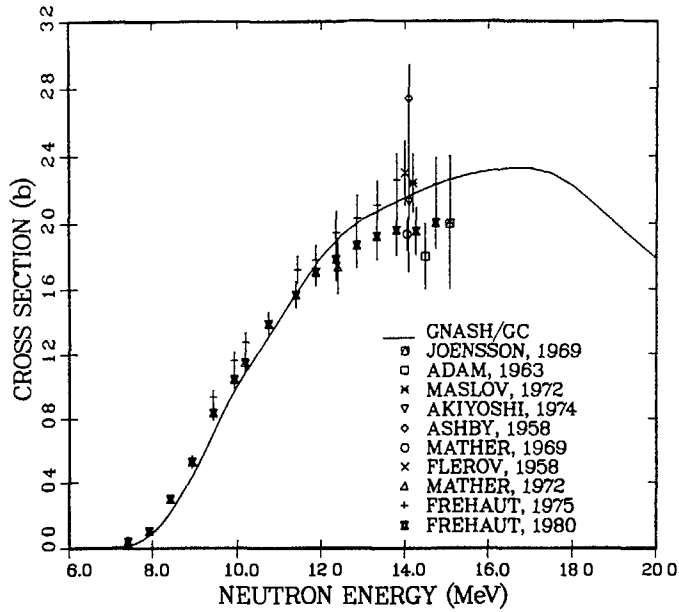


Fig. 5. Calculated and measured¹⁶ natPb(n,2n) cross sections. The solid curve was obtained by combining the GNASH calculations for individual isotopes using the Gilbert and Cameron level density model.⁶

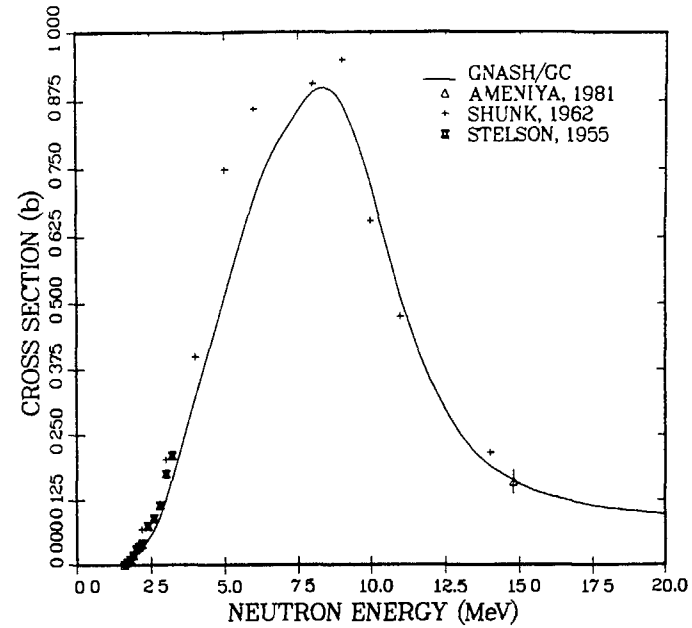


Fig. 7. Calculated and measured¹⁶ values of the ²⁰⁷Pb(n,n')^{207m}Pb cross section

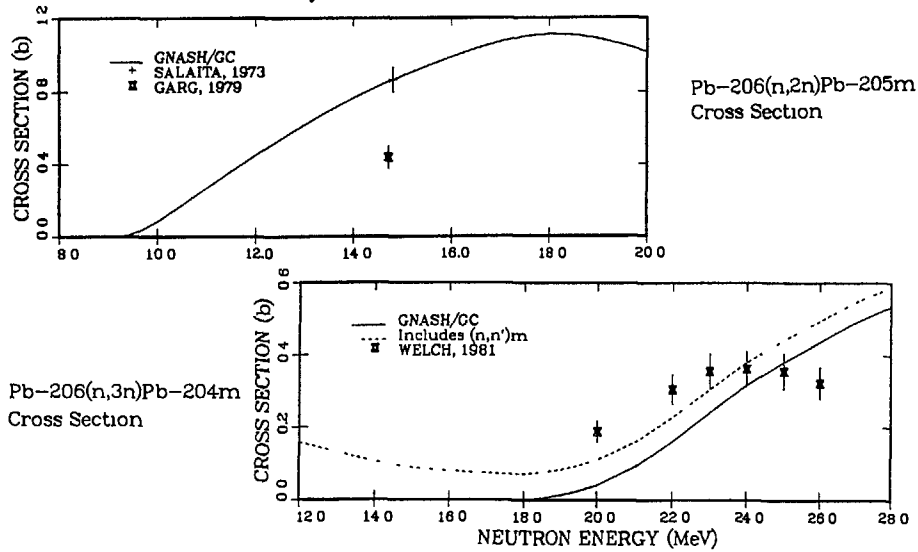


Fig. 6. Comparison of activation measurements of the ²⁰⁶Pb(n,2n)^{205m}Pb and ²⁰⁶Pb(n,3n)^{204m}Pb reactions with calculations using the Gilbert and Cameron level density representation.⁶ The dashed curve in the lower half of the figure includes the ²⁰⁴Pb(n,n')^{204m}Pb cross section.

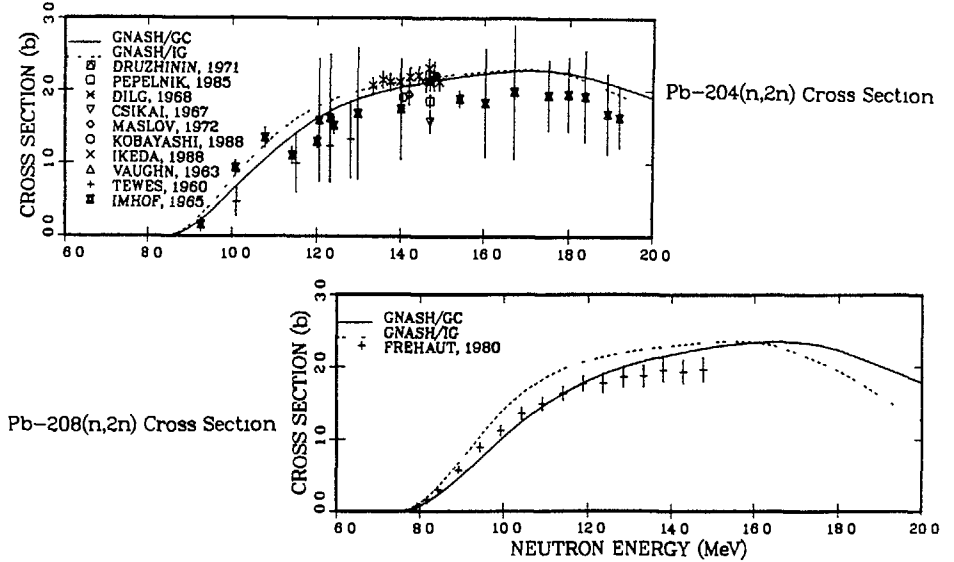


Fig. 8. Comparison of calculated and measured¹⁶ values of ²⁰⁴Pb(n,2n)²⁰³Pb and ²⁰⁸Pb(n,2n)²⁰⁷Pb cross sections. The solid curve was calculated using the Gilbert and Cameron⁶ model for level densities and the dashed curve was obtained using the representation of Ignatyuk et al.⁷

$^{nat}\text{Pb}(n,2n)$ cross section, obtained by summing the isotopic values weighted by their natural abundances, is compared to the available experimental data¹⁶ in Fig. 5. Again, the agreement is reasonable, although the calculation is higher than Frehaut's 1980 data at the highest energies. An earlier version of Frehaut's data, presumably without final corrections, is in better agreement with the calculations.

Several measurements of the activation cross sections for metastable states have been made for Pb isotopes. Such measurements impose additional requirements on calculations in that they are sensitive to the gamma cascades from higher states as well as the specific excitation cross sections of the levels involved. Comparisons of calculations (GC) and measurements are given in Fig. 6 of activation cross sections to metastable states in ^{205}Pb ($E_x = 1.014$ MeV, $J^\pi = 13/2^+$, $t_{1/2} = 5.5$ ms) and ^{204}Pb ($E_x = 2.186$ MeV, $J^\pi = 9^-$, $t_{1/2} = 67$ m) excited by (n,2n) and (n,3n) reactions on ^{206}Pb . In the lower half of Fig. 6, the dashed curve includes the calculated contribution from the $^{204}\text{Pb}(n,n')^{204m}\text{Pb}$ reaction as well as the $^{206}\text{Pb}(n,3n)^{204m}\text{Pb}$ cross section, because a natural lead target was used for the Welch et al.²³ measurements. In Fig. 7 the calculation of the $^{207}\text{Pb}(n,n')^{207m}\text{Pb}$ ($E_x = 1.633$ MeV, $J^\pi = 13/2^+$, $t_{1/2} = 0.8$ s) cross section is compared to the available data. In both Figs. 6 and 7, the agreement between calculation and measurement is reasonable.

The IG and GC calculations of the total $^{204}\text{Pb}(n,2n)$ and $^{208}\text{Pb}(n,2n)$ cross sections are compared to the available measurements in Fig. 8. The IG results are seen to increase with energy initially more rapidly than the GC calculations but to also fall off more rapidly at energies above the peak cross section. The GC results appear to agree somewhat better with the data in Fig. 8, particularly with the Frehaut results²² for the $^{208}\text{Pb}(n,2n)^{207}\text{Pb}$ cross section. It might be noted, however, that the recent Ikeda et al.²⁴ data for the $^{204}\text{Pb}(n,2n)$ cross section agree well with both calculations at higher energies whereas the Frehaut results for $^{206,207,208}\text{Pb}$ and ^{nat}Pb are systematically lower than the calculations.

Activation cross sections for the metastable states in ^{204}Pb and ^{207}Pb excited through the $^{204}\text{Pb}(n,n')^{204m}\text{Pb}$ and $^{208}\text{Pb}(n,2n)^{207m}\text{Pb}$ reactions are compared to the GC and IG calculations in Fig. 9. Both calculations underpredict the single measurement for ^{204m}Pb below 10 MeV but are in reasonable agreement near 14 MeV, especially the IG result. The IG calculation also appears to represent the ^{207m}Pb data best, although both calculations are somewhat lower than much of the data near 14 MeV.

B. Comparison with the WNR/LAMPF $^{208}\text{Pb}(n,xn\gamma)$ Measurements

Because of the higher incident neutron energies involved, a broad span of residual nuclei are covered in the WNR/LAMPF $^{204,206,207,208}\text{Pb}(n,xn\gamma)$ measurements by Haight et al.,² ranging from $N \sim 196$ to $N = 208$. A complication exists in interpreting the results of these measurements, however, because of the large number of high spin states (and therefore isomers) that are present. Because a white source of neutrons is utilized for the experiment, timing of the gamma-ray events is required to determine the incident neutron energy for any given event. States with very short or very long lifetimes clearly offer no problem in the measurement, as the former decay instantaneously relative to the experiment and the latter do not decay at all during the measurement intervals and can be simply removed from the cascades in the calculations. States that decay with half lives of the order of the timing of the experiment, however, produce a time-dependent "background" that will require a non-trivial correction. The details of the experiment are such that states with half lives in the range $10 \text{ ns} \leq t_{1/2} \leq 10 \mu\text{s}$ produce this time-dependent background. Final analysis and correction of the measurements has not yet been carried out, and additional measurements are planned during 1990. The preliminary results shown here are examples from several cases that are relatively straightforward to interpret.

The first example concerns the 0.803-MeV gamma ray from the $^{208}\text{Pb}(n,3n\gamma)^{206}\text{Pb}$ reaction and is illustrated in Fig. 10. Shown in the figure is the preliminary measured cross section for this line together with calculated values using the GC and IG level density models. This gamma ray corresponds to the $J^\pi = 2^+ \rightarrow 0^+$ transition from the first excited state in ^{206}Pb to the ground state.²⁵ One of the states that ultimately feeds this 2^+ level (through several cascades) is

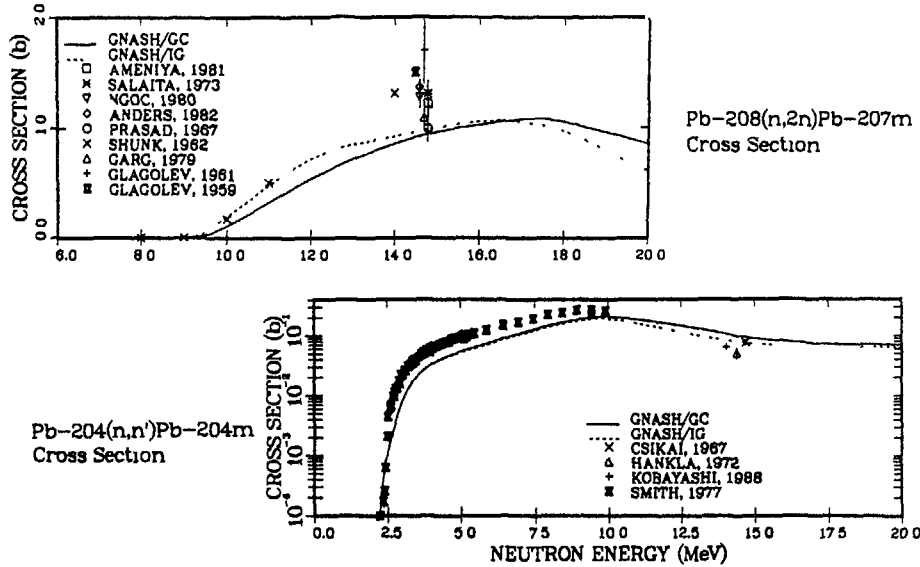


Fig. 9. Calculated and measured¹⁶ values of the ²⁰⁴Pb(n,n')^{204m}Pb and ²⁰⁸Pb(n,2n)^{207m}Pb cross sections. See caption of Fig. 8 for explanation of curves.

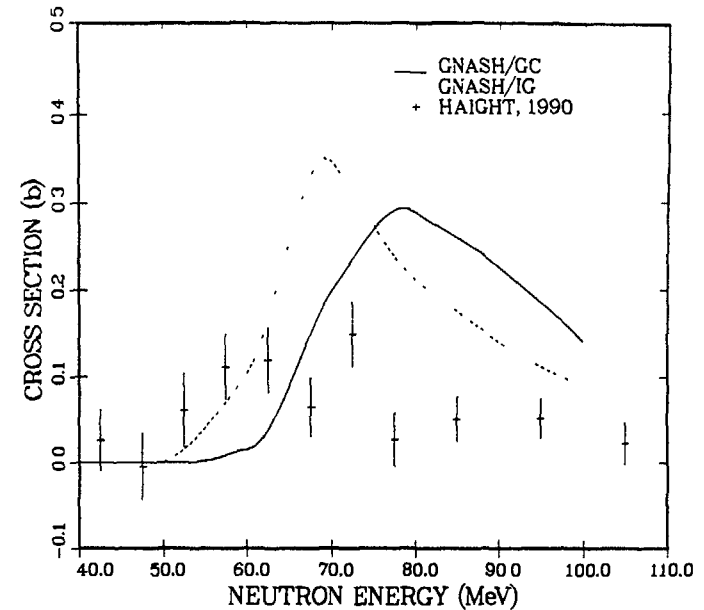


Fig. 11. Comparison of calculated and measured² values of the ²⁰⁸Pb(n,7n)²⁰²Pb cross section for the 0.960-MeV gamma ray. See caption of Fig. 8 for explanation of curves.

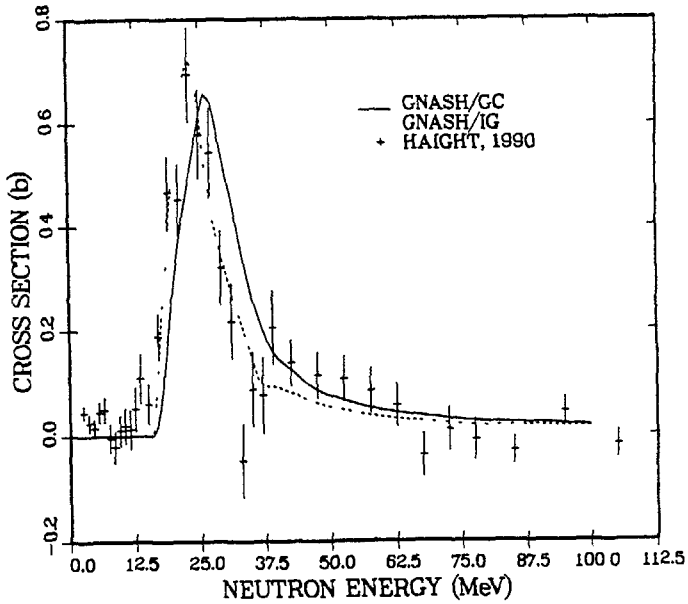


Fig. 10. Comparison of calculated and measured² values of the ²⁰⁸Pb(n,3n)²⁰⁶Pb cross section for the 0.803-MeV gamma ray. See caption of Fig. 8 for explanation of curves.

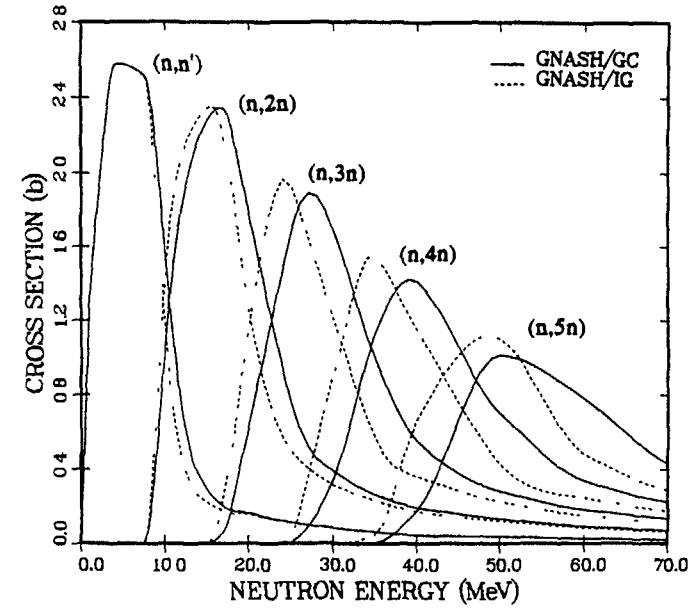


Fig. 12. Calculation of ²⁰⁸Pb(n,xn) cross sections between threshold and 70 MeV, where 1 ≤ x ≤ 5, using the Gilbert and Cameron⁶ (solid curves) and Ignatyuk et al.⁷ (dashed curves) level density representations.

the $J^\pi = 7^-$ level at $E_x = 2.200$ MeV.²⁵ Because the 7^- level has a half life of $t_{1/2} = 124$ μ s, which is relatively long compared to the measurement times, all contributions from this level were removed from both calculated curves in Fig. 10. The calculated excitation cross section for the 7^- level is significant (maximum of ~ 1 b near 25-30 MeV), so this adjustment is essential. When the experimental results are completely analyzed, this correction should be verified by the absence of gamma rays from the 7^- level.

The second example considered here is the WNR/LAMPF measurement of the 0.960-MeV gamma ray from the $^{208}\text{Pb}(n,7n\gamma)^{202}\text{Pb}$ reaction, shown in Fig. 11. This gamma ray results from the $J^\pi = 2^+ \rightarrow 0^+$ transition from the first excited state in ^{202}Pb to the ground state.²⁶ This case also requires correction of the calculations for a higher isomer that does not decay on the time scale of the experiment. In particular, there is a 3.5-h, $J^\pi = 9^-$ state at $E_x = 2.170$ MeV that decays ultimately 100% through the first excited state.²⁶ The calculated curves in Fig. 11 both have all contributions from the 9^- level removed.

The comparisons in both Figs. 10 and 11 show the same effect noted earlier for the $(n,2n)$ cross sections, namely, that the calculations with the IG level densities tend to rise sooner near threshold and fall off with energy more rapidly after peaking than do the GC calculations. In both figures the IG calculations appear to better represent the experimental data. In Fig. 10, the $^{208}\text{Pb}(n,3n\gamma)$ measurement is reproduced quite well over the entire range of the measurement. The calculations for the $^{208}\text{Pb}(n,7n\gamma)$ measurement in Fig. 11 overpredict the measurement by a factor of ~ 2 . In this case as well, however, the more rapid rise of the IG calculation appears to be supported by the data.

To further explore the observed differences between the calculations with the GC and IG level densities, the integrated $^{208}\text{Pb}(n,xn)$ cross sections obtained using both models are illustrated in Fig. 12 for $1 \leq x \leq 5$ and in Fig. 13 for $6 \leq x \leq 10$. The effects noted earlier in isolated comparisons are seen to occur systematically in the (n,xn) reactions. It is interesting to note that at certain energies the differences in the calculations are quite significant, which underscores the potential usefulness of measurements such as those described here in providing insight on level density models.

IV. RESULTS OF THE ^{56}Fe CALCULATIONS

The first preliminary data taken in the WNR/LAMPF gamma ray measurements described above were for $^{nat}\text{Fe}(n,x\gamma)$ reactions.¹ The lifetimes of levels in most of the important residual nuclei formed in these reactions are in the picosecond range, and interpretation of the results is less ambiguous. While the impact of shell effects in this case should be considerably less than for ^{208}Pb , it was felt worthwhile to compare calculational results using both the GC and IG level densities with these preliminary measurements as was done for ^{208}Pb .

The same models and calculational methods were used as are described in Section II. In this case, however, the optical model potentials developed in an earlier analysis⁸ of neutron-induced reactions with $^{54,56}\text{Fe}$ were used to calculate neutron and charged-particle transmission coefficients. All significant proton, deuteron, and alpha-particle emitting reactions were included in the calculations, as well as the neutron and gamma ray emitting processes. Calculations were performed between 1 and 60 MeV using the GNASH code with the GC and the IG level density options alternatively activated.

The results of the calculations are compared in Fig. 14 to the preliminary data reported by Nelson et al.¹ for the 0.931-MeV gamma ray, corresponding to a $^{56}\text{Fe}(n,2n\gamma)^{55}\text{Fe}$ reaction, and to the results of an earlier, more extensive measurement at ORELA by Larson.²⁷ This gamma ray corresponds to a transition from the $5/2^-$ second excited state of ^{55}Fe to the $3/2^-$ ground state. As expected, the difference in the calculations using the different level density models is not as great as was observed for the ^{208}Pb cases. The shift in energy of the peak cross sections between the models that was seen in the ^{208}Pb calculations is not apparent in Fig. 14. There does appear to be

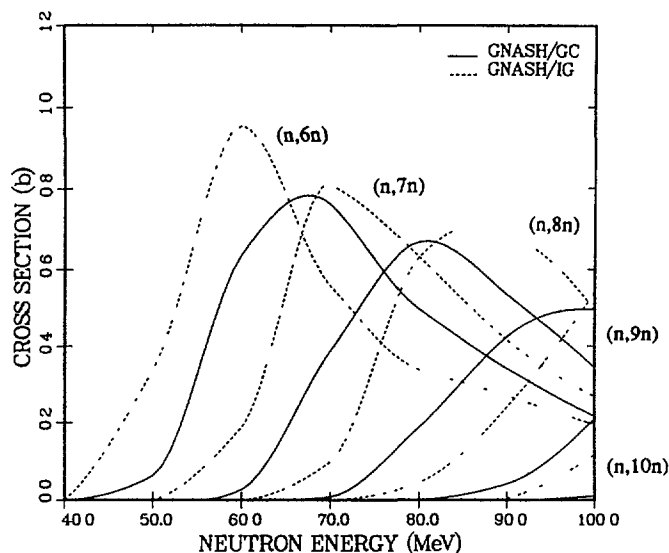


Fig. 13 Calculation of $^{208}\text{Pb}(n,xn)$ cross sections between threshold and 100 MeV, where $6 \leq x \leq 10$, using the Gilbert and Cameron⁶ (solid curves) and Ignatyuk et al.⁷ (dashed curves) level density representations.

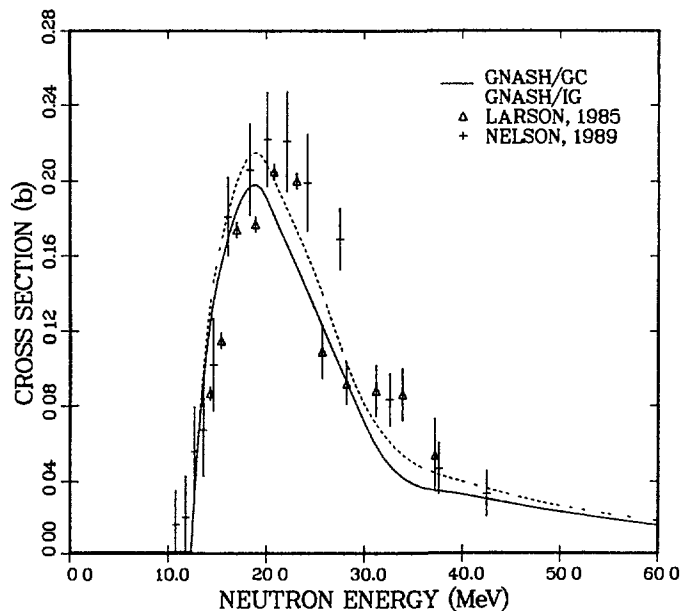


Fig. 14. Comparison of calculated and measured^{1,25} values of the $^{56}\text{Fe}(n,2n)^{55}\text{Fe}$ cross section for the 0.931-MeV gamma ray. See caption of Fig. 8 for explanation of curves.

better agreement, however, between the experimental data and the calculation using the IG level density model, which results in a somewhat higher cross section near 20 MeV.

V. CONCLUDING REMARKS

The comparisons of the calculations with experimental data at the lower energies given in Figs. 4-9 generally indicate reasonable agreement using either level density model. The agreement between the GC calculations of the $^{208}\text{Pb}(n,2n)^{207}\text{Pb}$ cross section with experiment in Fig. 8 is better than the IG case, although the reverse is true for the $^{208}\text{Pb}(n,2n)^{207\text{m}}\text{Pb}$ comparison in Fig. 9. Additionally, it is likely that some refinement in the parameters used in Eq. 8 to obtain $a(U)$ in the IG level density model might be possible.

Although the calculations at higher energies described here as well as the new WNR/LAMPF experimental data^{1,2} are regarded as preliminary, several observations can be made.

It appears clear that measurements of this nature should be useful in refining theoretical models used for calculations in the $\sim 10 - 100$ MeV range. The differences seen in the ^{208}Pb calculations with the two level density models indicate a sensitivity of these measurements that should be useful in model refinement, particularly for target nuclei near closed shells. While firm conclusions must await complete analysis of the final data from the ^{56}Fe and $^{208}\text{Pb}(n,xn\gamma)$ measurements, there appears to be better agreement at higher energies between the measurements and calculations using the IG level densities than with those that utilize the GC model. The $^{208}\text{Pb}(n,3n\gamma)^{206}\text{Pb}$ measurement (Fig. 10) agrees quite reasonably with the IG calculations, as do the results for the $^{56}\text{Fe}(n,2n\gamma)$ reaction in Fig. 14. Both sets of calculations significantly overpredict the $^{208}\text{Pb}(n,7n\gamma)^{202}\text{Pb}$ measurement shown in Fig. 11. These differences could be symptomatic of the inadequacy of the nuclear reaction models used in the 70-100 MeV range, where the discrepancies occur, or they could simply indicate the presence of additional isomers in ^{202}Pb that are not decaying rapidly enough to be included in the measurements, particularly at higher energies where shorter neutron flight times are involved. We expect that, as these measurements and analyses are refined, information will become available on a wide range of transitions and firmer conclusions can be reached.

REFERENCES

1. R. O. Nelson, S. A. Wender, and G. L. Morgan, "High Resolution Measurement of $^{nat}\text{Fe}(n,x\gamma)$ at the WNR," *Bull. Am. Phys. Soc.* **34**, 1233, J7.12 (1989).
2. R. C. Haight, D. M. Drake, M. Drogg, C. M. Laymon, G. L. Morgan, R. O. Nelson, S. A. Wender, P. G. Young, H. Vonach, A. Pavlik, S. Tagesen, D. C. Larson, and D. S. Dale, "Cross Sections for the Reactions $^{204,206,207,208}\text{Pb}(n,xn)$, $1 \leq x \leq 11$, from Threshold to Over 100 MeV," *Bull. Am. Phys. Soc.* **35**, 1038, I6.8 (1990).
3. E. Arthur, P. Young, and C. Kalbach, "New Developments in the GNASH Nuclear Theory Code," *Proc. Int. Conf. on Nucl. Data for Science and Tech.*, Mito, Japan, 30 May - 3 June 1988 [Ed. S. Igarasi, Saikon Publishing. Co., Ltd., Tokyo, 1988], p. 607; E. D. Arthur, M. Bozoian, D. G. Madland, R. T. Perry, W. B. Wilson, and P. G. Young, "Application of Nuclear Models to the Calculation of 20-100 MeV Neutron-Induced Reaction Data," International Atomic Energy Agency report IAEA-TECDOC-483 (1988) p. 278.
4. E. D. Arthur, "The GNASH Preequilibrium-Statistical Model Code," Los Alamos National Laboratory manuscript LA-UR-88-382 (1988); P. G. Young and E. D. Arthur, "GNASH: A Preequilibrium, Statistical Nuclear-Model Code for Calculation of Cross Sections and Emission Spectra," Los Alamos Scientific Laboratory report LA-6947 (1977).
5. P. G. Young, E. D. Arthur, M. Bozoian, T. R. England, G. M. Hale, R. J. LaBauve, R. C. Little, R. E. MacFarlane, D. G. Madland, R. T. Perry, and W. B. Wilson, "Transport Data Libraries for Incident Proton and Neutron Energies to 100 MeV," *Trans. Amer. Nucl. Soc.* **60**, 271 (1989) and Los Alamos National Laboratory report LA-11753-MS (1990).
6. A. Gilbert and A. G. W. Cameron, "A Composite Nuclear-Level Density formula with Shell Corrections," *Can. J. Phys.* **43**, 1446 (1965).
7. A. V. Ignatyuk, G. N. Smirenkin, and A. S. Tishin, "Phenomenological Description of the Energy Dependence of the Level Density Parameter," *Sov. J. Nucl. Phys.* **21**, 255 (1975).
8. E. D. Arthur and P. G. Young, "Evaluated Neutron-Induced Cross Sections for $^{54,56}\text{Fe}$ to 40 MeV," Los Alamos National Laboratory report LA-8626-MS (1980).
9. C. Kalbach, "The Griffin Model, Complex Particles and Direct Nuclear Reactions," *Z. Phys.* **A283**, 401 (1977).
10. C. L. Dunford, "Compound Nucleus Reaction Analysis Programs COMNUC and CASCADE," AI-AEC-12931, *Atomics Int.* (1970).

11. P. A. Moldauer, "Statistical Theory of Nuclear Collision Cross Sections," *Phys. Rev.* **135**, 642 (1964); *ibid.*, *Nucl. Phys.* **A344**, 185 (1980); *ibid.*, "Why the Hauser-Feshbach Formula Works," *Phys. Rev. C* **11**, 426 (1975).
12. D. M. Brink, D.Ph. Thesis, Oxford (1955); D. M. Brink, "Individual Particle and Collective Aspects of the Nuclear Photoeffect," *Nucl. Phys.* **4**, 215 (1957); P. Axel, "Electric Dipole Ground State Transition Width Strength Function," *Phys. Rev.* **126**, 671 (1962).
13. R. W. Finlay, J. R. M. Annand, T. S. Cheema, J. Rapaport, and F. S. Dietrich, "Energy Dependence of Neutron Scattering from ^{208}Pb in the Energy Range 7 - 50 MeV," *Phys. Rev. C* **30**, 796 (1984).
14. D. G. Madland, "A Preliminary Medium Energy Nucleon-Nucleus Phenomenological Optical Model Potential," International Atomic Energy Agency report IAEA-TECDOC-483 (1988) p. 80.
15. O. Bersillon, "SCAT2 - A Spherical Optical Model Code," in *Progress Report of the Nuclear Physics Division, Bruyères-le-Châtel 1977*, CEA-N-2037, p. 111 (1978).
16. Experimental data obtained from the National Nuclear Data Center, Brookhaven National Laboratory, Upton, New York.
17. S. S. Dietrich and B. L. Berman, "Atlas of Photoneutron Cross Sections Obtained with Monoenergetic Photons," *At. and Nucl. Data Tables* , 199 (1988).
18. S. F. Mughabghab, "Neutron Resonance Parameters and Thermal Cross Sections," Parts A and B, in *Neutron Cross Sections*, V. 1 [Academic Press Inc., 1981 (Part A) and 1984 (Part B)].
19. J. L. Cook, H. Ferguson, and A. R. Musgrove, "Nuclear Level Densities in Intermediate and Heavy Nuclei," *Aust. J. Phys.* **20**, 477 (1967).
20. W. Dilg, W. Schantl, H. Vonach, and M. Uhl, "Level Density Parameters for the Back-Shifted Fermi Gas Model in the Mass Range $40 < A < 250$," *Nucl. Phys.* **A217**, 269 (1973).
21. A. H. Wapstra, G. Audi, and R. Hoekstra, "Atomic Masses from (Mainly) Experimental Data," *At. Data and Nucl. Data Tables* **39**, 281 (1988).
22. J. Frehaut, A. Bertin, R. Bois, and J. Jary, "Status of (n,2n) Cross Section Measurements at Bruyères-le-Châtel," *Proc. Sym. on Neutron Cross Sections from 10-50 MeV*, Brookhaven National Laboratory, May 12-14, 1980, BNL-NCS-51245, V.1, p.399.
23. P. Welch, J. Johnson, G. Randers-Pehrson, and J. Rapaport, "Neutron Activation Cross Section on Al, ^{12}C , and Pb with 20-26 MeV Monoenergetic Neutrons," *Bull. Am. Phys. Soc.* **26**, 708 (1981).
24. Y. Ikeda, C. Konno, K. Oishi, T. Nakamura, H. Miyade, K. Kawade, H. Yamamoto, and T. Katoh, "Activation Cross Section Measurements for Fusion Reactor Structural Materials at Neutron Energies from 13.3 to 15.0 MeV Using the FNS Facility," Japanese Atomic Energy Research Institute report JAERI-1312 (1988).
25. M. P. Webb, "Nuclear Data Sheets for A = 206," *Nucl. Data Sheets* **26**, 145 (1979).
26. M. R. Schmorak, "Nuclear Data Sheets for A = 202," *Nucl. Data Sheets* **50**, 669 (1987).
27. D. C. Larson, "High-Resolution Structural Material (n,x γ) Production Cross Sections for $0.2 < E_n \leq 40$ MeV," *Proc. Int. Conf. on Nuclear Data for Basic and Applied Science*, May 13, 1985, Santa Fe, N. M. (Ed. P. G. Young, R. E. Brown, G. F. Auchampaugh, P. W. Lisowski, and L. Stewart, Gordon and Breach, New York, 1986) V. 1, p. 71.

The Statistics of Multi-Step Direct Reactions

A.J. Koning^b and J.M. Akkermans[#]

Netherlands Energy Research Foundation ECN

^bNuclear Analysis Department

[#]Software Engineering & Research Department

P.O. Box 1, NL-1755 ZG Petten, The Netherlands

Abstract

We propose a quantum-statistical framework that provides an integrated perspective on the differences and similarities between the many current models for multi-step direct reactions in the continuum. It is argued that to obtain a statistical theory two physically different approaches are conceivable to postulate randomness, respectively called leading-particle statistics and residual-system statistics. We present a new leading-particle statistics theory for multi-step direct reactions. It is shown that the model of Feshbach *et al.* can be derived as a simplification of this theory and thus can be founded solely upon leading-particle statistics. The models developed by Tamura *et al.* and Nishioka *et al.* are based upon residual-system statistics and hence fall into a physically different class of multi-step direct theories, although the resulting cross-section formulae for the important first step are shown to be the same. The widely used semi-classical models such as the generalized exciton model can be interpreted as further phenomenological simplifications of the leading-particle statistics theory. A more comprehensive exposition will appear before long¹).

1 Introduction

Multi-step direct (MSD) reactions in the continuum are experimentally characterized by strongly forward-peaked, but smooth, angular distributions and by pronounced high energy tails in the emission spectra. In applied experimental and phenomenological work they are also commonly called precompound or pre-equilibrium reactions, and they are viewed as intermediate between direct and (multi-step) compound reactions. A wide variety of MSD theories has been proposed in past years. The oldest are the so-called generalized exciton models that go back to the work of Mantzouranis *et al.*²); for a survey see³). These statistical models have a clear phenomenological and semi-classical background, and they have been shown to be quite successful in practice⁴) and are still being used in the analysis of experiments⁵). In more recent years several quantum-statistical theories of MSD reactions have been developed. The most important ones are those of Feshbach *et al.*⁶) (henceforth denoted the FKK model), of Tamura *et al.*⁷) (the TUL model), and of Nishioka *et al.*⁸) (called here the NWY model).

At a global level, these MSD models have several ideas and concepts in common. They share the physical picture of a fast, 'leading', incident particle in the continuum (> 10 MeV per nucleon) that creates new particle-hole pairs on its way through the nucleus. The

fact that it usually leaves the nucleus after only a few interactions ('steps') implies that upon emission it retains some memory of the incident energy and direction. This explains the high energy tails in the spectra and the forward-peaked angular distributions. Another idea all MSD models have in common is that some statistical approach is warranted, since one is dealing with regions with a high level density.

If we look more closely, however, it appears that the various MSD models are quite diverse. First, there is the split between semi-classical and quantum models. They further differ in the nature and the way of application of statistical hypotheses and of other simplifying assumptions. Most importantly, the derived expressions for MSD cross-sections are clearly different. In general, it can be said that the relationships between the various MSD theories are only partially understood.

In this paper we will propose a quantum-mechanical framework that clarifies the similarities and dissimilarities of the various MSD models. A salient feature of this framework is that we consider two possible, and physically different, randomness postulates that provide a foundation for a statistical MSD theory. The first postulate, that we call *leading-particle statistics*, supposes that at each step the leading particle can create many configurations from the given one, and that this process can be described in a probabilistic fashion. This idea of branching or of a "garden of forking paths" matches very well with the classical physical intuition and provides an explanation for the widespread occurrence of Markov chain concepts in work on nuclear reactions far from equilibrium⁹). The second statistical postulate, denoted *residual-system statistics* here, assigns the randomness properties not to the leading particle but to the residual nucleus, by assuming a random configuration mixing. This type of statistics was first proposed by ¹⁰).

On this quantum-statistical basis, we will construct a new leading-particle statistics theory of MSD reactions, of which the FKK model is a special case. This implies that the FKK model cannot be well interpreted as a simplification¹¹) of the TUL model, since the latter has a fundamentally different physical basis, *viz.*, residual-system statistics. Nevertheless, it will be shown that in certain cases different physical assumptions may still lead to the same expressions for MSD cross-sections. Finally, we will indicate how the semi-classical approaches can be understood in a quantum-mechanical context.

2 The MSD Born Series

In this section we give two expressions for the MSD cross-section distributions that are representative of the MSD reaction process *before* any statistical hypothesis has been introduced. The first expression corresponds to the general case whereby all residual interactions have been included, whereas the second one is a limiting case of the first and gives a description purely in terms of independent particle states. The latter form is of interest, since it provides the link with the widely used semi-classical pre-equilibrium models as well as with computer implementations of the FKK model. We will restrict ourselves to nucleon-induced inelastic scattering and charge exchange. Furthermore, we assume the leading particle to have no internal structure (*i.e.*, its nuclear eigenstate can simply be omitted). This is to avoid an overburdening of the notation that would divert the attention from the more important statistical issues. A generalization to other reaction types poses, in principle, no problems.

2.1 Hamiltonian and Eigenstates

The total Hamiltonian that describes the direct reaction process is:

$$H = H_0 + H_1 + K(A) + U_{opt}(A) + V, \quad (1)$$

where H_0 is the shell-model Hamiltonian, H_1 the residual interaction of the residual nucleus, K the kinetic energy, U_{opt} the optical potential and V the residual interaction of the leading particle with the residual nucleus. The explicit distinction between a residual nucleus and a leading particle is typical both for the description of a direct reaction process and for models of precompound processes²). It is also essential in the discussion of statistical assumptions in this paper.

The shell-model Hamiltonian generates a complete set of particle-hole eigenstates $|m\mu\rangle$, being anti-symmetrized direct products of $A - 1$ one-particle states,

$$H_0|m\mu\rangle = E_{m\mu}|m\mu\rangle, \quad (2)$$

where m determines the exciton class ($mpmh$ -states), μ is a running index for the particular particle-hole configuration within each class and $E_{m\mu}$ is the energy of the particle-hole state. Similarly, the real residual states $|n\rangle$ (with eigenenergies E_n) are eigenstates of H_{0+1} :

$$H_{0+1}|n\rangle = E_n|n\rangle. \quad (3)$$

The presence of H_1 causes configuration mixing, which is represented by the expansion of $|n\rangle$ as a linear combination of particle-hole states

$$|n\rangle = \sum_{m\mu} a_{m\mu}^n |m\mu\rangle. \quad (4)$$

Thus, each particle-hole state $|m\mu\rangle$ is distributed over the real states $|n\rangle$ and the strength of each contribution is determined by the distribution amplitude $a_{m\mu}^n$. If H_1 vanishes, $a_{m\mu}^n = \delta_{m\mu,n}$, corresponding to no configuration mixing.

The dynamics of the leading particle is described by a distorted wave $\chi^{(+)}$

$$[K(A) + U_{opt}(A)]|\chi^{(+)}(\mathbf{k})\rangle = E_k|\chi^{(+)}(\mathbf{k})\rangle, \quad (5)$$

where E_k is the relative kinetic energy. Together with their bi-orthogonally conjugated counterparts $\hat{\chi}^{(+)}$, they form a complete and orthonormal set.

2.2 The Cross-Section Distribution

As discussed in detail in ref.¹), standard perturbation theory gives us the cross-section distribution, a convenient tool in the description of multi-step direct reactions to the continuum. For the real nuclear model (i.e., in the presence of H_1) the one-step cross-section distribution is

$$\begin{aligned}
\frac{d^2\sigma^{(1)}}{d\Omega dE_k} &= \sum_f |T_{f\leftarrow 0}^{(1)}|^2 \delta(E_f - E_x) \\
&= \sum_f \sum_\mu \sum_{\mu'} a_{1\mu'}^f a_{1\mu}^f \langle \chi^{(+)}(\mathbf{k}_0) | \langle 0 | V | 1\mu' \rangle | \chi^{(-)}(\mathbf{k}) \rangle \\
&\times \langle \chi^{(-)}(\mathbf{k}) | \langle 1\mu | V | 0 \rangle | \chi^{(+)}(\mathbf{k}_0) \rangle \delta(E_f - E_x). \tag{6}
\end{aligned}$$

The corresponding expression for the independent particle model i.e., obtained by taking the limit $H_1 \rightarrow 0$ is,

$$\begin{aligned}
\frac{d^2\sigma^{(1)}}{d\Omega dE_k} &= \sum_\mu |t_{1\mu\leftarrow 0}^{(1)}|^2 \delta(E_{1\mu} - E_x) \\
&= \sum_\mu |\langle \chi^{(-)}(\mathbf{k}) | \langle 1\mu | V | 0 \rangle | \chi^{(+)}(\mathbf{k}_0) \rangle|^2 \delta(E_{1\mu} - E_x). \tag{7}
\end{aligned}$$

The two-step cross-section distribution in the real nuclear model is

$$\begin{aligned}
\frac{d^2\sigma^{(2)}}{d\Omega dE_k} &= \sum_f |T_{f\leftarrow 0}^{(2)}|^2 \delta(E_f - E_x) \\
&= \sum_f \sum_n \sum_{n'} \sum_\mu \sum_{\mu'} \int d\mathbf{k}'_1 \int d\mathbf{k}_1 \langle \chi^{(+)}(\mathbf{k}_0) | \langle 0 | V | 1\mu' \rangle | \hat{\chi}^{(+)}(\mathbf{k}'_1) \rangle a_{1\mu'}^{n'} \\
&\times \frac{1}{E - E_{n'} - E_{k'_1} - i\epsilon} \langle \chi^{(+)}(\mathbf{k}'_1) | \langle n' | V | f \rangle | \chi^{(-)}(\mathbf{k}) \rangle \langle \chi^{(-)}(\mathbf{k}) | \langle f | V | n \rangle | \chi^{(+)}(\mathbf{k}_1) \rangle \\
&\times a_{1\mu}^n \frac{1}{E - E_n - E_{k_1} + i\epsilon} \langle \hat{\chi}^{(+)}(\mathbf{k}_1) | \langle 1\mu | V | 0 \rangle | \chi^{(+)}(\mathbf{k}_0) \rangle \delta(E_f - E_x), \tag{8}
\end{aligned}$$

whereas we have in the independent particle model

$$\begin{aligned}
\frac{d^2\sigma^{(2)}}{d\Omega dE_k} &= \sum_\nu |t_{2\nu\leftarrow 0}^{(2)}|^2 \delta(E_{2\nu} - E_x) \\
&= \sum_\nu \sum_\mu \sum_{\mu'} \int d\mathbf{k}'_1 \int d\mathbf{k}_1 \langle \chi^{(+)}(\mathbf{k}_0) | \langle 0 | V | 1\mu' \rangle | \hat{\chi}^{(+)}(\mathbf{k}'_1) \rangle \\
&\times \frac{1}{E - E_{1\mu'} - E_{k'_1} - i\epsilon} \langle \chi^{(+)}(\mathbf{k}'_1) | \langle 1\mu' | V | 2\nu \rangle | \chi^{(-)}(\mathbf{k}) \rangle \langle \chi^{(-)}(\mathbf{k}) | \\
&\times \langle 2\nu | V | 1\mu \rangle | \chi^{(+)}(\mathbf{k}_1) \rangle \frac{1}{E - E_{1\mu} - E_{k_1} + i\epsilon} \langle \hat{\chi}^{(+)}(\mathbf{k}_1) | \langle 1\mu | V | 0 \rangle | \chi^{(+)}(\mathbf{k}_0) \rangle \\
&\times \delta(E_{2\nu} - E_x). \tag{9}
\end{aligned}$$

The importance of the above equations lies in the fact that all statistical MSD reaction models discussed in this paper have Eqs. (6)–(9) as their starting point.

3 The Statistical Problem: Postulating Randomness

It is clear from the previous section that the non-statistical expressions for MSD reactions are highly complicated, due the presence of quantum interference effects in the cross-section formulae. This makes it virtually impossible to perform (individual) cross-section calculations in regions with a high level density. Naturally, it is at this point that statistical assumptions are introduced in order to remove interference effects (upon energy averaging) to give relatively simple expressions for the energy-averaged cross-section. An additional reason to do so is the observation that the experimental characteristics of MSD reactions are rather simple, and can be reasonably well predicted by straightforward semi-classical models or even by systematics^{12,13}).

3.1 Different types of randomness

From the structure of the total Hamiltonian (1) it follows that there are two candidates for generating the statistical properties desired for manageable pre-equilibrium reaction theories: the residual interactions H_1 and V , respectively. With these interactions we can associate two physically different types of randomness:

1. *leading-particle statistics.* The interaction of the leading particle with the nucleus is modeled by V . If it is assumed that in a certain energy interval many states can be created by the leading particle, and that the corresponding matrix elements vary widely both in magnitude and sign, we obtain what we will call leading-particle statistics. Actually, this is the intuitive picture behind most of the semi-classical pre-equilibrium models.
2. *residual-system statistics.* The interactions within the residual nucleus are given by H_1 . If it is assumed that the resulting configuration mixing has a random character,

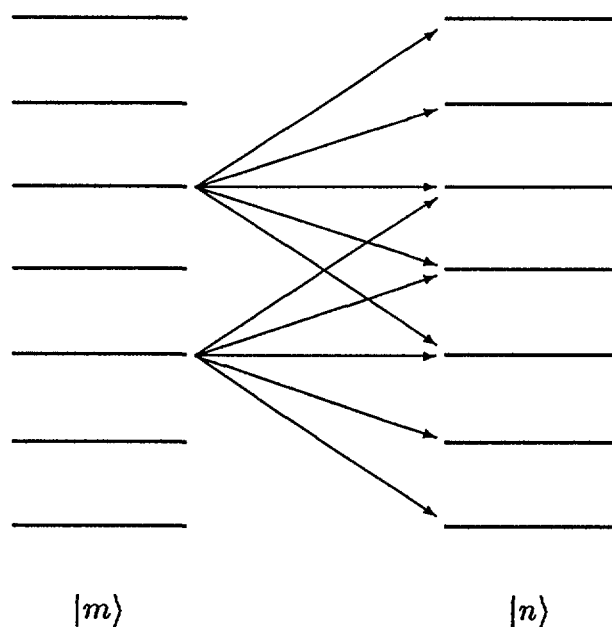


Figure 1: Leading-particle statistics: many $|n\rangle$ -states can be created in a random manner by the leading particle from a given state $|m\rangle$.

we have what we will call residual-system statistics. This type of randomness lies at the basis of the MSD theories of Tamura *et al.*⁷⁾ and of Nishioka *et al.*⁸⁾ and relates to recent studies of quantum chaos in nuclei^{14,15)}.

Below we will discuss the formal expressions for the respective statistical hypotheses. In subsequent sections we will explore their consequences for theories of MSD reactions.

3.2 Leading-Particle Statistics

Leading-particle statistics¹⁶⁾ supposes that V connects a given nuclear state to many other nuclear states (of the residual nucleus, as depicted in Fig. 1), and that the associated set of matrix elements is randomly distributed. The residual nucleus is viewed here as a subsystem of the reacting composite system consisting of residual nucleus plus leading particle.

Leading-particle statistics can formally be expressed as follows:

$$\begin{aligned} & \overline{\sum_{m,n} \sum_{m',n'} \int \int dk_1 dk'_1 \langle \hat{\chi}^{(+)}(\mathbf{k}_2) | \langle n' | V | m' \rangle | \chi^{(+)}(\mathbf{k}'_1) \rangle \langle \chi^{(+)}(\mathbf{k}_1) | \langle m | V | n \rangle | \hat{\chi}^{(+)}(\mathbf{k}_2) \rangle} = \\ & = \frac{1}{\Delta E} \sum_{m,n} \sum_{m',n'} \int \int dk_1 dk'_1 \delta_{mm'} \delta_{nn'} \delta(\mathbf{k}_1 - \mathbf{k}'_1) \langle \hat{\chi}^{(+)}(\mathbf{k}_2) | \langle n' | V | m' \rangle | \chi^{(+)}(\mathbf{k}'_1) \rangle \\ & \times \langle \chi^{(+)}(\mathbf{k}_1) | \langle m | V | n \rangle | \hat{\chi}^{(+)}(\mathbf{k}_2) \rangle = \frac{1}{\Delta E} \sum_{m,n} \int dk_1 |\langle \hat{\chi}^{(+)}(\mathbf{k}_2) | \langle n | V | m \rangle | \chi^{(+)}(\mathbf{k}_1) \rangle|^2. \quad (10) \end{aligned}$$

The bar denotes an average over the residual excitation energy $E_x (= E_{k_0} - E_{k_1})$, whereby the averaging interval ΔE is chosen such that it contains a sufficiently large number of accessible states. The physical assumption here is that non-diagonal cross-products of matrix elements cancel upon energy averaging, because these matrix elements widely vary both in magnitude and sign and therefore can be considered to be random variables. Eq. (10) refers to the intermediate steps in a multi-step process. A similar postulate for the final steps will be used whereby χ occurs instead of $\hat{\chi}$. As a consequence of the assumed two-body nature of V , there is at most a $1p1h$ difference in complexity between the $|m\rangle$ and $|n\rangle$ states of the residual nucleus. Thus, a special instance, important for the first step, of Eq. (10) is:

$$\begin{aligned} & \overline{\sum_{\mu} \sum_{\mu'} \int \int dk_1 dk'_1 \langle \hat{\chi}^{(+)}(\mathbf{k}_2) | \langle 1\mu' | V | 0 \rangle | \chi^{(+)}(\mathbf{k}'_1) \rangle \langle \chi^{(+)}(\mathbf{k}_1) | \langle 0 | V | 1\mu \rangle | \hat{\chi}^{(+)}(\mathbf{k}_2) \rangle} = \\ & = \frac{1}{\Delta E} \sum_{\mu} \int dk_1 |\langle \hat{\chi}^{(+)}(\mathbf{k}_2) | \langle 1\mu | V | 0 \rangle | \chi^{(+)}(\mathbf{k}_1) \rangle|^2. \quad (11) \end{aligned}$$

The above form of statistics resembles that of Ref. ¹⁷⁾, but here it is worked out for MSD rather than for multi-step compound reactions. The difference lies in whether or not it makes sense to retain the distinction between a leading continuum particle and other,

slower, particles in the composite nuclear system. Leading-particle statistics is a necessary condition for the —both conceptually and computationally attractive— convolution-type structure of the FKK model and the generalized exciton models.

3.3 Residual-System Statistics

This type of randomness^{8,10)} is based on the properties of the residual nucleus alone, in other words, its existence is not related to the particular dynamics of the reaction. For sufficiently high excitation energies E_x , the spectrum of the residual nucleus contains many states within a relatively small interval ΔE around E_x . For each state, we expect the linear combination (4) to be very complicated. Now, residual-system statistics is introduced by assuming a random configuration mixing, *i.e.*, the amplitudes $a_{m\mu}^n$ are supposed to be elements of a random probability distribution. As a consequence, the non-diagonal elements vanish upon energy averaging:

$$\overline{\sum_n a_{m'\mu'}^n a_{m\mu}^n \delta(E_n - E_x)} = \delta_{mm'} \delta_{\mu\mu'} \overline{\sum_n |a_{m\mu}^n|^2 \delta(E_n - E_x)} \quad (12)$$

the bar denoting the average over the residual excitation energy. More detailed discussions of the nuclear structure aspects concerning the distribution of the amplitudes can be found in Refs. ^{18–22}). In this paper, we assume the above statistical hypothesis to be valid and apply it to the previously derived MSD cross-section distributions.

As an illustration, let us consider the one-step cross-section distribution (6). Upon energy averaging, the non-diagonal terms vanish and the distribution $c_{1\mu}(E_x) = \sum_n |a_{m\mu}^n|^2 \delta(E_n - E_x)$ can now be interpreted as the relative contribution of the model state $|1\mu\rangle$ to the real level with energy E_x . The statistical mixing between the particle-hole model states and the real nuclear states is depicted in Fig. 2. It is imagined that

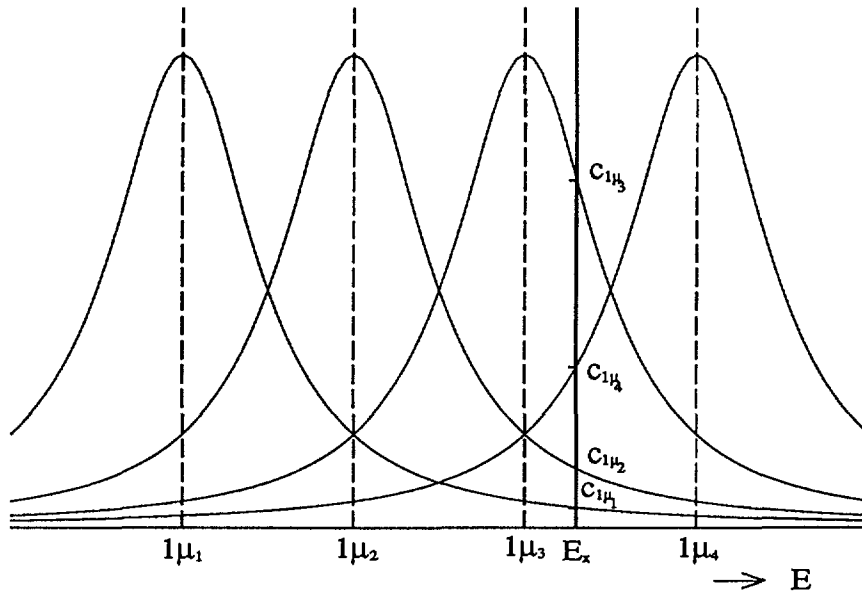


Figure 2: Residual-system statistics: the dashed lines represent the particle-hole states, each contributing differently to the real nuclear state (solid line) according to some random distribution (here: a Lorentzian).

around each particle-hole state a probability distribution $c_{1\mu}$ is given, its width being a measure for the magnitude of the residual interaction H_1 . Then, the contribution of each particle-hole state to a real state is represented by the value of $c_{1\mu}$ at the considered excitation energy. Existing examples of the application of residual-system statistics are the TUL and the NWY models, which will be discussed later.

3.4 Generating simple MSD models

Even with the introduction of statistical hypotheses, the quantum MSD theories tend to become quite complicated. On the other hand, as already pointed out, experimental data concerning MSD reactions display a simple, smooth structure and are fairly well explained by simple approaches. In addition to the mentioned statistical postulates, we will therefore also investigate further approximations that are useful to obtain simple MSD models. The most important of these are the on-shell approximation and the independent-particle limit. With these ingredients, it will be sketched how one can generate a variety of different theories that includes both existing and new MSD models. In particular, it is possible to give a quantum-statistical interpretation of the phenomenological models that are most widely used in practice.

4 The One-Step Cross-Sections

4.1 The Real Nuclear Model

The cross-section distribution for the first step given by Eq. (6) can now be averaged over the final energy using *either* leading-particle statistics (11) *or* residual-system statistics (12). Recalling the previously discussed physical difference between the two hypotheses, we come to the interesting conclusion that in either case the *same* expression for the averaged one-step cross-section is found:

$$\overline{\frac{d^2\sigma(i)}{d\Omega dE_k}} = \sum_{\mu} \hat{\rho}_{1\mu}(E_x) |\langle \chi^{(-)}(\mathbf{k}) | (1\mu | V | 0) | \chi^{(+)}(\mathbf{k}_0) \rangle|^2, \quad (13)$$

where the true partial level density $\hat{\rho}_{m\mu}$ is defined by

$$\hat{\rho}_{m\mu} = \overline{c_{m\mu}(E_x)}. \quad (14)$$

This coincides with the expression obtained for the TUL model in ⁷⁾ and for the NWY model in ⁸⁾, although there it was specifically associated with residual-system statistics.

In the practical implementation of (13) by the computer code ORION-TRISTAR²³⁾, the diagonal terms of Eq. (6) are averaged over an energy interval, whereby the distribution $c_{1\mu}(E_x)$ of Eq. (12) is taken to be a Gaussian or a Lorentzian. The DWBA cross-section is calculated for each particle-hole state and the result is multiplied by the corresponding statistical factor (*cf.* Fig. 2). Repeating this procedure for some neighbouring values of E_x yields the averaged result (13).

4.2 The Independent Particle Model

Also the independent particle model leads to an interesting finding, since Eq. (7) shows that in this case there are no interference effects to be destroyed and, thus, *no randomness hypothesis* whatsoever is necessary to obtain the desired result. In this case, the energy-averaged one-step cross-section becomes

$$\overline{\frac{d^2\sigma^{(1)}}{d\Omega dE_k}} = \frac{1}{\Delta E} \sum_{\mu} |\langle \chi^{(-)}(\mathbf{k}) | \langle 1\mu | V | 0 \rangle | \chi^{(+)}(\mathbf{k}_0) \rangle|^2. \quad (15)$$

We see that in the independent particle model the individual DWBA cross-sections have equal weights in the averaged cross-section. This is in contrast to the previous case where each DWBA cross-section is weighted by a factor $c_{1\mu}(E_x)$. Eq. (15) can be rewritten in the equivalent form

$$\overline{\frac{d^2\sigma^{(1)}}{d\Omega dE_k}} = \rho_{1p1h}(E_x) \overline{|\langle \chi^{(-)}(\mathbf{k}) | \langle 1p1h | V | 0 \rangle | \chi^{(+)}(\mathbf{k}_0) \rangle|^2}^{1p1h}, \quad (16)$$

where $\rho_{1p1h}(E_x)$ denotes the particle-hole model level density of the residual nucleus. Usually it is estimated by the Williams formula²⁴). In the computer code of Bonetti *et al.*²⁵), Eq. (16) has been implemented as the one-step cross-section of the FKK model. This is done by decomposing Eq. (16) into different transferred angular momenta and estimating the average for each angular-momentum value by drawing a small sample.

In sum, for the real nuclear model we find that both leading-particle statistics and residual-system statistics lead to the same expression for the one-step cross-section. For the independent particle model we do not even need a statistical assumption to obtain the desired energy-averaged result. The model level density ρ differs from the true level density $\hat{\rho}$ and therefore Eq. (16) differs from the TUL, NWY and leading-particle statistics models already in the first step. In the limit $H_1 \rightarrow 0$ the probability distributions $c_{1\mu}(E_x)$ of Fig. 2 reduce to delta functions and, consequently, Eq. (13) will then coincide with Eq. (16).

4.3 A computational illustration

As already pointed out, Eqs. (13) and (16) have both been implemented as part of a multi-step direct computer program, in the TUL code of Tamura *et al.*²³) and in the FKK model code of Bonetti *et al.*²⁵), respectively. As an illustration, we have carried out some calculations with these computer codes and the results are presented in Fig. 3. Here, a comparison is given between the calculated one-step cross-sections, for inelastic proton scattering on ⁵⁸Ni at 65 MeV of incident energy and 51 MeV of outgoing energy. For the sake of comparison, the input parameters were made equal as much as possible (same optical model, same maximum ℓ -value for distorted waves, *etc.*). In the FKK code the energy average is taken over an interval of 20 MeV. The distribution $c_{1\mu}$ has been taken in the TUL code to be a Lorentzian with a width of 4 MeV which is also the used

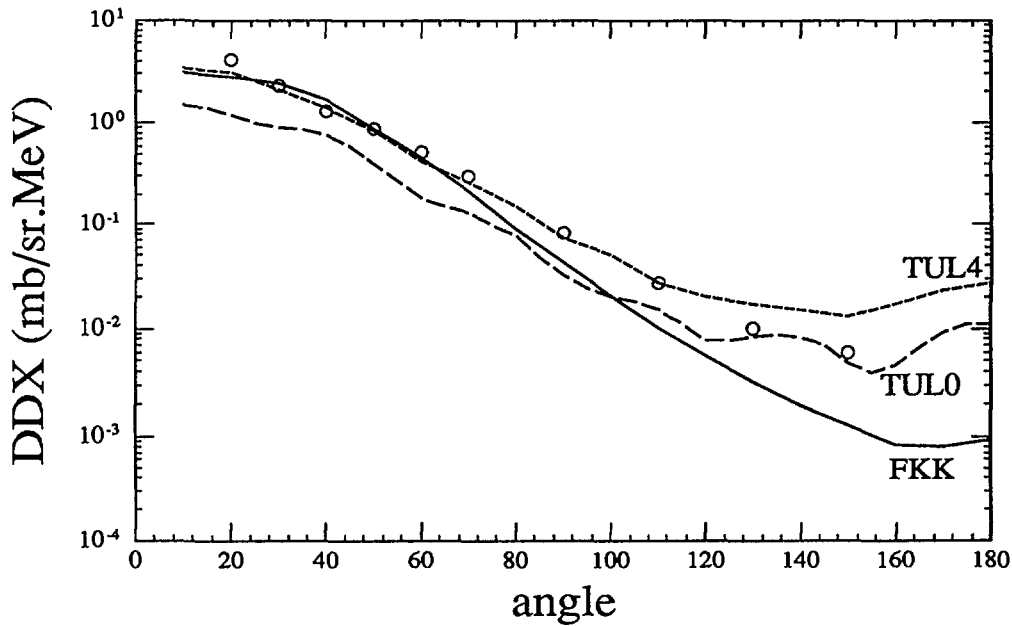


Figure 3: Double-differential one-step cross-sections for $^{58}\text{Ni}(p,p')$ at 65 MeV incident energy and 51 MeV outgoing energy. The solid line is the FKK result, the short-dashed line is the TUL result with a width of 4 MeV, and the long-dashed line is the TUL result in the limit of zero width.

averaging interval. In the figure we have also displayed the result for a distribution width that is virtually zero, thus computationally simulating the independent particle limit. The experimental data are from Ref.²⁶).

It is perhaps helpful to add a remark on the calculation of the true and model level densities $\hat{\rho}$ and ρ . The difference between them is that $\hat{\rho}$ includes the configuration mixing of the residual states, whereas ρ neglects this effect. The FKK code uses the model level density ρ , for which the Williams formula is generally used. The TUL code uses the true level density $\hat{\rho}$. Here, a problem is that this is the concept that naturally occurs in the theory, but it is very difficult to give an adequate computational prescription for it. Only a few recent papers deal with this problem^{27,28}). In our calculations, we follow the suggestion of Tamura *et al.* who estimate $\hat{\rho}$ by an energy average over Lorentzian distributions.

A first conclusion from the figure is that all models—and we recall that the TUL result also represents that of the NWY model and of our leading-particle statistics theory—indeed predict that the first step provides the major contribution (say, 80 per cent of the total cross-section) to the MSD cross-section. This reconfirms the results from the many studies done on the basis of the generalized exciton models. The various models also roughly predict the same shapes and absolute values, although at a more detailed level there are clear differences. The independent-particle limit of the TUL code should, theoretically speaking, yield the same result as that of the FKK code. That this is actually not the case can therefore not be attributed to differences in the underlying physics of the models, but it is rather located in more practical aspects like different choices for various model parameters that are embedded in the computer codes. Accordingly, the results presented should not be taken as a detailed comparison of MSD-theories with

experimental data. The figure as a whole shows that practical parameter choices are at least as important as physical differences in the implemented MSD theories and, thus, that a proper computational comparison of theories is not simple and needs to be carried out with care. Accordingly, a more thorough model and code comparison for the quantum MSD theories would be very useful.

5 The Two-Step Cross-Section: Leading-Particle Statistics

In the previous section it has been demonstrated that different physical routes lead to more or less the same first-order expressions. We will see, however, that the descriptions for the two-step process show more diversity. In this section, we will give the various two-step results that have their physical basis in leading-particle statistics, whereas the corresponding results for residual-system statistics are discussed in the next section. For detailed derivations we refer to ref.¹⁾.

5.1 The General Leading-Particle Statistics Theory

Our starting point is Eq. (8) and we employ the usual never-come-back assumption by supposing that the dominant process is that the leading particle creates a new particle-hole pair, leaving the rest of the nucleons as spectators. Then, applying leading-particle statistics on the intermediate and the final states yields the result:

$$\begin{aligned} \overline{\frac{d^2\sigma^{(2)}}{d\Omega dE_k}} &= \sum_{\mu} \sum_{\nu} \int dE'_x \hat{\rho}_{1\mu}(E'_x) \hat{\rho}_{1\nu}(E''_x) \int dk_1 |\langle \chi^{(-)}(\mathbf{k}) | \langle 1\nu | V | 0 \rangle | \chi^{(+)}(\mathbf{k}_1) \rangle \\ &\times \frac{1}{E - E'_x - E_{k_1} + i\epsilon} |\langle \hat{\chi}^{(+)}(\mathbf{k}_1) | \langle 1\mu | V | 0 \rangle | \chi^{(+)}(\mathbf{k}_0) \rangle|^2. \end{aligned} \quad (17)$$

We stress that although the distribution amplitudes $a_{1\mu}^n$ and $a_{(1\nu)n}^f$ have been averaged over energy, *no* random configuration mixing was used to eliminate the associated interference effects.

5.2 The FKK model as a Simplified Leading-Particle Statistics Theory

The FKK model⁶⁾ can be viewed as a simplification of the above leading-particle statistics theory¹⁶⁾. An attractive feature of the FKK model is its simple convolution structure, which is not present in the above equation as a result of the occurrence of the Green function. The basic ingredient to obtain this convolution structure is the use of the on-shell approximation, which physically corresponds to the classical idea of energy conservation at each step. Except for the additional use of this approximation, the derivation of the FKK result employs the same assumptions as in the previous subsection. It reads:

$$\begin{aligned} \overline{\frac{d^2\sigma^{(2)}}{d\Omega dE_k}} &= \pi^2 \int dk_1 \rho(k_1) \rho_{1p1h}(E''_x) \rho_{1p1h}(E'_x) \overline{|\langle \chi^{(-)}(\mathbf{k}) | \langle 1p1h | V | 0 \rangle | \chi^{(+)}(\mathbf{k}_1) \rangle|^2}^{1p1h} \\ &\times \overline{|\langle \hat{\chi}^{(+)}(\mathbf{k}_1) | \langle 1p1h | V | 0 \rangle | \chi^{(+)}(\mathbf{k}_0) \rangle|^2}^{1p1h}. \end{aligned} \quad (18)$$

This is basically the two-step result for the FKK theory (see Eq. (2.5) of Ref.⁶) and the expression that has been implemented in the computer codes of Bonetti *et al.*²⁵) and of Marcinkowski *et al.*²⁹). There are two differences with the result given in the original FKK paper⁶). First, these authors introduced a further simplification by replacing $\hat{\chi}$ by χ , a choice argued in more detail in³⁰), but criticized in¹¹). Although computationally very convenient (and present in the mentioned computer programs), in our opinion this assumption is likely to constitute an oversimplification, since it would imply that the probability of emission equals that of particle-hole creation. The second difference lies in an additional summation over neighboring particle-hole states in the original FKK expression. This summation is not present here as a result of our use of the never-come-back assumption. We mention in passing that it does also not occur in the implementations of²⁵) and²⁹).

Further, we point out that the independent-particle limit is not a crucial element in the above derivation, although it is employed in the computer codes of²⁵) and²⁹). In other words, the FKK result for the real nuclear model can be obtained by replacing ρ by $\hat{\rho}$.

The derivation given in¹) demonstrates that the FKK result can be seen as only based upon leading-particle statistics. There is no need at all to invoke residual-system statistics, although this was explicitly mentioned in⁶). In addition, we have shown that the FKK model is a simplification of a more general leading-particle statistics theory, resulting from the additional introduction of the on-shell approximation. Both leading-particle statistics and the on-shell approximation are necessary to obtain its characteristic convolution structure.

5.3 The generalized exciton model

In this subsection we will sketch how the generalized exciton model²), which is still widely used in practice but has a semi-classical and phenomenological character³), can be interpreted in terms of our theory. Basically, it can be viewed as a classical interpretation and a further phenomenological simplification of the FKK model. We point out that a rigorous derivation will not be possible, because the exciton model treats the precompound process as a whole and therefore embodies a mixture of multi-step compound and MSD concepts. Nevertheless, its physical ideas can be qualitatively explained and its main characteristics, in particular the shape of the angular distributions and of the energy spectra, can be semi-quantitatively understood in terms of the present quantum-statistical framework¹⁶).

Several of the physical ideas behind the generalized exciton model can be interpreted in a straightforward manner. It consistently employs particle-hole model states and thus neglects the residual interaction H_1 within the final nucleus. Accordingly, residual-system statistics does not play an essential role in the exciton model. Indeed, the picture behind the generalized exciton model is that the fast incident particle can at each step create many different configurations in a probabilistic manner. This idea is formally expressed in our leading-particle statistics postulate. That Eq. (10) is indeed a proper quantum-statistical formalization of the MSD part of the exciton model is corroborated by comparing it to the statistical hypothesis proposed by¹⁷) for (what now would be called) multi-step compound reactions and its attempted extension to the leading-particle concept in²). Furthermore,

the exciton model assumes that classical conservation of energy applies to all transitions, these being expressed in terms of particle-hole model states.

Thus, the MSD part of the exciton model can be reformulated in a quantum-mechanical framework in a manner that is truthful to its conceptual ideas by employing: (i) leading-particle statistics; (ii) the on-shell approximation; (iii) the independent-particle limit. Hence, this reformulation is given by Eq. (16) for the first step and by Eq. (18) for the second step. This conclusion has some interesting corollaries¹⁶). First, in contrast to what is often stated in exciton-model studies, no equiprobability assumption for the creation of different configurations is being invoked. Second, no statistical assumption is needed in obtaining the one-step expression, since it is simply proportional to the sum of the squared residual DWBA matrix elements within the considered energy interval. Finally, and most importantly, the above discussion shows that the FKK model (as we have interpreted it here) represents the proper quantum-mechanical reformulation of the MSD part of the exciton model, in the sense that it embodies the same conceptual physical ideas, but avoids the classical and *ad hoc* aspects of the exciton model.

We will now shortly discuss the phenomenological simplifications used by the generalized exciton model and to be introduced into Eqs. (16) and (18). A peculiar feature of the exciton model is that it displays a convolution-type structure for the double-differential cross-sections, but unlike the FKK model only for the angle dependency and not for the energy-dependent part^{2,3}). The reason for this is mainly historical: the original exciton model was an extension of statistical compound ideas³¹) and the leading-particle concept was only introduced later on and is therefore something of a patch-up. We can obtain this structure from Eqs. (16) and (18) by assuming (as is indeed done in the generalized exciton model) that the occurring averaged matrix elements factorize into an angular and an energy-dependent part. An additional simplification is then introduced by not estimating the angle-dependent factor (called the "scattering kernel" in phenomenological work) from DWBA theory, but from classical isotropic (in the nucleon-nucleon center-of mass system) scattering or, in later work, from the Kikuchi-Kawai expressions³²). These assumptions generate from Eqs. (16) and (18) the angular distributions as given by the generalized exciton model. Although very simple, they nevertheless produce reasonable predictions^{4,5}).

In order to explain how the exciton model obtains expressions for the emitted energy spectra from Eqs. (16) and (18), even more simplifications are needed. The intermediate matrix elements are replaced by global quantities independent of the intermediate energy (albeit that we do not need this assumption for the first step). As a result, the n -step cross-sections become proportional to $\rho_{nph}(E_x)$. Next, an additional average over E_k is carried out and the final step matrix elements are then estimated from the inverse process using detailed balance considerations. This yields the energy dependence of the exciton-model emission rates as discussed in the Appendix of³¹). Although these procedures are not very convincing in the MSD context (as they clearly have their roots in compound concepts), they again yield reasonable results for the emission spectra. It is to be noted, however, that the main precompound contribution stems from the first step.

From this discussion it is evident, first, that the generalized exciton model is physically speaking a simplified version of the leading-particle statistics theory and especially of the

FKK model and, second, that the estimates and simplifications used in the final expressions of the exciton model are very crude. Accordingly, if one adheres to the physics as embodied in the exciton model, we would recommend to employ FKK model implementations for practical applications.

6 The Two-Step Cross-Section: Residual-System Statistics

In this section we will outline the consequences of the residual-system statistics hypothesis (12). Using the previously developed framework both the TUL⁷) and the NWY⁸) models can be derived¹). We will also mention the implications of the on-shell approximation in conjunction with residual-system statistics, and give a comparison with the leading-particle statistics results.

6.1 The TUL Model

Here, the formal development is completely analogous to that of Sec. 5, with the exception that we use residual-system statistics instead of leading-particle statistics. Assuming residual-system statistics for the final states *and* the intermediate states (this is called the adiabatic approximation), we find for the two-step energy averaged cross-section:

$$\begin{aligned} \frac{d^2\sigma^{(2)}}{d\Omega dE_k} &= \sum_{\mu} \sum_{\nu} \int dE'_x \hat{\rho}_{1\mu}(E'_x) \hat{\rho}_{1\nu}(E''_x) \left| \int dk_1 \langle \chi^{(-)}(\mathbf{k}) | \langle 1\nu | V | 0 \rangle | \chi^{(+)}(\mathbf{k}_1) \rangle \right. \\ &\times \left. \frac{1}{E - E'_x - E_{k_1} + i\epsilon} \langle \hat{\chi}^{(+)}(\mathbf{k}_1) | \langle 1\mu | V | 0 \rangle | \chi^{(+)}(\mathbf{k}_0) \rangle \right|^2. \end{aligned} \quad (19)$$

Together with Eq. (13) for the one-step cross-section, this constitutes the TUL model. Taking the independent-particle limit here does not make much sense, since the presence of H_1 is necessary to generate the statistics, in contrast to the leading-particle statistics case.

Comparing Eq. (19) with the analogous leading-particle statistics cross-section (17) demonstrates that leading-particle statistics is a stronger assumption than residual-system statistics. Equation (17) resembles, but is simpler than the TUL equation (19), since in the former the interference effects related to the leading particle are also eliminated (*i.e.*, the integral over \mathbf{k}_1 is *outside* the square), while the residual-system statistics employed in this section merely destroys those of the $A - 1$ particle states. This is physically understandable, because leading-particle statistics makes assumptions about the behavior of the leading particle, whereas residual-system statistics does not.

6.2 The NWY Model

The NWY model⁸) is identical to the TUL model for the first step. For the intermediate stage of the second step the NWY model assumes that additional particle-hole creation is a much faster process than residual configuration mixing (while the TUL model takes it the other way around). This so-called sudden approximation gives the two-step cross-section:

$$\begin{aligned}
\overline{\frac{d^2\sigma^{(2)}}{d\Omega dE_k}} &= \sum_{i,j,k,l} \hat{\rho}_{2ijkl}(E_x) \left| \int d\mathbf{k}_1 \langle \chi^{(-)}(\mathbf{k}) \right| \\
& \left[\langle p_i h_j | V | 0 \rangle | \chi^{(+)}(\mathbf{k}_1) \rangle \frac{1}{E - E_{1kl} - E_{k_1} + i\epsilon} \langle \hat{\chi}^{(-)}(\mathbf{k}_1) | \langle p_k h_l | V | 0 \rangle \right. \\
& + \langle p_i h_l | V | 0 \rangle | \chi^{(+)}(\mathbf{k}_1) \rangle \frac{1}{E - E_{1kj} - E_{k_1} + i\epsilon} \langle \hat{\chi}^{(-)}(\mathbf{k}_1) | \langle p_k h_j | V | 0 \rangle \\
& + \langle p_k h_l | V | 0 \rangle | \chi^{(+)}(\mathbf{k}_1) \rangle \frac{1}{E - E_{1ij} - E_{k_1} + i\epsilon} \langle \hat{\chi}^{(-)}(\mathbf{k}_1) | \langle p_i h_j | V | 0 \rangle \\
& \left. + \langle p_k h_j | V | 0 \rangle | \chi^{(+)}(\mathbf{k}_1) \rangle \frac{1}{E - E_{1il} - E_{k_1} + i\epsilon} \langle \hat{\chi}^{(-)}(\mathbf{k}_1) | \langle p_i h_l | V | 0 \rangle \right] \\
& \left| \chi^{(+)}(\mathbf{k}_0) \right|^2. \tag{20}
\end{aligned}$$

where we have used a more explicit particle-hole notation. In contrast to the other two-step models we have discussed so far, the two-step cross-section of the NWY model employs a statistical energy average only once. As a consequence, the final state ‘remembers’ which particle-hole pair was created in the intermediate step. Thus, the NWY model uses a weaker statistical hypothesis than the other models and gives therefore rise to a more complicated expression.

6.3 Residual-System Statistics and the On-Shell Approximation

Previously we have argued that in conjunction with leading-particle statistics the on-shell approximation yields a simple and transparent model, *i.e.* the FKK model. Combining residual-system statistics and the on-shell approximation gives the two-step cross-section:

$$\begin{aligned}
\overline{\frac{d^2\sigma^{(2)}}{d\Omega dE_k}} &= \pi^2 \sum_{\mu} \sum_{\nu} \int d\mathbf{k}_1 \int d\Omega'_1 \rho(k_1) \hat{\rho}_{1\nu}(E'_x) \hat{\rho}_{1\mu}(E'_x) \\
& \times \langle \chi^{(+)}(\mathbf{k}_0) | \langle 0 | V | 1\mu \rangle | \hat{\chi}^{(+)}(k_1, \Omega'_1) \rangle \langle \chi^{(+)}(k_1, \Omega'_1) | \langle 0 | V | 1\nu \rangle | \chi^{(-)}(\mathbf{k}) \rangle \\
& \times \langle \chi^{(-)}(\mathbf{k}) | \langle 1\nu | V | 0 \rangle | \chi^{(+)}(\mathbf{k}_1) \rangle \langle \hat{\chi}^{(+)}(\mathbf{k}_1) | \langle 1\mu | V | 0 \rangle | \chi^{(+)}(\mathbf{k}_0) \rangle. \tag{21}
\end{aligned}$$

Accordingly, residual-system statistics together with the on-shell approximation leads to a model that is simpler than the full TUL model. It is interesting to compare the above result with the FKK result which was obtained by using leading-particle statistics combined with the on-shell approximation. We see that in the case discussed here there is energy conservation in the intermediate step (due to the on-shell approximation), but there are still interference terms left regarding the intermediate angle related to the leading particle. This is to be expected because residual-system statistics does not say anything about the leading particle. Hence, it does not lead to a convolution structure as is the case in the leading-particle statistics theory. This confirms that the structure of the FKK model cannot be obtained by means of residual-system statistics, and thus that the FKK theory is essentially a leading-particle statistics theory.

7 Summary

The analysis given in this paper intends to provide an integrated perspective on the similarities and differences between the many current theories of MSD reactions in the continuum. We have argued that, starting from the framework of distorted wave theory, there are essentially two different possibilities to generate a statistical MSD theory. The first is to introduce a randomness postulate that we have denoted *leading-particle statistics*. Here, it is assumed that at each step many states are accessible to the leading continuum particle and that the associated residual matrix elements are randomly distributed. The second possible randomness postulate, called *residual-system statistics*, is to assume that there is a random configuration mixing due to the residual interactions within the residual nucleus. The latter hypothesis does not make any statistical assumption about the interactions of the leading particle. These physically different randomness postulates generate two distinct classes of statistical MSD theories.

As discussed in Sec. 3, residual-system statistics is related to H_1 and leading-particle statistics is related to V . Employing these statistical hypotheses produces a variety of different MSD models. Using residual-system statistics yields the TUL model⁷) as well as the NWY model⁸). The difference is that the former applies residual-system statistics at all steps (the ‘adiabatic’ approximation), while the latter applies it only in the final step, because it was argued in⁸) that in the intermediate steps particle-hole creation is a faster process than configuration mixing (the ‘sudden’ approximation). This is shortly discussed in Sec. 4 for the first step and in Sec. 6 for the second step.

We have presented a new leading-particle statistics theory for MSD reactions. Its one-step cross-section is given by Eq. (13) and its two-step cross-section by Eq. (17).

Interestingly, the one-step expression (??) of our leading-particle statistics model is identical to that of the TUL and NWY models, although the physical basis of the derivation is entirely different. In addition, it has been shown that no statistical hypothesis is needed in obtaining the first-step result (16) of the independent particle model. These conclusions are of practical importance, because the first step provides the major contribution (typically 80 per cent, as also illustrated in Sec. 4.3) to the MSD cross-sections.

Another interesting conclusion is that the above leading-particle statistics theory reduces to the FKK model if we in addition employ the on-shell approximation and take the independent-particle limit (*i.e.*, neglect H_1), see Sec. 5.2. This shows that the FKK model⁶) is to be understood as being based upon leading-particle statistics. Hence, it is physically not justified to view the FKK model as a simplification of the TUL model, as argued in¹¹), since the latter employs residual-system statistics. In other words, the TUL model needs to employ the presence of H_1 to generate its statistical foundation, whereas the FKK model can completely neglect this term of the Hamiltonian. We have furthermore indicated (Sec. 5.3) how the semi-classical approaches such as the generalized exciton models^{2,3}) can be interpreted as further phenomenological simplifications of the leading-particle statistics and FKK models. Accordingly, the relationships between the various MSD models can be represented as in Fig. 4. Here, LPS stands for leading-particle statistics, RSS for residual-system statistics and IPM for independent particle model.

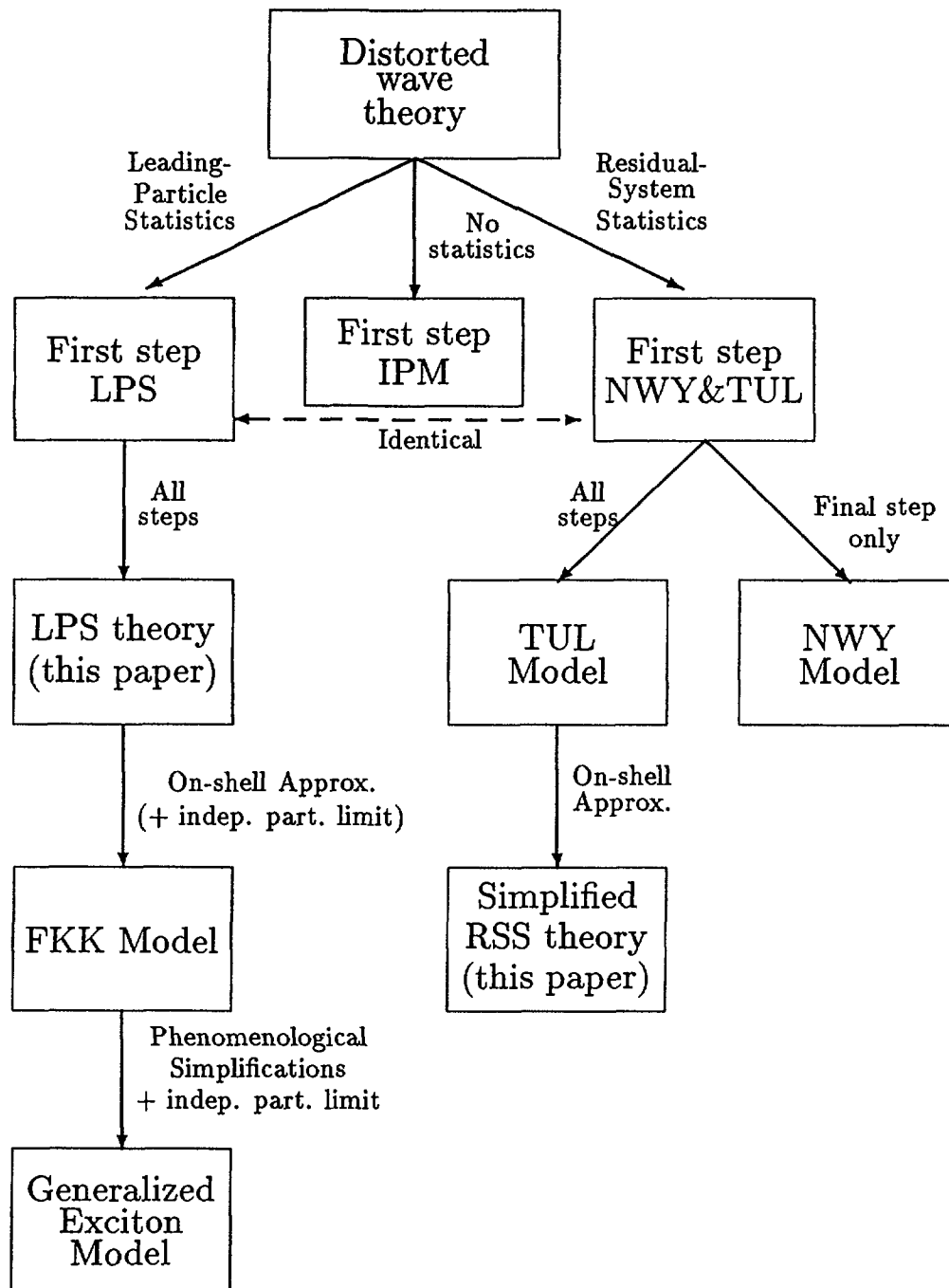


Figure 4: Family tree of statistical MSD-theories

References

1. A. J. Koning and J. M. Akkermans, to appear in *Ann. of Phys.* (1991)
2. G. Mantzouranis, H. A. Weidenmüller and D. Agassi, *Z. Phys.* **A276** (1976) 145
3. H. Gruppelaar, P. Nagel and P. E. Hodgson, *Riv. Nuovo Cimento* **9** (1986) 1
4. J. M. Akkermans, H. Gruppelaar and G. Reffo, *Phys. Rev.* **C22** (1980) 73
5. I. Kumabe and Y. Watanabe, *Phys. Rev.* **C40** (1989) 535

6. H. Feshbach, A. Kerman and S. Koonin, *Ann. Phys.* **125** (1980) 429
7. T. Tamura, T. Udagawa and H. Lenske, *Phys. Rev.* **C26** (1982) 379
8. H. Nishioka, H. A. Weidenmüller and S. Yoshida, *Ann. Phys.* **183** (1988) 166
9. J. M. Akkermans and E. Běták, *Ann. Phys.* **194** (1989) 148
10. T. Tamura, T. Udagawa, D. H. Feng and K. K. Kan, *Phys. Lett.* **66B** (1977) 109
11. T. Udagawa, K. S. Low and T. Tamura, *Phys. Rev.* **C28** (1983) 1033
12. C. Kalbach and F. M. Mann, *Phys. Rev.* **C23** (1981) 112
13. C. Kalbach, *Phys. Rev.* **C37** (1988) 2350
14. O. Bohigas and H. A. Weidenmüller, *Ann.Rev.Nucl.Part.Sci.* **38** (1988) 421
15. H. A. Weidenmüller, *Ann. Phys.* **192** (1989) 231
16. J. M. Akkermans and A. J. Koning, *Phys. Lett.* **234B** (1990) 417
17. D. Agassi, H. A. Weidenmüller and G. Mantzouranis, *Phys. Rep.* **22** (1975) 145
18. R. R. Whitehead, A. Watt, D. Kelvin and A. Conkie, *Phys. Lett.* **76B** (1978) 149
19. J. J. M. Verbaarschot and P. J. Brussaard, *Phys. Lett.* **87B** (1979) 155
20. M. R. Zirnbauer, J. J. M. Verbaarschot and H. A. Weidenmüller, *Nuc. Phys.* **A411** (1983) 161
21. B. A. Brown and G. Bertsch, *Phys. Lett.* **148B** (1984) 5
22. H. Dias, M. S. Hussein, N. A. de Oliviera and B. H. Wildenthal, *J. Phys.* **G15** (1989) L79
23. T. Tamura, T. Udagawa and M. Benhamou, *Comput. Phys. Commun.* **29** (1983) 391
24. F. C. Williams, *Nucl. Phys.* **A166** (1971) 231
25. R. Bonetti, M. Camnasio, L. C. Milazzo and P. E. Hodgson, *Phys. Rev.* **C24** (1981) 71
26. H. Sakai, *Nucl. Phys.* **A344** (1980) 41
27. K. Sato and S. Yoshida, *Z. Phys.* **A327** (1987) 421
28. K. Sato and S. Yoshida, *Z. Phys.* **A330** (1988) 265
29. A. Marcinkowski, R. W. Finlay, J. Rapaport, P. E. Hodgson and M. B. Chadwick, *Nucl. Phys.* **A501** (1989) 1
30. H. Feshbach, *Ann. Phys.* **159** (1985) 150
31. C. K. Cline and M. Blann, *Nucl. Phys.* **A172** (1971) 225
32. K. Kikuchi and M. Kawai, *Nuclear matter and nuclear reactions* (North-Holland Publishing Co., Amsterdam, 1968)

INFLUENCE OF COLLECTIVE EXCITATIONS ON PREEQUILIBRIUM AND EQUILIBRIUM PROCESSES

A.V. Ignatyuk, V.P. Lunev

Institute of Physics and Power Engineering, Obninsk, USSR.

A B S T R A C T

In all models used for calculations of nuclear cross sections, the reaction mechanisms are separated into one-step and multistep direct, multistep compound, preequilibrium and compound equilibrium. However, essential variances in estimates of the direct and preequilibrium process contributions still exist. This paper presents a demonstration of the connection of these variances with the influence of collective excitations on the direct and compound processes.

In all models used for calculations of nuclear cross sections the reaction mechanisms are separated on one- and multistep direct, multistep compound preequilibrium and compound equilibrium /1/. But essential variances in estimations of the direct and preequilibrium processes contributions exist nowadays. We want to demonstrate the connection of these variances with the influence of collective excitations on the direct and compound processes.

Integral contribution of the direct processes

The results of calculations of integral cross sections for all three types of processes mentioned above are shown in Figs. 1-3. The dashed curves present the result of Feshbach-Kerman-Koonin approach with the direct processes contribution estimated empirically from the observed asymmetry of the angular distribution of secondary particles /2/. The solid lines are the results of more complex and consistent analysis, where the direct processes cross sections are calculated in terms of the couple channel and DWBA approaches /3/.

The direct transitions probabilities are determined by the dynamic deformation parameters β_λ of the multipole coherent nuclear excitations /4/. For the nuclei under consideration there

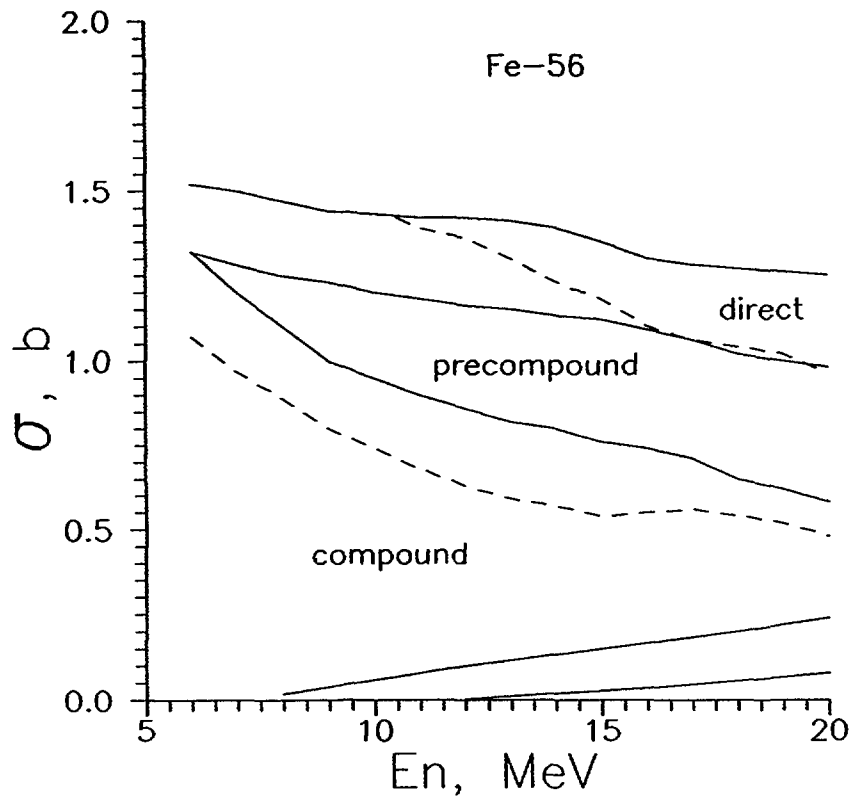


Fig.1. The contributions of different reaction mechanisms to the inelastic scattering cross sections as a function of incident neutron energy for the Fe-56 nucleus. The dashed lines represent the results of FKK approach and solid lines are the calculations taking into account the collective effects.

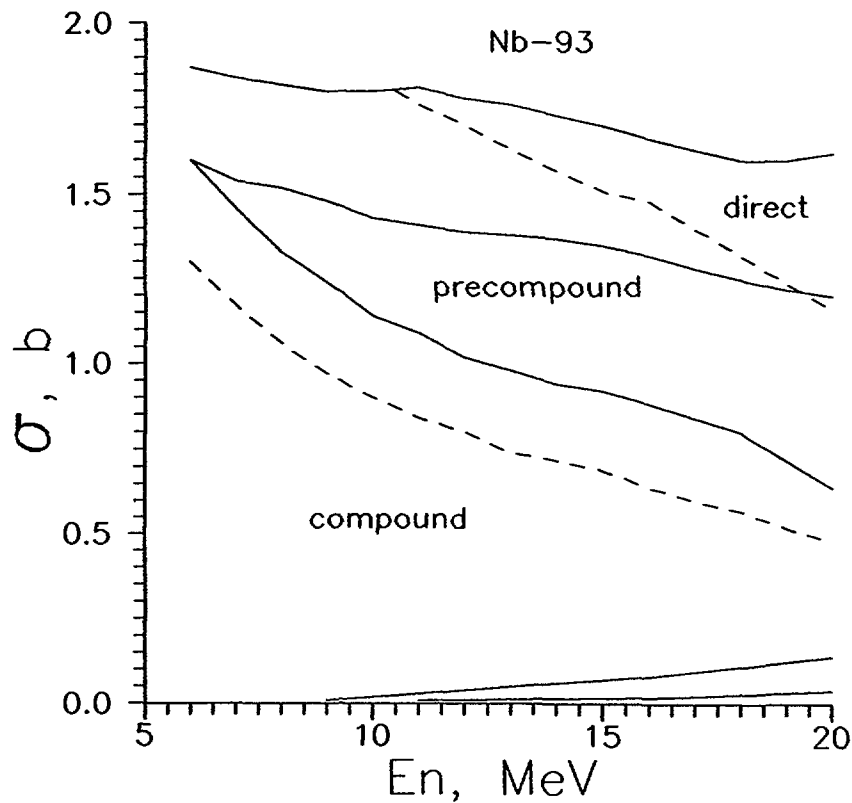


Fig.2. The same as fig.1 for Nb-93.

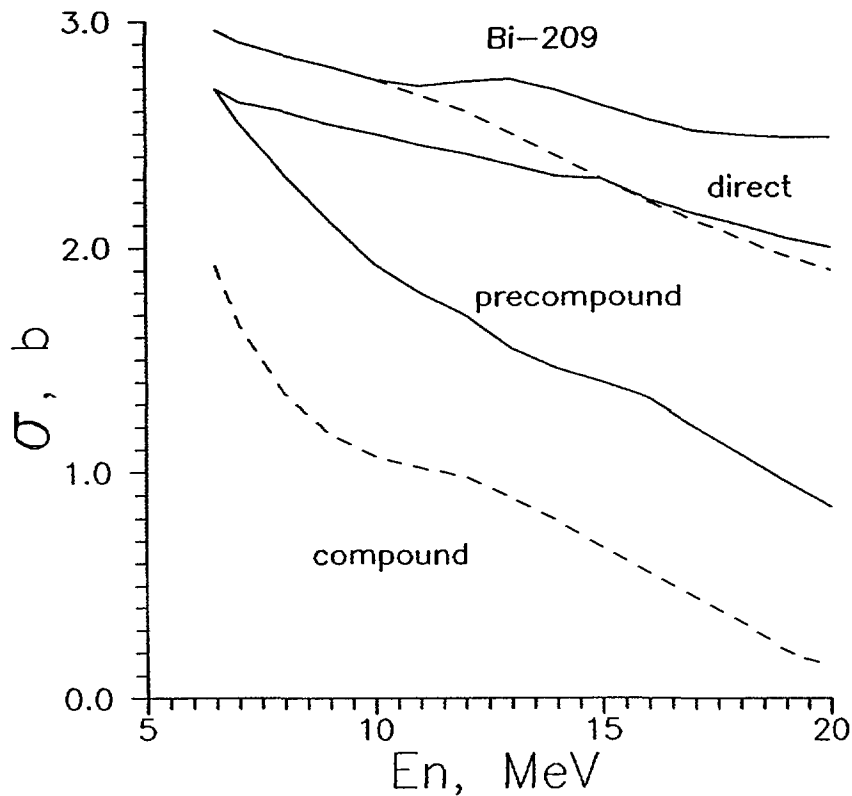


Fig.3. The same as fig.1 for Bi-209.

is relatively detailed experimental information about these parameters in the excitation energy region up to 7 MeV. These data allows to calculate correctly the contribution of the direct processes to the neutron scattering cross sections for incident energy up to 14 MeV. As the incident particles energy increases the pigmi and giant resonances of different multipolarity as well as superposition of these resonances with low-laying states begin to contribute to the direct transitions.

Large uncertainties exist nowday in the calculations of the parameters β_λ especially for multipolarities $\lambda > 4$ /3/. These uncertainties immediately transform into the ambiguities of the calculated cross sections for direct transitions. Also there are some problems concerning the calculations of multistep direct transitions via quasideuteron intermediate states /5/. Nevertheless the general conclusion about the dominant role of collective excitations in the description of the direct processes seems doubtless proved /3, 5, 6/.

Collective enhancement of the level density

The level density of excited nuclei is one of the main characteristic in the statistical description of compound processes. For its calculation the Fermi gas model most frequently is used with the parameters obtained from fitting the observed densities of neutron resonances and low-lying levels. But such a model does not considers correctly the shell effects, pairing correlations of the superconducting type and collective nuclear excitations. These effects must be included in the consistent analysis of experimental data. That can be done in frame of microscopic approaches based on the generalized superfluid model /7/.

Fig. 4 shows the results of the level density calculations in different approaches for the ^{91}Zr nucleus. The effective pairing interaction is reliably qualified from the odd-even differences of

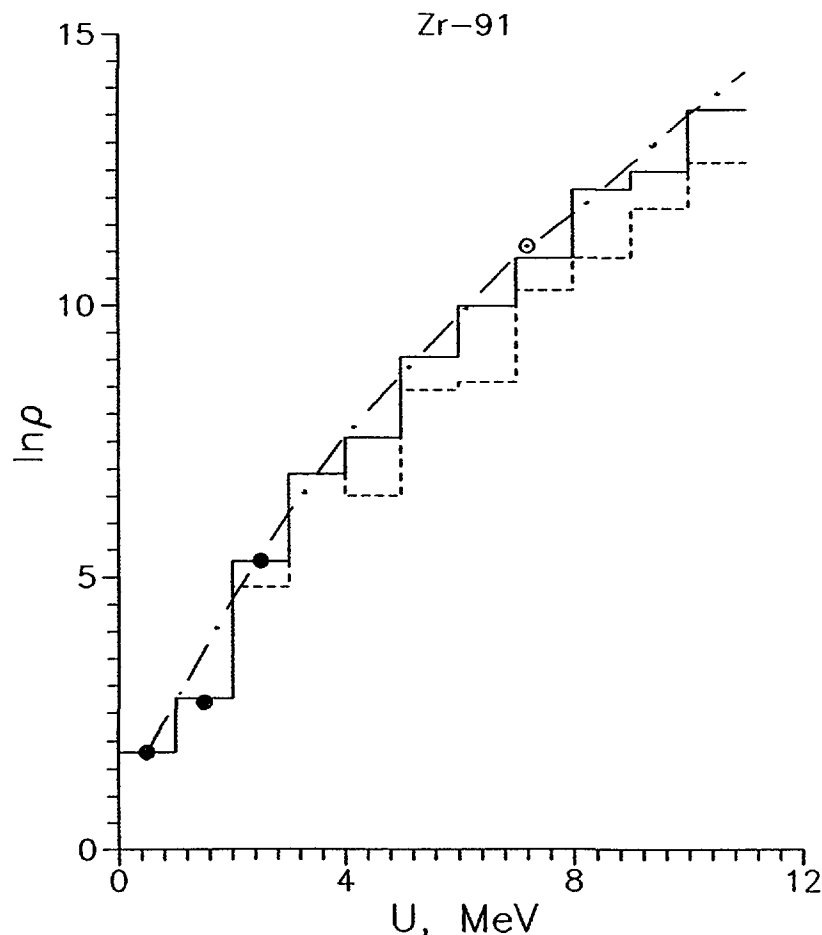


Fig.4. Energy dependence of states density for the Zr-91 nucleus. The histograms shows the microscopical combinatorial calculations of quasiparticle's excitations (dashed lines) and with addition of collective modes (solid lines), the dot-dashed line is the phenomenological description, dark and bright circles are the experimental data.

nuclear masses, therefore the total density calculations of all possible quasiparticles excitations do not contain fitting parameters. Still, we can see, that the level density calculated in this approach do not reproduce the experimental data. We should use the vibration enhancement of the level density both for low excitation energies and for region of neutron resonances. The methods of the collective enhancement calculations considered in Refs. /8, 9/. Only after inclusion of such enhancement we come to agreement with the experimental data.

In the phenomenological approach developed in Refs. /7,10/ we use the same relations of the superfluid nuclear model and nearly the same coefficient of the level density vibration enhancement, but the correlation functions and the level density parameters are obtained by fitting the experimental data. As a rule these parameters are noticeably distinguished from the parameters of the Fermi-gas model, that describes the same data. Differences of the phenomenological description and microscopic calculations are relatively small if we use the same factors of the level density enhancement.

In analysis of the description of collective effects in highly excited nuclei it is of more interest to compare the collective enhancement factors than the total level densities. Fig. 5 shows these factors calculated in different approaches /9/. All microscopic calculations prove invalidity of the adiabatic approximation for vibration modes in highly excited nuclei and the necessity of dumping for the vibration enhancement factors as the excitation energy increases. This is also indicated by "experimental" data obtained from the ratio of the observed level densities to the calculated ones in model without collective effects.

Recently new experimental information for the level density was obtained from the neutron spectra analysis in the iron mass region /11/. These data are shown in Fig. 6 together with the phenomenological description of neutron resonance density and low-laying levels. There are many similar examples of the neutron spectra and excitation functions analysis /11/. These examples demonstrate a good agreement between all sets of experimental data and the generalized superfluid model predictions.

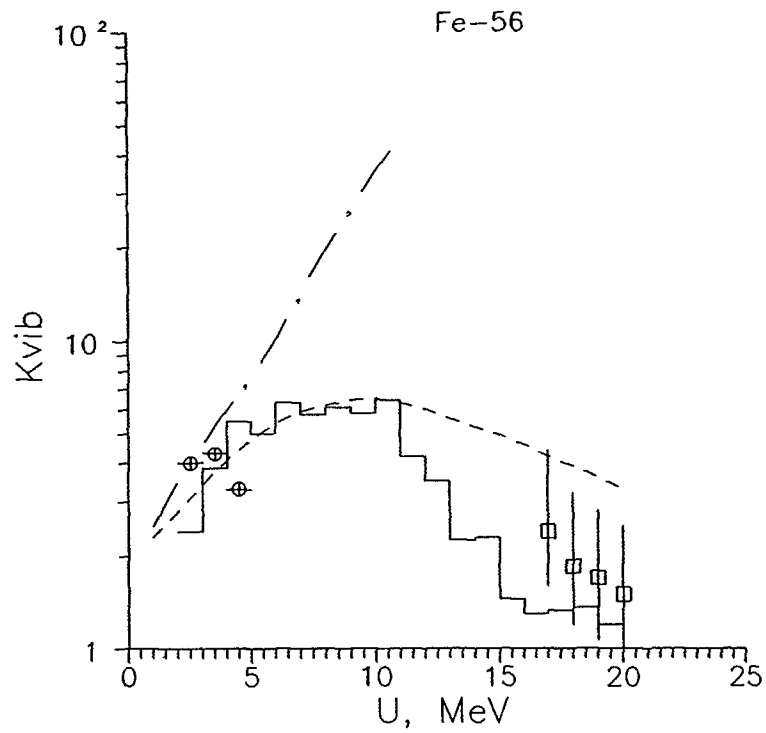


Fig.5. Energy dependence of the vibration enhancement factors for Fe-56 as a function of excitation energy. The dot-dashed lines are the adiabatic estimation, the dashed line is the phenomenological description /10/, the histogram is the combinatorial calculations /9/, the symbols are the evaluations from experimental data.

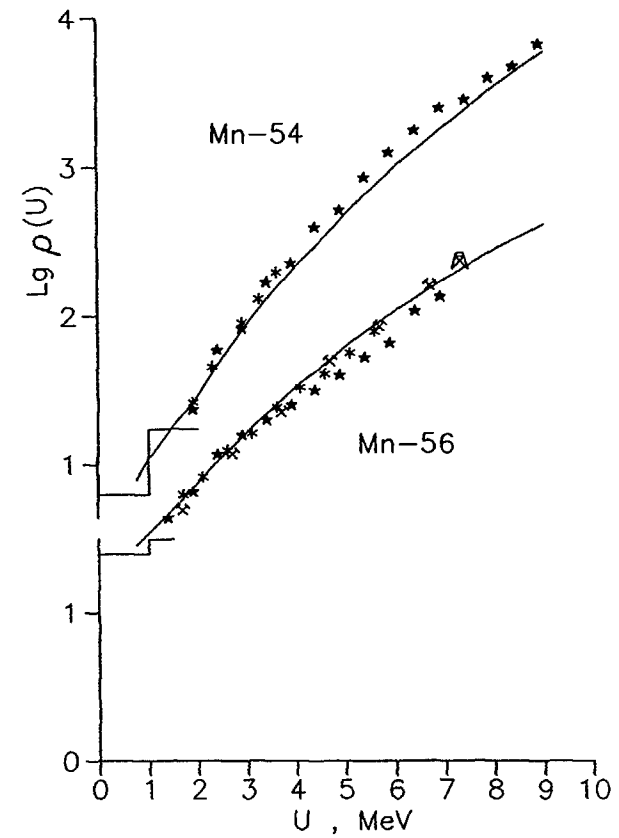


Fig.6. Level density data for Mn-54 and Mn-56 obtained from (n,p) and (n, α) spectrum analysis. The solid line shows the phenomenological description.

Influence of collective effects on the state densities with a fixed number of quasiparticles

If we want to achieve a consistent description of preequilibrium and equilibrium processes, the calculations of quasiparticle excitations in preequilibrium stage must be realized in the same approach as the total level density description. Within the framework of generalized superfluid model alongside with the particle-hole excitations the particle-particle and hole-hole excitations should be considered, as well as collective excitations, which correspond to coherent superposition of the interactive quasiparticle excitations. Stated differently, together with the diagrams in Fig. 7a usually considered in preequilibrium models /1, 2/, the diagrams in Figs. 7b and 7c should be taken into account.

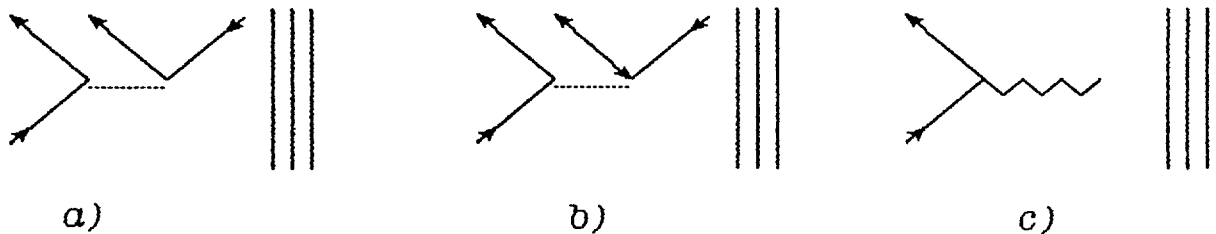


Fig.7. Diagrams for $n \rightarrow n+2$ transitions in the superfluid model (a,b) and with the collective excitation inclusion (c).

Fig. 8 demonstrates the differences of the 3- and 5- quasiparticles state densities connected with account particle-particle and hole-hole excitations as well as collective modes. Inclusion of collective effects results in n -quasiparticle excitation threshold's decrease and a certain increase in their density for low energy region. For higher energies the density of these excitations does not differ significantly from the predictions of the "pure" superfluid model /12,13/.

A more complicated problem is consideration of mean lifetimes of n -quasiparticles excitations. Using usual separation of active and passive quasiparticles the density of accessible states can be obtained on the basis of the relationship:

$$\omega_n^+(U) = \omega_n^{-1}(U) \int_0^U d\varepsilon \omega_1(\varepsilon) \omega_3(\varepsilon) \omega_{n-2}(U-\varepsilon)$$

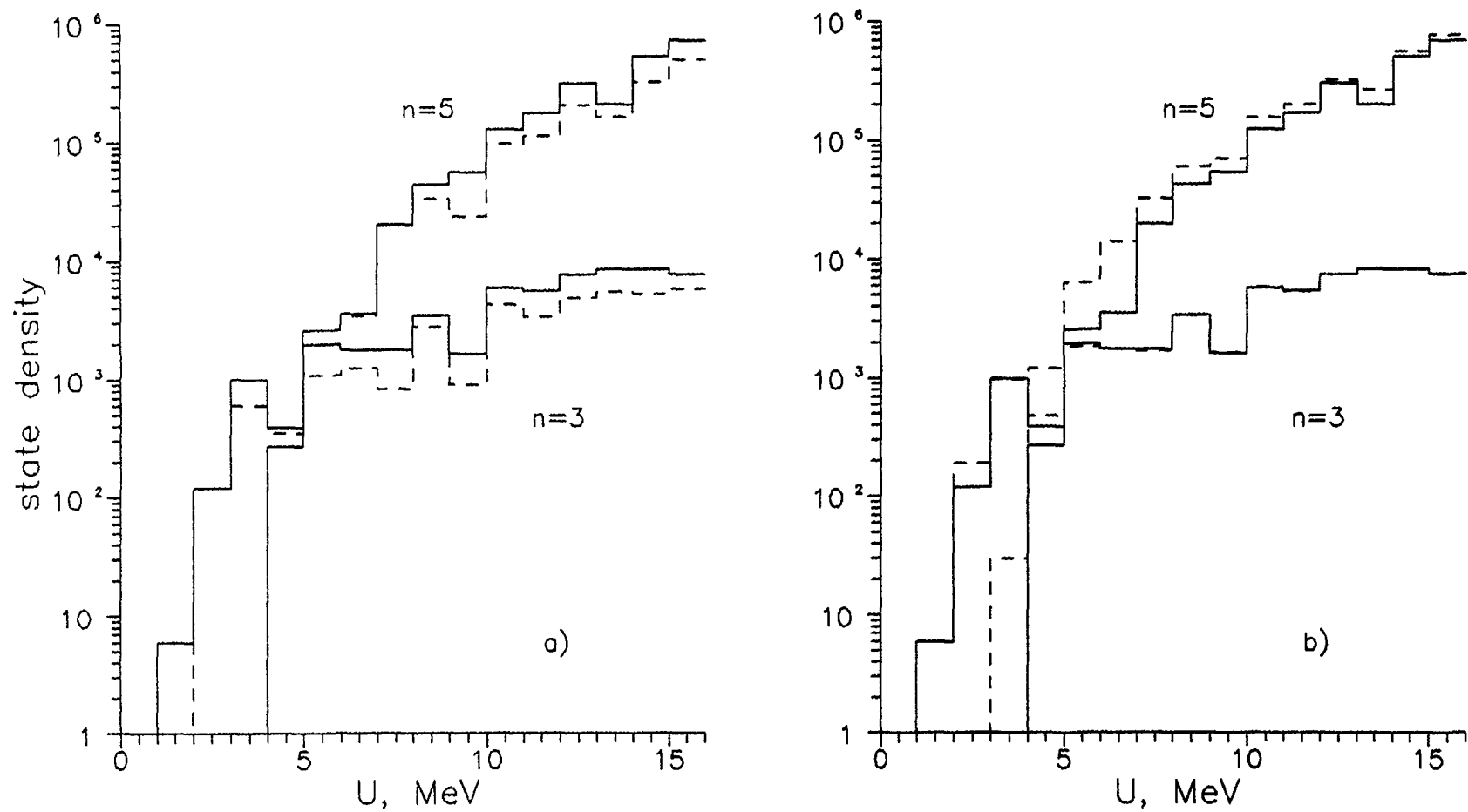


Fig.8. Energy dependence of the state densities for 3- and 5-quasiparticle excitations in Zr-91:
 a) p-h excitation only (dashed lines) and all quasiparticle excitation (solid lines);
 b) quasiparticle excitations only (solid lines) and collective modes included (dashed lines).

Collective effects should be included in the corresponding calculations of the partial densities. On the other hand, for the simplest configurations, $n = 3$ for example, the direct combinatorial calculations of the densities corresponding to diagrams Fig. 7 can be realized. Such calculations will demonstrate the influence of the Pauli's principle limitations and the discrete quasiparticle spectrum structure on the transition state densities.

But in lifetime calculations the issue of separating the density of accessible states and averaged matrix element remains to be settled. After inclusion of collective excitations this question became more important due to their higher values of transition probabilities in comparing with quasiparticles transitions. To answer on these questions we are going to make calculations of the mean lifetimes for 3-quasiparticle excitations with realistic residual interaction. We think that only such approach will be able to solve consistently the existing problem of the preequilibrium processes description.

REFERENCES

1. Feshbach H., Kerman A., Koonin S. Ann. Phys., 1980, v.125, p.429.
2. Hodgson P.E. In: Proc. Meeting on Nuclear Theory for Fast Neutron Nuclear Data Evaluation. Vienna: IAEA-TECDOC-483, 1988, p.214.
3. Ignatyuk A.V., Lunev V.P. In: Proc. Meeting on Preequilibrium Nuclear Reactions. Paris: OECD, 1988, p. 233.
4. Bohr A., Mottelson B. Nuclear Structure. v.2. N.Y.: Benjamin W.A. INC., 1974.
5. Tamura T., Udagava T. Phys.Rev., 1982, v.C26, p.379.
6. Marcinkowski A. In Ref./4/, p.209.
7. Ignatyuk A.V. Statistical properties of excited atomic nuclei /Russian/. Moscow: Energoatomizdat, 1983.
8. Blokhin A.I., Ignatyuk A.V. In: Proc. Meeting on Methods for Calculations of Nuclear Data for Structural Materials. Vienna, INDC-193/L, 1988, p.81.
9. Ignatyuk A.V., Lunev V.P., Shubin Yu.N. -In Ref./2/, p.122.

10. Grudzevich O.T., Ignatyuk A.V., Plyaskin V.I., Zelenetsky A.V.
In: Nucl.Data for Science and Technology. (Mito 1988). JAERI,
1988, p.767.
11. Grudzevich O.T. et al. In: Proc.Meeting on Nuclear Level
Density. Bologna,1989.
12. Fu C.Y. Nucl.Sci.Eng.,1984, v.86, p.344.
13. Herman M., Reffo G. Phys.Rev.,1987, v.C36, p.1546.